Hierarchical modelling of softwood hygro-elastic properties

by
Jonathan J. Harrington

A thesis presented for the degree of
Doctor of Philosophy
in
Mechanical Engineering
at the
University of Canterbury,
Christchurch, New Zealand.

18 September 2002

For Kiri.

Takoto kau ana te whaānau a Tāne.

Abstract

The hygro-elastic behaviour of wood under load or when subjected to environmental changes is of considerable practical interest. This behaviour can be determined by exhaustive experimentation, but such an approach makes explaining its origin, which from some perspectives can be more important than its prediction, problematic. This thesis attempts to establish a model (actually a hierarchical set of models) that goes some way toward both predicting and explaining the mechanics of wood. Attention is focused on radiata pine because of the commercial importance of this species in New Zealand, but much of the modelling is applicable to other softwoods and, to a lesser extent, hardwoods.

Wood can be looked on as a hierarchical material, that is as a material possessing structure at multiple scales. For many problems involving such materials the heterogeneous structure at a particular scale can be replaced by a homogeneous one possessing similar properties. Homogenization theory defines what is meant by similar and also provides the means for determining these effective properties.

In this thesis wood structure is treated at three different scales: namely the supramolecular or nanostructural, the cell-wall or ultrastructural and the cellular or microstructural scales. Homogenization across these levels is performed either analytically or numerically, using the finite element method.

At the smallest scale, the constituent phases are treated as homogeneous continua. Models for the hygro-elastic phase properties, as functions of temperature and moisture content are developed based on available experimental data.

The models devised to describe wood at each of the above mentioned scales introduce a large number of structural parameters, such as constituent mass fractions and cell-wall layer volume fractions. In the abscence of specific data, estimates for these parameters are developed based on data from the literature. Together with these auxiliary models, the main sequence of structural models can then be used to obtain estimates for the material properties of small domains within macrostuctural models.

Acknowledgements

The research presented in this thesis was supported by a scholarship from the New Zealand Forest Research Institute, and was originally jointly supervised by Prof Jeremy Astley from the Department of Mechanical Engineering at the University of Canterbury and by Dr Rolf Booker of the New Zealand Forest Research Institute. Latterly, supervision has been provided by the late Dr Ken Whybrew and Dr John Smaill, both of the Department of Mechanical Engineering at the University of Canterbury. The guidance offered by these supervisors has been much appreciated.

Over the years numerous people have patiently answered my questions. In particular I would like to thank Dr Brian Butterfield (Department of Plant and Microbial Sciences, University of Canterbury), Dr John Walker (School of Forestry, University of Canterbury), Dr Chris Damaren and Dr Ian Huntsman (Department of Mechanical Engineering, University of Canterbury). I am also indebted to Dr Roger Newman (Industrial Research Limited, Welington), Prof Julian Vincent (Department of Mechanical Engineering, University of Bath) and Dr John Cahn (Materials Science and Engineering Laboratory, NIST) for inspiring discussions.

Dr Ian Cave was responsible for significant advances in the modelling of wood mechanics nearly thirty years ago. The present work is a continuation of what he began and it has been a privelege to have his advice.

Manfred Ingerfeld (Department of Plant and Microbial Sciences, University of Canterbury), Dr Lloyd Donaldson (Forest Research, Rotorua) and Mike Flaws (Department of Mechanical Engineering, University of Canterbury) have all provided valuable assistance with aspects of microscopy.

Many thanks also to the staff of the Engineering Library at the University of Canterbury and the Forest Research Library who have tracked down numerous references, often from rather ill-formed requests.

Dr Robert Evans and colleagues at the CRC for Hardwood Fibre and Paper Science, CSIRO Forestry and Forest Products, generously tested several samples using their magnificent SilviScan tools.

Peter Currie, as well as regularly humiliating me on the squash court, performed sterling service tracing the outlines of thousands of barely discernible cell outlines. For

the latter, thanks Pete.

Stimulation, diversion and encouragement have been provided along the way by my fellow students. In particular, I am grateful to Ra Cleave and Steve Hunt for late night companionship and to Andrew Shaw for the same but in daylight hours.

Above all, I'd like to thank my family: my mother, Joan, whose blind faith in my abilities never wavers; my father, Robin, who no doubt could have done a much better job than I have; my brother, Mark, whose artwork graces chapter 1; and my children, Tui, Tai, Hine and Rua, for putting up my with absence even when I was physically present.

Finally, thank you Kiri, sorry it took so long.

Contents

List of Tables

List of Figures

Chapter 1

Introduction

Numerical simulations, particularly those employing finite element methods, are increasingly being used to investigate the mechanics of wood-based products and processes, e.g. Gustafsson (1997), Ormarsson et al. (1998), Pang (2001). These simulations require considerable quantities of material property data to be supplied, data which can be difficult, if not impossible, to obtain experimentally. Structural data is more readily available, and thus a model that can provide estimates for softwood properties based on structural information is desirable.

More importantly, as opportunities to modify wood increase, structure-property models have the potential to assist in identifying those structural modifications that will effect a particular goal. At the same time they may also help to avoid unwittingly making modifications with detrimental and potentially costly side effects.

Motivated by the above considerations this thesis develops models that relate the properties of softwood to its structure. These models are designed to be flexible so as to permit consideration of the effects on wood properties of a wide range of structural modifications. This flexibility means that there are numerous exogenous variables; so, for use in deriving input for numerical simulations, auxiliary models are provided for many of these variables over the ranges of temperature and moisture content encountered in practice (0–150°C, dry to saturated).

1.1. Softwood structure – a brief review

Before proceeding with discussing how structure-property models might be developed it is worthwhile briefly describing softwood structure. Further structural details can be found in subsequent chapters and in numerous texts, for example Greguss (1972), Côté (1967), Jane (1970), Core et al. (1976), Schweingruber (1978), Butterfield and Meylan (1980), Lewin and Goldstein (1991), Timell (1986a), Dinwoodie (1981, 1989), Fengel and Wegener (1984) Wangaard (1981), Kininmonth and Whitehouse (1991).

The term softwood refers to both a class of tree and to the wood from these trees. Softwoods are conifers, or cone-bearing trees, such as pines, spruces, larches, firs and cedars. Botanically speaking, these trees are gymnosperms of the division Coniferophyta also referred to as the Pinophyta (Sporne, 1965; Lawrence, 1989). Most

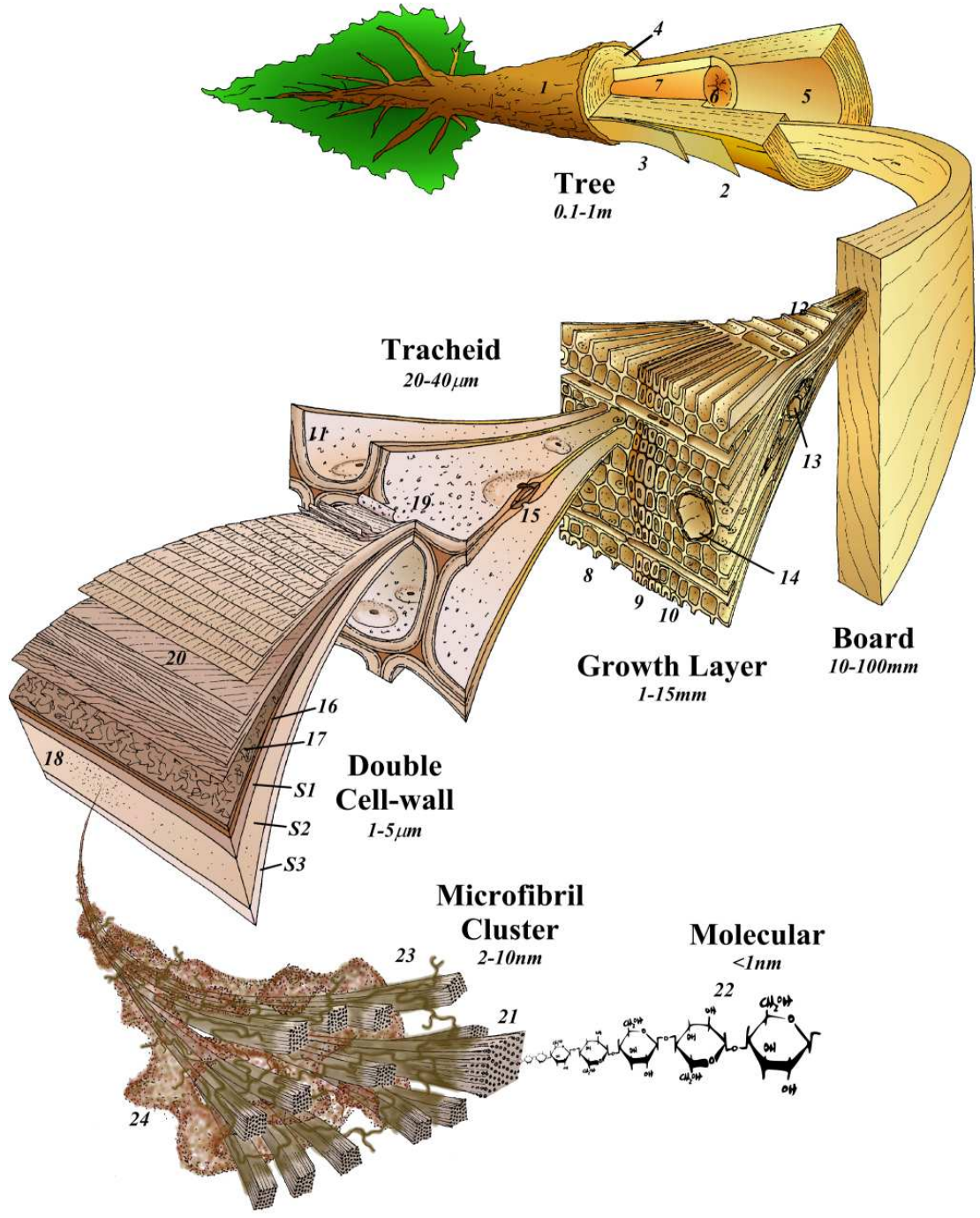

Figure 1.1.: A softwood schematic. The dimensions below each of the scale labels are indicative of the size of structural features at that scale. See the text for details.

softwoods are evergreens, have small narrow leaves and are native to temperate regions. Numerous authors have pointed out that the term softwood is a misnomer and this point is readily conceded as softwoods are not necessarily 'soft', yet the convenience and familiarity of the term outweighs its connotative failings.

The majority of the material in the stem [1][1] of a living tree is dead. However, there is a thin layer of living and dividing cells known as the cambium [2], from which both the phloem and xylem are derived. Outside the cambium is the inner bark [3] which contains the active phloem as well as other tissue. Outside that is the outer bark [4]. Inside the cambium is the xylem or wood. Very few of the cells in the sapwood [5], and none in the heartwood [6], remain alive. Water conduction from roots to crown occurs in the sapwood (primarily in the outer sapwood) but not in the heartwood. In many species the heartwood has a colour quite distinct from that of the sapwood.

Corewood [7] is formed near the centre of the stem, generally making up the first 10–20 growth rings. Depending on the age of the tree, the heartwood may or may not be contained within the corewood.

The shape of a softwood tree is controlled by the production of compression wood. The wood diametrically opposed to compression wood in either stem or branch is known as opposite wood. Normal wood and compression wood are not clearly delineated but form a continuum. While compression wood is vital to the living tree it is undesirable from a utilization standpoint.

Once the tree has been felled and sawn into boards other natural features become evident. These include knots, resin pockets, checks (splits), grain pattern and growth rings. The latter are due to radial variation in the shapes and sizes of cells, generally brought on by seasonal changes. Earlywood [8] is laid down upon commencement of new growth. As the season progresses this gradually changes to latewood [9], passing through a middlewood [10] zone. In some trees an abrupt boundary exists between one season's latewood and the following season's earlywood, in others (particularly those from milder climes) the growth rings are almost invisible.

The predominant type of cell in softwoods is the tracheid [11]. Tracheids make up over 90% of softwood volume and are highly elongated in the direction of the grain. These cells give the stem its strength and stiffness as well as conducting water from the roots to the crown.

In earlywood, the tracheids are larger and thin-walled whereas in the latewood the tracheids are smaller and thick-walled. While the tracheids are aligned with the grain, rays [12] are rows of cells oriented in the radial direction. Each tracheid comes into contact with a ray at some point along its length. The living parenchyma cells in the rays store food reserves and participate in damage control. Associated with some rays are radial resin canals [13]. These have a counterpart in the grain direction known as

[1] Within this section numbers in square brackets refer to the labels in figure 1.1

axial resin canals [14]. Resin canals are tunnels through the woody tissue, and are lined with epithelial cells.

Bordered pits [15] connect the lumens (the spaces previously occupied by the living cells) of adjacent tracheids forming a network in which water can flow. In the earlywood, bordered pits act as valves preventing vapour bubbles from spreading through the sapwood, rendering the tree's water conduction system useless. Other types of pits exist between tracheids and ray cells, and between adjacent ray cells.

The tracheids are glued together by a thin inter-cellular layer, the middle lamella [16]. A cell newly formed by the cambium has only a very thin primary wall [17]. After the cell attains its full size a much thicker secondary wall [18] is laid down inside the primary wall, and then the cell dies. In cross-section the secondary walls of tracheids appear to consist of three layers. These have been denoted S1, S2, and S3, with S1 immediately inside the primary wall and S3 adjacent to the lumen. The lumen surface is often covered with nodules known as warts [19][2].

The three secondary wall layers are built up from hundreds of concentric lamellae. Each cell wall lamella [20] consists of a sheet of long, aligned fibres known as microfibrils [21]. In general, the orientation of the microfibrils varies only a little from one lamella to the next. However, in zones between the major secondary layers abrupt and significant reorientations occur giving rise to layer boundaries. The microfibrils in the lamellae of the inner secondary wall are densely packed and well aligned whereas in the primary wall and the outer S1, the microfibrils have a looser texture.

The microfibrils are highly ordered bundles of cellulose molecules [22]. Each of these molecules is made up of tens of thousands of glucose residues strung together in a linear fashion.

The microfibrils themselves are each surrounded by a hemicellulosic sheath [23] and embedded in a matrix [24]. This matrix is a macromolecular complex of lignins, hemicelluloses and water. The hemicelluloses or polyoses are polysaccharides like cellulose but are much shorter, branched, and incorporate residues of other sugars as well as glucose. Portions of the hemicellulose chains may bind to the outermost parts of the microfibrils, creating the microfibrillar cortex or sheath. The hemicellulose chains in the sheath may form direct links with other microfibrils. The hemicelluloses are also chemically bonded to the lignins.

1.2. Hierarchical modelling

How then can softwood properties be related to structure? There are essentially two choices: the correlative and the constructive approaches. While these methodologies

[2] From a mechanical viewpoint the compound structure formed by the walls of two adjoining cells along with the intermediate middle lamella is a fundamental entity denoted herein as the 'cell-wall' as distinct from the 'cell wall' of a single cell.

are fundamentally different they both involve modelling.

A model is an object or concept that is used to represent something else, with the motivation for modelling usually being to reduce or translate the latter entity to a more tractable form. In many ways a model is a metaphor (a statement which itself is both model and metaphor). Models can be classified according to their intended function, for example predictive and illustrative models. Models can also be classified by the elements from which they are built, for example papier-maché and mathematical models. Herein it is predictive mathematical models which concern us, that is models built from mathematical concepts and which produce quantitatve results.

Correlative models take a set of observations, such as basic density or growth ring number, as input and produce a set of properties as output without making any causal connections between inputs and outputs. They are inherently 'black-box' in nature, using techniques such as regression or neural networks, and the wood science literature is replete with them, Bodig and Goodman (1973) is a good example.

Correlative models suffer from a number of drawbacks. Creation of the model requires measuring the properties of some set of specimens whose structure has also been determined. Except for extremely simple structures this means evaluating a large number of specimens. The lack of causal connections severely limits the insight that can be gained from a correlative model. In some circumstances the correlative approach is simply not possible, for example if the size of the specimen is too small to test, or if obtaining the test specimen alters its properties. Except to note that such models exist (in abundance), and can be of great utility, nothing further shall be said about them.

In contrast to the correlative approach, constructive models encapsulate structure-property relationships in a deterministic fashion and property predictions are based on reasoning regarding structure and composition. The structural inputs are processed within some suitable theoretical framework to yield the output properties.

All materials exhibit structure at multiple length scales. In softwood structure can be observed at spatial scales ranging from 10^0 m (knot whorls, branches) to 10^{-10} m (molecular structure). To include all of these features in a single constructive model is not practical. Instead the structure can be resolved at a finite number of scales or levels. The heterogeneous material structure at a given scale is replaced by a homogenous average material at a higher scale, a process referred to as homogenization. This approach, known as hierarchical or multiscale modelling, has been used before to model material structure-property relations , for example by Lakes (1993), Crolet et al. (1993), Hollister et al. (1991); Hollister and Kikuchi (1994), Akiva et al. (1998), Rho et al. (1998), Franciosi and Gaertner (1998), Rammerstorfer et al. (1999), Dimitrienko (1999), Su and Cui (1999), Takano et al. (1999), Tadmor et al. (2000), and has been applied to wood by Mark (1967), Cave (1973, 1978a,b), Norimoto et al. (1978), Salmén and

de Ruvo (1985), Navi (1988); Navi and Huet (1989), Koponen et al. (1989, 1991), Vieville and Guitard (1996), Harrington et al. (1998); Astley et al. (1998), Holmberg et al. (1999); Persson (2000).

1.3. Scope

In this thesis only linear hygro-elastic properties, that is the linear elastic moduli and hygral expansion coefficeients or their equivalents, are considered. While wood exhibits complex time and path dependent responses to mechanical loading and changes in moisture content, for short time scales, low loads and small environmental perturbations wood can usefully be treated as a linear hygro-elastic material. In other regimes, while the quantitative results may be unrealistic, useful qualitative results can be obtained by such a treatment. At the very least, a linear hygro-elastic analysis provides a starting point.

Softwoods, especially radiata pine (*Pinus radiata* D. Don.), are of primary commercial importance in New Zealand. Thus attention is restricted to softwoods in general and where possible to radiata pine in particular.

Only normal wood is modelled. Severe compression wood, that is to say compression wood having a qualitatively different structure to normal wood, is not considered. Nor is consideration given to degraded or treated wood.

While it was stated earlier that wood structure ranges over length scales of up to a metre, the largest structural features considered here have dimensions of millimetres. At the other end of the spectrum the modelling descends only to the supramolecular or nanostructural scales.

Changes in both temperature and moisture content significantly alter the mechanical properties of wood (Gerhards, 1982; Green et al., 1999) and these effects are considered. Changes in temperature and moisture content also lead to changes in volume. The direct influence of temperature on wood volume is usually considered to be neglible compared to the changes in volume associated with changes in moisture content (Dinwoodie, 1989). While this may not be the case in particular circumstances, it is assumed here, and consequently thermal expansion is not considered.

1.4. Thesis outline

The multiscale approach touched on above is employed within this thesis to model the relationship between softwood structure and hygro-elastic properties. Four scales are considered: namely the nanostructural, ultrastructural, cellular and mesoscopic scales, having characteristic dimensions of 10 nm, 1 μm, 100 μmand 1 mm respectively.

In chapter 2 the hierarchical modelling strategy is described, effective properties are defined and a finite element based method for computing the effective hygroelastic properties of prismatic materials is developed.

Chapters 3–5 present models that predict the effective properties of softwood at the nanostructural, ultrastructural and cellular scales.

Models for the nanophase and cell-wall layer volume fractions are the subject in chapters 7 and 6.

Chapter 8 describes models for the nanophase hygro-elastic properties, introduced in chapter 3, as functions of temperature and moisture content.

Figure 1.2 prvides a schematic representation of the various models, the connections between them and location of detailed descriptions within this thesis.

Finally, the use of the combined models is demonstrated and results are presented in chapter 9, and in chapter 10 some concluding remarks are made and recommendations for future work are given.

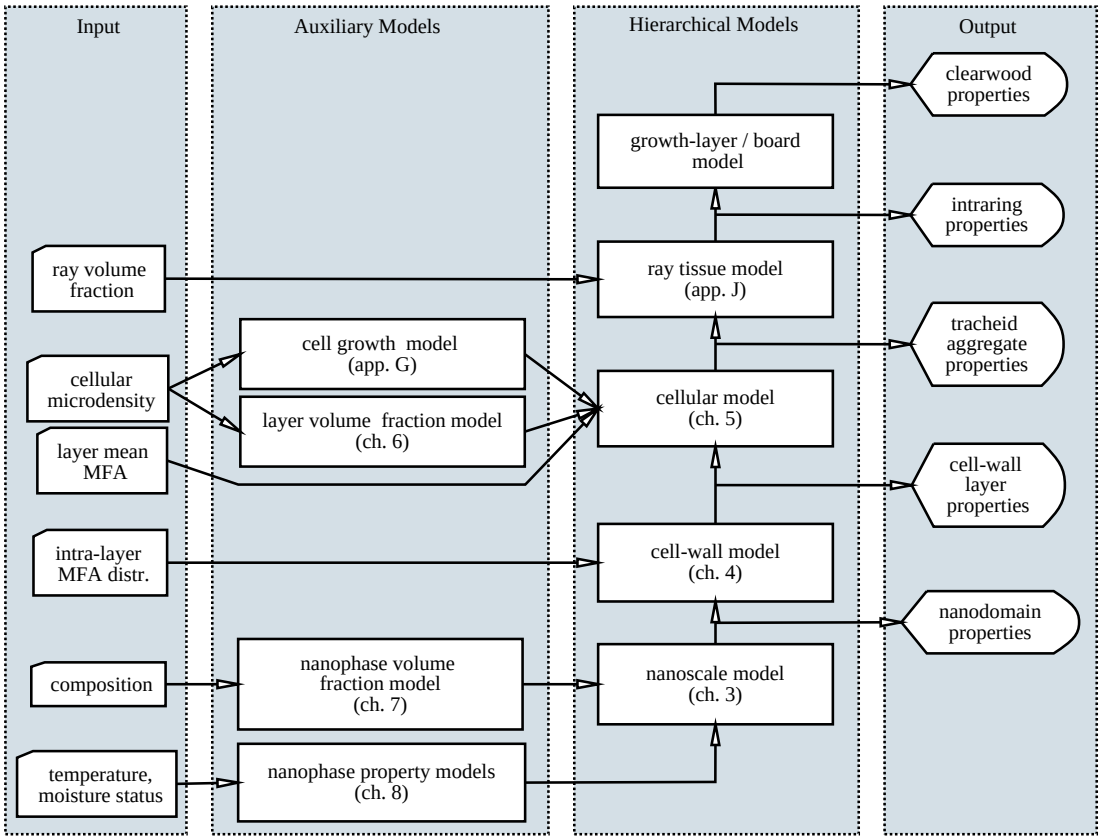

Figure 1.2.: Schematic overview of modelling and thesis layout.

Chapter 2

Effective properties and hierarchical modelling

In this thesis attention is confined to material properties arising in problems in uncoupled linear hygro-thermo-elasticity[1], specifically the elastic stiffnesses and hygro-expansional coefficients. In the absence of body forces such problems involve the solution of boundary value problems of the type

$$\begin{aligned} \boldsymbol{\partial}\boldsymbol{\sigma} &= 0, \\ \boldsymbol{\partial}^{\mathrm{t}}\mathbf{u} &= \boldsymbol{\epsilon}, \\ \mathbf{C}\left(\boldsymbol{\epsilon} - \boldsymbol{\epsilon}^{\circ}\right) + \boldsymbol{\sigma}_0 &= \boldsymbol{\sigma}, \end{aligned} \tag{2.1}$$

over some domain Ω where $\mathbf{u}$, $\boldsymbol{\epsilon}$ and $\boldsymbol{\sigma}$ are the displacements, strains and stresses, $\boldsymbol{\partial}$ is a differential operator defined by (A.39), $\mathbf{C}$ is the material stiffness, and $\boldsymbol{\sigma}_0$ and $\boldsymbol{\epsilon}^{\circ}$ are the prescribed initial stress and expansional strain fields. These equations together with suitable boundary conditions constitute a mathematically well posed problem whose solution yields the displacement, strain and stress fields within Ω. While analytic solutions to (2.1) are only available for a limited number of cases, numerical methods such as the finite element method (Zienkiewicz and Taylor, 2000) can, in theory, be used to compute approximate solutions for the general case.

Difficulties arise when the $\mathbf{C}$, $\boldsymbol{\epsilon}^{\circ}$ and $\boldsymbol{\sigma}_0$ are highly oscillatory, such as occurs when considering materials possessing structure over a wide range of length scales. Leaving aside the problem of how a complete specification for $\mathbf{C}$, $\boldsymbol{\epsilon}^{\circ}$ and $\boldsymbol{\sigma}_0$ might be obtained, a discretization sufficiently fine to capture the underlying multi-scale structure would result in a model that would exceed current, and indeed foreseeable future, computational capacity[2].

In a finite element context, substructuring and super-element techniques as well as special-purpose heterogenous element formulations (for examples see Zhang and Katsube (1995) or Ghosh et al. (1995)) are available for treating structures that span a limited range of length scales. More generally two basic approaches can be identified for

[1] A brief outline of this continuum field theory can be found in appendix A which introduces the notation and presents pertinent results.

[2] To emphasize this point consider a three dimensional finite element model of a single 3 m long 100×50 mm board. If the structure in this board were resolved to a microfibrillar scale then just to store this model would require a stack of CD-ROMs stretching over a tenth of a light year.

resolving the difficulties presented by highly heterogenous domains, namely the mean-field and homogenization theories. Introductions to mean-field theory can be found in Taya and Arsenault (1989), Mura (1987) and Nemat-Nasser and Hori (1993); and to homogenization theory in Persson et al. (1993) and Kalamkarov (1992); Kalamkarov and Kolpakov (1997). Further details are contained in the references given in these works. Connections between the mean-field and homogenization theories are explored in Hori and Nemat-Nasser (1999). While homogenization theory has a more rigorous mathematical grounding, the mean-field theory has an appealing physical interpretation, as the abstract equivalent of experimental material characterization, and provides the basis for the hierachical modelling methodology employed herein.

2.1. Effective properties

2.1.1. Stiffness and expansional strain

Instead of trying to solve a boundary value problem like (2.1), whose coefficients ($\mathbf{C}$, $\boldsymbol{\sigma}_0$ and $\boldsymbol{\epsilon}^\circ$) fluctuate rapidly in space, an approximate problem is formulated

$$\begin{aligned} \boldsymbol{\partial}\bar{\boldsymbol{\sigma}} &= 0, \\ \boldsymbol{\partial}^{\mathrm{t}}\bar{\mathbf{u}} &= \boldsymbol{\epsilon}, \\ \mathbf{C}^*\left(\bar{\boldsymbol{\epsilon}} - \boldsymbol{\epsilon}^{\circ *}\right) + \boldsymbol{\sigma}_0{}^* &= \bar{\boldsymbol{\sigma}} \end{aligned} \tag{2.2}$$

in which $\bar{\mathbf{u}}$, $\bar{\boldsymbol{\epsilon}}$ and $\bar{\boldsymbol{\sigma}}$ are the mean displacement, strain and stress fields and $\mathbf{C}^*$, $\boldsymbol{\epsilon}^{\circ *}$ and $\boldsymbol{\sigma}_0{}^*$ are the effective stiffness, expansional strain and initial stress coefficients. The benefit derived from making this substitution lies in the fact that if the effective properties are well chosen then, while they vary acceptably slowly in space, the mean fields resulting from solution of (2.2) are a good approximation to the mean fields that would have resulted from the solution of (2.1).

Let Ω^0 be the domain on which the (2.1) and (2.2) are defined. Denote by d^0 the scale of Ω^0, that is d^0 is a measure of how large Ω^0 is. Associated with each material point in Ω^0 is a representative volume (RV) Ω^1_X whose scale is d^1. Doing this amounts to resolving the structure within Ω^0 to scale d^1.

Each RV is a heterogeneous domain that represents the structure resolved to scale d^2 in the neighbourhood of the associated point X^0 in Ω^0. It should be emphasized that the RV need not be a subdomain of Ω^0 containing X^0, it need only characterize such subdomains. Within the RV the material properties may, in general, vary arbitrarily in space. Material domains in which the variation is piecewise homogeneous are said to be composite domains since they are composed of two or more homogeneous phases. All the material domains considered in this thesis are composite domains.

The mean strain $\bar{\boldsymbol{\epsilon}}$ and stress $\bar{\boldsymbol{\sigma}}$ at a point X^0 in Ω^0 are defined to be the volume

average of the corresponding fields over the associated RV Ω_X^1, that is

$$\bar{\boldsymbol{\epsilon}} \triangleq \langle \boldsymbol{\epsilon} \rangle_{\Omega_X^1} \tag{2.3}$$

$$\bar{\boldsymbol{\sigma}} \triangleq \langle \boldsymbol{\sigma} \rangle_{\Omega_X^1} \tag{2.4}$$

where $\langle \cdot \rangle_\Omega \equiv \frac{1}{|\Omega|} \int_\Omega \cdot \, d\Omega$.

If $\boldsymbol{\epsilon} = \boldsymbol{\epsilon}^\circ = 0$ everywhere in Ω_X^1 then $\boldsymbol{\sigma} = \boldsymbol{\sigma}_0$ so to be consistent with (2.4) the effective initial stress is

$$\boldsymbol{\sigma}_0{}^* = \langle \boldsymbol{\sigma}_0 \rangle_{\Omega_X^1} . \tag{2.5}$$

From the solution over Ω_X^1 of six different boundary value problems,

$$\begin{aligned}
\boldsymbol{\partial}\boldsymbol{\sigma}(\boldsymbol{x}) &= 0, \quad \boldsymbol{x} \in \Omega_x^n \\
\boldsymbol{\partial}^{\mathrm{t}}\mathbf{u}(\boldsymbol{x}) &= \boldsymbol{\epsilon}(\boldsymbol{x}), \quad \boldsymbol{x} \in \Omega_x^n \\
\mathbf{C}(\boldsymbol{x})\left(\boldsymbol{\epsilon}(\boldsymbol{x}) - \boldsymbol{\epsilon}^\circ(\boldsymbol{x})\right) + \boldsymbol{\sigma}_0 &= \boldsymbol{\sigma}, \quad \boldsymbol{x} \in \Omega_x^n \\
\mathbf{n}(\boldsymbol{x})\boldsymbol{\sigma}(\boldsymbol{x}) &= \mathbf{t}^{(k)}(\boldsymbol{x}), \quad \boldsymbol{x} \in \Gamma_x^{n\boldsymbol{t}^{(k)}} \\
\mathbf{u}(\boldsymbol{x}) &= \mathbf{u}^{(k)}(\boldsymbol{x}), \quad \boldsymbol{x} \in \Gamma_x^{n\boldsymbol{u}^{(k)}} \\
\boldsymbol{\epsilon}^\circ(\boldsymbol{x}) &= 0, \quad \boldsymbol{x} \in \Omega_x^n
\end{aligned} \tag{2.6}$$

six sets of volume averaged stresses $\langle \boldsymbol{\sigma} \rangle_{\Omega_X^1}^{(k)}$ and strains $\langle \boldsymbol{\epsilon} \rangle_{\Omega_X^1}^{(k)}$ may be determined. Then, since by (2.3) $\bar{\boldsymbol{\epsilon}}^{(k)} = \langle \boldsymbol{\epsilon} \rangle_{\Omega_X^1}^{(k)}$ and by (2.4) $\bar{\boldsymbol{\sigma}}^{(k)} = \langle \boldsymbol{\sigma} \rangle_{\Omega_X^1}^{(k)}$, the consitutive relationship of (2.2), $\mathbf{C}^* \left(\bar{\boldsymbol{\epsilon}} - \boldsymbol{\epsilon}^{\circ *}\right) + \boldsymbol{\sigma}_0{}^* = \bar{\boldsymbol{\sigma}}$, implies that the effective stiffness $\mathbf{C}^*$ is given by

$$\mathbf{C}^* = \left(\bigsqcup_{k=1}^{6} \langle \boldsymbol{\sigma} \rangle_{\Omega_X^1}^{(k)} - \bigsqcup_{k=1}^{6} \boldsymbol{\sigma}_0{}^* \right) \left(\bigsqcup_{k=1}^{6} \langle \boldsymbol{\epsilon} \rangle_{\Omega_X^1}^{(k)} \right)^{-1} \tag{2.7}$$

where $\bigsqcup_k$ denotes the columnwise matrix concatenation. The six boundary value problems of (2.6) must be independent, so that the inverse of $\bigsqcup_{k=1}^6 \langle \boldsymbol{\epsilon} \rangle_{\Omega_X^1}^{(k)}$ exists, but are otherwise arbitrary. Consequently $\mathbf{C}^*$ depends on the choice of boundary conditions, a point on which more will be said later.

In keeping with (2.3) and the constitutive relation in (2.2) and from the solution of a seventh boundary value problem, of the same type as (2.6) but with $\boldsymbol{\epsilon}^\circ$ prescribed, the effective expansional strain is

$$\boldsymbol{\epsilon}^{\circ *} = \langle \boldsymbol{\epsilon} \rangle_\Omega^{(7)} - \mathbf{C}^{*-1} \left(\langle \boldsymbol{\sigma} \rangle_\Omega^{(7)} - \boldsymbol{\sigma}_0{}^* \right) . \tag{2.8}$$

Solving (2.6) for determining the effective properties is clearly similar to the original problem (2.1). So if it happens that within Ω_X^1 the coefficients still vary too rapidly

then another approximation like (2.2) can be made and so on until finally a scale is reached for which the variation in material coefficients within the RV is acceptably slow. This recursive process is illustrated schematically in figure 2.1, and from the hierarchy of representative volumes it derives its name, the hierarchical modelling methodology.

The process of computing the effective properties of an RV is referred to as homogenization. The inverse process of determining the field variables within an RV given particular values of the mean field variables, a process which is not discussed further in this thesis, is known as localization.

2.1.2. Moisture content

The moisture content $w|_\Omega$ of some material domain Ω is defined as

$$w|_\Omega \triangleq \frac{M_w|_\Omega}{M_o|_\Omega} \tag{2.9}$$

where $M_w|_\Omega$ is the mass of water held in Ω and $M_o|_\Omega$ is the dry mass of Ω.

If Ω is a composite (piecewise homogeneous) domain consisting of N^p phases then the $w|_\Omega$ and the mean phase moisture contents $w|^p_\Omega$ are related by

$$w|_\Omega = \sum_{p=1}^{N^p} w|^p_\Omega m_o|^p_\Omega \tag{2.10}$$

where $m_o|^p_\Omega$ are the dry phase mass fractions.

The phase hygroscopicity is defined by

$$\chi(\vartheta, w^\star)|^p \triangleq \frac{w|^p}{w^\star}, \tag{2.11}$$

where $w^\star$ is the moisture content of some, possibly fictitious, reference material in equilibrium with the Ω. From (2.10) and (2.11) it can be concluded that the effective hygroscopicity of Ω, $\chi^*|_\Omega$, is given by

$$\chi^*|_\Omega = \sum_{p=1}^{N^p} \chi|^p m_o|^p_\Omega. \tag{2.12}$$

If the system is at equilibrium, then given $w|_\Omega$ the phase moisture contents are determined by

$$w|^p_\Omega = \frac{\chi|^p}{\chi^*|_\Omega} w|_\Omega \tag{2.13}$$

and a vanishing (and thermodynamically reversible) change in $w|_\Omega$, $\delta w|_\Omega$, results in

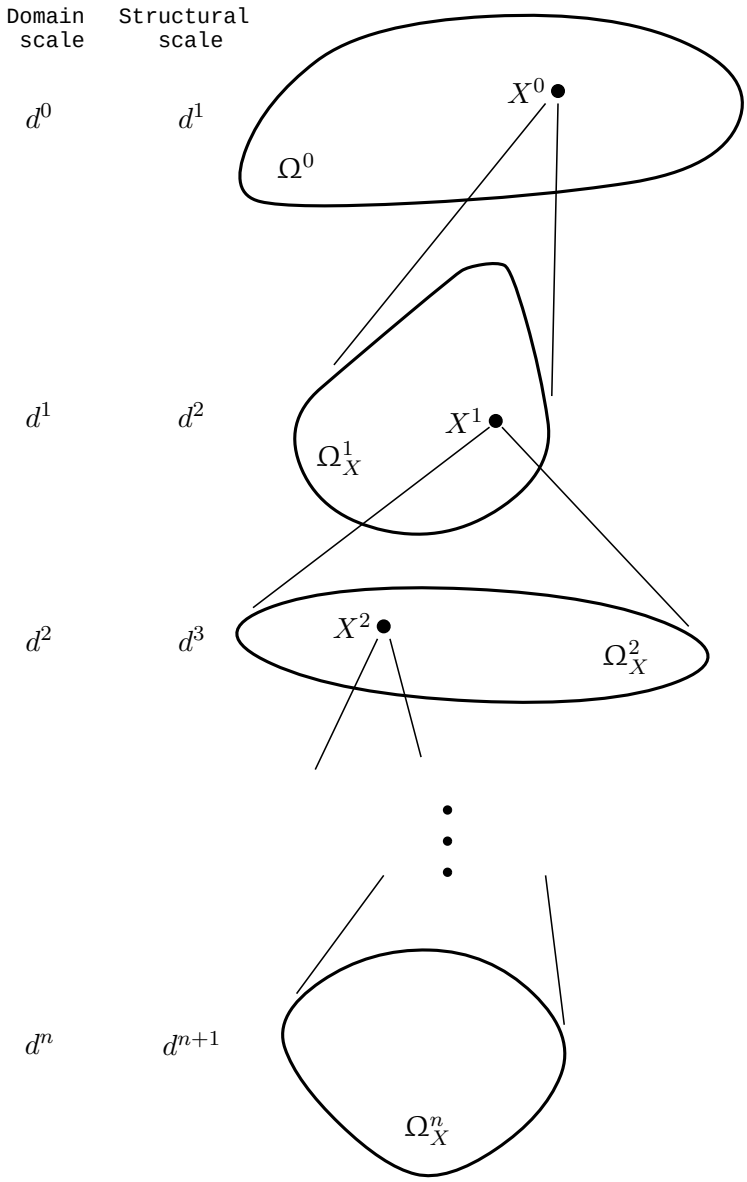

Figure 2.1.: Hierarchical modelling schematic.

changes in the phase moisture contents $\delta w|_\Omega^p$ given by

$$\delta w|_\Omega^p = \frac{w^\star \dfrac{\partial \chi|_\Omega^p}{\partial w^\star} + \chi|_\Omega^p}{w^\star \dfrac{\partial \chi^*|_\Omega}{\partial w^\star} + \chi^*|_\Omega} \delta w|_\Omega. \tag{2.14}$$

2.1.3. Hygro-expansional coefficients

Expansional strains are generated by changes in temperature and moisture content. For a material such as wood, changes in temperature and moisture content are coupled unless mass transfer between the material and its environment, including internal pore space, is prevented. Usually the expansion or contraction of wood due directly to changes in temperature are negligible compared to those caused by changes in moisture content (Kollmann and Côté, 1968; Kubler, 1973). Thus the expansional strains are here considered to be caused by changes in moisture content only, that is

$$\boldsymbol{\epsilon}^\circ = \boldsymbol{\alpha}^w \delta w. \tag{2.15}$$

The effective hygro-expansional coefficients $\boldsymbol{\alpha}^{w*}$ of Ω are then

$$\boldsymbol{\alpha}^{w*}|_\Omega = \frac{\boldsymbol{\epsilon}^{\circ *}|_\Omega}{\delta w|_\Omega} \tag{2.16}$$

with $\boldsymbol{\epsilon}^{\circ *}$ determined by (2.8) and the corresponding phase expansional strains are

$$\boldsymbol{\epsilon}^\circ|_\Omega^p = \boldsymbol{\alpha}^w|_\Omega^p \delta w|_\Omega^p \tag{2.17}$$

with $\delta w|_\Omega^p$ determined from $\delta w|_\Omega$ by (2.14).

2.2. A finite element homogenization procedure

Considerable effort has been expended, and ingenuity displayed, in developing schemes for determining the effective properties of heterogeneous materials. These schemes can be classified as:

(i) Semi-empirical methods which fit a mathematical model, particularly the Halpin-Tsai model(Halpin, 1984), to experimental data.

(ii) Ad hoc methods (also known as mechanics of materials methods or 'methods of hypotheses') making use of various 'reasonable' assumptions regarding the stress and strain states within the composite, e.g. Chou et al. (1972), Pochiraju and Chou (1999), Hopkins and Chamis (1988), Jones (1999),

(iii) Micromechanics methods making use of results from classical elasticity theory, in particular Eshelby's solution that states that an ellipsoidal inclusion

embedded in an infinite elastic medium undergoes a homogenous deformation (hence uniform stresses and strains) when a homogenous deformation is applied at infinity (Eshelby, 1957). Theories in this category include

- the self-consistent method (Hill, 1965; Budiansky, 1965),
- the generalised self-consistent method (Christensen and Lo, 1990),
- the differential method (Cleary et al., 1980; Norris, 1985; Avellaneda, 1987),
- the Mori-Tanaka method (Mori and Tanaka, 1973; Benveniste, 1987),
- the double-inclusion method (Hori and Nemat-Nasser, 1993),
- the Ponte Casteneda-Willis method (Ponte Castaneda and Willis, 1995),
- the Kuster-Toksoz method (Kuster and Toksöz, 1974),
- the composite spheres or cylinders method (Hashin, 1962; Hashin and Rosen, 1964),
- and the multiparticle effective field method (Buryachenko, 1996).

Many of these theories have been shown to be interrelated (Dasgupta and Bhandarkar, 1992; Berryman, 1997; Hu and Weng, 2000).

(iv) Variational methods whose aim is to bound the effective properties of particular classes of composites (Voigt, 1889; Reuss, 1929; Hashin and Shtrikman, 1962, 1963; Walpole, 1969; Kröner, 1972, 1981; Wu and McCullough, 1977).

(v) Asymptotic homogenization methods that come out of the study of differential equations with rapidly oscillating coefficients (Babuška, 1976, 1977; Bensoussan et al., 1978; Sanchez-Palencia, 1980; Bakhvalov and Panasenko, 1984; Kalamkarov, 1992; Kalamkarov and Kolpakov, 1997; Persson et al., 1993; Cioranescu and Paulin, 1998; Oleinik et al., 1992).

(vi) Field approximation methods including

- Fourier series (Nemat-Nasser et al., 1982; Nemat-Nasser and Hori, 1993) and Fourier transform (Michel and Suquet, 1998; Michel et al., 1999, 2000) methods,
- the 'method of cells' (Aboudi, 1991), and its generalization (Paley and Aboudi, 1992),
- finite element based methods Kamiński and Kleiber (2000), Hollister and Kikuchi (1992), Naciri et al. (1994a,b).

In addition to the references already given further discussion of these and other methods for determing effective properties can be found in Chamis and Sendeckjy (1968), Christensen (1979),Hashin (1983), Halpin (1984), Mura (1987), Avellaneda (1991), Torquato (1991), Whitney and McCullough (1990), Hollister and Kikuchi (1992), Nemat-Nasser

and Hori (1993), Rammerstorfer and Böhm (1994), Tucker III and Liang (1999), Torquato (2000).

In this section a method for computing the effective hygro-elastic properties of composite materials with arbitrary structure and phase material symmetries is developed. This is done by using the finite element method to evaluate the strain and stress fields in representative domain Ω for particular set of boundary conditions; from which the average stresses and strains and hence the effective properties can be computed using the definitions and relationships of §2.1.1. An implementation of this method for prismatic materials is then described and results presented to verify the correctness of this implementation.

2.2.1. General formulation

It is useful, particularly when using the periodic boundary conditions and prismatic elements described below, to treat the displacement field in Ω as the sum of a homogeneous strain and a perturbation displacement. To this end split the displacement into a linear and perturbation fields

$$\mathbf{u}(\boldsymbol{x}) = \mathbf{x}\mathbf{W}^{-1}\bar{\boldsymbol{\epsilon}} + \tilde{\mathbf{u}}(\boldsymbol{x}) \tag{2.18}$$

in which $\tilde{\mathbf{u}}(\boldsymbol{x})$ is the perturbation displacement, $\mathbf{x}$ is defined by (A.48), and $\mathbf{W}$ is defined by (A.36). The perturbation strains $\tilde{\boldsymbol{\epsilon}}$ are defined such that they correspond to the perturbation part of the displacement field, i.e.

$$\tilde{\boldsymbol{\epsilon}}(\boldsymbol{x}) \triangleq \boldsymbol{\partial}^{\mathrm{t}}\tilde{\mathbf{u}}(\boldsymbol{x}), \tag{2.19}$$

and if $\langle\boldsymbol{\epsilon}\rangle_{\Omega} = \bar{\boldsymbol{\epsilon}}$, then since $\boldsymbol{\epsilon} = \boldsymbol{\partial}^{\mathrm{t}}\mathbf{u} = \boldsymbol{\partial}^{\mathrm{t}}\mathbf{x}\mathbf{W}^{-1}\bar{\boldsymbol{\epsilon}} + \boldsymbol{\partial}^{\mathrm{t}}\tilde{\mathbf{u}}(\boldsymbol{x}) = \bar{\boldsymbol{\epsilon}} + \tilde{\boldsymbol{\epsilon}}$

$$\langle\tilde{\boldsymbol{\epsilon}}\rangle_{\Omega} = \left\langle\boldsymbol{\partial}^{\mathrm{t}}\tilde{\mathbf{u}}(\boldsymbol{x})\right\rangle_{\Omega} = 0. \tag{2.20}$$

The finite element method involves discretizing Ω into a finite set of pairwise disjoint open bounded subdomains Ω_e of simple shape so that $\Omega_e \cap \Omega_f = \emptyset, \forall e \neq f$ and $\Omega \approx \bigcup_e \Omega_e$. A 'finite element' $\bar{\Omega}_e$ is identified with the closure of Ω_e i.e. $\bar{\Omega}_e = \Omega_e \cup \partial\Omega_e$, where $\partial\Omega_e$ is the boundary of Ω_e. Then

$$\tilde{\mathbf{u}}(\boldsymbol{x}) \approx \sum_e \begin{cases} \mathbf{N}_e(\boldsymbol{x})\tilde{\mathbf{u}}_e & \boldsymbol{x} \in \bar{\Omega}_e \\ 0 & \text{otherwise} \end{cases} \tag{2.21}$$

is introduced as a local approximation for $\tilde{\mathbf{u}}(\boldsymbol{x})$. $\mathbf{N}_e(\boldsymbol{x})$ is a matrix containing the local interpolation functions (element shape functions) and $\tilde{\mathbf{u}}_e$ is a column matrix containing the local interpolation coefficients (nodal perturbation displacements). It can be shown

that finding $\mathbf{u}(\boldsymbol{x})$ that minimises the potential energy functional

$$\Pi = \frac{1}{2}\int_\Omega (\boldsymbol{\partial}^{\mathrm{t}}\mathbf{u})^{\mathrm{t}}\mathbf{C}\boldsymbol{\partial}^{\mathrm{t}}\mathbf{u}\, d\Omega - \int_\Omega (\boldsymbol{\partial}^{\mathrm{t}}\mathbf{u})^{\mathrm{t}}\mathbf{C}\boldsymbol{\epsilon}^\circ\, d\Omega + \int_\Omega (\boldsymbol{\partial}^{\mathrm{t}}\mathbf{u})^{\mathrm{t}}\boldsymbol{\sigma}_0\, d\Omega - \int_\Gamma \mathbf{u}^{\mathrm{t}}\mathbf{t}\, d\Gamma \tag{2.22}$$

is equivalent to solving the boundary value problem (2.6) (Zienkiewicz and Taylor, 2000). After defining $\mathbf{B}_e(\boldsymbol{x}) \triangleq \boldsymbol{\partial}^{\mathrm{t}}\mathbf{N}_e(\boldsymbol{x})$, putting (2.18) and (2.21) into (2.22) then yields

$$\begin{aligned}\Pi =& \frac{1}{2}\sum_e \int_{\Omega_e} \bar{\boldsymbol{\epsilon}}^{\mathrm{t}}\mathbf{C}\bar{\boldsymbol{\epsilon}}\, d\Omega + \sum_e \int_{\Omega_e} \bar{\boldsymbol{\epsilon}}^{\mathrm{t}}\mathbf{C}\mathbf{B}_e\tilde{\mathbf{u}}_e\, d\Omega + \frac{1}{2}\sum_e \int_{\Omega_e} \tilde{\mathbf{u}}_e^{\mathrm{t}}\mathbf{B}_e^{\mathrm{t}}\mathbf{C}\mathbf{B}_e\tilde{\mathbf{u}}_e\, d\Omega \\ & - \sum_e \int_{\Omega_e} \bar{\boldsymbol{\epsilon}}^{\mathrm{t}}\mathbf{C}\boldsymbol{\epsilon}^\circ\, d\Omega - \sum_e \int_{\Omega_e} \tilde{\mathbf{u}}_e^{\mathrm{t}}\mathbf{B}_e^{\mathrm{t}}\mathbf{C}\boldsymbol{\epsilon}^\circ\, d\Omega + \sum_e \int_{\Omega_e} \bar{\boldsymbol{\epsilon}}^{\mathrm{t}}\boldsymbol{\sigma}_0\, d\Omega \\ & + \sum_e \int_{\Omega_e} \tilde{\mathbf{u}}_e^{\mathrm{t}}\mathbf{B}_e^{\mathrm{t}}\boldsymbol{\sigma}_0\, d\Omega - \sum_e \int_{\Gamma\cap\Gamma_e} \bar{\boldsymbol{\epsilon}}^{\mathrm{t}}\mathbf{W}^{-1}\mathbf{x}^{\mathrm{t}}\mathbf{t}\, d\Gamma - \sum_e \int_{\Gamma\cap\Gamma_e} \tilde{\mathbf{u}}_e^{\mathrm{t}}\mathbf{N}_e^{\mathrm{t}}\mathbf{t}\, d\Gamma.\end{aligned} \tag{2.23}$$

The total potential energy can also be written in terms $\tilde{\mathbf{u}}_g$, $\mathbf{N}$ and $\mathbf{B}$, which are the global (assembled) equivalents of $\tilde{\mathbf{u}}_e$, $\mathbf{N}_e$ and $\mathbf{B}_e$, as

$$\begin{aligned}\Pi =& \frac{1}{2}\tilde{\mathbf{u}}_g^{\mathrm{t}}\mathbf{K}_{11}\tilde{\mathbf{u}}_g + \tilde{\mathbf{u}}_g^{\mathrm{t}}\mathbf{K}_{12}\bar{\boldsymbol{\epsilon}} + \frac{1}{2}\bar{\boldsymbol{\epsilon}}^{\mathrm{t}}\mathbf{K}_{22}\bar{\boldsymbol{\epsilon}} \\ & - \tilde{\mathbf{u}}_g^{\mathrm{t}}\left(\mathbf{F}^{\boldsymbol{\epsilon}^\circ} - \mathbf{F}^{\boldsymbol{\sigma}_0} + \mathbf{F}^{t}\right) - \bar{\boldsymbol{\epsilon}}^{\mathrm{t}}\left(\bar{\mathbf{F}}^{\boldsymbol{\epsilon}^\circ} - \bar{\mathbf{F}}^{\boldsymbol{\sigma}_0} + |\Omega|\bar{\boldsymbol{\sigma}}\right)\end{aligned} \tag{2.24}$$

where

$$\mathbf{K}_{11} = \sum_e \int_{\Omega_e} \mathbf{B}^{\mathrm{t}}\mathbf{C}\mathbf{B}\, d\Omega \tag{2.25}$$

$$\mathbf{K}_{12} = \sum_e \int_{\Omega_e} \mathbf{B}^{\mathrm{t}}\mathbf{C}\, d\Omega \tag{2.26}$$

$$\mathbf{K}_{22} = \int_\Omega \mathbf{C}\, d\Omega \tag{2.27}$$

$$\mathbf{F}^{\boldsymbol{\epsilon}^\circ} = \sum_e \int_{\Omega_e} \mathbf{B}^{\mathrm{t}}\mathbf{C}\boldsymbol{\epsilon}^\circ\, d\Omega \tag{2.28}$$

$$\mathbf{F}^{\boldsymbol{\sigma}_0} = \sum_e \int_{\Omega_e} \mathbf{B}^{\mathrm{t}}\boldsymbol{\sigma}_0\, d\Omega \tag{2.29}$$

$$\mathbf{F}^{t} = \sum_e \int_{\Gamma\cap\Gamma_e} \mathbf{N}^{\mathrm{t}}\mathbf{t}\, d\Gamma \tag{2.30}$$

$$\bar{\mathbf{F}}^{\boldsymbol{\epsilon}^\circ} = \int_\Omega \mathbf{C}\boldsymbol{\epsilon}^\circ\, d\Omega \tag{2.31}$$

$$\bar{\mathbf{F}}^{\boldsymbol{\sigma}_0} = \int_\Omega \boldsymbol{\sigma}_0\, d\Omega \tag{2.32}$$

$$\bar{\boldsymbol{\sigma}} = \frac{1}{|\Omega|}\int_\Gamma \mathbf{W}^{-1}\mathbf{x}^{\mathrm{t}}\mathbf{t}\, d\Omega = \langle\boldsymbol{\sigma}\rangle_\Omega\,. \tag{2.33}$$

2.2.2. Boundary conditions

The boundary conditions to be used in (2.6) are yet to be satisfied. In order that energy be conserved they should be chosen such that

$$\left\langle \boldsymbol{\epsilon}^{\mathrm{t}} \mathbf{C} \boldsymbol{\epsilon} \right\rangle_{\Omega} = \bar{\boldsymbol{\epsilon}}^{\mathrm{t}} \mathbf{C}^{*} \bar{\boldsymbol{\epsilon}} \tag{2.34}$$

which implies that (Nemat-Nasser and Hori, 1993)

$$\left\langle \boldsymbol{\epsilon}^{\mathrm{t}} \boldsymbol{\sigma} \right\rangle_{\Omega} - \left\langle \boldsymbol{\epsilon} \right\rangle_{\Omega}^{\mathrm{t}} \left\langle \boldsymbol{\sigma} \right\rangle_{\Omega} = \frac{1}{|\Omega|} \int_{\Gamma} (\mathbf{u} - \mathbf{x}\mathbf{W}^{-1}\boldsymbol{\epsilon})^{\mathrm{t}} (\mathbf{t} - \mathbf{n}\boldsymbol{\sigma}) \, d\Gamma. \tag{2.35}$$

Three kinds of boundary conditions that meet this criterion are in common use; namely the uniform strain, uniform stress and periodic boundary conditions described in detail in subsequent subsections.

The first two of these kinds of boundary conditions would give rise to homogeneous stress and strain fields if applied to a homogeneous body. They are useful since it can be shown (see Hori and Nemat-Nasser (1999) for a proof) that they provide universal bounds on the effective stiffness in the sense that if $\boldsymbol{\epsilon}^{\sigma}$, $\boldsymbol{\epsilon}^{g}$ and $\boldsymbol{\epsilon}^{\epsilon}$ are the strain fields in Ω when subjected to uniform stress, general and uniform strain boundary conditions then

$$\left\langle \boldsymbol{\epsilon}^{\sigma \mathrm{t}} \mathbf{C} \boldsymbol{\epsilon}^{\sigma} \right\rangle_{\Omega} \leq \left\langle \boldsymbol{\epsilon}^{g \mathrm{t}} \mathbf{C} \boldsymbol{\epsilon}^{g} \right\rangle_{\Omega} \leq \left\langle \boldsymbol{\epsilon}^{\epsilon \mathrm{t}} \mathbf{C} \boldsymbol{\epsilon}^{\epsilon} \right\rangle_{\Omega}. \tag{2.36}$$

If the RV is chosen appropriately then the effective stiffness determined using uniform strain and uniform stress boundary conditions will coincide and the effective stiffness will be uniquely defined.

Periodic boundary conditions are motivated by consideration of periodic materials of infinite extent, i.e materials for which if A is any material property then

$$A(\boldsymbol{x} + \sum_{i} m_i \boldsymbol{a}_i) = A(\boldsymbol{x}), m_i \in \mathbb{I} \tag{2.37}$$

where $\boldsymbol{a}_i$ are the periodicity vectors. If such a material is subjected to uniform tractions or linear displacements at infinity then the stress and strain fields in any unit cell can be assumed to be the same as those in any other and hence will also be periodic[3]. Put another way, if a material is periodic then using periodic boundary conditions with a unit cell as the RV will yield the same result as uniform stress or uniform strain boundary conditions applied to an infinite RV. If a material is not periodic, but periodic boundary conditions are used with some finite RV then because of (2.36) the effective properties will lie between those for uniform stress and strain BCs. Hollister

[3]It is possible that the deformations may be periodic over a super-cell, that is a collection of unit cells, rather than over individual unit cells.

and Kikuchi (1992) compared homogenized solutions with their exact equivalent and found that the effective properties determined using periodic boundary conditions gave better results than those resulting from application on the boundary of either uniform stress or uniform strain.

2.2.2.1. Uniform boundary strain

If linear displacements are prescribed on the boundary Γ, i.e.

$$\mathbf{u}(\boldsymbol{x}) = \mathbf{x}(\boldsymbol{x})\mathbf{W}^{-1}\boldsymbol{\epsilon}^{\Gamma}, \boldsymbol{x} \in \Gamma, \tag{2.38}$$

then by (A.29), and since the divergence theorem implies $\frac{1}{|\Omega|}\int_{\Gamma} \mathbf{n}^{\mathrm{t}}\mathbf{x}\, d\Gamma = \mathbf{W}$,

$$\begin{aligned} \langle\boldsymbol{\epsilon}\rangle_{\Omega} &= \frac{1}{|\Omega|}\int_{\Gamma} \mathbf{n}^{\mathrm{t}}\mathbf{x}\mathbf{W}^{-1}\boldsymbol{\epsilon}^{\Gamma}\, d\Gamma \\ &= \boldsymbol{\epsilon}^{\Gamma}. \end{aligned} \tag{2.39}$$

From (2.18) and (2.38)

$$\tilde{\mathbf{u}}(\boldsymbol{x}) = 0, \boldsymbol{x} \in \Gamma \tag{2.40}$$

and by (A.29) $\langle\tilde{\boldsymbol{\epsilon}}\rangle_{\Omega} = 0$ so (2.20) is satisfied and $\bar{\boldsymbol{\epsilon}} = \langle\boldsymbol{\epsilon}\rangle_{\Omega} = \boldsymbol{\epsilon}^{\Gamma}$.

On prescribing $\bigsqcup_{k=1}^{6} \bar{\boldsymbol{\epsilon}}^{(k)} = \mathbf{I}_6$, and $\boldsymbol{\epsilon}^{\circ}(\boldsymbol{x}) = 0, \forall \boldsymbol{x} \in \Omega$ then if Π is stationary $\dfrac{\partial\Pi}{\partial\tilde{\mathbf{u}}_g} = 0$, thus from (2.24) we obtain

$$\tilde{\mathbf{u}}_g^{(k)} = -\mathbf{K}_{11}^{-1}\left(\mathbf{K}_{12}\bar{\boldsymbol{\epsilon}}^{(k)} + \mathbf{F}^{\boldsymbol{\sigma}_0}\right). \tag{2.41}$$

The average stress in Ω is

$$\begin{aligned} \langle\boldsymbol{\sigma}\rangle_{\Omega}^{(k)} =& \bar{\boldsymbol{\sigma}}^{(k)} \\ =& \frac{1}{|\Omega|}\int_{\Omega} \mathbf{C}\boldsymbol{\epsilon}^{(k)} + \boldsymbol{\sigma}_0\, d\Omega \\ =& \frac{1}{|\Omega|}\int_{\Omega} \mathbf{C}\left(\bar{\boldsymbol{\epsilon}}^{(k)} + \boldsymbol{\partial}^{\mathrm{t}}\mathbf{N}\tilde{\mathbf{u}}_g^{(k)} -\right) + \boldsymbol{\sigma}_0\, d\Omega \end{aligned}$$

so

$$|\Omega|\bar{\boldsymbol{\sigma}}^{(k)} = \mathbf{K}_{12}^{\mathrm{t}}\tilde{\mathbf{u}}_g^{(k)} + \mathbf{K}_{22}\bar{\boldsymbol{\epsilon}}^{(k)} + \bar{\mathbf{F}}^{\boldsymbol{\sigma}_0} \tag{2.42}$$

or on substituting (2.41)

$$|\Omega|\bar{\boldsymbol{\sigma}}^{(k)} + \mathbf{K}_{12}^{\mathrm{t}}\mathbf{K}_{11}^{-1}\mathbf{F}^{\boldsymbol{\sigma}_0} - \bar{\mathbf{F}}^{\boldsymbol{\sigma}_0} = \left(\mathbf{K}_{22} - \mathbf{K}_{12}^{\mathrm{t}}\mathbf{K}_{11}^{-1}\mathbf{K}_{12}\right)\bar{\boldsymbol{\epsilon}}^{(k)}. \tag{2.43}$$

Combining (2.7) and (2.43) yields the effective stiffness

$$\bar{\mathbf{C}} = \frac{1}{|\Omega|}\left(\left(\left(\mathbf{K}_{22} - \mathbf{K}_{12}^{\mathrm{t}}\mathbf{K}_{11}^{-1}\mathbf{K}_{12}\right) - \mathbf{K}_{12}^{\mathrm{t}}\mathbf{K}_{11}^{-1}\bigsqcup_{k=1}^{6}\mathbf{F}^{\boldsymbol{\sigma}_0} + \bigsqcup_{k=1}^{6}\bar{\mathbf{F}}^{\boldsymbol{\sigma}_0}\right) - \bigsqcup_{k=1}^{6}\bar{\boldsymbol{\sigma}}_0\right). \tag{2.44}$$

From the solution of a seventh boundary value problem, for which $\boldsymbol{\epsilon}^{\circ}(\boldsymbol{x}) = \boldsymbol{\epsilon}^{\circ}(\boldsymbol{x})|_n$ and $\bar{\boldsymbol{\epsilon}}^{(7)} = 0$, and using

$$\tilde{\mathbf{u}}_g^{(7)} = \mathbf{K}_{11}^{-1}\left(\mathbf{F}^{\boldsymbol{\epsilon}^{\circ}(7)} - \mathbf{F}^{\boldsymbol{\sigma}_0}\right) \tag{2.45}$$

and

$$|\Omega|\bar{\boldsymbol{\sigma}}^{(7)} = \mathbf{K}_{12}^{\mathrm{t}}\tilde{\mathbf{u}}_g^{(7)} - \bar{\mathbf{F}}^{\boldsymbol{\epsilon}^{\circ}(7)} + \bar{\mathbf{F}}^{\boldsymbol{\sigma}_0}. \tag{2.46}$$

in place of (2.41) and (2.42), $\bar{\boldsymbol{\sigma}}^{(7)}$ can be determined. Equation (2.8) then gives the effective expansional strain as

$$\begin{aligned}\boldsymbol{\epsilon}^{\circ *} &= -\mathbf{C}^{*-1}\left(\bar{\boldsymbol{\sigma}}^{(7)} - \boldsymbol{\sigma}_0\right)\\ &= -\frac{1}{|\Omega|}\bar{\mathbf{C}}^{-1}\left(\mathbf{K}_{12}^{\mathrm{t}}\mathbf{K}_{11}^{-1}\left(\mathbf{F}^{\boldsymbol{\epsilon}^{\circ}(7)} - \mathbf{F}^{\boldsymbol{\sigma}_0}\right) - \bar{\mathbf{F}}^{\boldsymbol{\epsilon}^{\circ}(7)} + \bar{\mathbf{F}}^{\boldsymbol{\sigma}_0}\right).\end{aligned} \tag{2.47}$$

2.2.2.2. Uniform boundary stress

If uniform tractions are prescribed on the boundary Γ, i.e.

$$\mathbf{t}(\boldsymbol{x}) = \mathbf{n}(\boldsymbol{x})\boldsymbol{\sigma}^{\Gamma}, \forall \boldsymbol{x} \in \Gamma, \tag{2.48}$$

then from (2.33) and as $\frac{1}{|\Omega|}\int_{\Gamma}\mathbf{x}^{\mathrm{t}}\mathbf{n}\,d\Gamma = \mathbf{W}$,

$$\begin{aligned}\bar{\boldsymbol{\sigma}} &= \frac{1}{|\Omega|}\int_{\Gamma}\mathbf{W}^{-1}\mathbf{x}^{\mathrm{t}}\mathbf{n}\boldsymbol{\sigma}^{\Gamma}\,d\Gamma\\ &= \boldsymbol{\sigma}^{\Gamma}.\end{aligned} \tag{2.49}$$

The condition of (2.20), i.e. $\langle\tilde{\boldsymbol{\epsilon}}\rangle_{\Omega} \approx \langle\mathbf{B}\rangle_{\Omega}\,\tilde{\mathbf{u}}_g = 0$ must be enforced. This is done by adding a term

$$\boldsymbol{\lambda}^{\mathrm{t}}\mathbf{K}_{31}\tilde{\mathbf{u}}_g \tag{2.50}$$

to (2.24), where $\boldsymbol{\lambda}$ is a column matrix of Lagrange multipliers and $\mathbf{K}_{31} = \langle\mathbf{B}\rangle_{\Omega}$. Then if Π is stationary $\dfrac{\partial\Pi}{\partial\tilde{\mathbf{u}}_g} = 0$, $\dfrac{\partial\Pi}{\partial\bar{\boldsymbol{\epsilon}}} = 0$ and $\dfrac{\partial\Pi}{\partial\boldsymbol{\lambda}} = 0$, thus the system of equations to be

solved is

$$\begin{bmatrix} \mathbf{K}_{11} & \mathbf{K}_{12} & \mathbf{K}_{31}^{\mathrm{t}} \\ \mathbf{K}_{12}^{\mathrm{t}} & \mathbf{K}_{22} & 0 \\ \mathbf{K}_{31} & 0 & 0 \end{bmatrix} \begin{bmatrix} \tilde{\mathbf{u}}_g \\ \bar{\boldsymbol{\epsilon}} \\ \boldsymbol{\lambda} \end{bmatrix} = \begin{bmatrix} \mathbf{F}^{\boldsymbol{\epsilon}^\circ} - \mathbf{F}^{\boldsymbol{\sigma}_0} + \mathbf{F}^{t} \\ \bar{\mathbf{F}}^{\boldsymbol{\epsilon}^\circ} - \bar{\mathbf{F}}^{\boldsymbol{\sigma}_0} + |\Omega|\bar{\boldsymbol{\sigma}} \\ 0 \end{bmatrix}. \tag{2.51}$$

On setting $\bigsqcup_{k=1}^{6} \bar{\boldsymbol{\sigma}}^{(k)} = \mathbf{I}_6$ and $\boldsymbol{\epsilon}^\circ(\boldsymbol{x}) = 0, \forall \boldsymbol{x} \in \Omega$, and with suitable restraints against rigid body motions in place, (2.51) can be solved for $\bar{\boldsymbol{\epsilon}}^{(k)}$. Then, by way of (2.7), the effective stiffness is

$$\mathbf{C}^* = \left(\mathbf{I}_6 - \bigsqcup_{k=1}^{6} {\boldsymbol{\sigma}_0}^* \right) \left(\bigsqcup_{k=1}^{6} \bar{\boldsymbol{\epsilon}}^{(k)} \right)^{-1}. \tag{2.52}$$

From the solution of a seventh boundary value problem, for which $\boldsymbol{\epsilon}^\circ(\boldsymbol{x}) = \boldsymbol{\epsilon}^\circ(\boldsymbol{x})|_n$ and $\bar{\boldsymbol{\sigma}}^{(7)} = 0$, the effective expansional strain is, from (2.8),

$${\boldsymbol{\epsilon}^\circ}^* = \langle \boldsymbol{\epsilon} \rangle_{\Omega}^{(7)} + \mathbf{C}^{*-1} {\boldsymbol{\sigma}_0}^*. \tag{2.53}$$

2.2.2.3. Periodic boundary conditions

For periodic boundary conditions to be applicable, the boundary Γ of Ω must be such that it can be broken into two parts of equal measure, Γ^- and Γ^+, which for every point $\boldsymbol{x}^- \in \Gamma^-$ there exists a single corresponding point $\boldsymbol{x}^+ \in \Gamma^+$ such that for some set of $k_i \in \{-1, 0, 1\}$ all of which are not equal

$$\boldsymbol{x}^+ = \boldsymbol{x}^- + \sum_i k_i \boldsymbol{a}_i \tag{2.54}$$

where $\boldsymbol{a}_i$ are the set of independent periodicity vectors, and for which

$$\mathbf{n}(\boldsymbol{x}^+) = -\mathbf{n}(\boldsymbol{x}^-) \tag{2.55}$$

is true for nearly all $\boldsymbol{x}^+$[4]. If these conditions are met then periodic boundary conditions, i.e.

$$\tilde{\mathbf{u}}(\boldsymbol{x}^+) = \tilde{\mathbf{u}}(\boldsymbol{x}^-) \tag{2.56}$$

$$\mathbf{t}(\boldsymbol{x}^+) = -\mathbf{t}(\boldsymbol{x}^-) \tag{2.57}$$

can be prescribed.

[4] 'Nearly' is required to accomodate a finite number of points at which the boundary is not smooth, and for which $\mathbf{n}$ may not be defined.

Now by (A.49), (2.55) and (2.56)

$$\begin{aligned}\langle\tilde{\boldsymbol{\epsilon}}\rangle_{\Omega} &= \frac{1}{|\Omega|}\int_{\Gamma}\mathbf{n}^{\mathrm{t}}\tilde{\mathbf{u}}\,d\Gamma = \frac{1}{|\Omega|}\int_{\Gamma^-}\mathbf{n}^{\mathrm{t}}(\boldsymbol{x}^-)\tilde{\mathbf{u}}(\boldsymbol{x}^-)\,d\Gamma + \frac{1}{|\Omega|}\int_{\Gamma^+}\mathbf{n}^{\mathrm{t}}(\boldsymbol{x}^+)\tilde{\mathbf{u}}(\boldsymbol{x}^+)\,d\Gamma \\ &= \frac{1}{|\Omega|}\int_{\Gamma^-}\mathbf{n}^{\mathrm{t}}(\boldsymbol{x}^-)\tilde{\mathbf{u}}(\boldsymbol{x}^-)\,d\Gamma - \frac{1}{|\Omega|}\int_{\Gamma^-}\mathbf{n}^{\mathrm{t}}(\boldsymbol{x}^-)\tilde{\mathbf{u}}(\boldsymbol{x}^-)\,d\Gamma \\ &= 0\end{aligned} \tag{2.58}$$

so the condition of (2.20) is satisfied and $\langle\boldsymbol{\epsilon}\rangle_{\Omega} = \bar{\boldsymbol{\epsilon}}$.

If the average strains are prescribed then the analysis proceeds along the same lines as for the linear displacement case and the effective stiffness and effective expansional strains are given by (2.44) and (2.47).

Alternatively the average stresses may be prescribed and the analysis is similar to that for the uniform traction case except that because of (2.56) the zero average perturbation strain condition of (2.20) is already satisfied and need not be enforced separately. Thus if Π is to be stationary then $\dfrac{\partial\Pi}{\partial\tilde{\mathbf{u}}_g} = 0$ and $\dfrac{\partial\Pi}{\partial\bar{\boldsymbol{\epsilon}}} = 0$, and the system to be solved is

$$\begin{bmatrix}\mathbf{K}_{11} & \mathbf{K}_{12}\\ \mathbf{K}_{12}^{\mathrm{t}} & \mathbf{K}_{22}\end{bmatrix}\begin{bmatrix}\tilde{\mathbf{u}}_g^{(k)}\\ \bar{\boldsymbol{\epsilon}}^{(k)}\end{bmatrix} = \begin{bmatrix}\mathbf{F}^{\boldsymbol{\epsilon}^\circ} - \mathbf{F}^{\boldsymbol{\sigma}_0} + \mathbf{F}^{\boldsymbol{t}}\\ \bar{\mathbf{F}}^{\boldsymbol{\epsilon}^\circ} - \bar{\mathbf{F}}^{\boldsymbol{\sigma}_0} + |\Omega|\bar{\boldsymbol{\sigma}}\end{bmatrix}. \tag{2.59}$$

Because of (2.57) $\mathbf{F}^{\boldsymbol{t}} = 0$ and if $\boldsymbol{\epsilon}^\circ(\boldsymbol{x}) = 0, \forall\boldsymbol{x}\in\Omega$ then the average strain is

$$\left(\mathbf{K}_{22} - \mathbf{K}_{12}^{\mathrm{t}}\mathbf{K}_{11}^{-1}\mathbf{K}_{12}\right)\bar{\boldsymbol{\epsilon}}^{(k)} = |\Omega|\bar{\boldsymbol{\sigma}}^{(k)} + \mathbf{K}_{12}^{\mathrm{t}}\mathbf{K}_{11}^{-1}\mathbf{F}^{\boldsymbol{\sigma}_0} - \bar{\mathbf{F}}^{\boldsymbol{\sigma}_0}. \tag{2.60}$$

If the simplest prescription for the average stresses is made, i.e. $\bigsqcup_{k=1}^{6}\bar{\boldsymbol{\sigma}} = \mathbf{I}_6$, then the effective stiffness is

$$\mathbf{C}^* = \left(\mathbf{I}_6 - \bigsqcup_{k=1}^{6}{\boldsymbol{\sigma}_0}^*\right)\left(|\Omega|\mathbf{I}_6 + \mathbf{K}_{12}^{\mathrm{t}}\mathbf{K}_{11}^{-1}\bigsqcup_{k=1}^{6}\mathbf{F}^{\boldsymbol{\sigma}_0} - \bigsqcup_{k=1}^{6}\bar{\mathbf{F}}^{\boldsymbol{\sigma}_0}\right)^{-1}\left(\mathbf{K}_{22} - \mathbf{K}_{12}^{\mathrm{t}}\mathbf{K}_{11}^{-1}\mathbf{K}_{12}\right). \tag{2.61}$$

The effective expansional strain

$$\boldsymbol{\epsilon}^{\circ *} = \left(\mathbf{K}_{22} - \mathbf{K}_{12}^{\mathrm{t}}\mathbf{K}_{11}^{-1}\mathbf{K}_{12}\right)^{-1}\left(\mathbf{K}_{12}^{\mathrm{t}}\mathbf{K}_{11}^{-1}(\mathbf{F}^{\boldsymbol{\sigma}_0} - \mathbf{F}^{\boldsymbol{\epsilon}^\circ(7)}) + \bar{\mathbf{F}}^{\boldsymbol{\epsilon}^\circ(7)} - \bar{\mathbf{F}}^{\boldsymbol{\sigma}_0}\right) + \mathbf{C}^{*-1}{\boldsymbol{\sigma}_0}^* \tag{2.62}$$

is again found by solving a seventh boundary value problem, for which $\boldsymbol{\epsilon}^{\circ(7)}(\boldsymbol{x}) = \boldsymbol{\epsilon}^\circ(\boldsymbol{x})|_n$ and $\bar{\boldsymbol{\sigma}}^{(7)} = 0$.

2.2.3. Implementation

A fortran 90 code, named PPHMG, has been developed to compute the effective properties of prismatic materials using the method presented above.

A prismatic material, also reffered to as a unidirectional material, is one in which if X is any material property then in the reference state

$$X(\boldsymbol{x}) = X(\boldsymbol{x} + \alpha \boldsymbol{p}), \forall \alpha \in \mathbb{R} \tag{2.63}$$

where $\boldsymbol{p}$ is a vector defining the prismatic axis. Prismatic materials are of interest in this thesis because the structure of wood at several scales has a first order idealization which is prismatic.

As the boundary conditions discussed above are also uniform in the prismatic direction the perturbation displacements must be the same in any plane normal to the prismatic axis. Thus, it is sufficient to compute these displacements for a single plane thereby reducing the problem from three to two dimensions.

PPHMG can handle representative volumes of arbitrary shape, though if the periodic boundary conditions are to be used the boundary mesh must be such that each node on the boundary can be mapped to a single other node also on the boundary by a linear combination of the periodicity vectors. This requirement is more than sufficient to ensure that the boundary meets the criteria of (2.54). The need for a periodic boundary mesh for application of periodic boundary conditions could be relaxed by imposing the bounday conditions by constraints rather than through the shape functions though doing this would negate most of the advantages of the perturbation displacement formulation.

PPHMG uses the straight sided 6-node linear strain triangular element shown in figure 2.2 within which the perturbation displacements are approximated by

$$\tilde{\mathbf{u}} = \mathbf{N}_e \tilde{\mathbf{u}}_e \tag{2.64}$$

where

$$\tilde{\mathbf{u}} = \begin{bmatrix} \tilde{u}_1 & \tilde{u}_2 & \tilde{u}_3 \end{bmatrix}^{\mathrm{t}}, \tag{2.65}$$

$$\tilde{\mathbf{u}}_e = \begin{bmatrix} \tilde{\mathbf{u}}^1 & \tilde{\mathbf{u}}^2 & \tilde{\mathbf{u}}^3 & \tilde{\mathbf{u}}^4 & \tilde{\mathbf{u}}^5 & \tilde{\mathbf{u}}^6 \end{bmatrix}^{\mathrm{t}}, \tag{2.66}$$

$$\mathbf{u}^i = \begin{bmatrix} \tilde{u}^i_1 & \tilde{u}^i_2 & \tilde{u}^i_3 \end{bmatrix}^{\mathrm{t}}, \quad i \in \{1,2,3,4,5,6\} \tag{2.67}$$

$$\mathbf{N} = \begin{bmatrix} (2L_1 - 1)L_1\mathbf{I}_3 & (2L_2 - 1)L_2\mathbf{I}_3 & (2L_3 - 1)L_3\mathbf{I}_3 & 4L_1L_2\mathbf{I}_3 & 4L_2L_3\mathbf{I}_3 & 4L_3L_1\mathbf{I}_3 \end{bmatrix}^{\mathrm{t}}. \tag{2.68}$$

and L_1, L_2 and L_3 are triangular coordinates. This element permits material properties

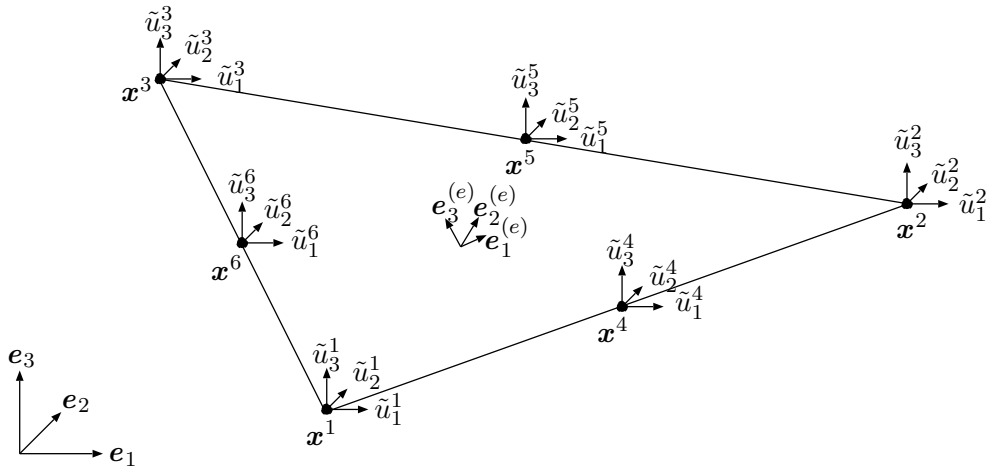

Figure 2.2.: Linear strain triangle (LST). Element nodes 4, 5, and 6 are placed exactly at the edge midpoint.

of arbitrary anisotropy, but within an element these properties are uniform, an assumption appropriate for composite (piecewise-homogeneous) domains. Material properties are specified with respect to an element coordinate system whose orientation relative to the global coordinate system is defined by three Euler angles.

A variety of linear equation solvers, both direct and iterative, are available within PPHMG for the solution of the system equations. All the results presented here have been computed using the SuperLU sparse direct solver freely available from `http://www.nersc.gov/~xiaoye/SuperLU`.

2.2.4. Verification

Any scheme for determining effective properties should meet certain criteria. These criteria include[5]

(i) The effective stiffness and compliance tensors should be symmetric and positive definite. In all cases the PPHMG produces symmetric and positive definite effective stiffness matrices.

(ii) Internal consistency relationships, such as those of Levin and Hill described below, between the effective moduli should be satisfied.

(iii) As the volume fraction of any phase tends towards unity the effective moduli should tend towards the properties of that phase. That PPHMG meets this criteria is guaranteed by the nature of the finite element process.

(iv) The effective properties should fall within any available variational bounds.

(v) The symmetries of the RV should be symmetries of effective properties.

[5]Discussions of criteria for evaluating homogenization schemes can be found in Aboudi (1991) and Li (1999).

Numerous tests have been conducted to verify that PPHMG meets the above criteria and can thus be considered to have been conceived and implemented correctly. Four of these tests are reported below.

2.2.4.1. Test 1 – layered composite

Consider a material consisting of intercalated layers, of equal thickness, of two phases whose properties are given in table 2.1.

Effective properties for this material have been computed with PPHMG on a coarse (8 elements), medium (200 elements) and fine mesh (3200 elements) and using uniform stress, uniform strain and periodic boundary conditions (see table 2.1).

From the symmetries of the layered medium and the individual phases the effective properties would be expected to orthotropic with principal axes coincident with the global coordinate system. This is indeed the case.

For two-phase composites a fundamental result,

$$\boldsymbol{\epsilon}^{\circ *} = \boldsymbol{\epsilon}^{\circ}|^1 + \left(\mathbf{D}^* - \mathbf{D}|^1\right)\left(\mathbf{D}|^2 - \mathbf{D}|^1\right)^{-1}\left(\boldsymbol{\epsilon}^{\circ}|^2 - \boldsymbol{\epsilon}^{\circ}|^1\right), \tag{2.69}$$

due to Levin (1967) and Rosen and Hashin (1970), relates the effective expansional strain $\boldsymbol{\epsilon}^{\circ *}$ and compliance $\mathbf{D}^*$ to the phase expansional strains and compliances $\boldsymbol{\epsilon}^{\circ}|^1$, $\boldsymbol{\epsilon}^{\circ}|^2$ and $\mathbf{D}|^1$, $\mathbf{D}|^1$ (Hashin, 1983). All the PPHMG results in table 2.1 satisfy the criteria of equation 2.69 indicating that PPHMG is a consistent homogenization procedure.

The layered media method described in appendix C can also be used to determine the effective properties of this material, and properties so obtained coincide with those computed by PPHMG using periodic boundary conditions.

2.2.4.2. Test 2 – fibre composite

Consider a two-phase prismatic composite, consisting of hexagonally packed cylindrical fibres in a matrix. Both the fibre and the matrix are isotropic with the properties given in table 2.2. The RV and base mesh used in conjunction with PPHMG for this test is shown in figure 2.3.

The effective properties computed using PPHMG for the base mesh with and a refined mesh, created from the base mesh by splitting each original triagle into 4 congruent triangles, appear in table 2.2. Clearly mesh refinement does not alter the effective properties significantly and it may be assumed that convergence has been attained.

Effective properties with hexagonal symmetry, equivalent to isotropy in the 12-plane, can be expected given the RV and the phase material symmetries. Properties with hexagonal symmetry are indeed obtained using PPHMG though it should be noted that the mesh used also posseses hexagonal symmetry. When the mesh does not share

	E_1 GPa	ν_{12}	ν_{13} GPa	E_2	ν_{23} GPa	E_3 GPa	G_{23}	G_{31}	G_{12}	$\epsilon_1^\circ \times 10^3$	$\epsilon_2^\circ \times 10^3$	$\epsilon_3^\circ \times 10^3$
Phase properties												
phase 1	3	0.5	0.3	3	0.3	50	1	1	1	600	600	10
phase 2	6	0.3	0.5	25	0.072	6	2	2	2	1200	40	1200
PPHMG results, uniform stress BCs												
coarse mesh	4.4157	0.48254	0.41190	6.3849	0.16287	28.018	1.4173	1.3333	1.3333	1169.2	293.75	138.76
medium mesh	4.3758	0.48343	0.40863	6.0653	0.16924	28.013	1.4121	1.3334	1.3334	1163.0	306.22	138.41
fine mesh	4.3796	0.48307	0.40886	6.0785	0.16893	28.013	1.4133	1.3349	1.3349	1164.0	305.29	138.45
PPHMG results, periodic BCs												
coarse mesh	4.8823	0.46006	0.44628	14.217	0.096073	28.070	1.5000	1.3333	1.3333	1234.7	163.04	142.38
medium mesh	4.8823	0.46006	0.44628	14.217	0.096073	28.070	1.5000	1.3333	1.3333	1234.7	163.04	142.38
fine mesh	4.8823	0.46006	0.44628	14.217	0.096073	28.070	1.5000	1.3333	1.3333	1234.7	163.04	142.38
PPHMG results, uniform strain BCs												
coarse mesh	5.0718	0.45702	0.45137	14.219	0.095941	28.073	1.5000	1.4222	1.4792	1290.6	161.46	143.69
medium mesh	5.0395	0.45752	0.45053	14.218	0.095963	28.073	1.5000	1.4169	1.4702	1281.3	161.72	143.47
fine mesh	5.0380	0.45754	0.45049	14.218	0.095964	28.073	1.5000	1.4167	1.4698	1280.9	161.73	143.46
Layered media method results												
	4.8823	0.46006	0.44628	14.217	0.096073	28.070	1.5000	1.3333	1.3333	1234.7	163.04	142.38

Table 2.1.: PPHMG verification test 1. Phase and effective properties.

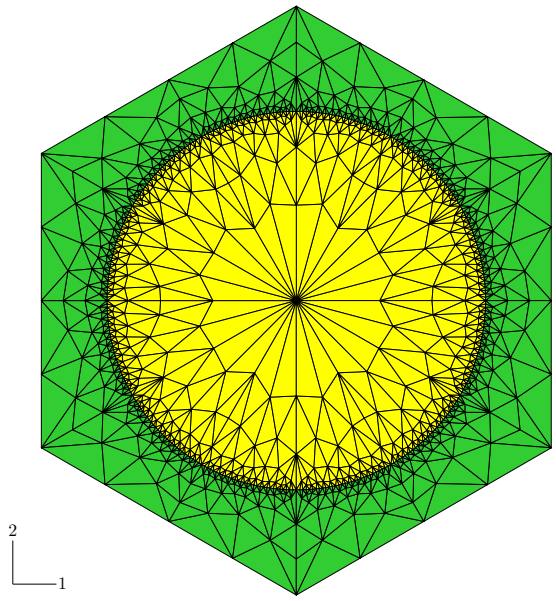

Figure 2.3.: RV used in PPHMG verification test 2.

	E_1 GPa	ν_{13}	E_3 GPa	G_{23} GPa	G_{12} GPa	$\epsilon_1^\circ \times 10^3$	$\epsilon_3^\circ \times 10^3$
			Phase properties				
fibre	100	0.25	100	40	40	0	0
matrix	1	0.35	1	0.37037	0.37037	1000	1000
			PPHMG results, periodic boundary conditions				
base mesh	2.9585	0.29357	50.501	1.0860	1.0150	585.04	10.764
refined mesh	2.9582	0.29357	50.501	1.0859	1.0148	585.04	10.764
			Primitive bounds				
$\mathbf{C}^*_\sigma$	1.9802	0.34901	1.9802	0.73394	0.73394	-	-
$\mathbf{C}^*_\epsilon$	50.524	0.25152	50.524	20.185	20.185	-	-
			Other homogenization procedures				
GSCM	2.8275	0.29359	50.503	1.0844	0.95448	585.33	10.760
MC ($\bar{\mathbf{C}}$)	2.9841	0.29481	50.503	0.98308	1.0376	601.75	10.597
MC ($\bar{\mathbf{D}}$)	2.7958	0.29481	50.503	0.98308	0.94876	601.75	10.597

Table 2.2.: PPHMG verification test 2. Phase and effective properties.

the RV symmetries, deviations from the expected effective material symmetries are observed. The magnitudes of these deviations decrease with increasing mesh refinement.

Hill (1964) showed that for a transversely isotropic prismatic composite with two isotropic phases (fibre and matrix) the effective axial Young's modulus E_3^*, the effective out-of-plane Poisson's ratio ν_{13}^* and the effective plane strain bulk modulus k^* are related to the Young's moduli $E|^f$, $E|^m$, Poisson's ratios $\nu|^f$, $\nu|^m$ and volume fractions $v|^f$, $v|^m$ of the fibre and matrix phases by

$$\begin{aligned} E_3^* &= v|^f E|^f + v|^m E|^m - 4\frac{(\nu|^f - \nu|^m)^2}{(1/k|^f - 1/k|^m)^2}\left(1/k^* - v|^f/k|^f - v|^m/k|^m\right) \\ \nu_{13}^* &= v|^f \nu|^f + v|^m \nu|^m + \frac{\nu|^f - \nu|^m}{1/k|^f - 1/k|^m}\left(1/k^* - v|^f/k|^f + v|^m/k|^m\right). \end{aligned} \tag{2.70}$$

The effective moduli produced by PPHMG for this test are in numerical agreement with both (2.70) and (2.69) indicating again that PPHMG is a consistent homogenization procedure.

The Voigt and Reuss models which assume uniform strain and stress fields within a heterogeneous body respectively provide primitive upper and lower bounds on the elastic constants (Whitney and McCullough, 1990). For the composite of this test the effective stifness predicted by the Voigt model is

$$\mathbf{C}_\epsilon^* = v|^f \mathbf{C}|^f + v|^m \mathbf{C}|^m \tag{2.71}$$

and the stiffness predicted by the Reuss model is

$$\mathbf{C}_\sigma^* = \left(v|^f (\mathbf{C}|^f)^{-1} + v|^m (\mathbf{C}|^m)^{-1}\right)^{-1}. \tag{2.72}$$

The engineering constants equivalent to these stiffnesses appear in table 2.2. Clearly they bound the results from PPHMG.

Numerous procedures for computing the effective properties of two-phase fibre composites are avaialable in the literature. Two of these, the generalized self-consistent method (GSCM) (Christensen and Lo, 1979, 1990) and the method of cells (MC) (Aboudi, 1991), have been used to compute effective properties for comparison with those produced by PPHMG. The generalized self-consistent method employs a cylindrical fibre cross-section and implicitly assumes that the fibres are randomly distributed and hence the composite is transversely isotropic (at least in a statistical sense). The method of cells is based on a model of square fibres distributed in a square array and consequently produces effective properties with square symmetry. For comparison with the transversely isotropic results obtained from the GSCM and PPHMG methods the method of cells results have been averaged using the orientational averaging procedure described in appendix B based on the stiffnesses and compliances. The agreement between the

ldiv	Ndofs	E_1	ν_{13}	E_3	G_{23}	G_{12}
1	1524	0.479374	0.250000	1.25001	0.328040	0.164501
2	5934	0.475327	0.250000	1.25001	0.327626	0.162779
3	13224	0.474207	0.250000	1.25001	0.327527	0.162308
4	23394	0.473704	0.250000	1.25001	0.327487	0.162097
5	36444	0.473423	0.250000	1.25001	0.327465	0.161979

Table 2.3.: Convergence results for test 3 PPHMG sharp model

ldiv	Ndofs	E_1	ν_{13}	E_3	G_{23}	G_{12}
1	1524	0.555764	0.250000	1.25001	0.332877	0.200314
2	5934	0.555027	0.250000	1.25001	0.332815	0.199962
3	13224	0.554904	0.250000	1.25001	0.332800	0.199909
4	23394	0.554860	0.250000	1.25001	0.332795	0.199890
5	36444	0.554839	0.250000	1.25001	0.332793	0.199881

Table 2.4.: Convergence results for test 3 PPHMG smooth model

various sets of effective properties table 2.2 can clearly be seen to be reasonable.

In figure 2.4 the effective properties computed using uniform stress (σ) and strain (ϵ) boundary conditions are compared to those computed using periodic boundary conditions for RVs containing different numbers of fibres. One such RV is shown in figure 2.5. Note that the mesh is much coarser than that shown in figure 2.3 so that computational capacity is not exceeded for RVs containing hundreds of fibres. Clearly all the moduli converge to those predicted using periodic boundary consditions as the size of the RV increases.

2.2.4.3. Test 3 – Hexagonal honeycomb

Consider a regular hexagonal honeycomb whose wall are composed of an homogeneous and isotropic material with a Young's modulus $E_s = 2.5$ GPa and a Poisson's ratio $\nu_s = 0.25$. Two models for this honeycomb with different internal cell geometries are shown in figure 2.6[6].

Convergence of PPHMG results with mesh refinement for these models appear in tables 2.3 and 2.4.

As should be expected all the effective properties computed using PPHMG are transversely isotropic, with effective expansional strains and longitudinal Poisson's ratios the same as those of the wall material.

[6]These models are generated using the cell mesher described in chapter 5.

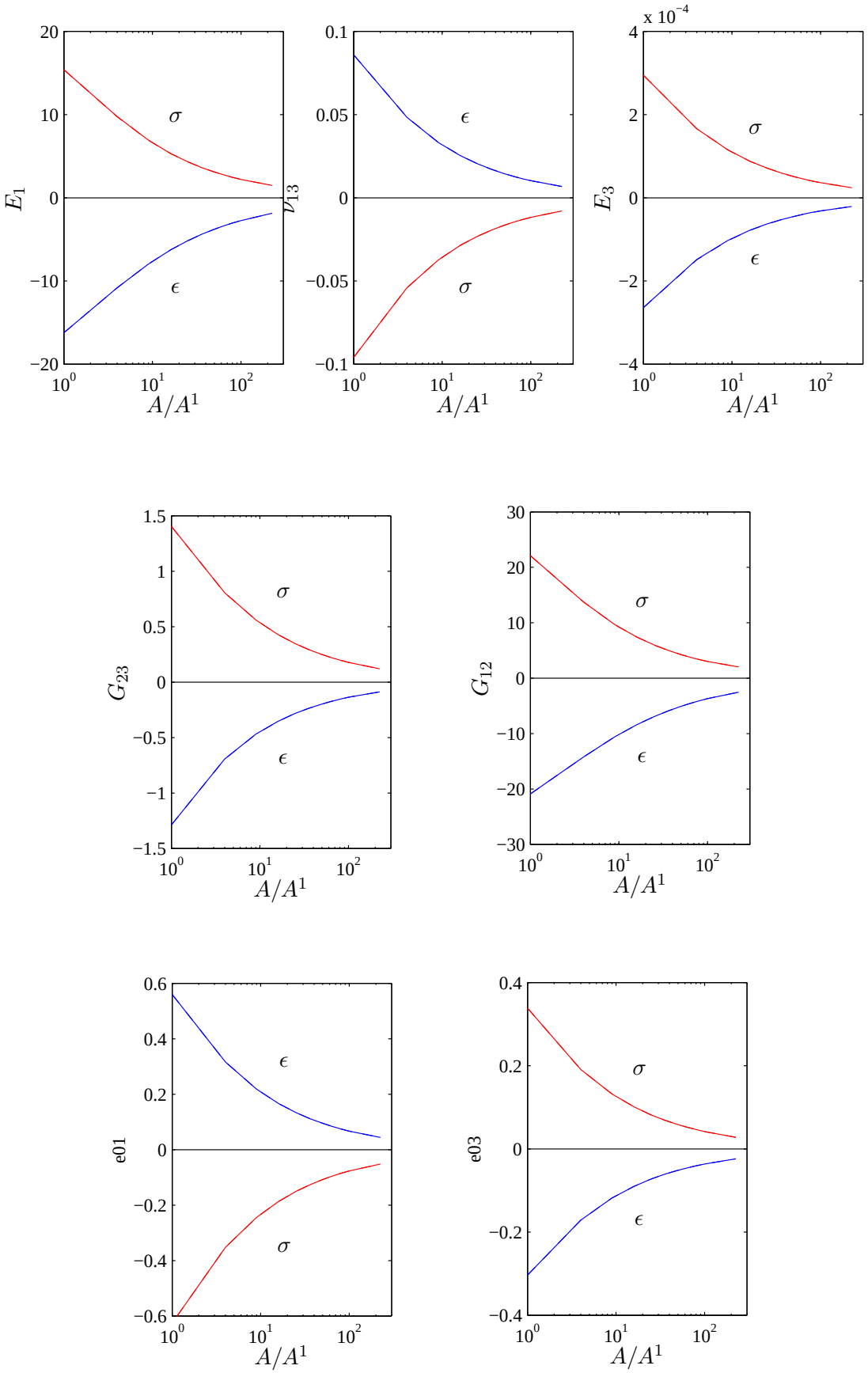

Figure 2.4.: Percentage differences between effective engineering constants computed by PPHMG using uniform stress (σ) and strain (ϵ) boundary conditions and those computed using periodic boundary conditions for various RV sizes.

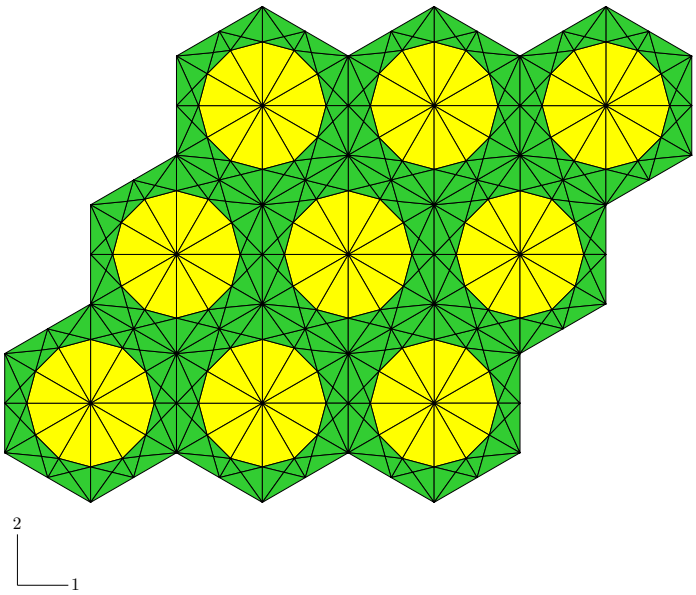

Figure 2.5.: Example RV for test 2b.

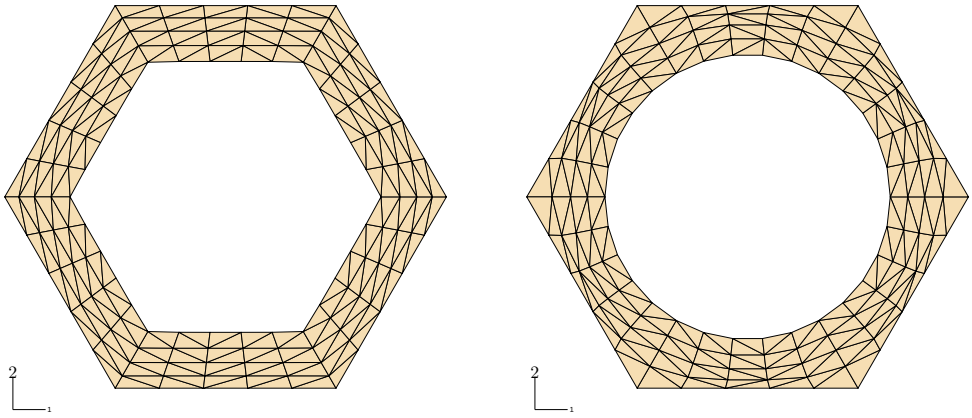

(a) sharp **(b)** smooth

Figure 2.6.: Test 3 PPHMG RVs

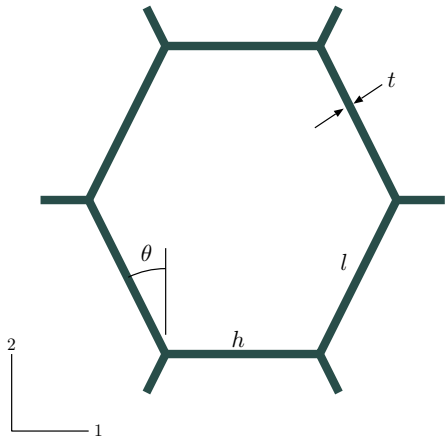

Figure 2.7.: Definition of geometry used in equations (2.73)–(2.74)

Gibson and Ashby (1988) give expressions for the transverse elastic moduli of a hexagonal honeycomb with homogeneous isotropic walls:

$$\begin{aligned} E_2^* &= E_s \left(\frac{t}{l}\right)^3 \frac{\cos\theta}{(h/l+\sin\theta)\sin^2\theta} \\ E_1^* &= E_s \left(\frac{t}{l}\right)^3 \frac{(h/l+\sin\theta)}{\cos^3\theta} \\ \nu_{21}^* &= \frac{\cos^2\theta}{(h/l+\sin\theta)\sin\theta} \\ G_{12}^* &= E_s \left(\frac{t}{l}\right)^3 \frac{(h/l+\sin\theta)}{(h/l)^3(1+2h/l)\cos\theta} \end{aligned} \tag{2.73}$$

where h, l, t and θ are defined as shown in figure 2.7, E_s is the Young's modulus of the wall material and the cellular and solid densities, ρ^* and ρ_s respectively, are related to the geometry by

$$\frac{\rho^*}{\rho_s} = \frac{t(h+2l)}{2\cos\theta(h+l\sin\theta)}.$$

These results were derived using standard beam theory and consider only deformation due to bending. Gibson and Ashby (1988) claim they give reasonable results when $l/t > 4$.

Stol (1995) (see also Gibson (1981) and Warren and Kreynik (1987)) presents extensions to these formulae that include shear and membrane contributions to the

deformation,

$$
\begin{aligned}
E_1^* &= E_s \frac{t^3(h + l\sin\theta)}{l^4\cos^3\theta\left(1 + \left(2.4 + 1.5\nu_s + \tan^2\theta + \frac{2h}{l\cos^2\theta}\right)\left(\frac{t}{l}\right)^2\right)} \\
E_2^* &= E_s \frac{t^3\cos\theta}{l^2\sin^2\theta(h + l\sin\theta)\left(1 + (2.4 + 1.5\nu_s + \cot^2\theta)\left(\frac{t}{l}\right)^2\right)} \\
E_3^* &= E_s \frac{t(h + 2l)}{2l\cos\theta(h + l\sin\theta)} \\
\nu_{12}^* &= \frac{l\cos^2\theta\left(1 + (1.4 + 1.5\nu_s)\left(\frac{t}{l}\right)^2\right)}{\sin\theta(h + l\sin\theta)\left(1 + (2.4 + 1.5\nu_s + \cot^2\theta)\left(\frac{t}{l}\right)^2\right)} \\
G_{23}^* &= E_s \frac{t(h + l\sin\theta)}{2l\cos\theta(1 + \nu_s)(2h + l)} \\
G_{12}^* &= E_s \frac{t^3(h + l\sin\theta)}{h^2 l\cos\theta(2h + l)\left(1 + \left(\frac{(l + h\sin\theta)^2}{2l\cos^2\theta} + \frac{6h(2l + h)}{5l(1 + \nu_s)}\right)\frac{2t^2}{h^2(2h + l)}\right)}
\end{aligned}
\tag{2.74}
$$

In figure 2.8 effective moduli from the two PPHMG models over the full range of cellular densities are compared with those from equations (2.73) and (2.74) as well as with those computed using another periodic homogenization procedure (shcmdl) employing thick-shell finite elements similar to that described in Astley et al. (1998). To get the closest correspondence with the formulae of (2.73) the wall material used for these comparisons has a Poisson's ratio $\nu_s = 0$. The longitudinal Poisson's ratio is not plotted since, as stated previously, it should be the same as that of the wall material.

At low effective densities all of these models give very similar results. As the effective densities increase however they diverge, except for the longitudinal modulus which is virtually insensitive to the cellular geometry. As the effective density approaches that of the wall material, the effective moduli computed using PPHMG, unlike those from the other models, approach the properties of the solid material. Curiously the simpler analytic model of (2.73) give estimates for the transverse moduli (E_1 and G_{12}) closer to those of PPHMG than do the improved model of (2.74). The details of the internal cell geometry make a small but detectable difference to the effective transverse moduli, but little or no difference to the longitudinal moduli.

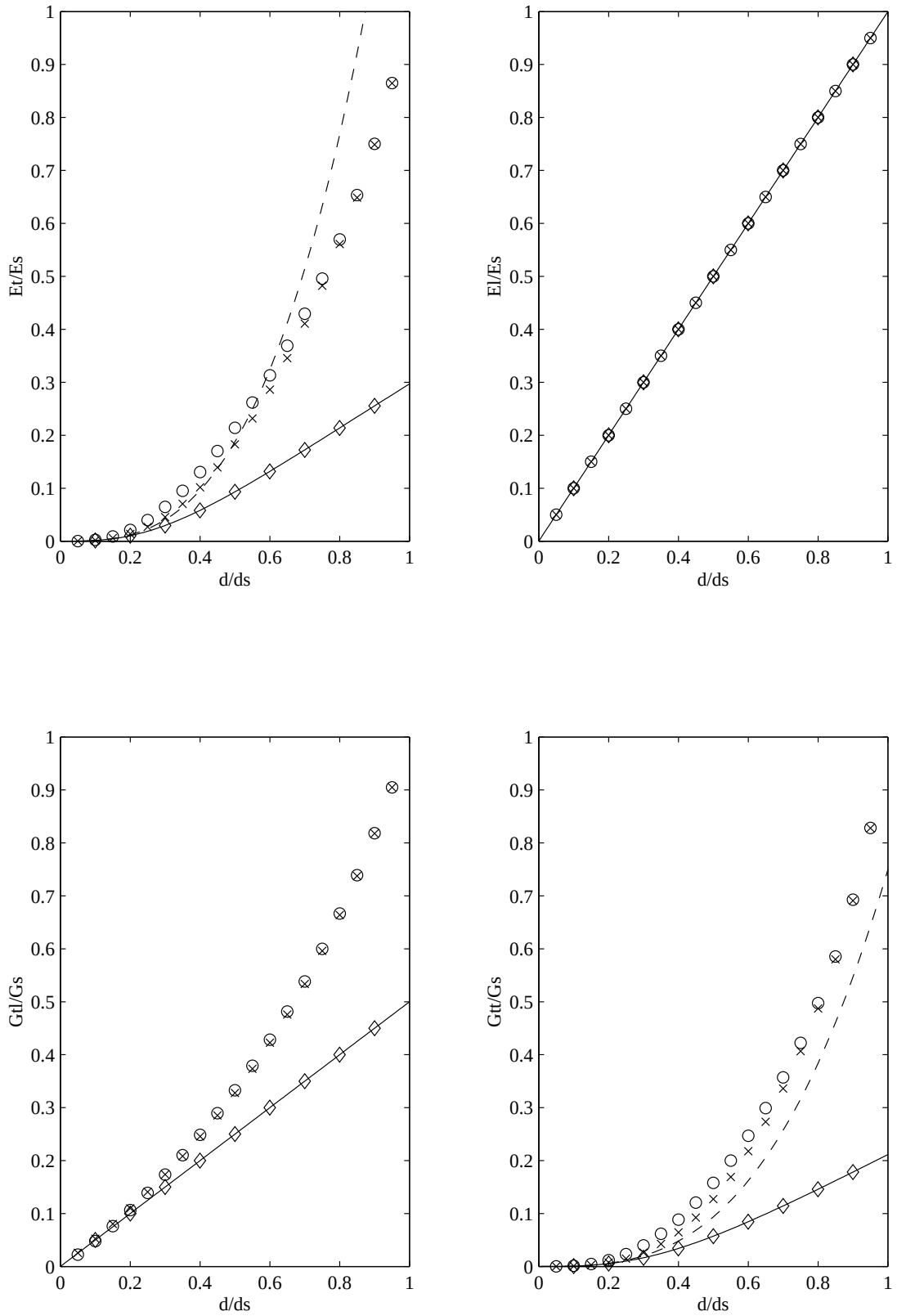

Figure 2.8.: Comparison of effective properties for a regular hexagonal honeycomb with isotropic material properties ($E_s = 1$, $\nu_s = 0$). - - equations (2.73), — equations (2.74), ∘ PPHMG smooth, × PPHMG sharp, ⋄ shcmdl.

Chapter 3

Nanoscale modelling

3.1. Introduction

Modelling at the nanoscale attempts to account for the influence on wood properties of the supramolecular organization including the local composition.

Three qualitatively distinct nanostructures can be identified with softwood xylem cell-walls. Specifically, these nanostructures are those of the inter-cellular middle lamella, the primary cell wall and the secondary cell wall.

Structure within the middle lamella primarily arises at a molecular level (Kibble-white and Thompson, 1973; Daniel et al., 1991; Fujino and Itoh, 1998; Hafreén et al., 2000; Donaldson, 2001a) and at a nanoscopic scale the middle lamella can be regarded as homogeneous and isotropic. The primary wall possesses the most complex of the cell-wall nanostructures, not suprising given its capacity for controlled and localised flow during cell expansion. Recent articles discussing primary wall architecture include: McCann et al. (1990); McCann and Roberts (1991); Carpita and Gibeaut (1993); Iiyama et al. (1994); Boylston and Hebert (1995); Salmén and Petterson (1995); Newman et al. (1996); Carpita (1996); Cosgrove (1997, 1999); Fenwick et al. (1997); Ha et al. (1997); Kataoka and Kondo (1998); Hafren et al. (1999); Vincent (1999); McCann et al. (2001). However, the primary wall is less than 100 nm thick and it is not thought to affect the mechanical properties of wood to a degree sufficient to warrant the extra complexity that modelling it separately would entail. Instead the material from the primary wall is included in either the middle lamella or secondary wall. Thus the secondary wall nanostructure is the focus of this chapter.

This chapter begins with a description of secondary wall nanostructure. Then the nanophases are defined and two composite representative volumes are proposed. Using these representative volumes, together with an assumed set of nanophase properties, the effects of varying the phase volume fractions and the shape and distribution of the microfibrils are considered. The chapter ends with a summary and discussion of the models presented along with suggestions for future work.

3.2. Secondary wall nanostructure

From a molecular standpoint the secondary wall consists of three dimensional interpenetrating networks of celluloses, hemicelluloses and lignins[1] with water and small quantities of other compounds distributed throughout. That these networks are contiguous can be deduced from the physical integrity of the unlignified cambial zone in case of the polysaccharide network and of the lignin skeleton created on removal of the carbohydrates by enzymatic (Reese, 1977) or hydrofluoric acid (Sachs et al., 1963; Cote et al., 1968) treatments.

Based on observations made using techniques such as: optical and electron micoscopy, X-ray diffraction, nuclear magnetic resonance, atomic force microscopy scanning-tunneling microscopy, Raman spectroscopy, and thermo-mechanical analysis, a number of models for the nanostructure of the secondary wall have been proposed (Fengel, 1969, 1970a; Fengel and Wegener, 1984; Preston, 1974; Scallan and Green, 1974; Kerr and Goring, 1975; Page, 1976; Ruel et al., 1978; Cave, 1978a; Salmén, 1991; Salmén and Olsson, 1998; Kataoka et al., 1992; Terashima et al., 1993; Hafren et al., 1999). The more recent of these models differ in detail but agree on generalities. Essentially the secondary wall consists of clusters of straight cellulosic microfibrils (CMFs) held in a steep layered trellis arrangement by hemicelluloses that coat and crosslink the CMFs. Lignins occupy the remaining spaces and, while no pore space is present within the cell wall, water is distributed throughout, except within the CMFs, held in varying degrees by the hemicelluloses and lignins and on the CMF surfaces. This structure is illustrated schematically in figure 3.1 though the trellis pattern has been omitted for clarity. Figure 3.1 also serves to define the coordinate system used in this chapter. The local CMF direction defines the 3-axis, the 1-axis is the normal to the 3-axis lying in the plane of the cell-wall. In this chapter the 1-, 2- and 3-directions are also referred to as the tangential, radial and longitudinal directions and the 12-plane is referred to as the transverse plane.

3.2.1. Cellulosic microfibrils

Cellulose chains are synthesized in bundles by terminal complexes travelling on the exterior of the cell plasma membrane. In wood, as in other higher plants, the terminal complexes consist of six globular synthases arranged in a rosette form (Fujino and Itoh, 1998; Hafren et al., 1999), and are thought to be capable of concurrently synthesizing 36 cellulose chains, though not all the synthetic sites are necessarily active at any given time. Recent reviews of this biosynthetic process can be found in Delmer (1999); Atalla (1999a); Brown (1999); Brown and Saxena (2000); Brett (2000); Lewis and Bolwell (2001).

[1] These chemical constituents are described in appendix D.

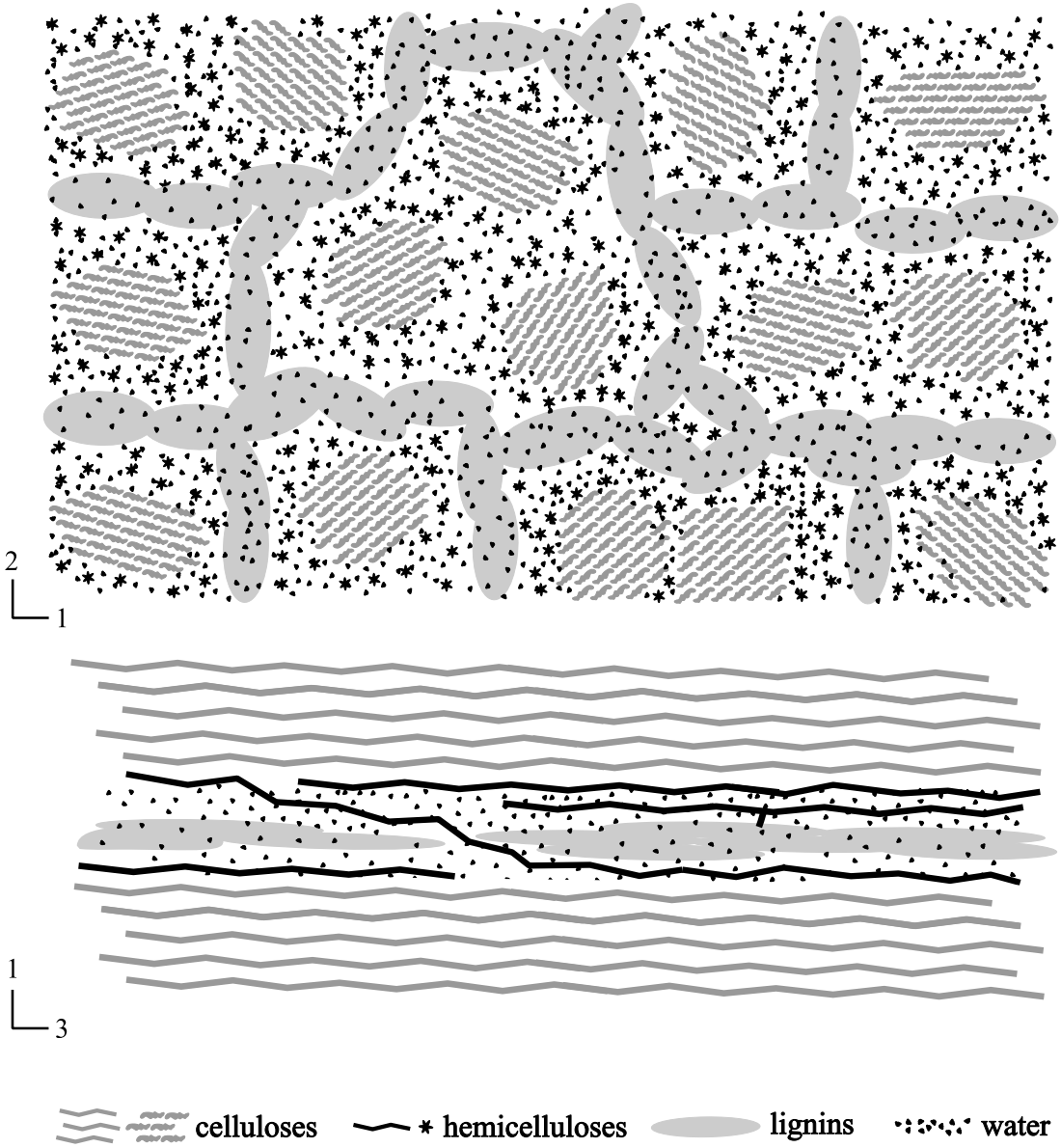

Figure 3.1.: Idealised secondary wall nanostructure.

Cellulose chains created at a single synthase aggregate to form a cellulosic microfibril. These microfibrils are of indefinite length (Mark, 1980), they may wrap continuously around the cell and certainly they are longer than the cellulose chains they contain. Generally CMFs are described as being straight and prismatic though twisted forms have also been described (Willison and Abeysekera, 1985; Hanley et al., 1997; Ruben et al., 1989; Hotchkiss, 1989).

Current estimates of CMF diameter in higher plants range from 2–4 nm (McCann et al., 1990; Jakob et al., 1994, 1995; O'Sullivan, 1997; Zhang et al., 1997; Newman, 1998, 1999a; Donaldson, 2001b), with the variation being attributable primarily to the method of measurement and the source rather than to variation within a sample. In cross-section CMFs from algal sources are square (Sugiyama et al., 1984; Harada and Sugiyama, 1985). Approximately square cross-sections have also been observed for CMFs from wood (Harada, 1982; Sugiyama et al., 1986), although rectangular and irregular hexagonal shapes have also been proposed (Beall and Murphy, 1970; Preston, 1974; Fengel and Wegener, 1984; Newman, 1998). In all likelihood the cross-section is variable, both along the length of an individual microfibril and between microfibrils.

Within the microfibrils the cellulose chains are highly ordered(O'Sullivan, 1997; Millane, 1998; Atalla, 1999a). This order was first demonstrated by Carl von Nägeli in 1858 who interpreted the cell walls birefringence as evidence that it contained at least one crystalline component (Preston, 1986). This notion of crystallinity has persisted although the CMF order may well be better thought of in terms of secondary and tertiary molecular structure (Atalla, 1999b,c). With rare exceptions, two crystalline forms have been detected in native celluloses (Atalla and van der Hart, 1984; van der Hart and Atalla, 1984; Sugiyama et al., 1990). These allomorphs, referred to as cellulose Iα and cellulose Iβ, have closely related (Baker et al., 1997, 1998) unit cells although Iα is triclinic and Iβ monoclinic. Both Iα and cellulose Iβ domains can be found within an individual microfibril and the transition between the two forms occurs abruptly Sugiyama et al. (1991). The Iα form is less stable and converts to Iβ on annealing (Yamamoto et al., 1989). Wada et al. (1994) claim that the Iβ form is more prevalent in wood, however, Newman (1999b) found that in radiata pine 51% by weight of the ordered cellulose is found in an I_α environment.

X-ray diffraction data indicates that crystallites in wood are 12–33 nm in length (Tanaka et al., 1981) and that the CMF diameter is slightly less than that measured by electron microscopy (Newman, 1998). These facts, combined with the fact that no matter how it is defined or measured, the crystallinity of cellulose is found to be less than complete, have been interpreted to mean that a fraction of the cellulose in wood is amorphous or disordered. It has been proposed that the disordered cellulose forms a cortex surrounding the crystalline core of a CMF and that zones of disorder occur along the length of a CMF. However, NMR studies indicate that the cellulose chains on the surface of the CMFs remain highly ordered (Newman, 1994) and small angle X-

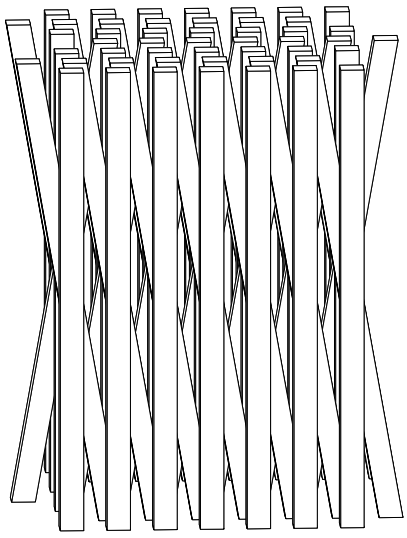

Figure 3.2.: 'Layered trellis' pattern of CMFs in S2.

ray scattering patterns of native cellulose fibres do not show the meridonial reflections typical of serial two-phase (crystalline/amorphous) polymers, though these reflections are observed upon degradation (Northolt and de Vries, 1985). Thus it would appear that all the cellulose present is highly ordered and that along their length the CMFs possess a homogenous structure.

During secondary wall development the CMFs are laid down on the inner surface of the cell wall in concentric lamellae. Within these lamellae the CMFs are parallel but between lamellae the CMF direction oscillates (Wardrop and Harada, 1965; Boyd and Foster, 1975; Kataoka et al., 1992; Hafren et al., 1999). This oscillation, through angles of around ten degrees in the S2 layer (Kataoka et al., 1992), gives rise to the steep layered trellis configuration illustrated in figure 3.2.

Cellulose chains are directed, that is one end differs from the other. Within a CMF the chains all point in the same direction (Millane, 1998) hence the CMFs are also directed. Within the cell wall equal numbers of 'up' and 'down' CMFs are present (Harada and Sugiyama, 1985; Preston, 1974).

In the cells walls of cellulosic algae, X-ray diffraction studies indicate that the crystalline regions within the CMFs are preferentially aligned in the plane normal to the chain direction (Preston, 1974). It is possible that this is also the case in wood cell walls, though a number of studies have concluded the opposite (Prud'homme and Noah, 1975; Revol et al., 1982; Lichtenegger et al., 1999). Even if the transverse orientation were uniplanar within the cell wall, on the whole it would appear to be evenly distributed due to the cylindrical nature of the cells.

While the microfibrils are deposited in concentric lamellae (Kataoka et al., 1992), concentric (tangential), radial, clustered and random arrangements have been proposed

for the microfibrils in the secondary wall layers (Kerr and Goring, 1975; Sugiyama et al., 1986; Abe et al., 1992; Sell and Zimmermann, 1993; Zimmermann, 1997). The aggregation of microfibrils give rise to macrofibrils with diameters of 20–100 nm (Abe et al., 1991, 1992; Sell and Zimmermann, 1993; Zimmermann, 1997; Daniel and Duchesne, 1998; Duchesne and Daniel, 1999)[2]. Donaldson (2001c) constructed a number of models for the transverse distribution of CMFs in the cell wall and found that the models that best agreed with observational data were those in which microfibrils occurred in a random arrangements with weak clustering.

3.2.2. Hemicelluloses and lignins

From a structural viewpoint the hemicelluloses can be divided into two groups, those associated with the celluloses and those associated with the lignins. Very approximately, in softwoods the former group correspond to the glucomannans and the latter group to the galactoglucomannans and xylans (Newman, 1992; Iiyama et al., 1994; Salmén and Olsson, 1998).

That fraction of the hemicelluloses associated with the cellulose forms a sheath surrounding the microfibrils (Keegstra et al., 1973; Kerr and Goring, 1975). These hemicelluloses are bound to the cellulose by secondary intermolecular forces (Erikson et al., 1980) and are aligned more or less with the cellulose (Liang et al., 1960; Preston, 1964; Fushitani, 1973; Page, 1976)

In primary cell walls hemicelluloses are thought to crosslink the CMFs (McCann et al., 1990; Cosgrove, 1999). Donaldson (1998) claims to have observed similar crosslinks, which he refers to as interfibrillar bridges, in the secondary wall of wood cells of *Pinus radiata*. These crosslinks form a secondary 'fibre' network, orthogonal to the primary network of the CMFs and serve to tether the microfibrils. Crosslinks have also been observed in the secondary wall by Nakashima et al. (1997).

Hemicelluloses are added to the cell wall at the same time as the cellulose (Takabe et al., 1989) and act as structure regulators (Hansson, 1970; Atalla et al., 1993; Uhlin et al., 1995; Whitney et al., 1997; Gregory and Bolwell, 1999) holding the CMFs in place prior to, and serving as a template for, lignification (Atalla, 1998).

During lignification the lenticular spaces formed by the hemicelluloses between the microfibrils are filled in by the lignins which polymerize *in situ* (Donaldson, 1994, 2001a). The lignins and hemicelluloses are bound together by covalent and hydrogen bonds (Erikson et al., 1980; Whistler and Chen, 1991) as well as by mechanical entanglement, resulting in a ligno-sachharide complex.

The lignins can be viewed as serving to crosslink the polysachharide networks (Gregory and Bolwell, 1999), or alternatively, the hemicelluloses can be viewed as coupling

[2]Considerable confusion exists as to what constitutes a microfibril. Macrofibrils are sometimes called microfibrils, especially by pulp technologists, and the CMFs are referred to as elementary fibrils.

agents connecting the CMFs and lignin (Page, 1976).

In the past lignin has been described as a globular, amorphous macromolecule (Frey-Wyssling, 1964; Erins et al., 1976) resulting from a random polymerization process (Fengel and Wegener, 1984). This view is currently undergoing dramatic change (Lewis, 1999) and the aromatic rings in lignins are now believed to be preferentially oriented in the plane of the cell wall (Atalla and Agarwal, 1985; Bond and Atalla, 1999).

3.3. Effective properties

At the supramolecular scale the lignified secondary wall is frequently likened to steel reinforced concrete or to fibre reinforced composites. These analogies, apparently introduced by Freudenberg (1932), have served qualitatively, as pedagogical aids, as well as quantitatively where they permit the computational apparatus of continuum micromechanics to be applied to the problem of determining effective properties for nanostructural domains. This approach has been taken by, for example, Mark (1967) and Cave (1968) and is adopted again herein. Alternative approaches to modelling the cell wall include the spring models of Hearle (1963); Cowdrey and Preston (1966), the discrete element model of Hepworth and Vincent (1998), models based on the theory of hydrogen bond dominated solids (Batten and Nissan, 1987a,b; Nissan, 1987; Nissan and Batten, 1997) and the atomistic models of Faulon et al. (1994); Faulon and Hatcher (1994) and Jurasek (1995, 1996, 1998b), although the latter type of models have as yet to be used to evaluate mechanical properties.

3.3.1. Nanophases

The cellulosic microfibrils, the hemicelluloses which coat the microfibrils and the ligno-saccharide complex in which the coated microfibrils are embedded are here treated as distinct phases, referred to below as the CF (cellulose fibre), HS (hemicellulose sheath) and LM (ligno-saccharide matrix) phases respectively. This division of wood substance into three phases appears to have originated with Wardrop (1963) who separated the molecular constituents into three classes based on their structural roles, designating them the 'framework', 'matrix' and 'encrusting' substances.

A three phase nanomechanics model was first proposed by Cave (1978a) and has subsequently been employed with variations by Salmén and de Ruvo (1985), Koponen et al. (1989), Persson (1997) and Harrington et al. (1998). In other nanomechanical models all of the non-microfibrillar material is lumped together as a matrix phase (Mark, 1967; Navi and Huet, 1989). Two phase models have also been explored in the course of this study. They have the advantage that they require fewer parameters, however, three phase models include two phase models as a degenerate case and,

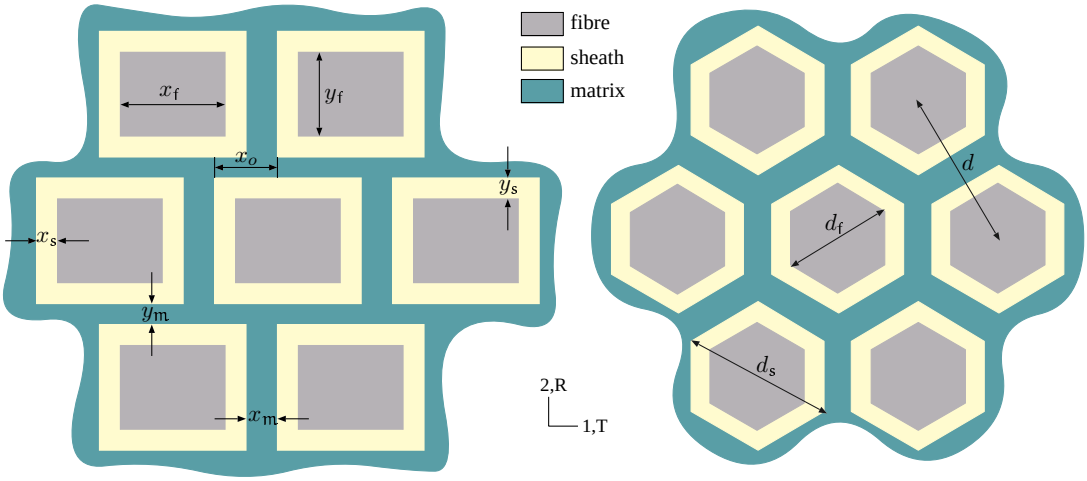

(a) RR3 model (b) HH3 model

Figure 3.3.: Nanostructural model geometries

since the molecules in the hemicellulose sheath behave quite differently to the lignosaccharide matrix in respect to moisture and are also differently oriented, it is easier to estimate the HS and LM phase properties independently rather than collectively. Consequently only three phase models are reported here.

Nanophase properties are discussed in detail in chapter 8. For the present it suffices to say that it is assumed that the all of the nanophases possess properties which are isotropic in the 12-plane.

3.3.2. Nanostructural representative volumes

Based on the structural description of the secondary wall nanostructure given above, two representative volumes shown in figure 3.3 are proposed. The first, the RR3 model shown in figure 3.3(a), has rectangular fibres in a regular rectangular packing. The second, the HH3 model shown in figure 3.3(b), has hexagonal fibres in a regular hexagonal packing.

In both the HH3 and RR3 models the CMFs are assumed to be continuous and homogeneous along their length. These concepts of longitudinal continuity and homogeneity are supported by results from the discontinuous model of Salmén and de Ruvo (1985) but may not be applicable to chemically treated or biologically degraded wood. Both the HH3 and RR3 models also assume that within a nanostructural domain the CMFs are straight and parallel. These assumptions admit a prismatic representation for the nanostructure, reducing the geometric description from three to two dimensions. The variation in CMF direction between layers is partially accounted for by the models presented in the next chapter.

3.3.2.1. The RR3 model

The RR3 model (see figure 3.3(a)), so called because it is a rectilinear three-phase composite model in a rectangular unit cell, requires six independent parameters to specify the relative geometry. For convenience the parameters selected are the CF and LM phase volume fractions, $v|^{\mathrm{f}}$ and $v|^{\mathrm{m}}$, the CF, HS and LM shape ratios, a_{f}, a_{s} and a_{m}, defined as

$$a_{\mathrm{f}} \triangleq \frac{x_{\mathrm{f}}}{x_{\mathrm{f}} + y_{\mathrm{f}}}, \tag{3.1}$$

$$a_{\mathrm{s}} \triangleq \frac{x_{\mathrm{s}}}{x_{\mathrm{s}} + y_{\mathrm{s}}}, \tag{3.2}$$

$$a_{\mathrm{m}} \triangleq \frac{x_{\mathrm{m}}}{x_{\mathrm{m}} + y_{\mathrm{m}}}, \tag{3.3}$$

and the fibre offset ratio, a_o,

$$a_o \triangleq \frac{d}{x} = \frac{x_o}{x_{\mathrm{f}} + 2x_{\mathrm{s}} + x_{\mathrm{m}}} \tag{3.4}$$

with the restriction $-0.5 \leq a_o \leq 0.5$ imposed for uniqueness[3]. On setting $y_{\mathrm{f}} \triangleq 1$ the cartesian parameters shown in figure 3.3(a) are given, in terms of the convenience parameters, by

$$y_{\mathrm{s}} = \frac{(a_{\mathrm{s}} - 1)\left[v|^{\mathrm{f}} K \left\{K a_{\mathrm{m}}(1 - a_{\mathrm{f}}) - 2a_{\mathrm{f}} a_{\mathrm{m}} + a_{\mathrm{f}} + a_{\mathrm{m}}\right\} + v|^{\mathrm{m}} a_{\mathrm{f}}(a_{\mathrm{m}} - 1)\right]}{2v|^{\mathrm{f}} K(a_{\mathrm{f}} - 1)(2a_{\mathrm{s}} a_{\mathrm{m}} - a_{\mathrm{s}} - a_{\mathrm{m}})} y_{\mathrm{f}}, \tag{3.5}$$

$$y_{\mathrm{m}} = K y_{\mathrm{f}}, \tag{3.6}$$

$$x_{\mathrm{f}} = \frac{a_{\mathrm{f}}}{1 - a_{\mathrm{f}}} y_{\mathrm{f}}, \tag{3.7}$$

$$x_{\mathrm{s}} = \frac{a_{\mathrm{s}}}{1 - a_{\mathrm{s}}} y_{\mathrm{s}}, \tag{3.8}$$

$$x_{\mathrm{m}} = \frac{a_{\mathrm{m}}}{1 - a_{\mathrm{m}}} y_{\mathrm{m}}, \tag{3.9}$$

$$x_o = a_o(x_{\mathrm{f}} + 2x_{\mathrm{s}} + x_{\mathrm{m}}), \tag{3.10}$$

[3] If the phase properties have the same symmetries as the RR3 unit cell, which is the case if all the nanophases are assumed to be isotropic in the 12-plane, then the a_o can be restricted further to $0 \leq a_o \leq 0.5$.

where K is the least positive real root of

$$\begin{aligned}
&v|^{\mathrm{f}2} a_{\mathrm{m}}^2 a_{\mathrm{s}} (a_{\mathrm{f}}-1)^2 (a_{\mathrm{s}}-1) K^4 \\
&+ v|^{\mathrm{f}2} a_{\mathrm{m}} (a_{\mathrm{f}}-1)(a_{\mathrm{f}}-a_{\mathrm{s}})(a_{\mathrm{s}}-a_{\mathrm{m}}) K^3 \\
&+ v|^{\mathrm{f}} \left[v|^{\mathrm{m}} a_{\mathrm{f}} (a_{\mathrm{f}}-1) \left\{ a_{\mathrm{s}}^2 (1-2a_{\mathrm{m}}) + 2a_{\mathrm{s}}^2 a_{\mathrm{m}}^2 + a_{\mathrm{m}}^2 (1-2a_{\mathrm{s}}) \right\} \right. \\
&\qquad \left. - v|^{\mathrm{f}} a_{\mathrm{m}} (a_{\mathrm{f}}-a_{\mathrm{s}})^2 (a_{\mathrm{m}}-1) - a_{\mathrm{f}} (2a_{\mathrm{s}} a_{\mathrm{m}} - a_{\mathrm{s}} - a_{\mathrm{m}})^2 (a_{\mathrm{f}}-1) \right] K^2 \\
&+ v|^{\mathrm{f}} v|^{\mathrm{m}} a_{\mathrm{f}} (a_{\mathrm{m}}-1)(a_{\mathrm{m}}-a_{\mathrm{s}})(a_{\mathrm{f}}-a_{\mathrm{s}}) K \\
&+ v|^{\mathrm{m}2} a_{\mathrm{f}}^2 a_{\mathrm{s}} (a_{\mathrm{m}}-1)^2 (a_{\mathrm{s}}-1) \\
&= 0.
\end{aligned} \tag{3.11}$$

Obviously these relations are undefined when $a_{\mathrm{f}} = 1$, $a_{\mathrm{s}} = 1$ or $a_{\mathrm{m}} = 1$ ($y_{\mathrm{f}} = 0$, $y_{\mathrm{s}} = 0$ or $y_{\mathrm{m}} = 0$). The first two of these degenerate cases are of no interest but when $a_{\mathrm{m}} = 1$

$$y_{\mathrm{s}} = \frac{(a_{\mathrm{s}}-1)\left[K(1-v|^{\mathrm{m}})(1-a_{\mathrm{f}}) - a_{\mathrm{f}}\right]}{2a_{\mathrm{s}}(a_{\mathrm{f}}-1)} y_{\mathrm{f}}, \tag{3.12}$$

$$x_{\mathrm{m}} = v|^{\mathrm{m}} K y_{\mathrm{f}}, \tag{3.13}$$

with K being a root of

$$v|^{\mathrm{f}} (v|^{\mathrm{m}} - 1)(a_{\mathrm{s}}-1)(a_{\mathrm{f}}-1) K^2 + 2v|^{\mathrm{f}} (a_{\mathrm{f}} - a_{\mathrm{s}}) K + (a_{\mathrm{s}}+1)(1+a_{\mathrm{f}}) = 0. \tag{3.14}$$

With suitable choices of a_{f}, a_{s}, a_{m} and a_o RR3 models can represent both radial and tangential CMF distributions as shown in figures 3.3 and 3.4.

The RR3 model has reflectional symmetries in the 13-plane and 12-planes. If the phase properties share these symmetries, and it is assumed that they do, then the effective properties of an RR3 model will be orthotropic.

3.3.2.2. The HH3 model

If the CMFs are distributed randomly in transverse planes (and this seems quite reasonable) and randomly oriented in these planes (i.e. no preferred crystalographic direction other than the chain direction), then the nanoscale properties would be expected to be transversely isotropic. The orthotopic properties produced by RR3 models could be averged using the orientational averaging described in appendix B to yield transversely isotropic properties. Alternatively an RV could be devised with hexagonal symmetry which would yield transversely isotropic properties if the phase properties are also transversely isotropic[4]. Several such apossibilities are illustrated in figure 3.5, The HH3 model (see figure 3.3(b)), which derives its name from being a 3-phase model with

[4]Tiling theory is a rich source for periodic representative volumes. See Grünbaum and Shephard (1986) for an introduction.

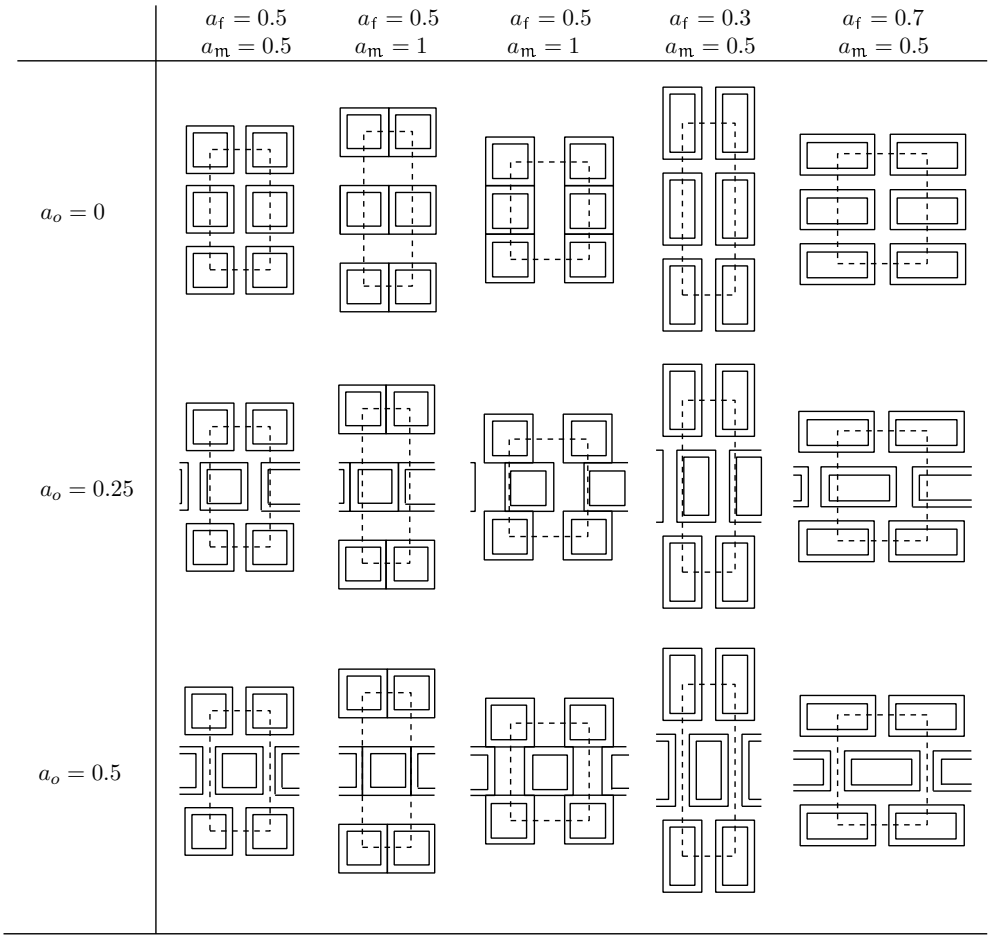

Figure 3.4.: Various RR3 configurations. Dashed lines indicate possible unit cells.

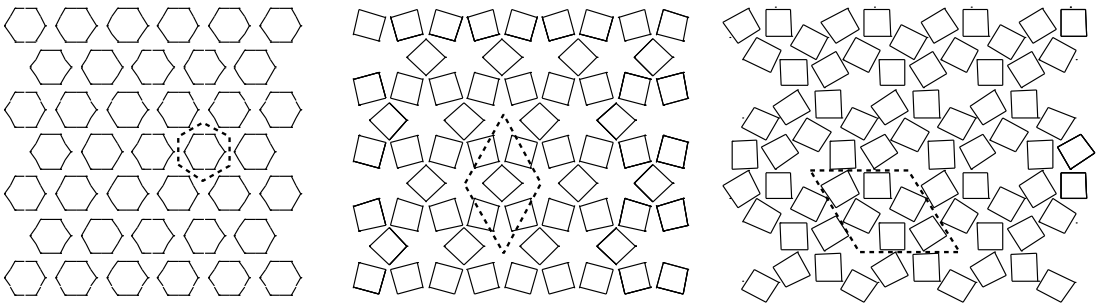

Figure 3.5.: Examples of RVs with hexagonal symmetry. Possible unit cells are indicated by dashed lines.

hexagonal CF domains in a hexagonal unit cell, is the simplest of these possibilities and allows the complete range of possible phase volume fractions to be treated without allowances having to be made for changing phase geometries. While the transverse isotropy of the effective properties produced by an HH3 model is the product of symmetry rather than disorder they are expected to be closer to the disordered properties than the effective properties determined using regular grid models such as the RR3.

The hexagonal CF phase domains in the HH3 model also provide an opportunity to investigate whether or not the transvserse shape of the microfibrils has any effect on the effective properties.

The relative geometry of the HH3 model is specified by the CF and LM phase volume fractions, $v|^{\mathrm{f}}$ and $v|^{\mathrm{m}}$ respectively. Setting $d = \sqrt{3}$

$$d_{\mathrm{f}} = \frac{\sqrt{3v|^{\mathrm{f}}}}{2}, \tag{3.15}$$

$$d_{\mathrm{s}} = \frac{\sqrt{3(1 - v|^{\mathrm{m}})}}{2}. \tag{3.16}$$

3.3.3. Convergence

Effective properties for the RR3 and HH3 models can be computed using the finite element based homogenizer, PPHMG, described in chapter 2. Since the HH3 and RR3 models represent periodic materials, periodic boundary conditions are applicable and only a single unit cell need be considered.

Determination of effective properties at the macroscale (board scale) involves numerous nanoscale homogenizations (currently each evaluation of macroscale effective properties involves 4 nanostructural homogenizations), so it is important that the process is as efficient as possible. On the other hand the accuracy of the finite element approximation depends on the number of elements used. In this section an FE mesh representing an optimal tradeoff between accuracy and efficiency is sought.

The base meshes used with the HH3 and RR3 models are shown in figure 3.6.

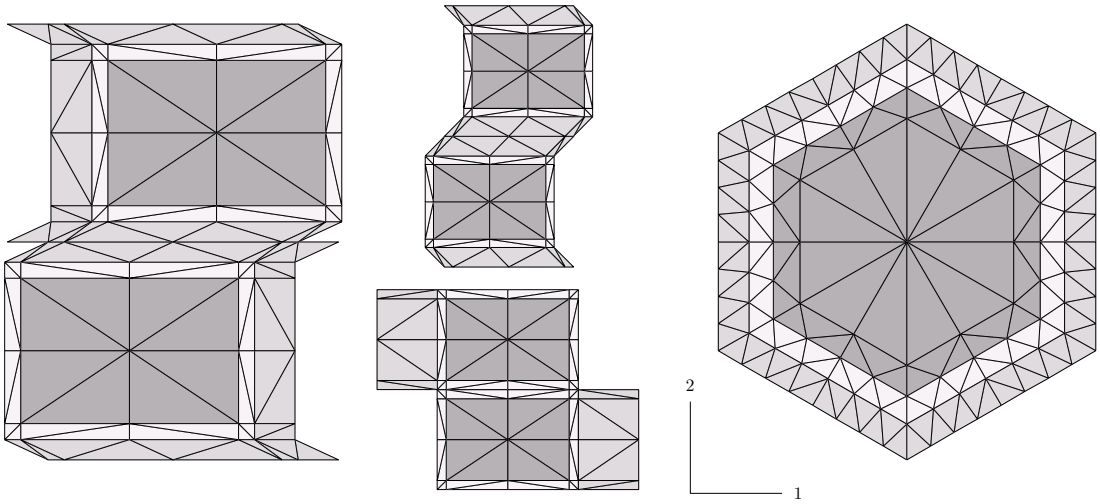

(a) RR3 model (b) HH3 model

Figure 3.6.: RR3 and HH3 model base meshes.

Within PPHMG a simple mesh refinement facility is provided which splits each edge in the base mesh into N_l new edges, producing N_l^2 new triangles for each original triangle.

The results of experiments performed on models with typical geometries and with the nanophase properties of table 3.1 appear in tables 3.2 and 3.3[5]. The nanophase volume fractions employed are $v|^{\mathsf{f}} = 0.32$, $v|^{\mathsf{s}} = 0.30$, $v|^{\mathsf{m}} = 0.38$. These nanophase properties and volume fractions are the product of the models described in chapters 8 and 7. They correspond to a nanostructural domain with a dry CF mass fraction of 0.5 g/g, at saturated moisture content and ambient temperature. This state was chosen so as to provide a critical test of the homogenization procedure as in this condition the HS phase has passed through its glass transition whereas the LM phase has not and consequently the nanophase stiffnesses are spread over three orders of magnitude.

For both models covergence is observed for all the effective material parameters. As might be expected the longitudinal stiffness (C_{33})) and the hygroexpansional coefficients converge rapidly. The remaining stiffnesses are converge more slowly with the transverse shear stiffness (C_{66}) usually being the most difficult effective property to compute.

Properties computed using the HH3 model converge more rapidly with N_l than those computed using the RR3 model due to the greater stress concentration at the phase corners in the RR3 model and the better initial mesh of the HH3 model.

If it is assumed that the single test case studied is representative then from these convergence studies a reasonable tradeoff between accuracy and efficiency is obtained

[5]The times reported in tables 3.2 and 3.3 are CPU times on a 1200 MHz AMD Athlon processor with 768 MB RAM running Linux 2.2 and should be considered as a guide only as considerable variation is observed between repetitions.

	w	χ	$\chi_{,w^\star}$ g/cc	ρ GPa	E_1 GPa	ν_{13} GPa	E_3 GPa	G_{23} GPa	G_{12} $\times 10^{-3}$	α_1^w $\times 10^{-3}$	α_3^w
CF	0	0	0	1.6	10.08	0.02083	140.0	3.700	3.600	0	0
HS	0.80	1	0	1.2	7.244×10^{-3}	0.5640	0.06606	5.900×10^{-3}	2.400×10^{-3}	930	130
LM	0.47	0.59	0	1.2	0.9838	0.4054	0.9838	0.3500	0.3500	270	270

Table 3.1.: Test case phase properties.

N_l	Ndofs $\times 10^3$	cpusec s	ρ g/cc	C_{11} GPa	C_{12} GPa	C_{13} GPa	C_{22} GPa	C_{23} GPa	C_{33} GPa	C_{44} GPa	C_{55} MPa	C_{66} MPa	α_1^w $\times 10^{-3}$	α_2^w $\times 10^{-3}$	α_3^w $\times 10^{-3}$
1	0.717	0.4	1.33	0.308	0.0522	0.140	0.190	0.0922	45.3	0.0921	0.100	0.0272	638	685	3.62
2	2.88	1.3	1.33	0.304	0.0489	0.137	0.180	0.0867	45.3	0.0912	0.0995	0.0239	639	692	3.62
3	6.48	2.9	1.33	0.303	0.0475	0.136	0.177	0.0851	45.3	0.0909	0.0992	0.0233	639	694	3.62
4	11.5	8.6	1.33	0.302	0.0469	0.135	0.176	0.0844	45.3	0.0908	0.0991	0.0230	639	695	3.62
5	18.0	13.3	1.33	0.302	0.0465	0.135	0.175	0.0839	45.3	0.0907	0.0991	0.0229	639	695	3.62
6	25.9	29.6	1.33	0.302	0.0462	0.135	0.175	0.0836	45.3	0.0907	0.0990	0.0228	639	696	3.62
7	35.3	59.5	1.33	0.301	0.0460	0.135	0.175	0.0834	45.3	0.0907	0.0990	0.0227	640	696	3.62
8	46.1	78.7	1.33	0.301	0.0459	0.135	0.174	0.0833	45.3	0.0907	0.0990	0.0227	640	696	3.62
9	58.3	118	1.33	0.301	0.0458	0.135	0.174	0.0831	45.3	0.0906	0.0990	0.0226	640	697	3.62
10	72.0	175	1.33	0.301	0.0457	0.135	0.174	0.0830	45.3	0.0906	0.0990	0.0226	640	697	3.62
11	87.1	325	1.33	0.301	0.0456	0.134	0.174	0.0830	45.3	0.0906	0.0990	0.0226	640	697	3.62
12	104	399	1.33	0.301	0.0455	0.134	0.174	0.0829	45.3	0.0906	0.0989	0.0226	640	697	3.62

Table 3.2.: RR3 model convergence. Model parameters: $v|^{\mathrm{f}} = 0.32$, $v|^{\mathrm{s}} = 0.30$, $v|^{\mathrm{m}} = 0.38$, $a_{\mathrm{f}} = 0.5$, $a_{\mathrm{s}} = 0.5$, $a_{\mathrm{m}} = 0.5$, $a_o = 0.5$.

N_l	Ndofs $\times 10^3$	cpusec s	ρ g/cc	C_{11} GPa	C_{13} GPa	C_{33} GPa	C_{44} GPa	C_{66} GPa	α_1^w $\times 10^{-3}$	α_3^w $\times 10^{-3}$
1	1.15	0.5	1.33	0.234	0.147	45.3	0.0989	0.0463	643	3.61
2	4.61	2.1	1.33	0.231	0.146	45.3	0.0987	0.0447	644	3.61
3	10.4	7.7	1.33	0.231	0.145	45.3	0.0986	0.0443	644	3.61
4	18.4	26.6	1.33	0.230	0.145	45.3	0.0986	0.0442	644	3.61
5	28.8	39.5	1.33	0.230	0.145	45.3	0.0986	0.0441	644	3.61
6	41.5	102	1.33	0.230	0.145	45.3	0.0985	0.0440	644	3.61
7	56.4	179	1.33	0.230	0.145	45.3	0.0985	0.0440	644	3.61
8	73.7	179	1.33	0.230	0.145	45.3	0.0985	0.0440	644	3.61
9	93.3	632	1.33	0.230	0.145	45.3	0.0985	0.0439	644	3.61
10	115	721	1.33	0.230	0.145	45.3	0.0985	0.0439	644	3.61

Table 3.3.: HH3 model convergence. Model parameters: $v|^{\mathrm{f}} = 0.32$, $v|^{\mathrm{s}} = 0.30$, $v|^{\mathrm{m}} = 0.38$.

when $N_l = 2$ for the HH3 model or $N_l = 3$ for the RR3 model and that at these levels of mesh refinement the effective properties computed differ by at most 5 % from those that would have have been computed if an exceedingly fine mesh were used. Unless stated otherwise these mesh refinement levels are used in all subsequent calculations.

3.3.4. Influence of phase volume fractions

To investigate the influence of the phase volume fractions on the effective properties, HH3 models with the nanophase properties of table 3.1, CF phase volume fractions $v|^{\mathrm{f}}$ and LM phase matrix volume fractions $v|^{\mathrm{m}}_{\mathrm{s+m}} = v|^{\mathrm{m}}/(v|^{\mathrm{s}} + v|^{\mathrm{m}})$ from 0.1 to 0.9 have been computed using PPHMG. The results are plotted in figure 3.7.

The linear dependence of the density on CF phase volume fraction is to be expected. The similar dependence of E_3 on CF phase volume fraction is also what would have been predicted by a simple rules of mixtures analysis.

The nanophase properties used correspond to wood in the green condition, and in this condition hemicelluloses are known to retain very little stiffness (see chapter 8) hence the HS phase moduli are up to 3 orders of magnitude less than those of the CF phase. Even though the HS phase is completely surrounded by the stiffer LM phase, from figure 3.7 it is clear that the effective transverse moduli, E_1^* and G_{12}^*, and the longitudinal shear modulus, G_{23}^*, are controlled by the less stiff HS phase.

3.3.5. Influence of MF shape and distribution

To investigate the influence of CMF shape and transverse distribution, effective nanoscale properties have been computed using an HH3 and various RR3 models. Once again, the nanophase properties used are those in table 3.1 and the volume fractions are $v|^{\mathrm{f}} = 0.32$, $v|^{\mathrm{s}} = 0.30$, $v|^{\mathrm{m}} = 0.38$. The results are plotted in figures 3.8 and 3.9.

Models with $a_{\mathrm{f}} > 0.5$ correspond to the tangentially fasciculated CMF models like those of Kerr and Goring (1975). Models with $a_{\mathrm{m}} = 1$ correspond to that used by Cave (1978a).

It is clear from figures 3.8 and 3.9 that while the longitudinal modulus (E_3), the longitudinal Poisson's ratios (ν_{13}, ν_{23}), and the hygro-expansional coefficients (α_1^w, α_2^w, α_3^w) are little affected by variation in the transverse distribution of the CMFs, the transverse moduli (E_1, E_2), the transverse Poisson's ratio ($\nu_1 2$) and the shear moduli (G_{23}, G_{31}, G_{12}) are significantly affected. In general, the HH3 model results in effective properties towards the middle of the range resulting from RR3 models, and in particular are similar to the RR3 models with square CF, HS and LM phases. Exceptions to this statement appear to be ν_{13}, ν_{13} and G_{12}, but this is primarily due to the choice of coordinate system in which the results are presented. If the RR3 results for aligned ($a_o = 0$) or staggered ($a_o = 0.5$) square models are averaged over all possible in-plane

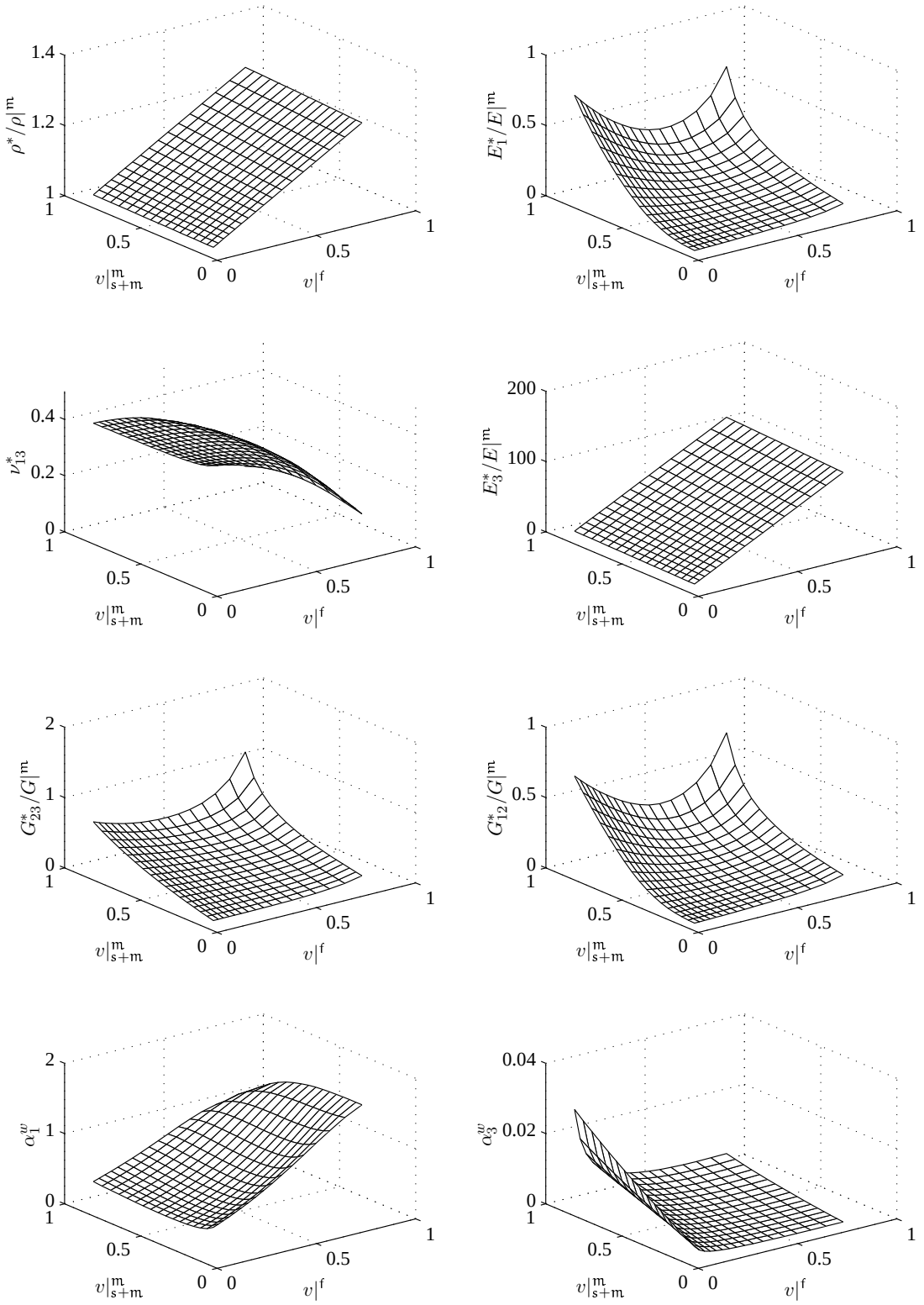

Figure 3.7.: Effect of varying phase volume fractions on effective properties.

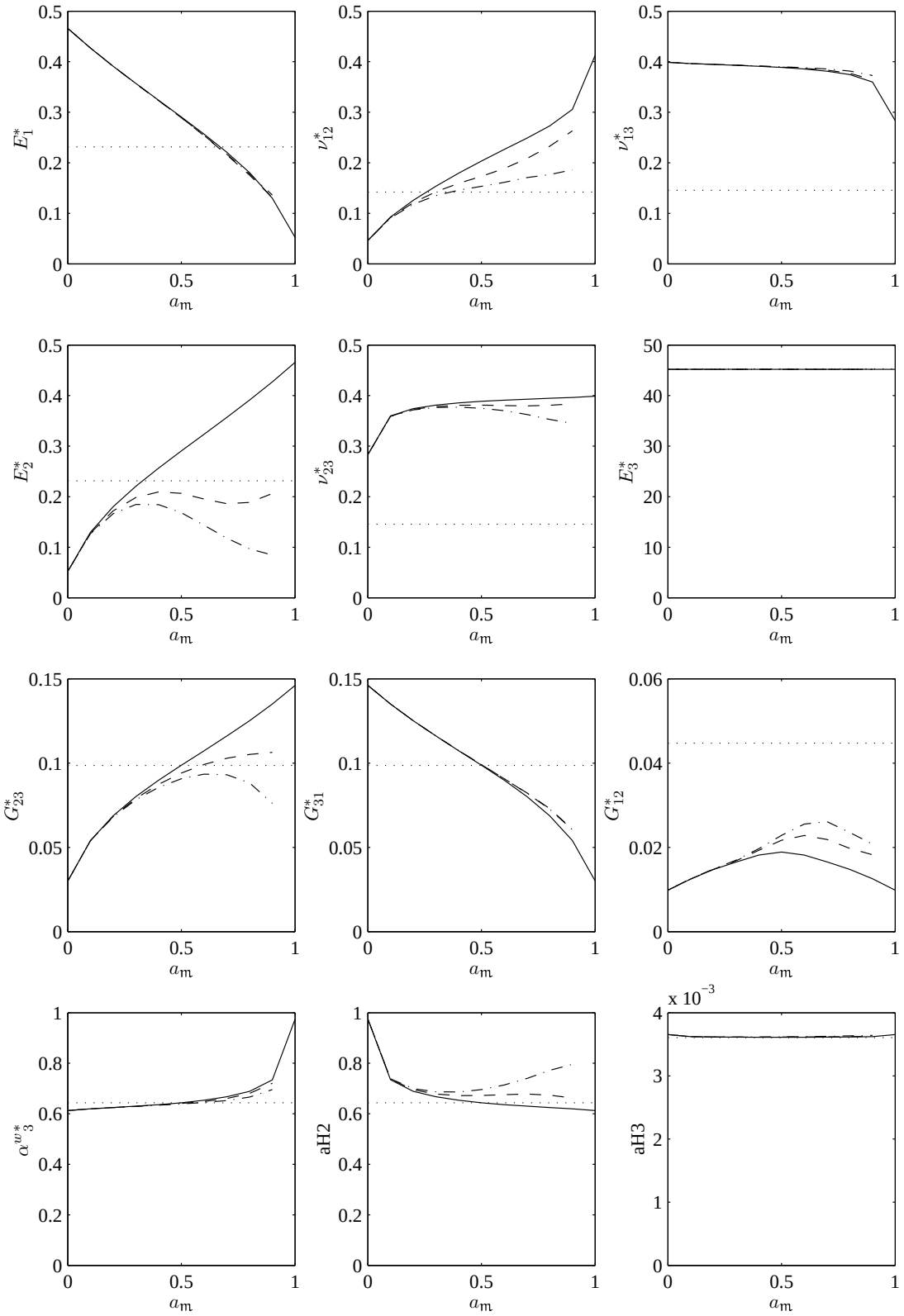

Figure 3.8.: Variation of effective nanoscale properties of RR3 models with a_m and a_o, $a_\mathrm{f} = 0.5$. Phase volume fractions: $v|^\mathrm{f} = 0.32$, $v|^\mathrm{s} = 0.30$, $v|^\mathrm{m} = 0.38$, $a_\mathrm{s} = 0.5$. —— RR3 $a_o = 0$, – – RR3 $a_o = 0.25$, – · – RR3 $a_o = 0.5$, ····· HH3.

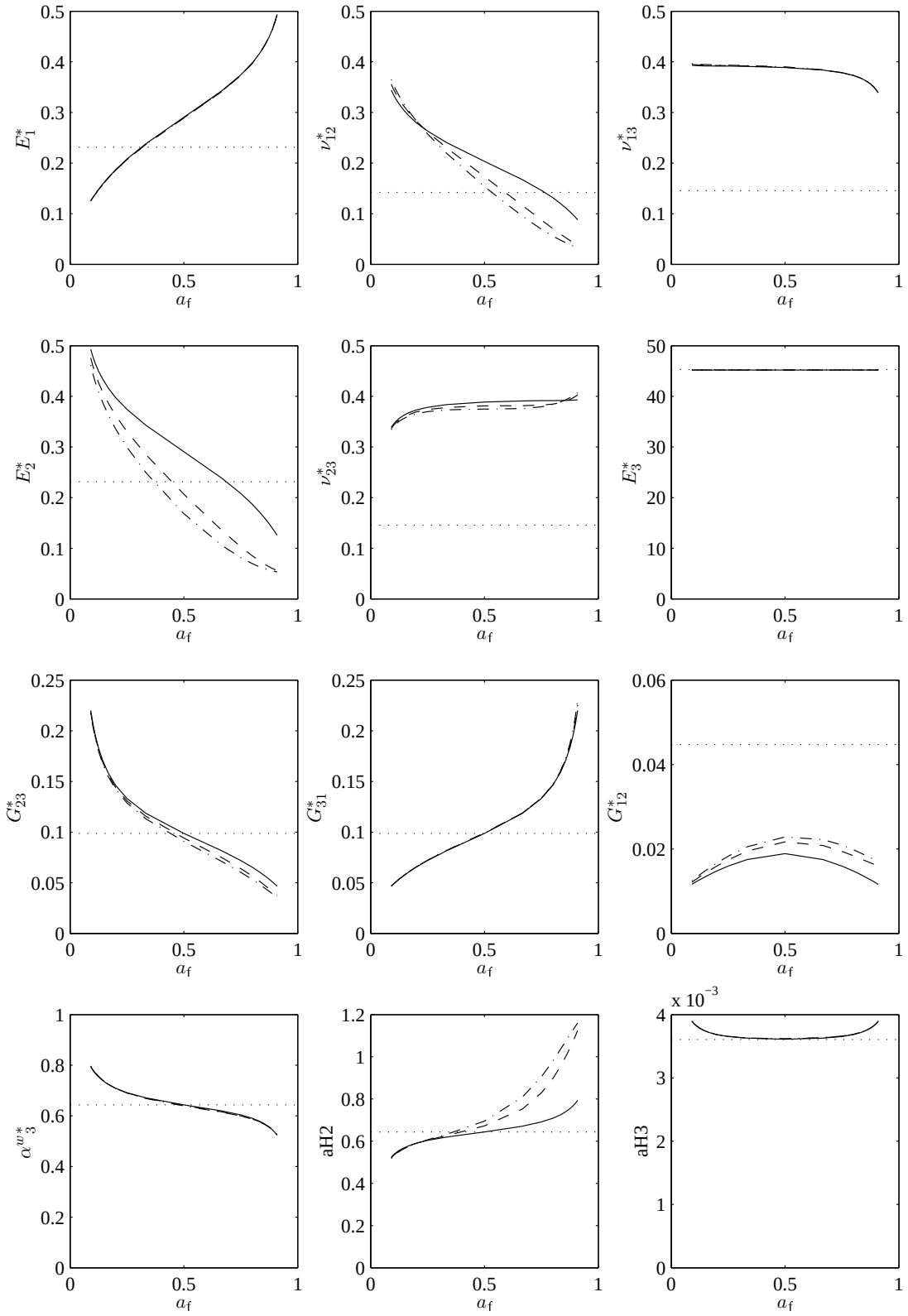

Figure 3.9.: Variation of effective nanoscale properties of RR3 models with a_f and a_o, $a_\mathrm{m} = 0.5$. Phase volume fractions: $v|^\mathrm{f} = 0.32$, $v|^\mathrm{s} = 0.30$, $v|^\mathrm{m} = 0.38$, $a_s = 0.5$. —— RR3 $a_o = 0$, – – RR3 $a_o = 0.25$, – · – RR3 $a_o = 0.5$, ····· HH3.

	E_1 GPa	ν_{13}	E_3 GPa	G_{23} GPa	G_{12} GPa	α_1^w $\times 10^{-3}$	α_3^w $\times 10^{-3}$
HH3	0.1443	0.3897	45.19	0.09866	0.04473	643.5	3.606
RR3, $a_o = 0$, $\bar{C}$	0.2019	0.3887	45.19	0.09874	0.06978	643.8	3.612
RR3, $a_o = 0$, $\bar{D}$	0.1108	0.3887	45.19	0.09874	0.03266	643.8	3.612
RR3, $a_o = 0.5$, $\bar{C}$	0.1678	0.3841	45.19	0.09490	0.05947	667.4	3.618
RR3, $a_o = 0.5$, $\bar{D}$	0.1141	0.3824	45.19	0.09472	0.03638	667.4	3.618

Table 3.4.: Comparison of square and hexagonal CMFs. $a_{\mathrm{f}} = 0.5$, $a_{\mathrm{s}} = 0.5$, $a_{\mathrm{m}} = 0.5$. $v|^{\mathrm{f}} = 0.32$, $v|^{\mathrm{s}} = 0.30$, $v|^{\mathrm{m}} = 0.38$.

orientations, using the method of appendix B, then the resulting transversely isotropic properties are similar to those of the HH3 model (see table 3.4).

The results of table 3.4 can also be interpreted to mean that the cross-sectional shape of the CMFs makes little difference to the effective properties. The stress concentrations arising at the corners are however considerably different, though it is unclear just how useful the notion of stress concentration is at atomic length scales.

3.4. Concluding remarks

In this chapter models for predicting the effective tangential hygro-elastic properties of nanostructural domains within the secondary wall of softwood cells have been presented and it has been shown that these models can account for the local composition via the CF, HS and LM phase volume fractions. It has also been shown that the transverse arrangement of the CMFs has a significant impact on some of the effective nanoproperties. In the remainder of this thesis the HH3 model is used exclusively to compute effective nanoscale properties as it is believed that this model produces results more in keeping with a random transverse distribution of CMFs.

Two fundamental assumptions have been made in developing these models. The first of these is that even at a nanoscopic scale matter may be treated as a continuum. While long experience indicates this assumption to be valid at the macroscale, it is questionable when the characteristic structural dimensions approach atomic scales.

The second fundamental assumption made is that the material may be treated as having properties that are piecewise constant in space. That is to say, that it can be partioned into homogeneous phases. In micromechanical analysis this is a common practice; but in truth, no clear phases, nor interfaces between phases, exist.

For average behaviours such as stiffness and shrinkage these assumptions in all probability provide acceptable results. However, in the future it would be interesting to compare effective properties for a highly simplified fibre composite determined using continuum and molecular mechanics methods.

Chapter 4

Cell-wall modelling

4.1. Introduction

It can be argued that the cell-wall, composed of the cell walls of two adjoining cells and the middle lamella that holds them together, is the basic structural element of wood at a microscopic level. The cell-wall is complex and highly variable. In particular, within the cell-wall the local composition and orientation of the CMFs varies.

In this chapter the structure of the cell-wall is first discussed and then models incorporating the most significant of features are proposed and specific results presented. The primary focus is on the variation in CMF orientation within the cell-wall; variation in cell-wall composition is touched upon but its modelling is deferred to chapter 7

Three sets of coordinate sytems are used: the cellular, wall and lamella systems. These coordinate systems are defined in figure 4.1, these definitions are somewhat imprecise owing to the organic nature of wood but in practice this imprecision causes little difficulty. The first of these, the cellular coordinate systems, have their 2-axes directed from pith to bark in the radial direction and their 3-axes aligned with the local tracheid longitudinal direction, that is the 3-direction is the local grain direction; the transverse direction (parallel to the 1-axis) then is tangent to the growth layers. A wall coordinate system has its 3-axis parallel to the local cellular 3-axis, but its 2-axis is normal to the plane of the cell-wall and directed towards the nearest lumen. The 2-axis of a lamella coordinate system is also normal to the plane of the cell-wall but the lamella 3-direction is parallel to the local CMF direction. The 1-, 2- and 3-directions for each of these sets of coordinate systems are also referred to as the transverse (T) or circumferential, radial (R) and longitudinal (T) or axial directions respectively.

Wood anatomists refer to cell-walls whose normals lie more or less in the cellular radial or tangential directions as tangential and radial walls respectively. This unfortunate nomenclature is no doubt a shorthand form for describing approximately which plane, either tangential-longitudinal or radial-longitudinal, these walls lie parallel to. It is, however, somewhat illogical. To avoid any confusion, radial and tangential walls are defined by example in figure 4.1.

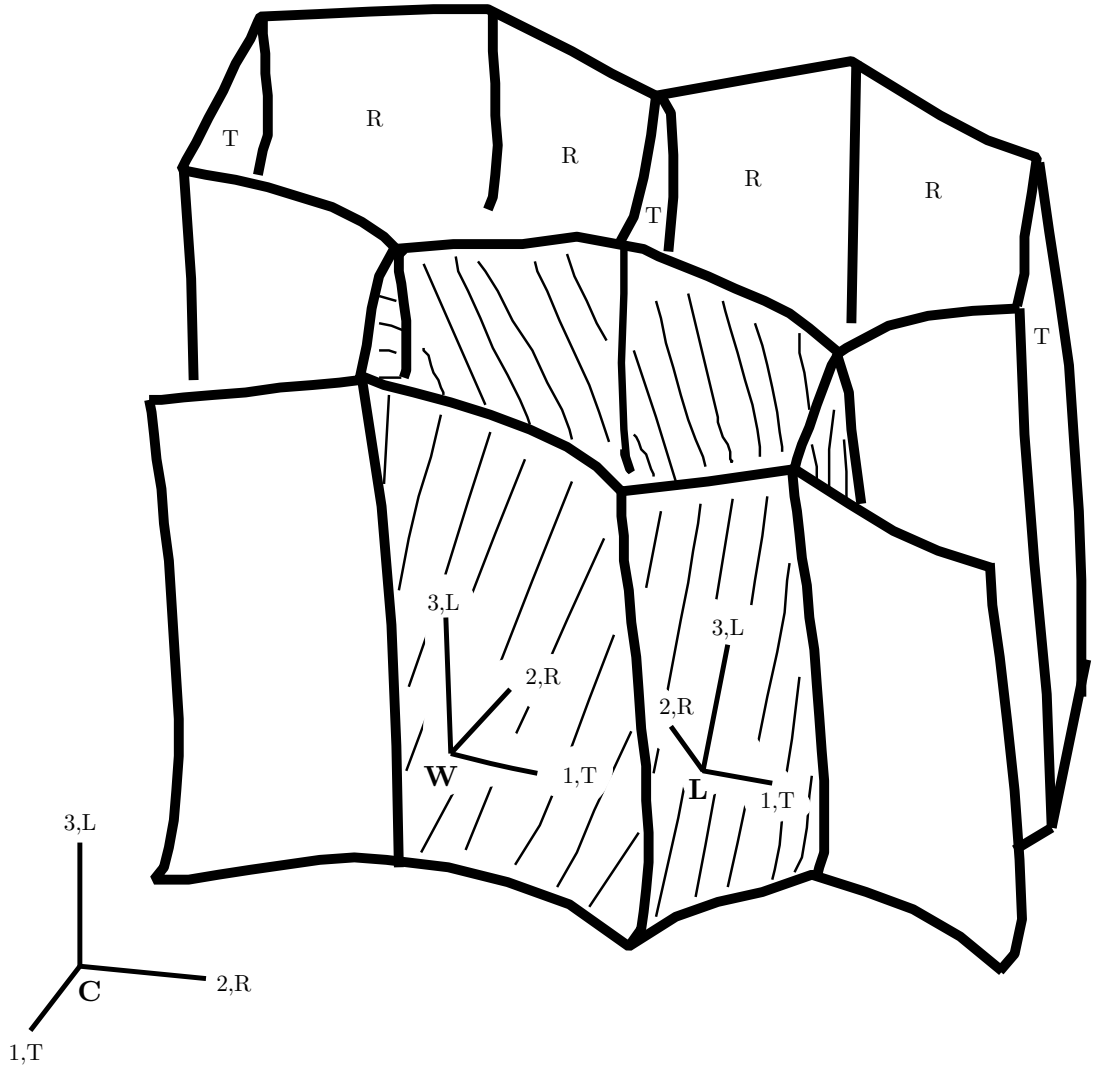

Figure 4.1.: Coordinate system definitions. Cellular (**C**), cell-wall (**W**), cell-wall lamella (**L**). Radial (R) and tangential (T) cell-walls are also identified.

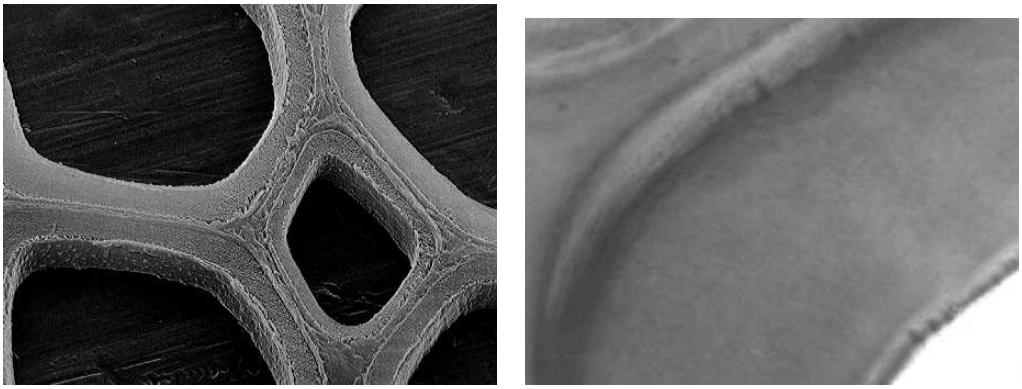

Figure 4.2.: SEM (left) and TEM (right) images of tracheid cell walls showing major wall layers.

4.2. Cell-wall structure

The ultrastructure of softwood trachied cell-walls is treated by numerous texts including: Wardrop (1964); Wardrop and Harada (1965); Harada (1965); Harada and W. A. Côté (1985); Côté (1967); Preston (1974); Côté (1977); Fengel and Wegener (1984); Fujita and Harada (1990) and has been recently reviewed by Brändström (2001). Cell-wall ultrastructure of other types of xylem elements is less well documented but some description can be found in: Harada and Wardrop (1960); Harada (1965); Miyakawa et al. (1973); Takahara et al. (1983); Fengel and Wegener (1984). Unless stated otherwise, what follows is drawn from these sources.

4.2.1. Cell-wall layers and lamellae

The tracheid cell-wall is divided on ontogenetic grounds into four zones: the middle lamella, the primary wall, the secondary wall and the warty layer. The warty layer is very thin and is not considered further; details of its structure can be found in Liese (1963, 1965); Wardrop and Davies (1962); Baird et al. (1974a,b); Takiya et al. (1976); Verhoff and Knigge (1976); Ohtani et al. (1984); Kuo and Manwiller (1986); Jansen et al. (1998). After lignification it is often difficult to distinguish the true middle lamella (ML), or intercellular layer, from the adjacent primary walls (P), particularly away from the cell corners. Consequently, the primary walls and middle lamellae are often treated as a single entity referred to as the compound middle lamella (CML). Within the secondary wall three major layers – denoted S1, S2 and S3 – are generally recognized (Bailey and Kerr, 1935; Wardrop, 1964), although exceptions to this are occasionally observed (Wardrop, 1957b; Côté, 1977; Preston, 1986) and in severe compression wood the S3 is often absent (Timell, 1986a). The major wall layers can be seen in the micrographs of figure 4.2.

The major wall layers occupy differing proportions of the cell-wall volume and vary considerably in thickness even within a single cell (see chapter 6). They are also highly heterogeneous.

Within the secondary wall layers, in particular S2, a variety of substructures occurring at scales greater than the nanostructural have been described. These substructures include:

- concentric or tangential lamellae (Page and DeGrace, 1967; Dunning, 1968, 1969; Stone et al., 1971; Ruel et al., 1978; Daniel and Nilsson, 1984; Maurer and Fengel, 1991, 1992; Singh and Donaldson, 1999; Singh and Daniel, 2001),
- radial lamellae (Sell and Zimmermann, 1993; Sell, 1994; Larsen et al., 1995; Schwarze and Engels, 1998; Singh et al., 1998; Singh and Donaldson, 1999; Singh and Daniel, 2001),
- stripe lamellae (Kataoka et al., 1992),
- bundles or macrofibrils (Daniel and Duchesne, 1998).

The variability in type and size of these substructures suggests that in some cases they are artifacts caused by the specimen prepartion technique, the imaging technique or the underlying helicoidal nature of the cell-wall. In other cases they appear genuine, particular the radial striations in moderate compression wood which Singh and Donaldson (1999) propose are precursors to the helical checks found in severe compression wood.

4.2.2. Microfibril angle

While local variations in composition occur across, around and along the cell-wall (see chapter 7) and the substructures just discussed may exist within the cell-wall, the primary source of cell-wall heterogeneity is the variation in CMF direction.

A single angle, the microfibril angle (MFA), is generally used to describe the CMF direction. Preston (1986) defines the MFA as "the angle the helical vector makes with the cell length". Cells are however only approximately prismatic, and the CMFs only approximately helical, making this definition somewhat imprecise. In experimental studies this imprecision is not normally a problem since it is just one of a number of factors giving rise to uncertainty in the measurement of MFA. For modelling on the other hand, it can be problematic, especially when considering tissue near the tracheid tips and in pit fields. When a more precise measure is required the local CMF direction can be described by a unit vector field over the cell-wall requiring two independent parameters at each point for its specification.

The term MFA can be used to describe either a property associated with any point within the cell-wall or to describe the predominant angle within some wall region, or

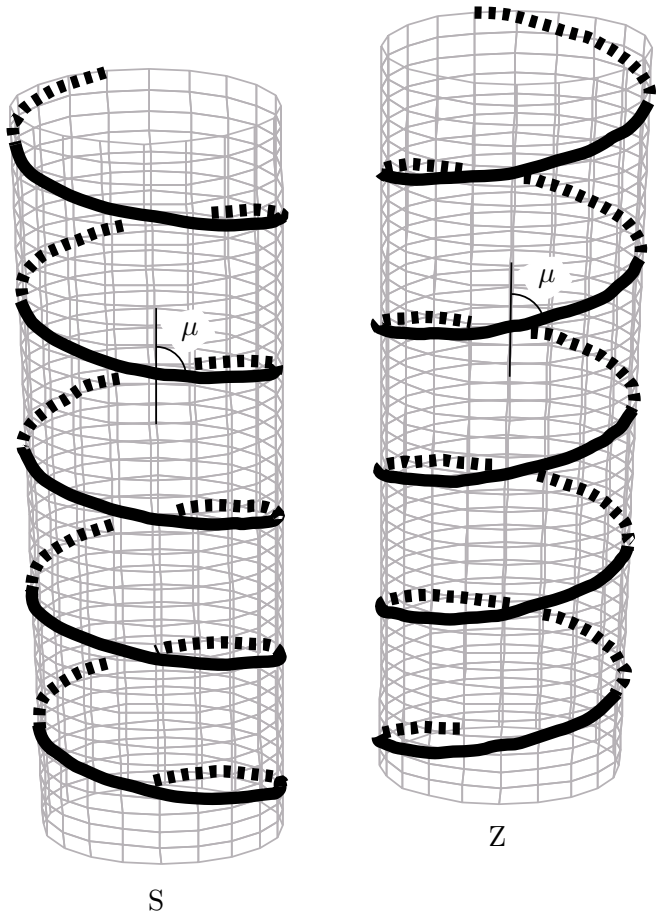

Figure 4.3.: Definition of MFA.

even within the wood as a whole. While this is a possible source of confusion, it is common usage and generally the intended meaning is made clear by the context.

The CMFs form both left- and right-handed helices within the cell-wall. Frequently the letters 'S' and 'Z' are used to indicate left- and right-handed helices respectively[1]. Alternatively, if the MFA, μ, is defined as shown in figure 4.3 and is constrained to be $0 \leq \mu < 180$ then right-handed (Z) helices are those for which $0 < \mu < 90°$ and left-handed helices (S) are those for which $90 < \mu < 180°$.

A very large number of studies have been conducted on MFA; the papers presented in a recent symposium on MFA serve as an excellent introduction (Butterfield, 1998). Indeed measurement of MFA is becoming as routine as measurement of density (Evans et al., 1996; Evans, 1998). Nevertheless determination of MFA is not straightfoward, and the value obtained can depend on the method used.

Methods for determining MFA can be classified in a number of ways: as direct or indirect methods, by the size of the domain over which they average the angle

[1]This notation is based on the similarity of the slope of the central stroke of the characters 'S' and 'Z' and slope of the helices closest to the viewer when viewed from the outside.

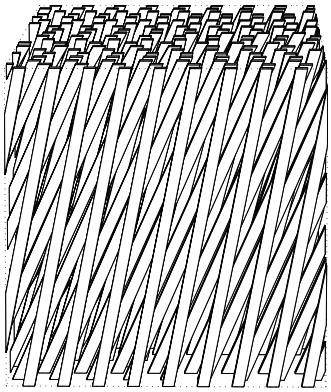

Figure 4.4.: CMF sheaves in S2.

(resolution), by the time, skill, or equipment required to make the measurement. In table 4.1 a number of methods for determining either the MFA throughout the wall, in wall layers or in wood as a whole are listed. Reviews of methods for determining MFA and comparisons between these methods can also be found in Crosby and Mark (1974); Meylan (1967); Prud'homme and Noah (1975); Mark and Murakami (1983); Saiki et al. (1989); Donaldson (1991b); Ohta et al. (1992); Huang et al. (1998); Long et al. (2000); Anagnost et al. (2000); Andersson et al. (2000).

The results of studies on the microfibrillar orientation in the major secondary wall layers of tracheids are summarized in table 4.2.

The S2 layer constitutes the bulk of the secondary wall, up to 90% by volume, and within it the MFA is low and the CMFs are well ordered. Meylan and Butterfield (1978) found that, without exception, microfibrils in the S2 layer form right-handed (Z) helices. Kataoka et al. (1992) report that in the S2 layer the MFA oscillates rapidly, through a total angle of approximately 20°, between sucessive microlamellae. This oscillation gives rise to the "sheaflike aggregates" described by Wardrop and Harada (1965) and the "trellis-like configurations" described by Boyd and Foster (1975) and Boyd (1982) and illustrated in figure 4.4. In radiata pine mean S2 MFAs of betweem 5 and 70° have been reported with typical values between 30 and 40° (Tsehaye et al., 1998; Matsumura and Butterfield, 2001; Donaldson, 1993; Donaldson and Burdon, 1995; Donaldson, 1998).

The S1 and S3 layers are thinner than the S2, the CMFs within them are less well aligned, the predominant orientation of the microfibrils is nearly perpendicular to the cell axis and the spread in MFA is higher. Both left- and right-handed helices have been reported leading to descriptions of crossed systems (Wardrop, 1957a; Wardrop and Davies, 1964; Liese, 1963; Abe et al., 1992). In the transition regions between S1 and S2, and between S2 and S3, the MFA varies stepwise between microlamellae (Wardrop and Harada, 1965; Dunning, 1968, 1969; Kataoka et al., 1992). Imamura et al. (1972)

Equipment	Technique	Ref.
Optical microscope	angle of natural or induced cracks and striations	Bailey et al. (1937); Marts (1955); Miniutti (1964); Hiller and Brown (1967); Huang (1995); Anagnost et al. (1999, 2000)
	pit aperture angles	Pillow et al. (1953); Echols (1965); Shumway et al. (1971)
	iodine crystal deposition	Bailey et al. (1937); Kobayashi (1952); Senft and Bendtsen (1985)
Polarised light	oblique transverse sections	Wardrop and Preston (1947); Wardrop and Dadswell (1951); Manwiller (1966); Preston (1974); Tang (1973); Mark (1967); Crosby et al. (1972)
	longitudinal sections	Preston (1934); Cousins (1972); Cave (1974); Leney (1981); Fujita and Saiki (1990)
	macerated fibres	Page (1969); Boyd (1973); El-Hosseiny and Page (1973); Page and El-Hosseiny (1974); Donaldson (1991b); Ye et al. (1994); Ye and Sundström (1997); Ye (1999)
Electron microscope	longitudinal sections and surfaces	Wardrop and Davies (1964); Harada (1965); Dunning (1968, 1969)
	transverse sections	see appendix E
X-ray diffraction	small angle scattering	Wardrop (1952); Heyn (1955); Kantola and Kähkönen (1963); Lichtenegger et al. (1998, 1999); Reiterer et al. (1998, 1999); Entwistle and Terrill (2000); Entwistle and Navaranjan (2001)
	wide angle scattering	Sisson (1935); Bailey and Berkley (1942); Preston (1946); Meredith (1951); Cave (1966); Meylan (1967); Cave (1997a,b); El-Osta et al. (1972, 1973); Boyd (1973, 1977a); Sobue et al. (1971); Nomura and Yamada (1972); Paakkari and Serimaa (1984); Tanaka and Koshijima (1984); Yamamoto et al. (1993); Stuart and Evans (1995); Sahlberg et al. (1997); Evans (1999); Evans et al. (1999)
Confocal microscope		Verbelen and Stickens (1995); Batchelor et al. (1997); Jang (1998); Bergander and Salmén (2000)
Micro-Raman spectroscopy		Pleasants et al. (1998)
Mechanical testing	via model from longitudinal modulus	Persson (1997)

Table 4.1.: Methods for determining MFA.

S1	S2	S3
10–140°	5–50°	0–180°

Table 4.2.: Summary of MFA in tracheid secondary wall layers. Sources: Wardrop (1957a); Dunning (1968); Tang (1973); Kataoka et al. (1992)

found the transition between S1 and S2 to be more gradual than the transition between S2 and S3. Dunning (1968) describes lamellae within the S3 layer rotating clockwise through 270° then rotating counter-clockwise and terminating with the microfibrils lying nearly perpendicular to the tracheid axis.

As well as the variation cross the cell wall described above, variation in MFA has been observed:

- between trees (Donaldson, 1992, 1993) and between clones (Donaldson and Burdon, 1995),
- within the stem, both from pith to bark (Donaldson, 1992; Ying et al., 1994; Herman et al., 1999) and from base to crown (Donaldson, 1992),
- between normal and compression wood (Nicholls, 1982; Timell, 1986a),
- within growth rings (Hiller, 1964; Tang, 1973; Saiki et al., 1989; Herman et al., 1999),
- between adjacent tracheids (Donaldson, 1998),
- along the length of individual tracheids (Ye and Sundström, 1997; Anagnost et al., 2000).

It has also been claimed that the MFA of radial walls is greater than that of tangential walls (Preston, 1934; Meylan, 1967; Tang, 1973; Boyd, 1974; Gorisek et al., 1999; Khalili et al., 2001), though other studies have found no such difference (Stuart and Evans, 1995; Kataoka et al., 1992; Brändström, 2001). It seems likely that even if the average MFA is the same in both radial and tangential walls the variance will be greater in radial walls owing to deviations induced by the presence of pits (Wilson and White, 1986; Gorisek et al., 1999).

As the wall shrinks, swells or undergoes any other large deformation the MFA may be altered. Prelimary results from X-ray studies show little or no difference between wet and dry samples, an observation which is in accord with previous claims (Boyd, 1977a; Hepworth and Vincent, 1998).

If it is assumed that the CMFs are helical and inextensible then the strain in the longitudinal direction ϵ_l is related to the change in microfibril angle $\delta\mu$ by

$$\epsilon_l = \frac{\cos(\mu + \delta\mu)}{\cos\mu} - 1 \approx \delta\mu \tan\mu, \delta\mu \ll \mu. \tag{4.1}$$

If the microfibril angle μ is 20°then to change the MFA by 1°requires a strain of 2.79%, a strain which most certainly will take the tracheid beyond its proportional limit and into the inelastic region.

4.2.3. A model for MFA within the cell wall

Based primarily on data from Kataoka et al. (1992) and appendix E, a model for the expected value of the MFA within the cell wall is proposed. This model neglects circumferential and longitudinal variation and describes the position across the wall using the cellular solid volume fraction $\hat{v}$ of the material lying outside of that point[2]. It assumes that in the S2 and portion of the S1 and S3 layers the MFA is constant ($\mu|^{\mathsf{S1}}$, $\mu|^{\mathsf{S2}}$ and $\mu|^{\mathsf{S3}}$ respectively) , and in the transition regions the variation is linear, thus

$$.\mu(\hat{v}) = \begin{cases} \mu|^{\mathsf{S1}} & \hat{v}_1 \leq \hat{v} < \hat{v}_2 \\ \mu|^{\mathsf{S1}} + \left(\mu|^{\mathsf{S2}} - \mu|^{\mathsf{S1}}\right)(\hat{v} - \hat{v}_2) / (\hat{v}_3 - \hat{v}_2) & \hat{v}_2 \leq \hat{v} < \hat{v}_3 \\ \mu|^{\mathsf{S2}} & \hat{v}_3 \leq \hat{v} < \hat{v}_4 \\ \mu|^{\mathsf{S2}} + \left(\mu|^{\mathsf{S3}} - \mu|^{\mathsf{S2}}\right)(\hat{v} - \hat{v}_4) / (\hat{v}_5 - \hat{v}_4) & \hat{v}_4 \leq \hat{v} < \hat{v}_5 \\ \mu|^{\mathsf{S3}} & \hat{v}_5 \leq \hat{v} \leq 1 \end{cases} \tag{4.2}$$

where $\hat{v}_i$ are the points in the wall where changes in MFA occur and $0 < \hat{v}_i < 1$. A visualization of this model with is shown in figure 4.5.

4.3. Modelling

The cellular models described in the next chapter require effective hygro-elastic properties for the S1, S2 and S3 layers. An element of the cell-wall, or of the cell-wall layers, can be treated as a layered composite (Mark, 1967; Cave, 1968; Schniewind and Barrett, 1969; Barrett and Schniewind, 1973; Salmén and de Ruvo, 1985; Koponen et al., 1989) and this approach is again adopted. The effective properties can then be computed using the homogenization scheme for periodic laminates described in appendix C. A periodic laminate theory is used rather than a thin or thick laminate theory as the cellular models require complete sets of properties rather than just the in-plane properties.

[2]Cellular solid volume fraction $\hat{v}$ and its use as a transwall coordinate will be discussed in chapter 5.

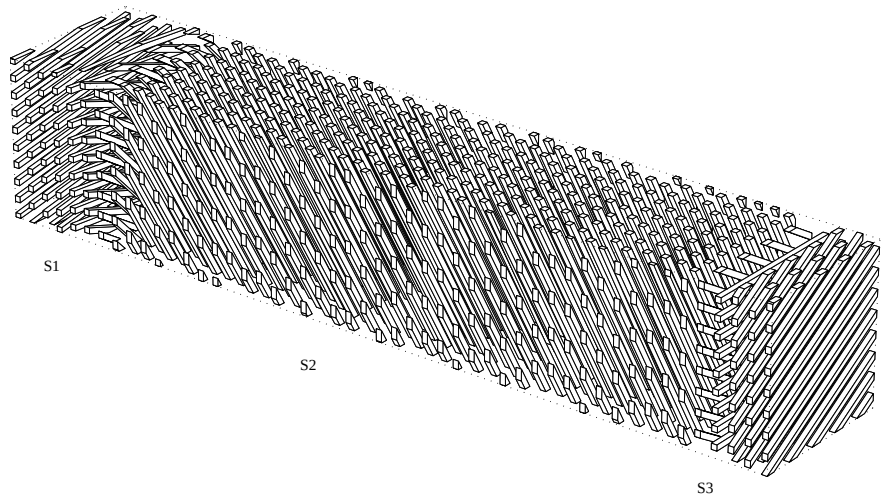

Figure 4.5.: CMF orientation across the cell wall based on the model of (4.2). Parameters used: $\mu|^{S1} = 100°$, $\mu|^{S2} = 20°$, $\mu|^{S3} = 120°$, $\hat{v}_1 = 0.05$, $\hat{v}_2 = 0.11$, $\hat{v}_3 = 0.23$, $\hat{v}_4 = 0.89$, $\hat{v}_5 = 0.96$.

While the composition varies continuously within the cell-wall, it is presently assumed that the composition, and hence the nanophase volume fractions, is homogeneous within the S1, S2 and S3 layers (see chapter 7). Three sets of effective properties for a nanostructural domain within each of these layers are computed using one of the nanostructural models described in the previous chapter. These nanoproperties are then 'smeared' based on an assumed gaussian distribution of CMF orientation with standard deviation $\sigma_\mu = \sigma_\mu(\hat{v})$ about the effective MFA. This smearing process is introduced to account for the variation in MFA

- within the layer along the length of the cell,
- within the layer around the cell,
- between the same layers in different cells within a particular cellular aggregate,

as well as to account for the rapid oscillation of MFA between sucessive microlamellae across through the layer thickness. The notion of including variation of MFA within a laminate to account for variation between cells originated with Cave (1968). A gaussian distribution is chosen primarily for convenience but also because it provides a reasonable representation of the variation observed across a cell-wall by Kataoka et al. (1992) and between tracheids by Donaldson (1998); though Donaldson (1998) found the inter-tracheid S2 MFA distribution to be slightly leptokurtic and skewed, meaning that a greater proportion of the measurements were near and above the mean than would be expected if the distribution were gaussian.

The smeared properties are used directly as the effective properties of the S2 layer. For the S1 and S3 layers on the other hand, a second homogenization is performed based

on the smeared properties to account for the systematic variation of MFA, introduced in (4.2), through the layer thickness.

4.4. Results

4.4.1. Cell-wall in-plane properties

To investigate the influence of MFA parameters – $\mu|^{S1}$, $\mu|^{S2}$, $\mu|^{S3}$, σ_μ – on the cell-wall properties the same procedure used to homogenize the secondary cell wall layers has been used to compute the effective cell-wall properties. The cell-wall is treated as a anti-symmetric parallel laminate with seven layers. Treating the cell-wall as a planar laminate ignores the curvature and variation in lamina thicknesses and assumes that the volume fractions are equivalent to the layer thickness fractions; a reasonable assumption for the secondary wall layers when the cell-wall is thin[3] but can be a poor approximation for thick walls and for the CML which has approximately one third of its volume is concentrated at the cell corners (Saka, 1990).

For the computations whose results are presented below:

- the MFA has been assumed to be constant in one third of the total volume fraction of the S1 and S3 layers,
- the dispersion in MFA has been assumed to be the same throughout the cell-wall, i.e. $\sigma_\mu = \text{constant}$,
- and the nanoscale effective properties and layer volume fractions appearing in table 4.3 have been used.

In figure 4.6 the in-plane cell-wall properties – transverse modulus E_1, Poisson's ratio ν_{13}, longitudinal modulus E_3, shear modulus G_{13}, transverse hygro-expansional coefficient α_1^w and longitudinal hygro-expansional coefficient α_3^w – are plotted against S2 MFA $\mu|^{S2}$ with various amounts of dispersion. For these plots $\mu|^{S1} = \mu|^{S2} = 120°$. Note that as the cell-wall is treated as a skew-symmetric laminate, no coupling exists between shear and normal forces; in reality the cell-wall is not skew-symmetric (both the MFA and the layer thicknesses vary between adjacent cells) and shear and normal forces will be coupled though there are indications that this coupling has negligible effect on the elastic properties (Stol, 1996a).

From the plots in figure 4.6, it is clear that the relationships between S2 MFA and the cell-wall properties are highly nonlinear and sensitive to the amount of dispersion in MFA. As S2 MFA increases, E_1, G_{31} and α_3^w also increase; whereas, E_3 and α_1^w decrease.

[3] 'Thin' and 'thick' are not being used here in an absolute sense but rather to describe the thickness of a wall relative to its span.

	$\hat{v}$	w	χ	$\chi_{,w^\star}$	ρ g/cc	E_1 GPa	ν_{13} GPa	E_3 GPa	G_{23} GPa	G_{12} GPa	α_1^w	α_3^w
CML	0.0700	0.131	0.519	0	1.30	1.50	0.300	1.50	0.577	0.577	0.350	0.350
S1	0.100	0.110	0.433	0	1.38	1.93	0.257	34.2	0.839	0.676	0.828	0.0313
S2	0.770	0.0954	0.376	0	1.42	2.21	0.228	58.2	1.12	0.768	1.14	0.0269
S3	0.0600	0.110	0.433	0	1.38	1.93	0.257	34.2	0.839	0.676	0.828	0.0313

Table 4.3.: Assumed effective nanoscale properties of the cell-wall layers.

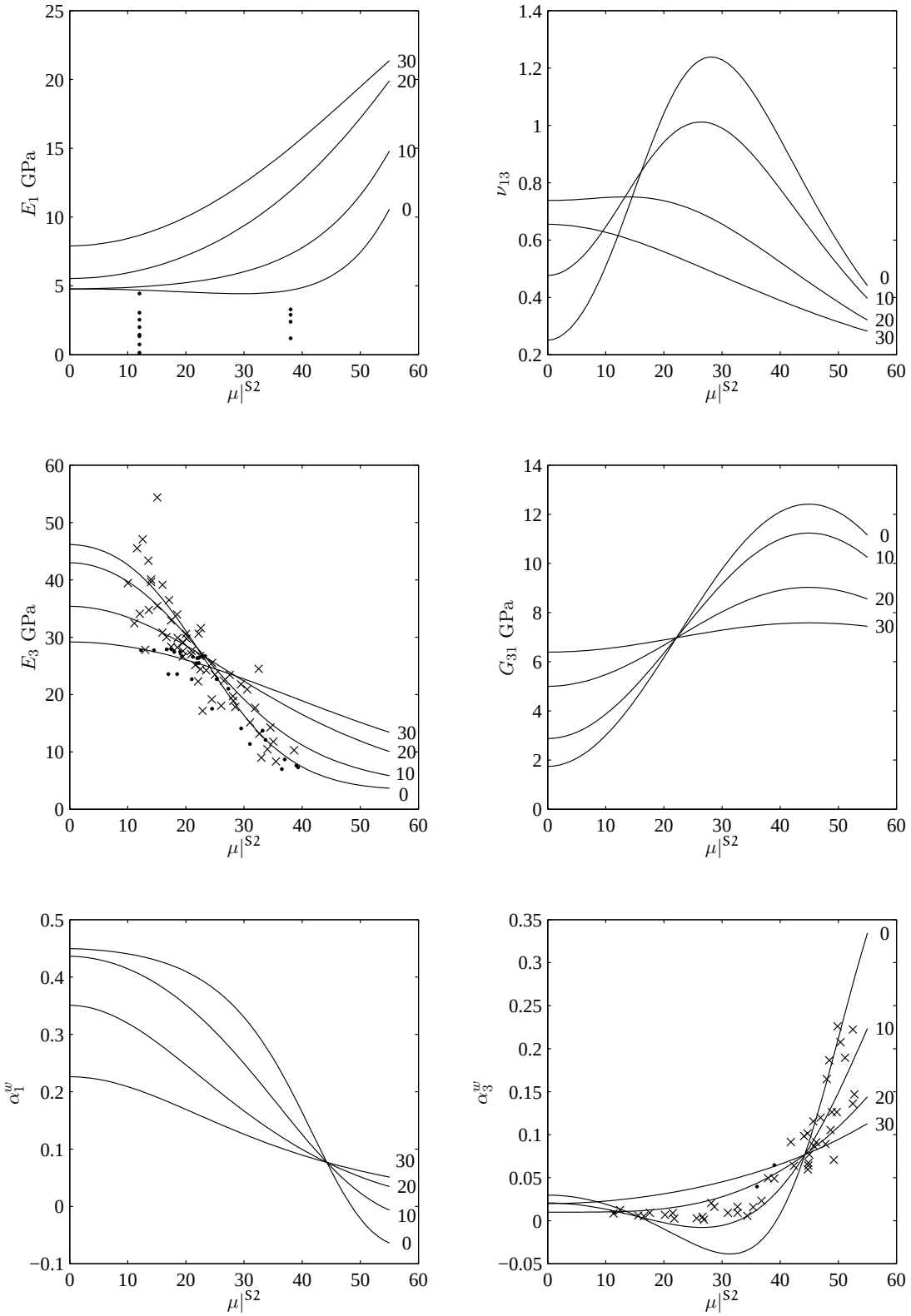

Figure 4.6.: Variation of in-plane cell-wall properties with S2 angle and random dispersion. Numeric labels refer to σ_μ.

As the MFA dispersion increases, the negative longitudinal hygro-expansion coefficients predicted for S2 MFAs of 20–40° by the current model – as well as by previous shrinkage models (Barber and Probine, 1969) – disappear.

If σ_μ is interpreted as representing the inter-tracheid variation in MFA then, from the results reported by Donaldson (1998), values of between 10 and 20° seem reasonable. This magnitude of MFA dispersion can significantly alter the cell-wall properties, particularly the transverse modulus and the hygro-expansional coefficients; an observation that has been made previously in the context of the longitudinal wall modulus by Cave and Robinson (1998). In fact, a change, of say 5°, in σ_μ can be of more significance than a change in mean S2 MFA of equal magnitude.

Also plotted in figure 4.6 are experimental results from: Bergander and Salmén (2000) for S2 MFA versus the transverse wall modulus E_1 of Norway spruce, Cave (1968) and Bendtsen and Senft (1986) for S2 MFA versus the longitudinal wall modulus E_3 of radiata and loblolly pine respectively, and Meylan (1968) and Meylan (1972) for S2 MFA versus the longitudinal hygro-expansional coefficient α_3^{w4}. Nominally all of these measurements were made in the air-dry condition at ambient temperature.

While the model predicts a transverse moduli somewhat greater than those measured by Bergander and Salmén (2000), the correspondence between model and experimental results for E_3 and α_3^w is reasonable indicating that the model is capable of representing realistic behaviour. It should however be borne in mind that this agreement was obtained by adjusting, within reasonable limits, model parameters specifying the: layer volume fractions, layer dry CF phase mass fractions, and the LM phase moduli.

In figure 4.7 the in-plane cell-wall properties are plotted against the terminal S1 and S3 MFAs. For these plots, $\mu|^{\mathsf{S2}} = \sigma_\mu = 10°$.

The longitudinal modulus is virtually unaffected by the MFA of the S1 and S3 layers. In contrast, the other cell-wall properties are significantly affected, particularly the longitudinal hygro-expansional coefficient. For the most part the S1 and S3 layers play similar roles, the slight differences being a result of the difference in the volume fraction and properties (though in the current example S1 and S3 have the same properties at the nanoscale).

The similar roles of S1 and S3 can also be seen in the plots of figure 4.8 showing the influence of layer volume fraction on the cell-wall in-plane properties. For these the same nanophase properties were used as for the previous plots, $\mu|^{\mathsf{S1}} = \mu|^{\mathsf{S3}} = 90°$, $\mu|^{\mathsf{S2}} = \sigma_\mu = 10°$ and the CML solid volume fraction is held constant $\hat{v}|^{\mathsf{CML}} = 0.05$. Note that the layer volume fractions in figure 4.8 are relative to the secondary wall rather than the entire wall.

[4]The hygro-expansional coefficents based on the data of Meylan (1968) are average rather than instantaneous values.

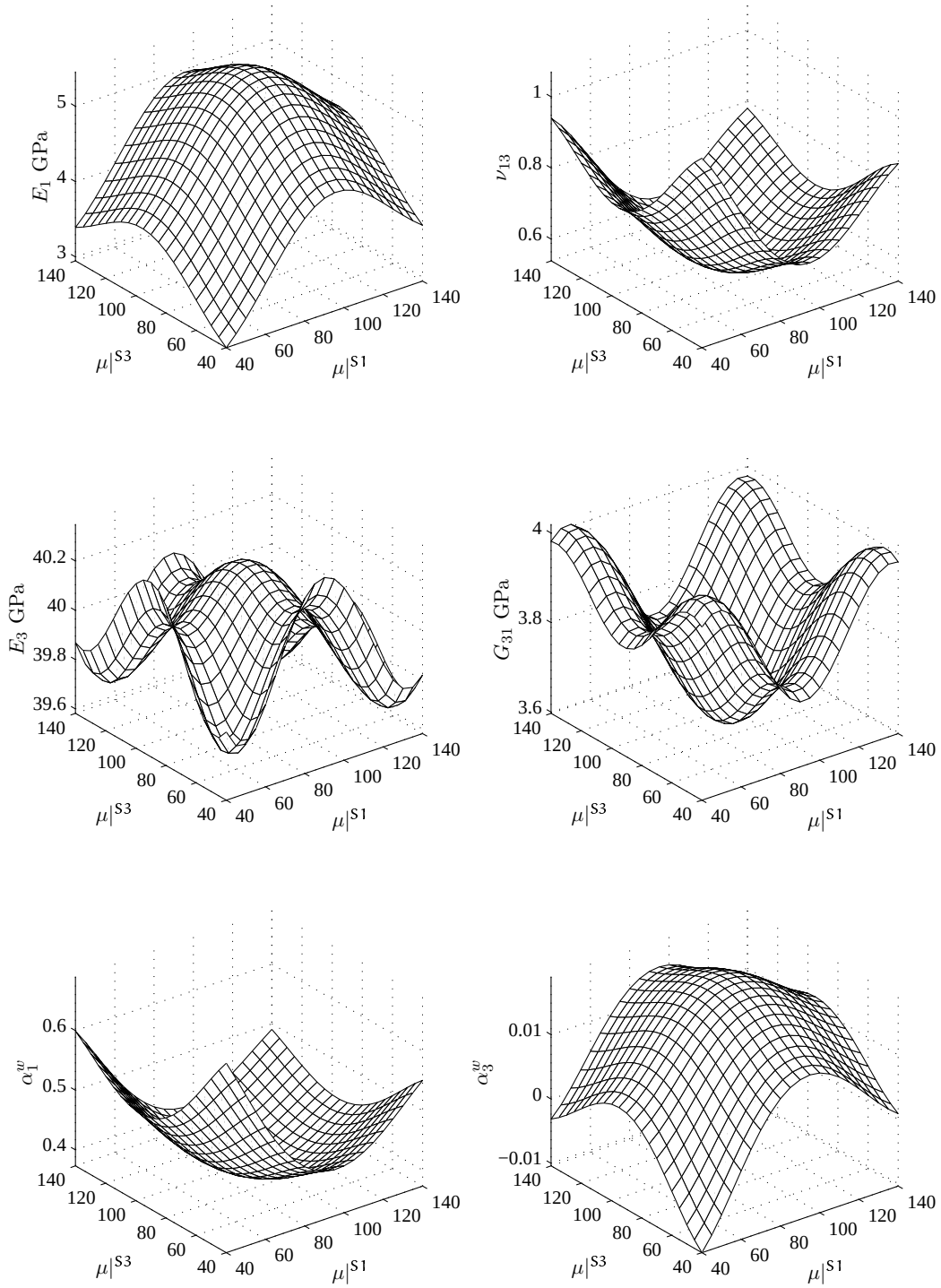

Figure 4.7.: Variation of in-plane cell-wall properties with S1 and S3 MFA.

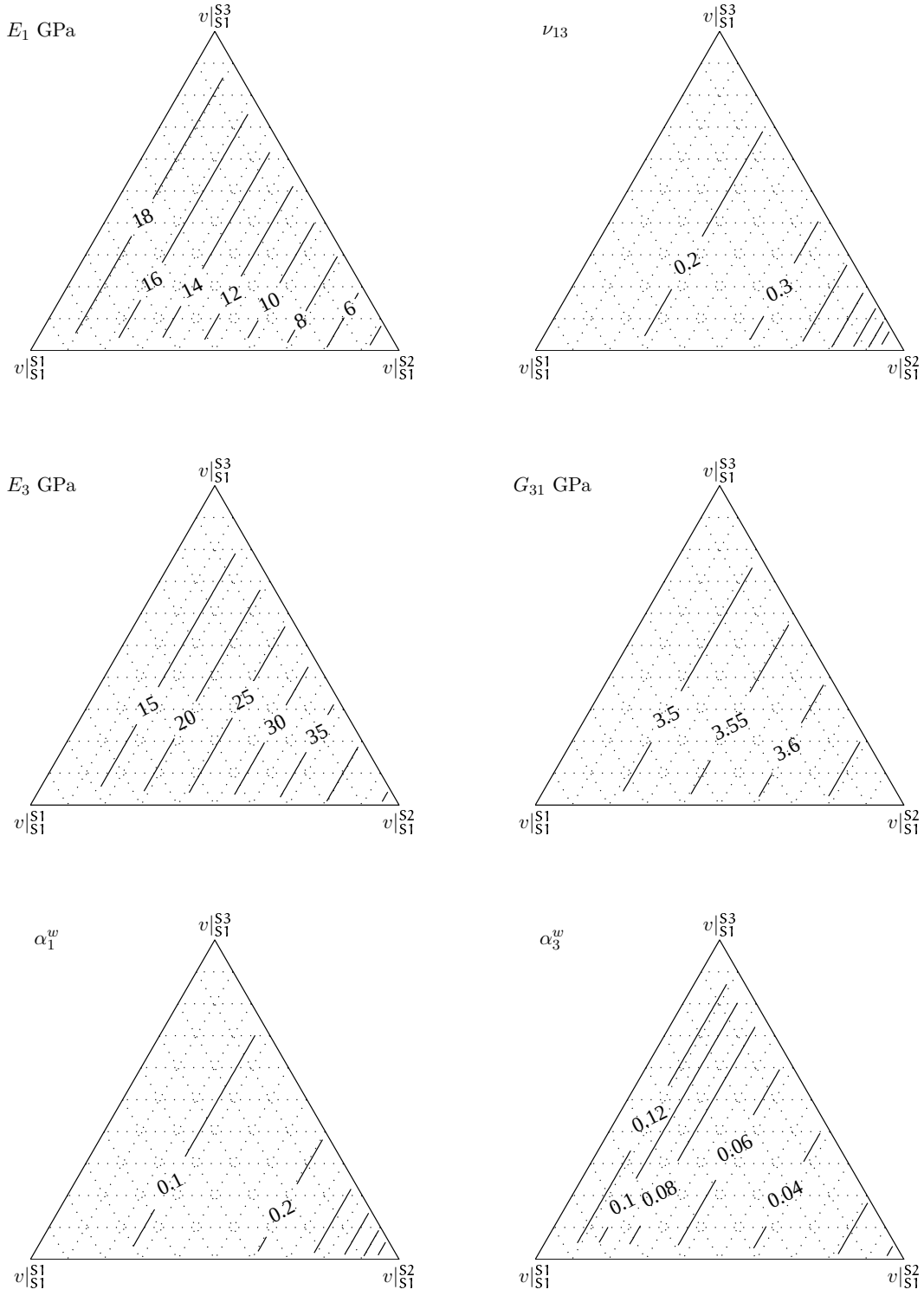

Figure 4.8.: Variation of in-plane cell-wall properties with the layer volume fractions.

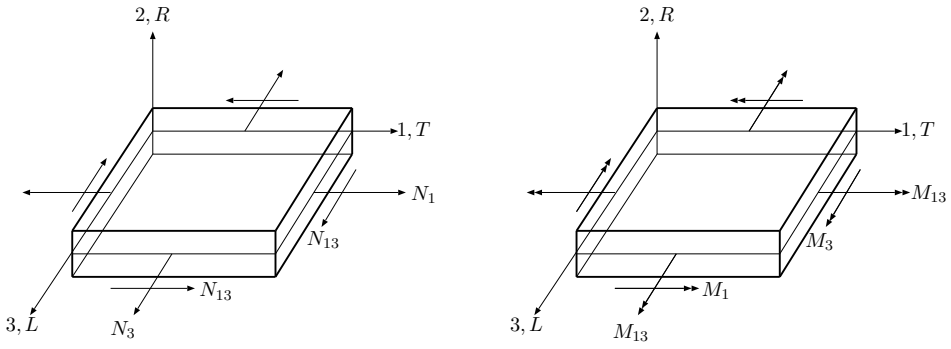

Figure 4.9.: Laminate theory definitions.

The in-plane moduli – E_1, E_3 and G_{31} – are essentially linearly correlated with S2 volume fraction, the correlation being positive for E_3 and negative for E_1 and G_{31}. The S2 volume fraction influences the remaining in-plane properties in a non-linear fashion. In particular, the transverse cell-wall shrinkage coefficient doubles from $v|_{\mathsf{S1}}^{\mathsf{S2}} = 0.6$ to $v|_{\mathsf{S1}}^{\mathsf{S2}} = 0.8$ and doubles again between $v|_{\mathsf{S1}}^{\mathsf{S2}} = 0.8$ and $v|_{\mathsf{S1}}^{\mathsf{S2}} = 0.95$.

4.4.2. Cell-wall flexural properties

The flexural properties of the cell-wall influence the transverse behaviour of wood, particularly the thin walled earlywood, at the cellular level. Thin laminate theory (Halpin, 1984; Tsai, 1980; Jones, 1999) can be used to obtain a qualitative understanding of the influence of MFA on the flexural properties of the cell-wall. Applying this theory to a skew-symmetric laminate, the midplane strains and curvatures are related to the stress and moment resultants (see figure 4.9) by

$$\begin{bmatrix} \epsilon_1^0 \\ \epsilon_3^0 \\ \epsilon_{13}^0 \\ \kappa_1 \\ \kappa_3 \\ \kappa_{13} \end{bmatrix} = \begin{bmatrix} E_{11} & E_{12} & 0 & 0 & 0 & L_{13} \\ E_{12} & E_{22} & 0 & 0 & 0 & L_{23} \\ 0 & 0 & E_{33} & L_{13} & L_{23} & 0 \\ 0 & 0 & L_{13} & H_{11} & H_{12} & 0 \\ 0 & 0 & L_{23} & H_{12} & H_{22} & 0 \\ L_{13} & L_{23} & 0 & 0 & 0 & H_{33} \end{bmatrix} \begin{bmatrix} N_1 \\ N_3 \\ N_{13} \\ M_1 \\ M_3 \\ M_{13} \end{bmatrix} \tag{4.3}$$

In figure 4.10 the flexural moduli – $\hat{F}_L = 1/H_{11}/t^3$, $\hat{F}_T = 1/H_{22}/t^3$ and $\hat{F}_{LT} = 1/H_{33}/t^3$, where t is the laminate thickness – are plotted against S2 MFA ($\mu|^{\mathsf{S2}}$) for various values of σ_μ. In figure 4.11 the flexural moduli are plotted against the terminal S1 and S3 MFAs ($\mu|^{\mathsf{S1}}$ and $\mu|^{\mathsf{S3}}$) and in figure 4.12 they are plotted against the layer volume fractions. The parameters used to compute these results are the same as those used in the corresponding plots of the previous section.

In contrast to the equivalent effects of S1 and S3 MFA on the in-plane cell-wall properties, figures 4.11 and 4.12 indicate that the volume fraction and MFA of the

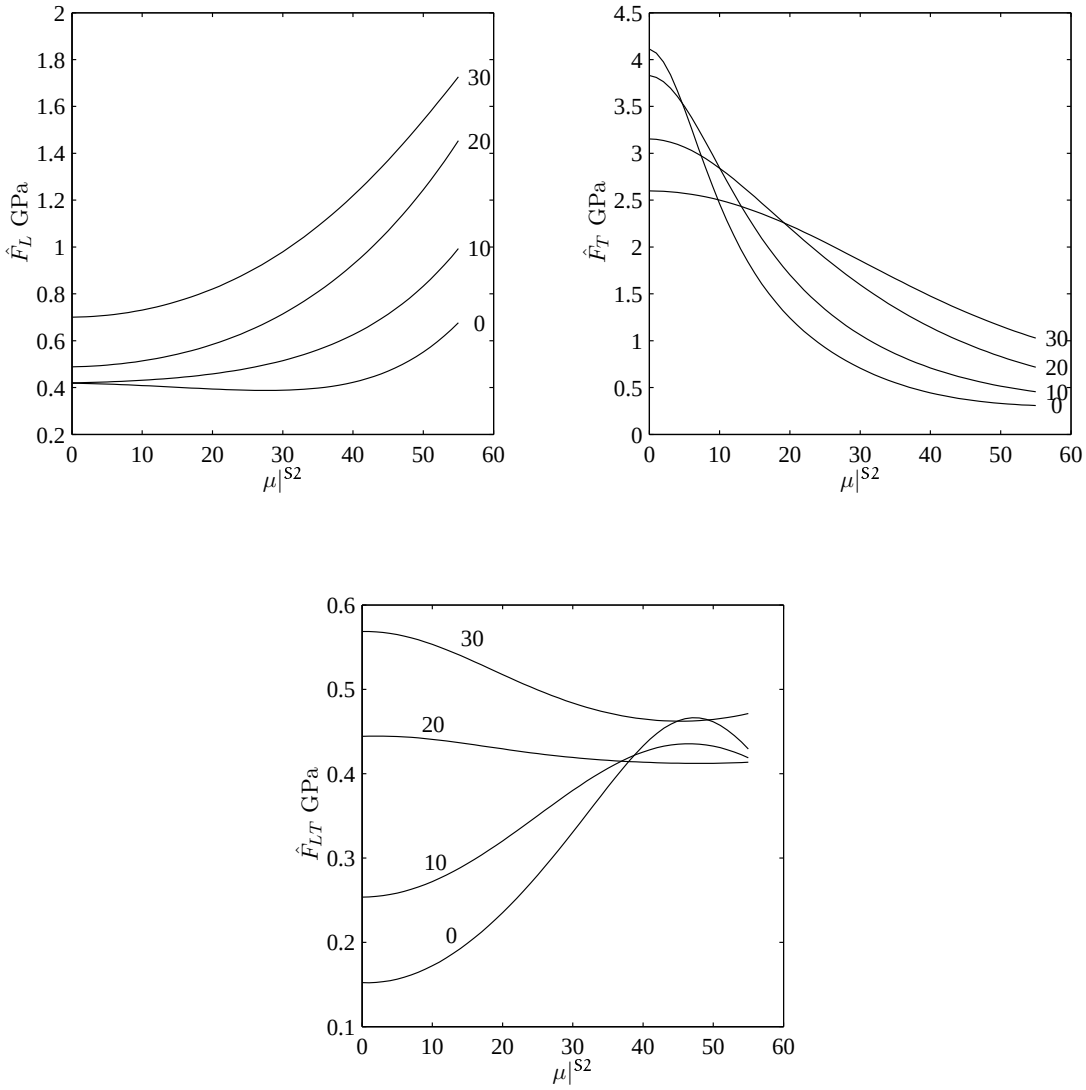

Figure 4.10.: Variation of cell-wall flexural properties with S2 MFA, $\mu|^{S2}$, and the standard deviation of the gaussian dispersion, σ_μ. Numeric labels refer to σ_μ. t is the thickness of the laminate.

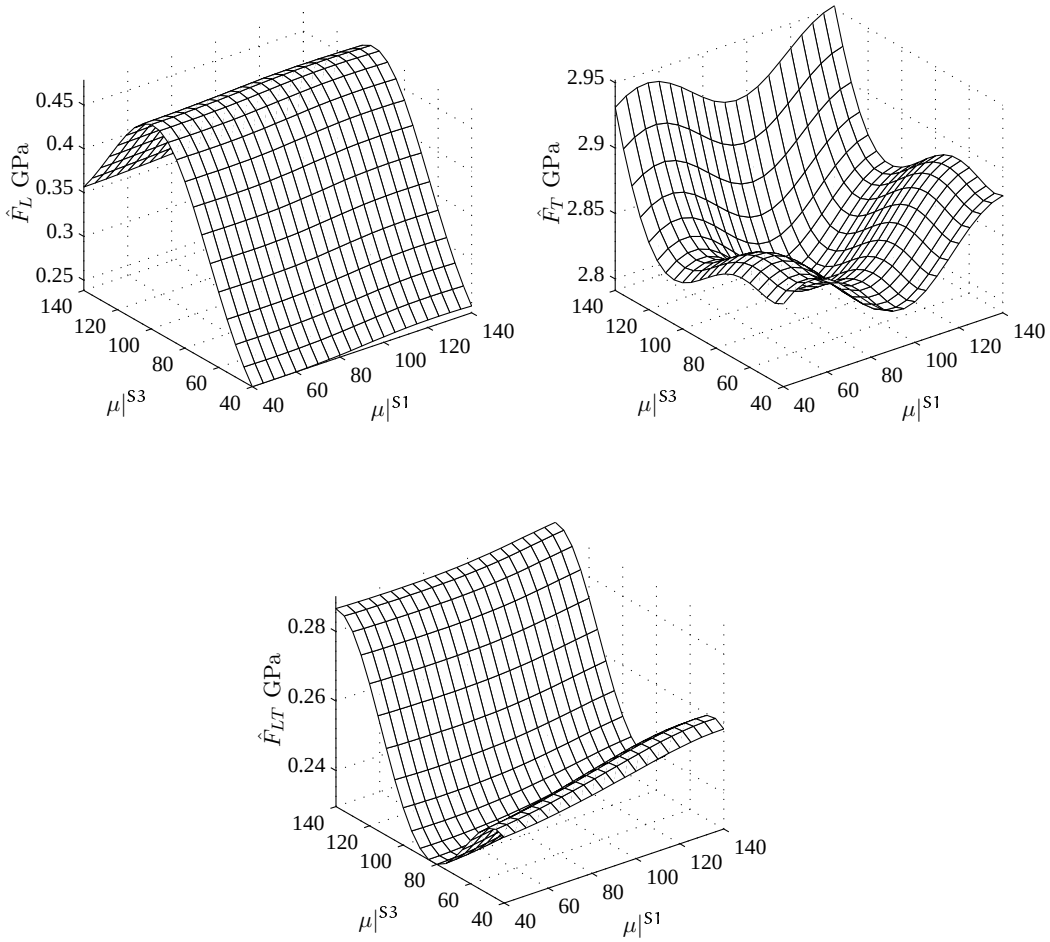

Figure 4.11.: Variation of flexural cell-wall properties with S1 and S3 MFA, $\mu|^{S1}$ and $\mu|^{S3}$. t is the thickness of the laminate.

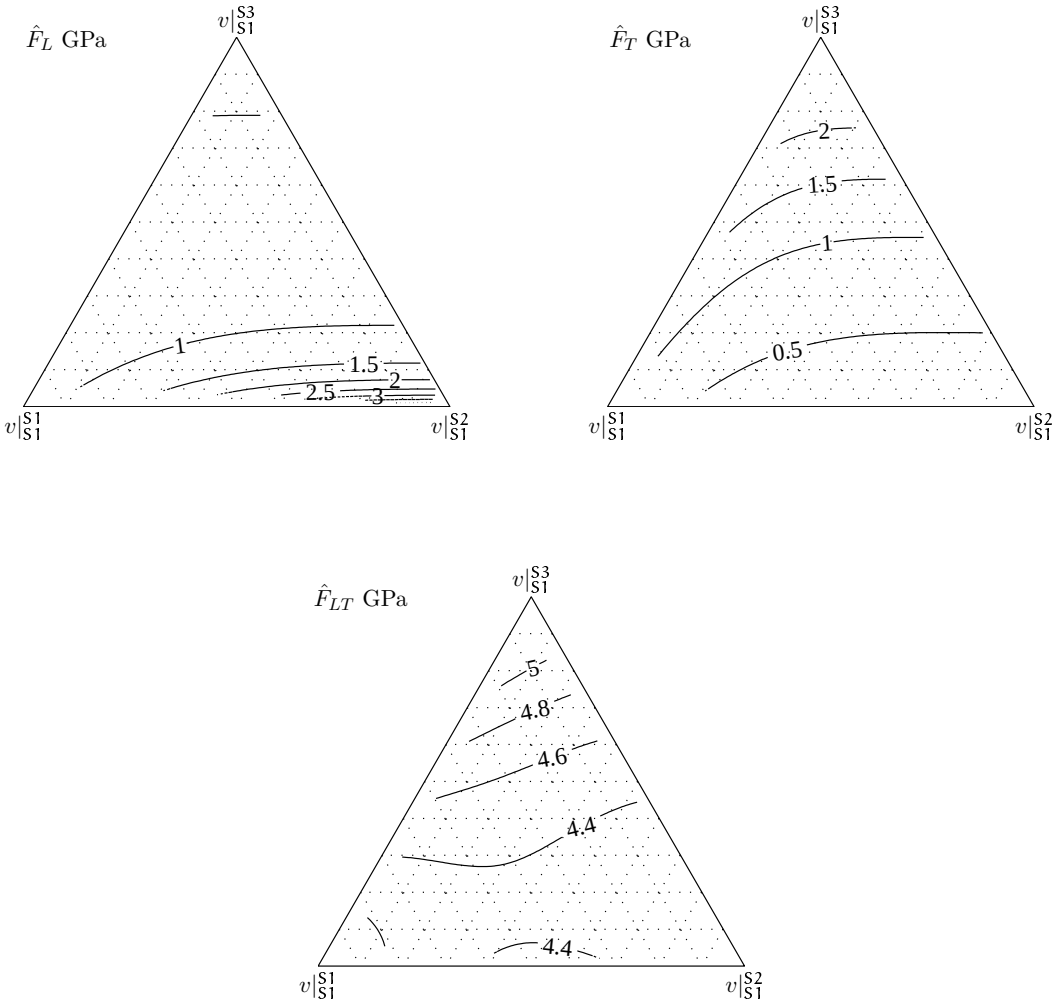

Figure 4.12.: Variation of flexural cell-wall properties with layer volume fractions.

S3 layer has a more significant influence on the flexural properties than the volume fraction and MFA of the S1 layer. This greater effectiveness of the S3 layer compared to the S1 layer is due to its being more distant from the center of the wall. In collapsed pulp fibres the S1 is more distant and its thickness and MFA will be more influential than those of S3.

It is worth noting that the flexural stiffnesses are proportional to t^3. This means that a 10% change in wall thickness will, for the same layup, result in a 33% increase in flexural stiffnesses. Thus, if bending plays a significant part in the cellular mechanics, as is the case for earlywood, the cell-wall thickness is highly influential.

4.5. Summary, comments and future work

In this chapter a model for the systematic variation of the MFA across the secondary cell wall has been proposed. A method, based on the periodic layered media homogenization procedure of appendix C, has been described for computing the effective properties of the major wall layers – CML, S1, S2 and S3 – that incorporates this systematic MFA variation as and also introduces a stochastic component to account for the variation within and between tracheids.

This method is used to derive major layer properties for use in the cellular models to be described in the next chapter from the nanostructural properties produced by the models described in the previous chapter. In this chapter, the wall layer properties have been combined using either the periodic method or classical thin laminate theory to yield the effective properties of the cell-wall. While these cell-wall models are not employed subsequently, they have illuminated the influence of layer MFAs and volume fractions and the process has been shown to be capable of yielding results consistent with experimental observtions.

In the anatomical discussion above, both radial and tangential lamellated structures were described. The influence of such structures can be partially addressed using the RR3 nanostructural models. Alternatively, another layered media homogenization can be introduced into the process for determing the effective properties of S2 layer. This has been investigated, and found not to have a great deal of impact on the overall properties of the cell-wall, though none of the results have been reported.

It is worth noting that the effective layer or cell-wall properties computed using the periodic homogenization procedure currently employed do not depend on the order of the lamellae within the layer, only on their relative thickness. Furthermore, specification of only eight 'orientation integrals' serves to completely characterize the distribution of MFA within the layer (see appendix C). If it were agreed that the periodic homogenization process gives acceptable results, and if these orientation integrals could be directly evaluated, from X-ray pole figures for example, then from a mechanical viewpoint there would be no need to fully characterize the distribution of MFA

throughout the layers or the wall. Such a compact description would certainly have its uses.

An assumption of macroscopic homogeneity is implicit in the process for determining effective properties. Such an assumption cannot be justified theoretically for the cell-wall layers, particularly the transition regions as they are not in any sense homogeneous when resolved at a cellular scale. Only empirical evidence can justify the use of the periodic layered media homogenization method.

The cell-wall layer models presented are computationally efficient and allow some of the natural variability of wood structure to be included. On the other hand they sit somewhat uncomfortably between the nanostructual and cellular scales. In the future a number of points could be considered:

- small scale cell-wall features, primarily local MFA variation, could be handled at the nanostructural level, though this would mean abandoning the prismatic treatment in favour of more expensive three-dimensional models
- large scale cell-wall inhomogeneity and variation between tracheids could be handled at the cellular scale.

Chapter 5

Cellular modelling

5.1. Introduction

This chapter presents models that predict the effective tangential hygro-elastic properties of homogenous cellular aggregates. These models account for the influence of:

(i) tracheid cross-sectional shape,

(ii) tracheid wall thickness and its circumferential variation

(iii) and the local arrangement of tracheids in the transverse plane.

5.2. Softwood microstructure

Six types of cell are recognized in softwood: axial tracheids, ray tracheids, strand tracheids, axial parenchyma, ray parenchyma and epithelial cells, although not all of these cell types are present in any given species or sample. Inter-cellular spaces also occur, and in some species – notably pines, spruces, larches and Douglas fir – axial and radial resin canals are regular features. Typically axial tracheids occupy 90-95% of softwood volume with the remaining volume primarily occupied by ray tissue (Panshin and de Zeeuw, 1980; Fengel and Wegener, 1984).

The cellular microstructure of radiata pine is illustrated in figure 5.1. The long axis of the axial tracheids lies parallel to the longitudinal direction, whereas cells in the rays have their long axes parallel to the radial direction.

Wood cells are formed by repeated cell division of so-called initial cells located in the cambium. Consequently, both the axial and ray elements are arranged in radial rows. The degree of tangential order within the axial tissue varies considerably between species and within samples.

Axial tracheids, often referred to as simply tracheids, are long slender cells with flattened or tapered ends and have tangential diameters of 10–80 μm and lengths of 1–6 mm (Core et al., 1976; Panshin and de Zeeuw, 1980; Fengel and Wegener, 1984). In radiata pine, tracheids are typically 3 mm in length; with this length increasing by 1–3 mm from pith to bark (Harris, 1991; Cown, 1992). Unlike the tangential diameter, which is relatively constant across growth rings, the radial diameter varies considerably;

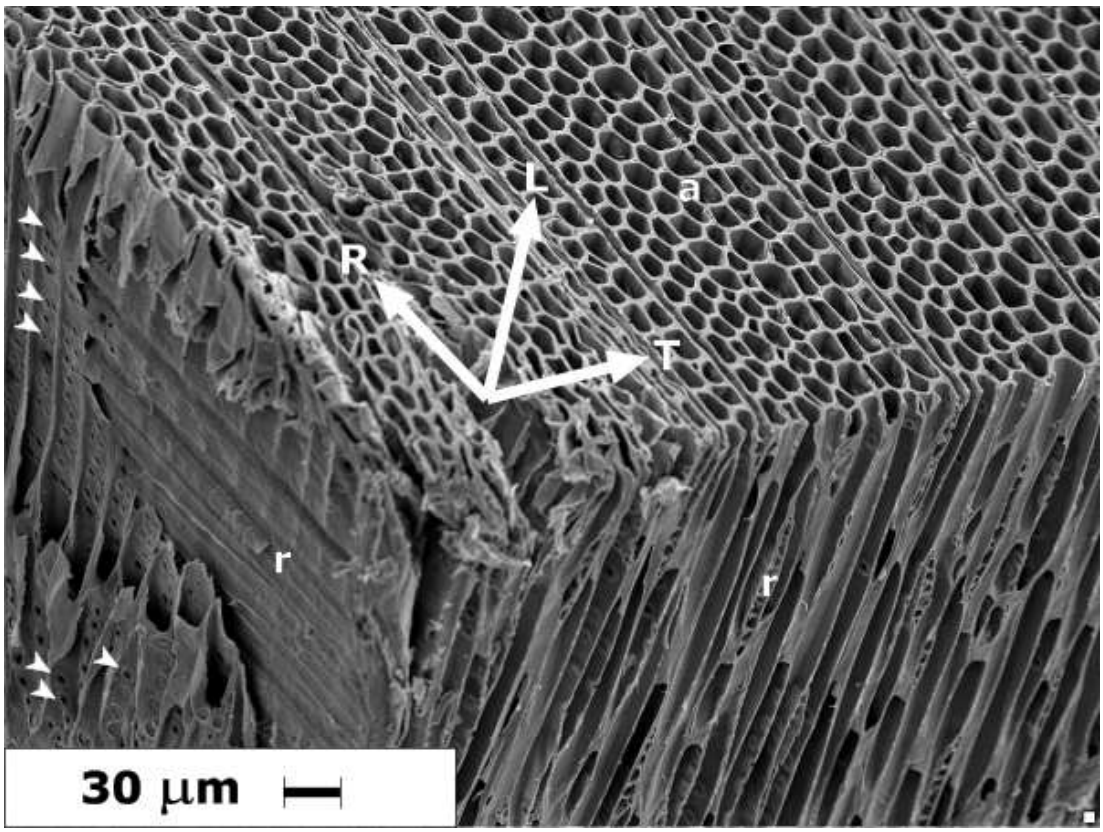

Figure 5.1.: Radiata pine microstructure. a–axial tracheids, r–rays. Arrows identify pits.

the most significant variation being that occurring within growth rings. In radiata pine the tangential diameter is typically between 26–34 μm and the radial diameter varies from 30–50 μm in earlywood to 20–25 μm in latewood. The pattern of variation across a growth ring of the tangential and radial tracheid diameters of radiata pine, as measured by SilviScan (Evans, 1994), are shown in figure 5.2.

In cross section, tracheids in normal wood are generally 4–7 sided polygons; earlywood tracheids tend to have hexagonal cross-sections whereas latewood tracheids tend to be rectangular. In severe compression wood, the transverse shape is rounded and intercellular spaces occur at cell corners (Timell, 1986a).

Radiata pine tracheid walls are 1–7 μm thick (Cown, 1975; Harris, 1991; Donaldson and Lausberg, 1998). Because of the very high aspect ratio of the tracheids and their prevalence within wood tissue, the void volume fraction within a small cellular domain is primarily governed by the transverse tracheid size and wall thickness. Void volume fraction in turn controls the cellular density, sometimes referred to as the microdensity, since the cell-wall substance density is relatively constant. The variation in microdensity across radiata pine growth rings is illustrated in figure 5.2.

The cell wall structure described in the preceding chapter is modified locally by a variety of microstructural features. Pits are the most prominent of these cell wall features and connect adjacent cells, permitting fluid transport. Different types of pits occur between different cell types. Bordered pits (see figure 5.3) connect circumferentially adjacent tracheids. Radial earlywood tracheid walls in radiata pine contain 20–70 bordered pits; radial latewood walls contain 10–20 (Jinxing, 1989). In other softwood species, the number of pits may be as high as 300 per radial wall (Siau, 1971). Bordered pits are usually confined to radial walls, but occasionally are found on tangential walls, particularly in the last formed latewood and the first formed earlywood (Koran, 1977; Laming and ter. Welle, 1971). Parenchyma cells are connected to one another by simple pits, and to tracheids by cross field pits, of which there are many varieties.

Other cell wall features include: helical thickenings (Wardrop and Dadswell, 1951; Timell, 1978; Butterfield and Meylan, 1980), callitrisoid thickenings (Davies and Ingle, 1966; Butterfield and Meylan, 1980; Heady, 1997), crassulae (Butterfield and Meylan, 1980), ray thickenings (Ladell, 1967; Keith, 1975), trabeculae (Keith, 1971; Butterfield and Meylan, 1980; Yumoto, 1984; Timell, 1986a; Grosser, 1986; Ohtani et al., 1987; Muller-Stoll and Casperson, 1987) and, in compression wood, helical cavities (Timell, 1978; Butterfield and Meylan, 1980; Takabe et al., 1992). These features are not universal; their presence or absence depends on the species and sample.

The preceding description of softwood microstruture has barely touched on the variety and complexity that exists. For further information the reader is directed to the references cited above and to Greguss (1955), Harlow (1970), Core et al. (1976), Schweingruber (1978), Panshin and de Zeeuw (1980), Butterfield and Meylan (1980);

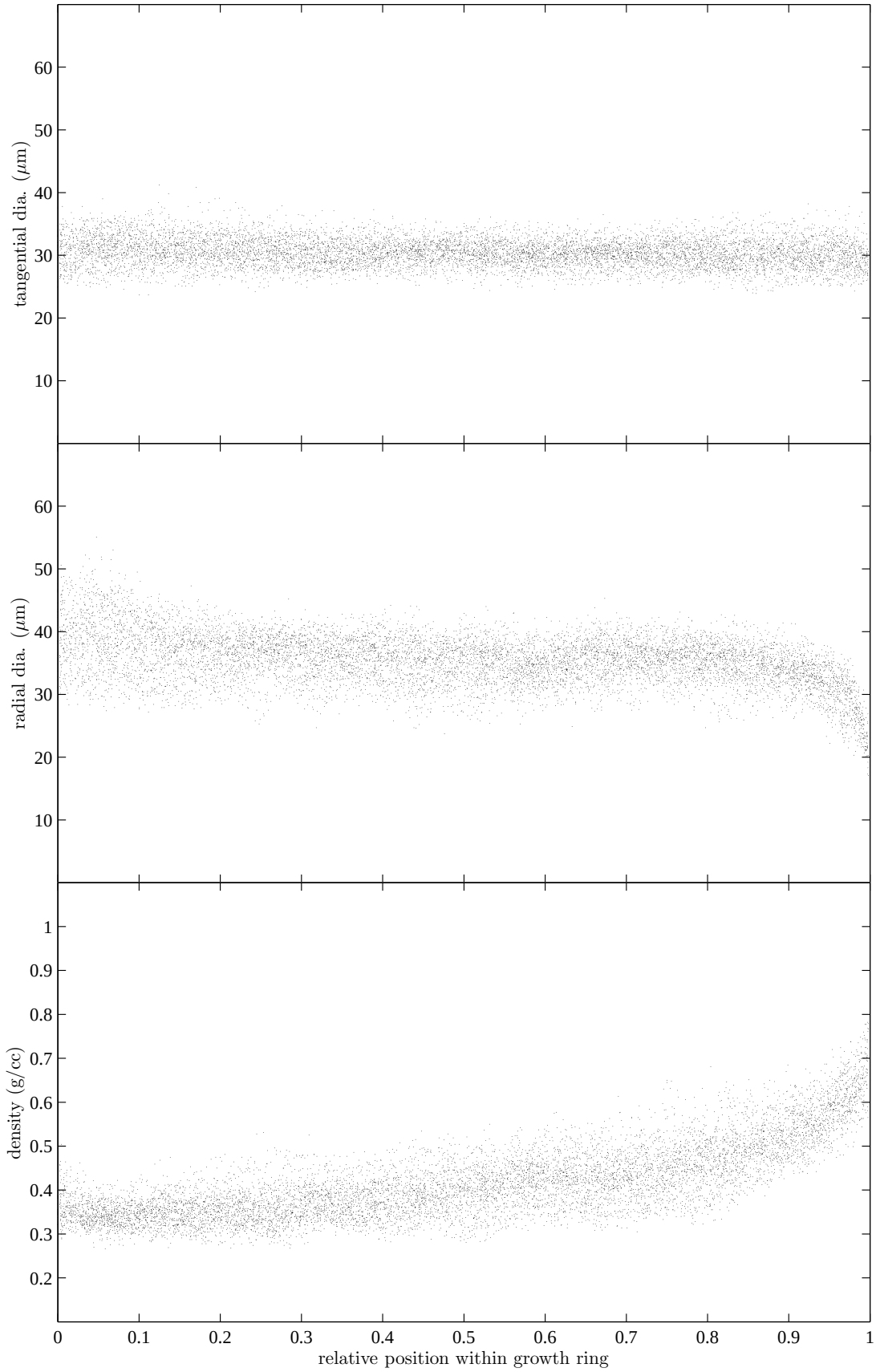

Figure 5.2.: Tangential and radial tracheid diameters of tracheids and microdensity vs relative position within growth ring. Radiata pine samples, measured using SilviScan.

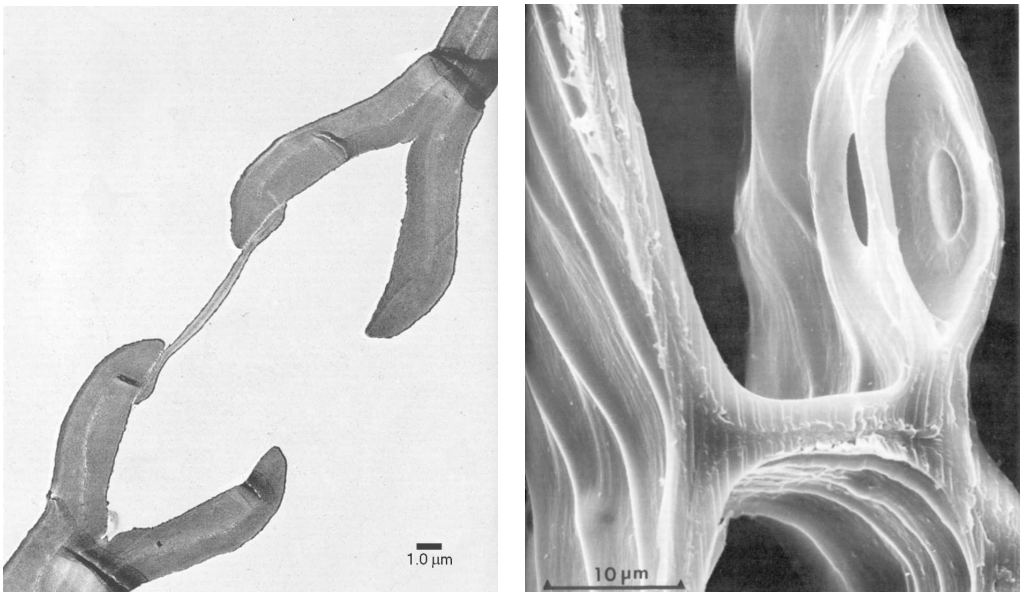

Figure 5.3.: Bordered pits. Source: Core et al. (1976).

Butterfield (1993) and Wilson and White (1986).

5.3. Cellular modelling

In the remainder of this chapter only tissue composed solely of axial tracheids is considered further. Preliminary models that incorporate the the effects of ray tissue are presented in appendix J.

Axial tissue is treated as being prismatic. This assumption has been made frequently in the past (Koponen et al., 1991; Persson, 1997; Astley et al., 1998), apparently being first used in the context of mechanical modelling by Price (1928). Thus cell wall sculpturing, including bordered pits, is ignored along with all other longitudinal variation, such as variation in tracheid cross-sectional size and shape associated with rays and cell tips.

The variation in structure across the tracheid wall is represented by the four layers – CML, S1, S2 and S3 – which, at the cellular scale, are treated as being homogeneous. Within a tracheid aggregate the layer total volume fractions, properties and mean microfibril angle are assumed to be the same in all cells. Consequently, differences between tangential and radial walls, as well as inter-tracheid variation are ignored. This approach is appropriate when the growth ring width is much greater than the transverse tracheid size and effective intra-ring properties are desired. Alternatively, when the growth rings are narrow, a radial strip across an entire growth ring can be modelled at the cellular scale, as was done by Persson (2000). When the growth rings

are wide and only macroscopic effective properties are required, it is also possible to represent the changing tracheid geometries and microdensity by a small number of representative 'cells' as was done by Tang (1997).

While it is possible, for the purpose of geometric description, to treat a tracheid aggregate as a single entity (Farruggia and Perré, 1997; Perré, 2001), it is more convenient to separate this task into two parts: the description of the surfaces separating individual cells (external geometry), and the description of the internal geometry of each cell and each cell wall layer.

5.3.1. External tracheid geometry and arrangement

In general, the external geometry of tracheid cross sections is well represented by convex polygons. That this is the case is a consequence of the competition for space taking place during the initial stages of cell formation. Frequently, tracheid cross sections are described as hexagonal or rectangular and these simple shapes have been used by previous cellular models (Norimoto et al., 1978; Navi, 1988; Koponen et al., 1991; Astley et al., 1998; Persson, 2000).

Herein, both idealized and actual external transverse tracheid geometries have been investigated. These approaches are discussed in the following subsections. Within the present study, Voronoi tessellations (Okabe et al., 1992) have also been investigated as a means for describing the external geometry of a tracheid aggregate based on centroid data for each cell. When constructed using an isotropic metric they do not provide good results. By using an anisotropic metric better results can be obtained (Stol, 1996c). Furthermore, they can be constructed on a tiled space and, when this is done, they yield a periodic aggregate. Another approach to describing irregular external geometries was employed by Persson (2000) who applied random perturbations to the vertices of a periodic array.

5.3.1.1. Idealized geometries

In the present work an idealized single cell model, referred to as the s1cell model and defined in figure 5.4, has also been employed. It is periodic, has two-fold rotational symmetry and can be used to represent staggered and aligned rectangular as well as hexagonal cell arrays[1].

A single polygon provides a compact description of the external geometry and it is a simple matter to chose a periodic shape – that is a shape capable of tiling the plane – permitting the periodic boundary conditions described in chapter 2 to be employed. However, within a tracheid aggregate considerable variation in cross-sectional shape and size is exhibited and obviously this variation cannot be represented using an s1cell

[1] An aligned rectangular array is obtained by setting $L_2 = \theta_2 = 0$

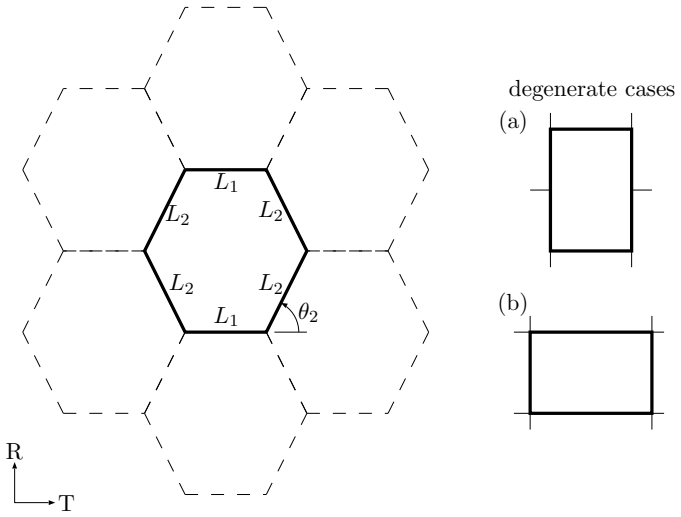

Figure 5.4.: s1cell model geometry.

model. To include this variation, periodic parametric models containing more than one cell have been investigated. One of these models, referred to as the g2cell model, is defined in figure 5.5. The g2cell model has nine independent parameters, which for convenience are taken to be the four edge lengths $L_1 \ldots L_4$ and the five edge orientations $\theta_1 \ldots \theta_5$. The remaining edge lengths and angles are given by

$$L_5 = -L_4 \frac{\cos\theta_4}{\cos\theta_5} \tag{5.1}$$

$$L_6 = \sqrt{\left(L_4 \sin\theta_4 + L_5 \sin\theta_5 - L_2 \sin\theta_2\right)^2 + \left(L_2 \cos\theta_2\right)^2} = -L_2 \frac{\cos\theta_2}{\cos\theta_6} \tag{5.2}$$

$$\theta_6 = \tan^{-1}\left(\frac{L_2 \sin\theta_2 - L_5 \sin\theta_5 - L_4 \sin\theta_4}{L_2 \cos\theta_2}\right). \tag{5.3}$$

In general, this model possesses no symmetry.

Using the tracheid transverse shape database described in appendix F, parameters for the s1cell and g2cell models for six intra-ring radial zones have been determined. These parameters appear in tables 5.1 and 5.2, and the corresponding geometries are illustrated in figures 5.6 and 5.7.

The parameters were obtained by minimizing the difference between the empirical and model cumulative wall length and length weighted orientation distribution functions. The minimization was performed using a Nelder-Mead (or downhill simplex) method (Press et al., 1989) with restarts. Edge lengths and orientations were used, rather than cell areas or diameters for example, because they have a natural and direct connection with the mechanics of a planar framework.

Parameterized periodic models containing up to nine cells have been trialed. As the number of cells increases, the problem of defining an independent set of parameters

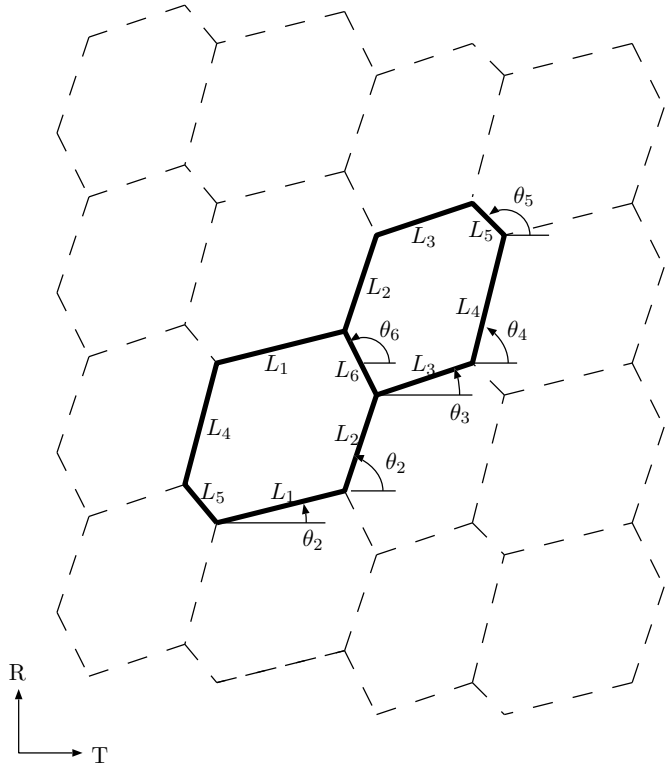

Figure 5.5.: g2cell model geometry.

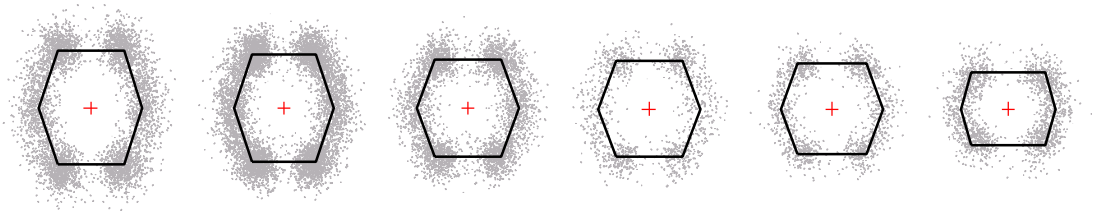

Figure 5.6.: s1cell model geometries.

ring coord.	L_1 μm	L_2 μm	θ_2 $^\circ$
0.00 – 0.20	25.37	23.01	71.84
0.20 – 0.60	24.81	21.67	72.40
0.60 – 0.80	25.33	19.86	69.94
0.80 – 0.90	25.26	19.58	68.71
0.90 – 0.95	26.36	18.36	69.92
0.95 – 1.00	28.68	14.58	74.14

Table 5.1.: s1cell model parameters.

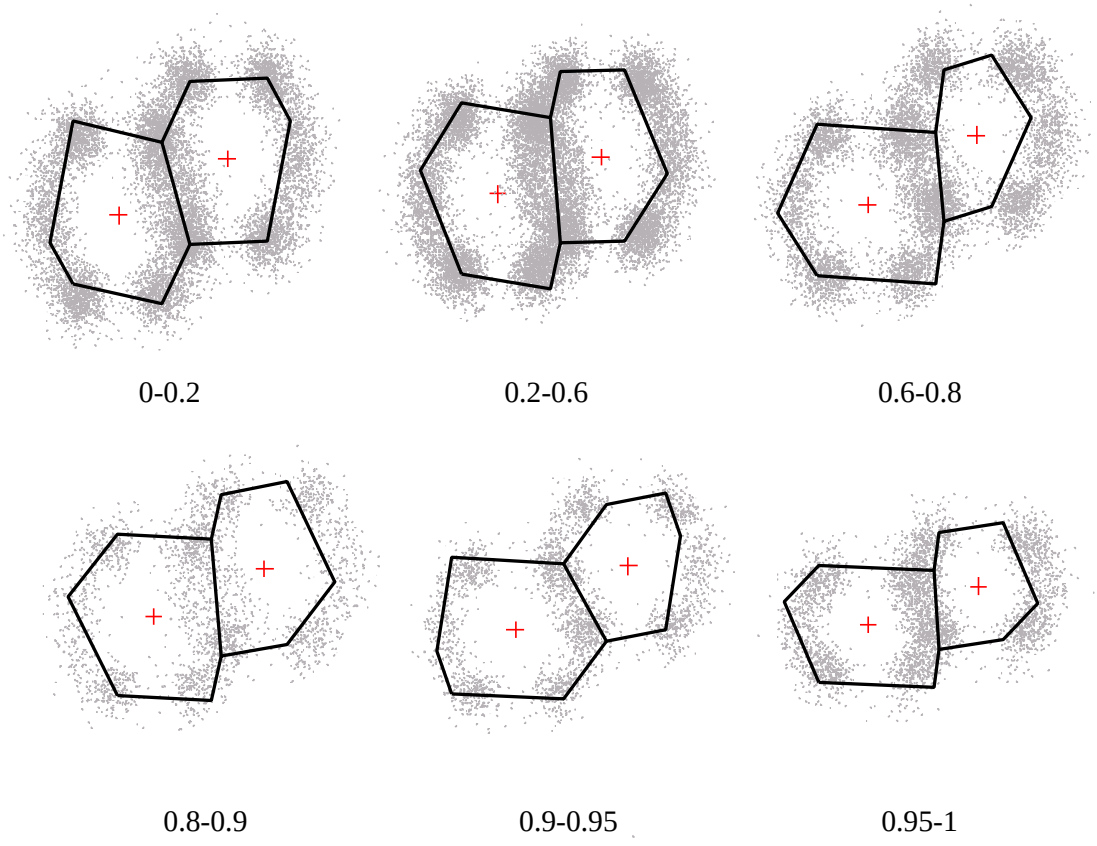

Figure 5.7.: g2cell model geometries.

ring coord.	L_1 μm	L_2 μm	L_3 μm	L_4 μm	θ_1 $^\circ$	θ_2 $^\circ$	θ_3 $^\circ$	θ_4 $^\circ$	θ_5 $^\circ$
0.00 – 0.20	26.56	19.46	22.53	35.82	-12.96	64.69	1.916	79.12	119.2
0.20 – 0.60	24.77	12.73	17.95	21.53	-9.299	78.20	2.210	58.11	111.6
0.60 – 0.80	31.78	17.12	13.40	25.98	-3.600	81.73	15.89	66.21	121.8
0.80 – 0.90	24.74	11.89	17.53	20.79	-2.385	78.10	10.26	51.80	116.2
0.90 – 0.95	30.29	19.39	16.39	25.33	-2.790	53.96	11.40	81.16	108.6
0.95 – 1.00	31.82	10.45	18.18	13.67	-2.451	82.32	8.776	47.20	112.6

Table 5.2.: g2cell model parameters.

that automatically satisfy the periodicity requirements increases in difficulty. Moreover, the topology of these models is fixed, that is the number of edges per polygon cannot be altered, unless cells of zero area are permitted, and doing so adds considerable complexity.

5.3.1.2. Actual geometries

The s1cell and g2cell models are both idealized models having parameters that are chosen such that they represent, in a statistical sense, the external tracheid geometry. An alternate approach is to use actual transverse geometries derived from micrographs. This approach has been taken previously by Astley et al. (1998) and Persson (2000).

The obvious method for obtaining tracheid aggregate outlines is to digitize them manually from transverse images. Examples of manually digitized tracheid aggregate skeletons are shown in figure 5.8. This method is straight forward and can be applied to less than ideal images but is tedious – typically digitizing an aggregate of 100 tracheids takes around an hour – and the results depend on choices made by the operator.

A semi-automated method has been developed using discrete Voronoi skeletons (Ogniewicz, 1992). This method proceeds as follows.

1. Take a digital image of a tracheid aggregate. See figure 5.9 (a).

2. Binarize this image by thresholding in such a way as to render wall pixels black and lumen pixels white. This monochrome image should have a solid white border and the cells at the edges should be open so that the medial axis that will be computed between two cells rather the between a cell and image border[2]. See figure 5.9 (b).

3. Manually remove small defects from the binarized image. Repeated erosion-dilation operations can be useful at this stage.

4. Compute and prune the discrete Voronoi skeleton. Currently this is done using freely available software[3]. See figure 5.9 (c).

5. Extract valid closed polygons from the Voronoi skeleton. See figure 5.9 (d).

Examples of external aggregate outlines obtained by this method are displayed in figure 5.10. To generate a aggregate skeleton containg 100 cells by this method takes around 5 minutes.

[2]The exception to this is when an image boundary corresponds to a ray. Such boundaries should not be avoided as the affect the wall orientation distribution (see appendix F).

[3]MAT-1.0.3, `http://www.hrl.harvard.edu/people/postdocs/rlo/rlo.dir/rlo-soft.html`.

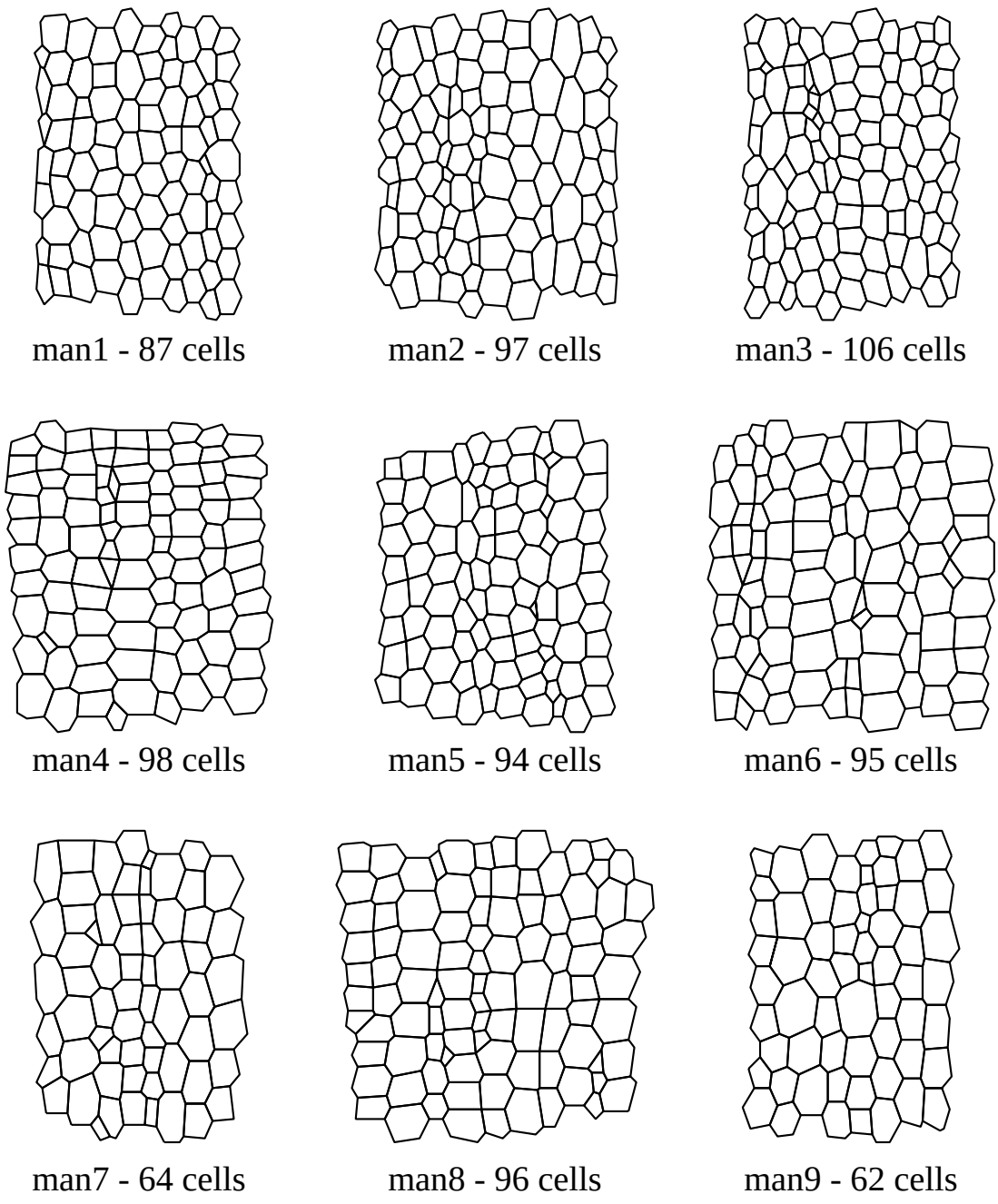

Figure 5.8.: Examples of manually digitized transverse tracheid aggregate skeletons.

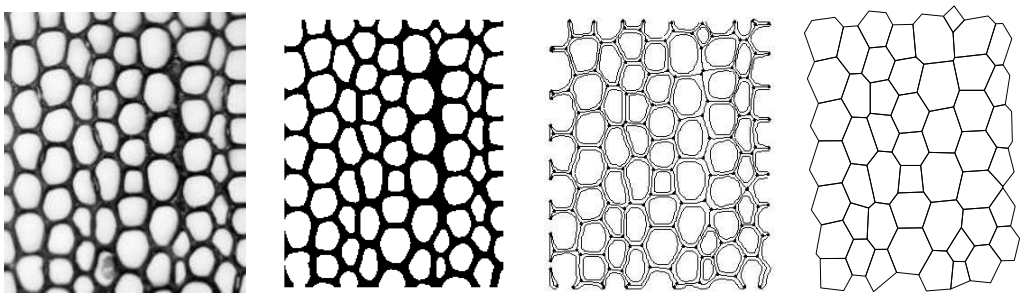

(a) **(b)** **(c)** **(d)**

Figure 5.9.: Semi-automated cell skeletonization procedure.

5.3.2. Internal tracheid geometry

The complexity of wood structure at a cellular scale, even when it is treated as being prismatic, makes the finite element method an attractive approach to determining effective properties. Cellular models using three dimensional layered shell (Astley et al., 1998), and layered solid elements (Persson, 2000) have been employed in previous studies and within the current work, although they are not presented in this thesis. Layered elements are economical but restrict the internal cellular geometries that can be considered and introduce further approximations regarding the stress and strains states within the cell-wall.

Models that use the prismatic two dimensional elements described in chapter 2 are presented in this chapter. Any candidate representation for the internal tracheid geometry for use with these models should:

(**R1**) be able to represent the lumen and layer interfaces as smooth surfaces,

(**R2**) capture the layer thickening, particularly of the CML, associated with cell corners,

(**R3**) and require a minimum number of parameters.

This last requirement essentially rules out representations based on layer thicknesses, as describing the circumferential variation introduces numerous parameters. Instead, layer volume fractions are used in conjuction with an idealized shape description. For this type of description a fourth requirement for any candidate representation is that it:

(**R4**) be able to easily and accurately produce layers of arbitrary total volume fraction.

A number of various approaches to describing internal cellular geometry have been investigated and rejected. These approaches include:

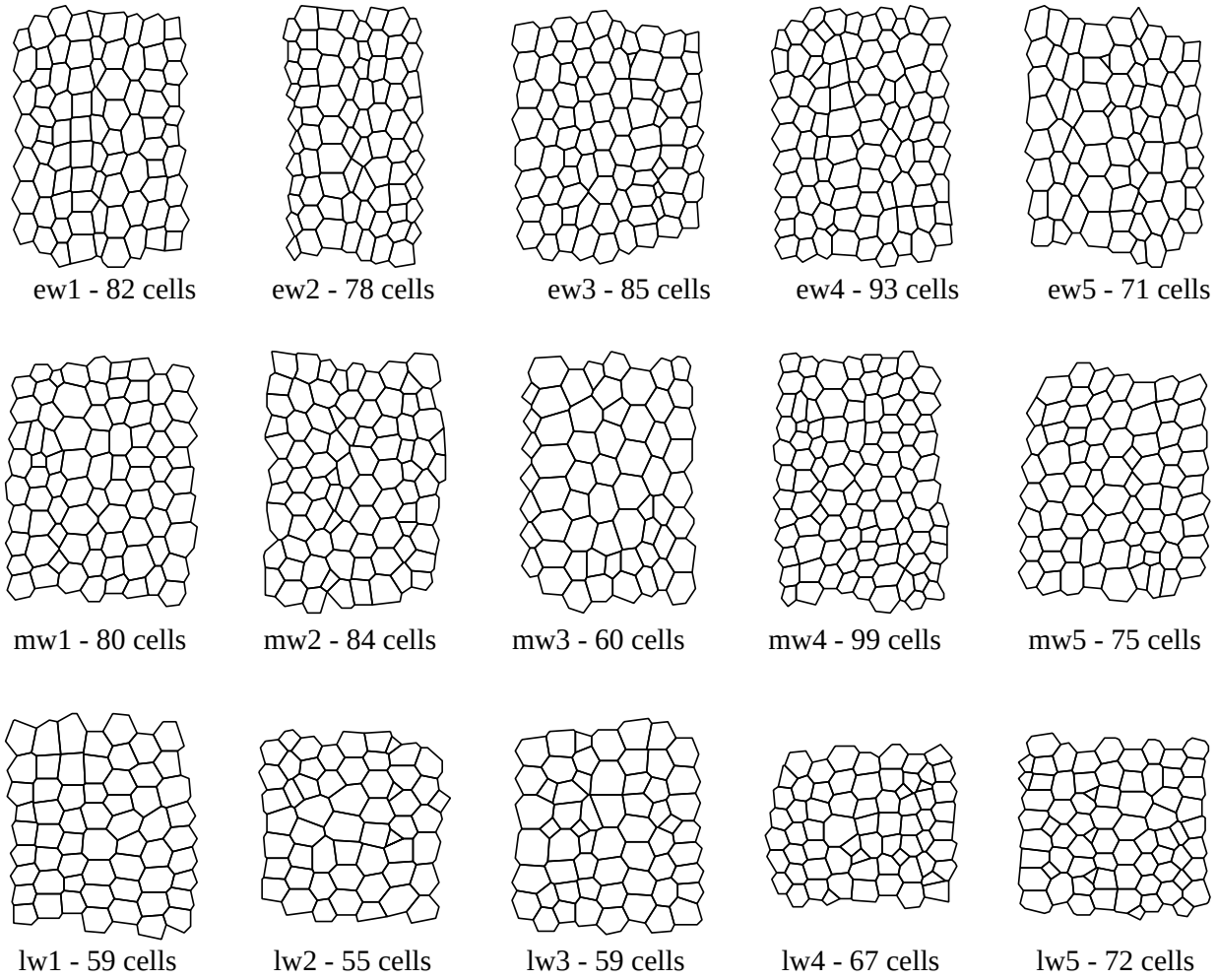

Figure 5.10.: Examples of tracheid transverse skeletons obtained by a semi-automated process.

- Interfaces represented by polygons geometrically similar to external shape with circular fillets at the corners. Progressing towards the lumen, the corner fillets can have either a constant or increasing radius.

- Conformal mapping, using the Schwarz-Christoffel transformation (Milne-Thomson, 1968; Moon and Spencer, 1971; Ivanov and Trubetskov, 1995), from the unit disk to the interior of the external polygon.

- Lumen shape represented by a circle or ellipse. Intermediate interfaces found by interpolating between control points on the external polygon and lumen surface. Note that a fictious lumen surface can also be used.

The approach adopted to describe the internal tracheid geometry is based on a simple physical model for devlopment of the cell wall. It is assumed that the growth rate normal to the surface depends on the surface curvature. The more tightly curved the surface is at a point, the higher the normal growth velocity is at that point. The initial surface is assumed to be the external polygonal shape described above. This model, and the algorithm used to compute the evolving surface, is described in appendix G. Examples of the output of this model appear below.

This internal growth model ignores any changes in shape associated with lignification and also neglects the initial curvature, resulting from turgor pressure and the finite cell plate thickness, at the cell corners. However, it does meet the criteria laid out above for an acceptable representation of internal geometry and the geometries it produces appear similar to those observed in transverse micrographs. Whether or not it is a quantitatively accurate model for actual wall layer thicknesses and cell lumen shapes is unknown. This should be investigated in the future, but to do so will require extensive measurements of real tracheid geometries. Currently this data is not available.

The algorithm used to compute the development of the lumen surface in time is based on a discretization of the surface. It is a simple matter to generate a finite element mesh from the isochrones (curves representing the growth surface at given points in time) and the paths traced by the mesh points on the developing surface. These two sets of curves also provide a convenient coordinate system for describing the variation of material properties within the cell wall.

Cell void fraction, layer solid volume fractions, circumferential mesh spacing and a velocity-curvature parameter are currently used to control the internal growth algorithm. When dealing with multicell models with prescribed overall densities, it can be assumed that each cell has the same void fraction – which leads to small cells having thinner walls than thicker cells – or that the wall thickness is the same for each cell and individual cell void fractions determined such that the overall density is that specified.

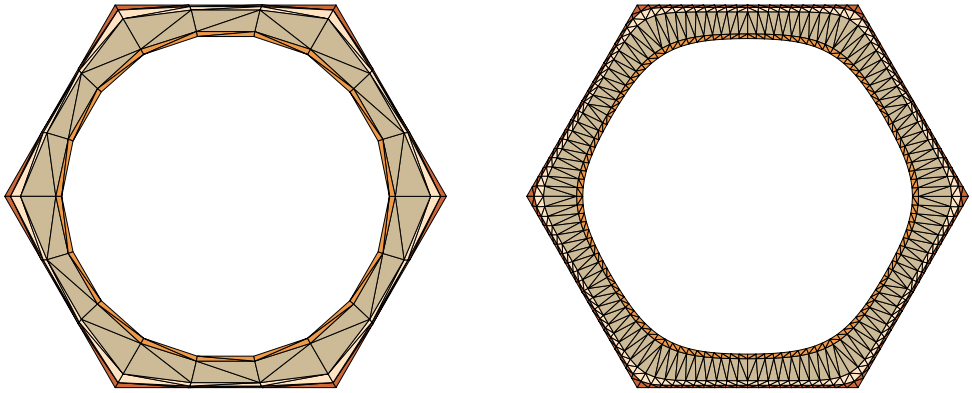

(a) CONVA **(b)** CONVB

Figure 5.11.: Base meshes used to study s1cell convergence.

Other assumptions are, of course, possible. Herein, for convenience, it is assumed that the void fraction in each cell is the same.

5.4. Convergence

A regular hexagonal s1cell model has been used to investigate the influence of mesh refinement on the computed effective properties.

The CML, S1, S2 and S3 layer properties of table 5.3 have been used. The properties of the secondary wall layers have been generated using the modelling procedure described elsewhere in this thesis. The CML properties are taken to be those of the LM phase, as modelled in chapter 8.

The internal geometry depends on the mesh used for the internal growth model and the same circumferential mesh is used in the base mesh for the mechanical model. In normal usage, mesh refinement is achieved by changing the parameters which control the internal growth model. Here however, to avoid confusing the effects of finite element discretization error with changing geometry, the two particular geometries shown in figure 5.11 are considered and the mesh refinement is perfomed using the same element division technique described in chapter 3. The effective density of both these models is 0.5 g/cc.

Both the models shown in figure 5.11 posses 6-fold rotational symmetry in the transverse plane and hence would be expected to yield transversely isotropic properties. This is indeed the case, and these properties for a range of mesh refinements appear in table 5.4.

layer	$\hat{v}$	MFA $^\circ$	χ	$\chi_{,w}$	ρ g/cc	C_{11} GPa	C_{12} GPa	C_{13} GPa	C_{22} GPa	C_{23} GPa	C_{33} GPa	C_{44} GPa	C_{55} GPa	C_{66} GPa	α_1^w $\times 10^{-3}$	α_2^w $\times 10^{-3}$	α_3^w $\times 10^{-3}$
CML	0.08	-	1.065	-1.239	1.294	8.098	5.399	5.399	8.098	5.399	8.098	1.350	1.350	1.350	34.20	34.20	34.20
S1	0.15	90	1.019	-0.2429	1.383	6.787	3.918	5.487	6.657	4.438	43.78	1.384	2.415	1.378	48.81	51.45	16.32
S2	0.65	30	0.9968	0.2234	1.422	6.210	3.279	5.529	6.022	3.936	62.24	1.383	2.953	1.382	52.02	55.53	4.714
S3	0.12	90	1.008	-0.01714	1.402	6.497	3.599	5.495	6.340	4.188	52.54	1.384	2.671	1.380	50.37	53.42	9.780

Table 5.3.: Assumed layer properties (with respect to layer TRL coordinate system).

ldiv	ndofs ×1000	time s	E_1 GPa	ν_{13}	E_3 GPa	G_{23} GPa	G_{12} GPa	α_1^w	α_3^w
				CONVA					
1	1	0.4	1.196	0.4502	6.955	1.516	0.3666	0.1671	0.03917
2	4	1.3	1.172	0.4538	6.907	1.507	0.3593	0.1682	0.03888
3	8	4.0	1.165	0.4563	6.887	1.505	0.3571	0.1687	0.03853
4	14	8.9	1.161	0.4577	6.877	1.504	0.3561	0.1691	0.03831
5	22	18	1.159	0.4585	6.872	1.503	0.3555	0.1692	0.03819
6	31	34	1.158	0.4590	6.869	1.503	0.3552	0.1693	0.03812
7	43	60	1.158	0.4593	6.867	1.503	0.3550	0.1694	0.03807
8	56	98	1.157	0.4595	6.866	1.502	0.3549	0.1695	0.03804
9	70	146	1.157	0.4597	6.865	1.502	0.3548	0.1695	0.03802
10	87	278	1.156	0.4598	6.864	1.502	0.3547	0.1695	0.03801
				CONVB					
1	6	2.310	1.130	0.4463	6.994	1.527	0.3400	0.1661	0.03781
2	24	16.27	1.129	0.4467	6.987	1.526	0.3397	0.1662	0.03772
3	53	76.49	1.129	0.4468	6.986	1.526	0.3396	0.1663	0.03770
4	94	291.8	1.129	0.4468	6.986	1.525	0.3396	0.1663	0.03769

Table 5.4.: Influence of mesh refinement on the effective properties of s1cell models.

From the results presented in table 5.4, it is concluded that the effective properties of both models do converge with increasing mesh refinement, and that the dicretization error associated with the base meshes is acceptable.

5.5. Influence of internal shape

Watanabe et al. (2000) concluded that "wall thickness around the cell corners as well as transverse cell shapes are important factors in [determining] the mechanical properties on the transverse plane of wood". The s1cell models shown in figure 5.12 have been used to investigate this statement. Internal geometries with low, medium and high 'roundness' are obtained by appropriately specifying the internal growth model velocity-curvature parameter. The external shape parameters corresponding to ring coordinates of 0, 0.6 and 1 – earlywood, middlewood and latewood respectively – and have densities of 0.3, 0.4 and 0.8 g/cc based on the density data presented in figure 5.2. The wall layer properties used are those of table 5.3.

The computed effective properties appear in table 5.5. From these results it is clear that the internal geometry does influence the effective properties, particularly in the transverse plane. The influence of roundness on the transverse properties can also be seen in the plots of directional modulus and hygroexpansional coefficient in figure 5.13.

The tangential modulus E_1 and the transverse shear modulus G_{12} both increase

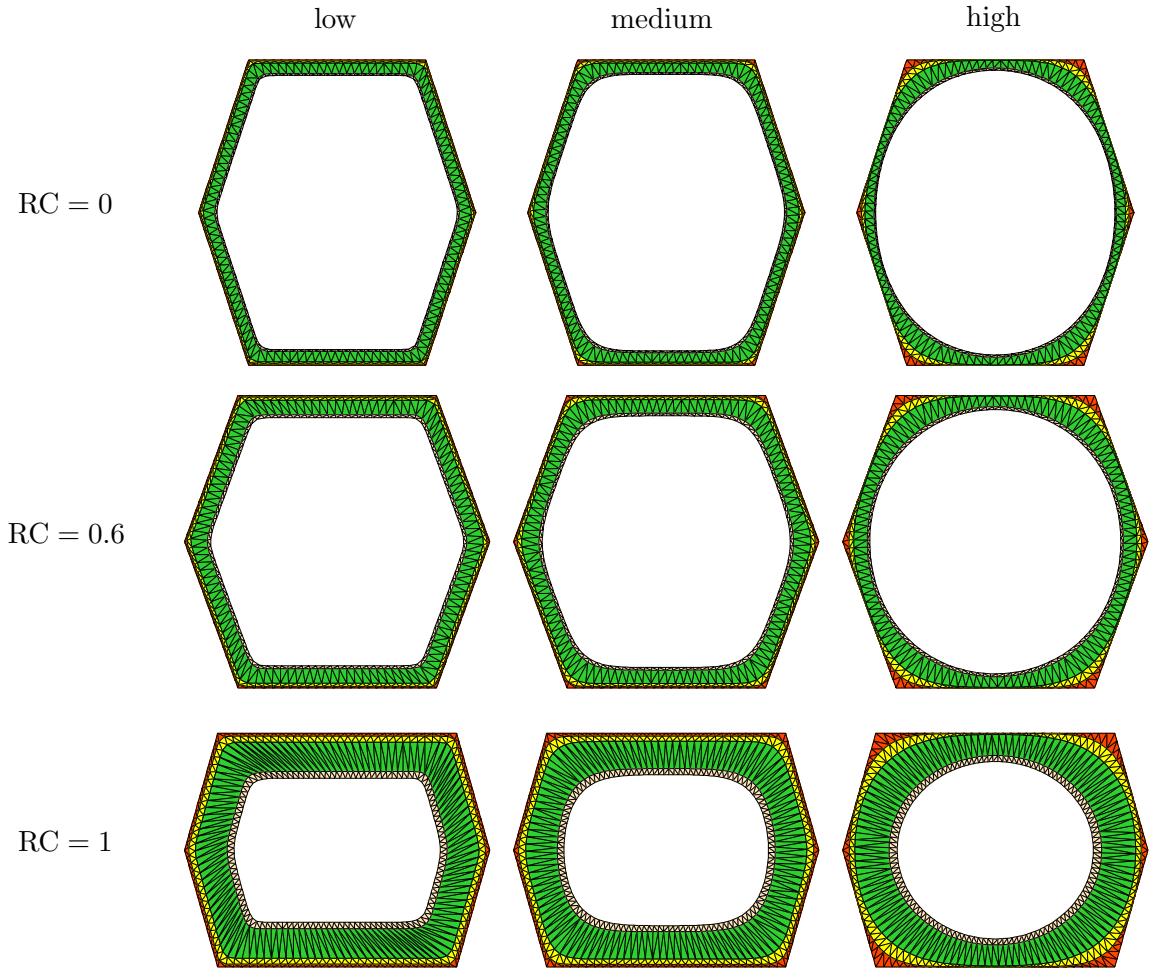

Figure 5.12.: Models with varying internal 'roundness'. Not to scale.

with increasing roundness, although the increase in shear modulus is more pronounced. This increase is greater for lower densities. The remaining properties may increase or decrease with increasing roundness depending on the density and external shape.

These results can be explained in terms of the relative roles of flexure and stretch. By moving cell wall material to the tracheid corners, the flexural stiffness is increased. When the cell-walls are thin, this has a significant effect on those effective properties dominated by cell-wall bending, namely the tangential and transverse shear moduli.

In the remainder of this chapter, internal growth models with medium roundness have been used.

5.6. Influence of external shape and arrangement

The influence of external tracheid geometry and transverse arrangement has been investigated by computing the effective properties of a variety of idealized s1cell and g2cell models as well as a large number of 'real' multicell tracheid aggregates. Periodic boundary conditions have been used with the s1cell and g2cell models. The geometry of an arbitrary tracheid aggregate does not permit these boundary conditions to be used. Instead the uniform stress and uniform strain boundary conditions described in chapter 2 have been used.

Once again, the layer properties and volume fractions used in all models are those of table 5.3. Note that the volume fractions do not change with density, unlike the models of chapter 6.

The s1cell and g2cell model external geometries employed are determined using the best-fit parameters described above at ring coordinates of 0.1, 0.4, 0.7, 0.85, 0.925 and 0.975. It has been assumed that the densities corresponding to these ring coordinates are those appearing in table 5.6. These densities are the values predicted by a sixth order polynomial model fitted to a subset of the density data of figure 5.2 corresponding to ring 15 going from pith to bark. The s1cell and g2cell models investigated are shown in figure 5.14.

The multicell models used are samples or sub-aggregates of the tracheid skeletons displayed in figure 5.10. Earlywood, middlewood and latewood aggregates have been investigated, the densitites assumed for these models are those of table 5.6 corresponding to ring coordinates of 0.4, 0.85 and 0.975 respectively. The multicell models contain between 16 and 36 cells, examples are shown in figure 5.15. The number of cells that can be included is currently limited by the implementation of the uniform stress boundary conditions, which results in high bandwidth system equations, and by the sparse solver which must operate within physical memory. To permit more cells to be included, the mesh used with the multicell models is the coarsest possible while still maintaining a reasonable approximation to the internal geometry. So that appropriate comparisons

roundness	E_1	ν_{12}	ν_{13}	E_2	ν_{23}	E_3	G_{23}	G_{31}	G_{12}	α_1^w	α_2^w	α_3^w
		GPa			GPa		GPa	GPa	GPa	GPa		
s1cell, RC = 0, $\rho = 0.3$ g/cc												
low	0.1774	1.439	0.4415	0.6101	0.4586	4.238	1.009	0.7233	0.04568	0.2188	0.08717	0.03731
medium	0.2308	1.280	0.3884	0.6855	0.4852	4.212	1.008	0.7463	0.06666	0.2246	0.08764	0.03857
high	0.2867	1.002	0.3135	0.5286	0.5819	3.977	0.8972	0.7993	0.1185	0.2221	0.08502	0.04442
s1cell, RC = 0.6, $\rho = 0.4$ g/cc												
low	0.4976	0.9695	0.4473	1.013	0.4530	5.624	1.252	1.091	0.09829	0.2043	0.1106	0.03692
medium	0.6414	0.8492	0.4151	1.128	0.4722	5.615	1.266	1.126	0.1403	0.2061	0.1129	0.03791
high	0.7813	0.6939	0.4126	0.9871	0.5298	5.466	1.230	1.164	0.2057	0.1925	0.1225	0.03917
s1cell, RC = 1, $\rho = 0.8$ g/cc												
low	3.053	0.4108	0.4441	3.232	0.4475	10.91	2.126	2.522	0.4659	0.2445	0.1968	0.03449
medium	3.466	0.4320	0.4154	3.162	0.4591	11.14	2.223	2.605	0.5971	0.2413	0.2036	0.03284
high	3.381	0.4529	0.4678	3.221	0.4376	11.06	2.447	2.466	0.6779	0.2088	0.2425	0.03248

Table 5.5.: Influence of internal roundness of effective properties of s1cell models.

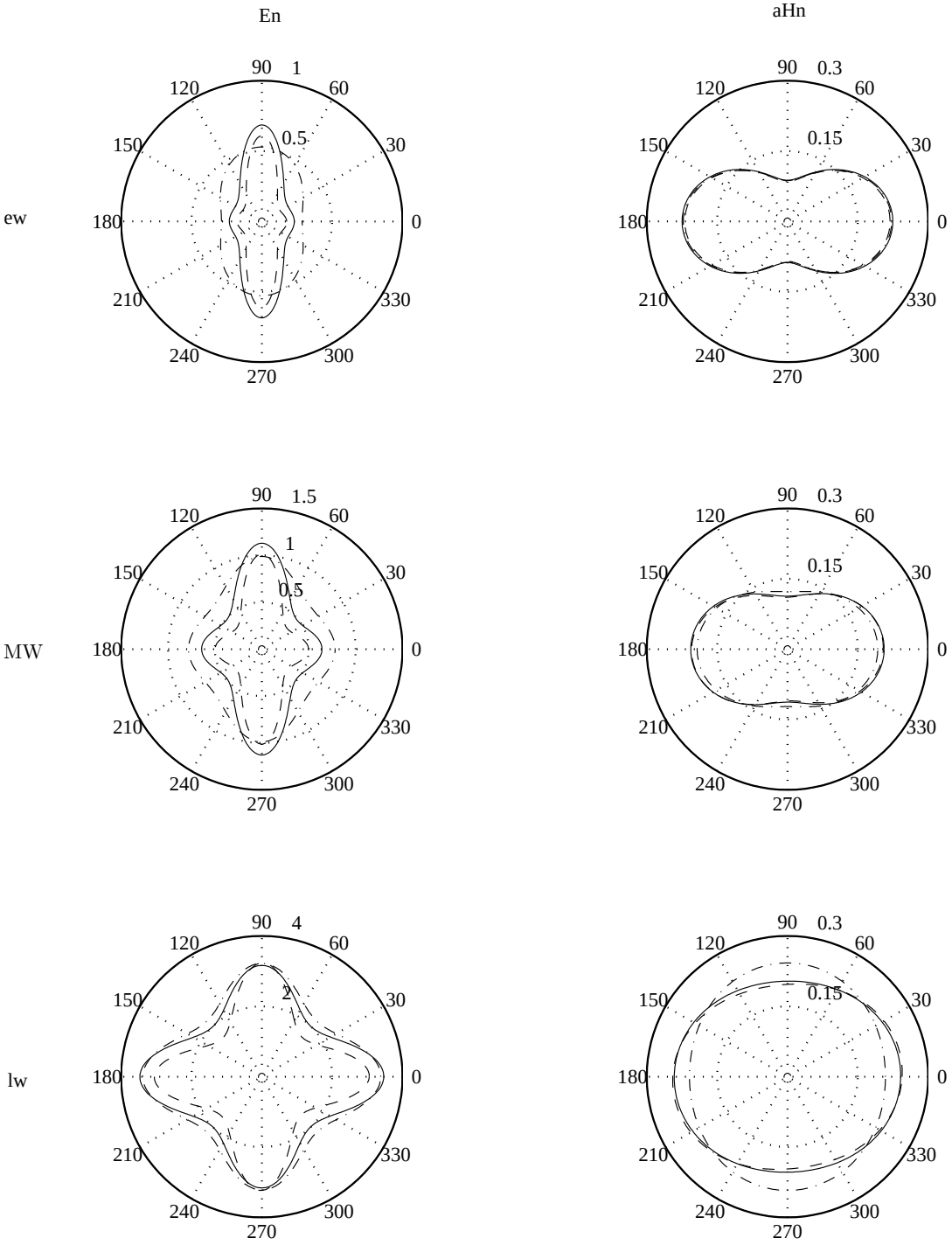

Figure 5.13.: Influence of internal geometry on the directional modulus and shrinkage coefficient in the transverse plane. – – low roundness, —— medium roundness, – · – high roundness.

ring coord.	0.1	0.4	0.7	0.85	0.925	0.975
density (g/cc)	0.38	0.42	0.47	0.52	0.59	0.68

Table 5.6.: Microdensities of growth ring zones.

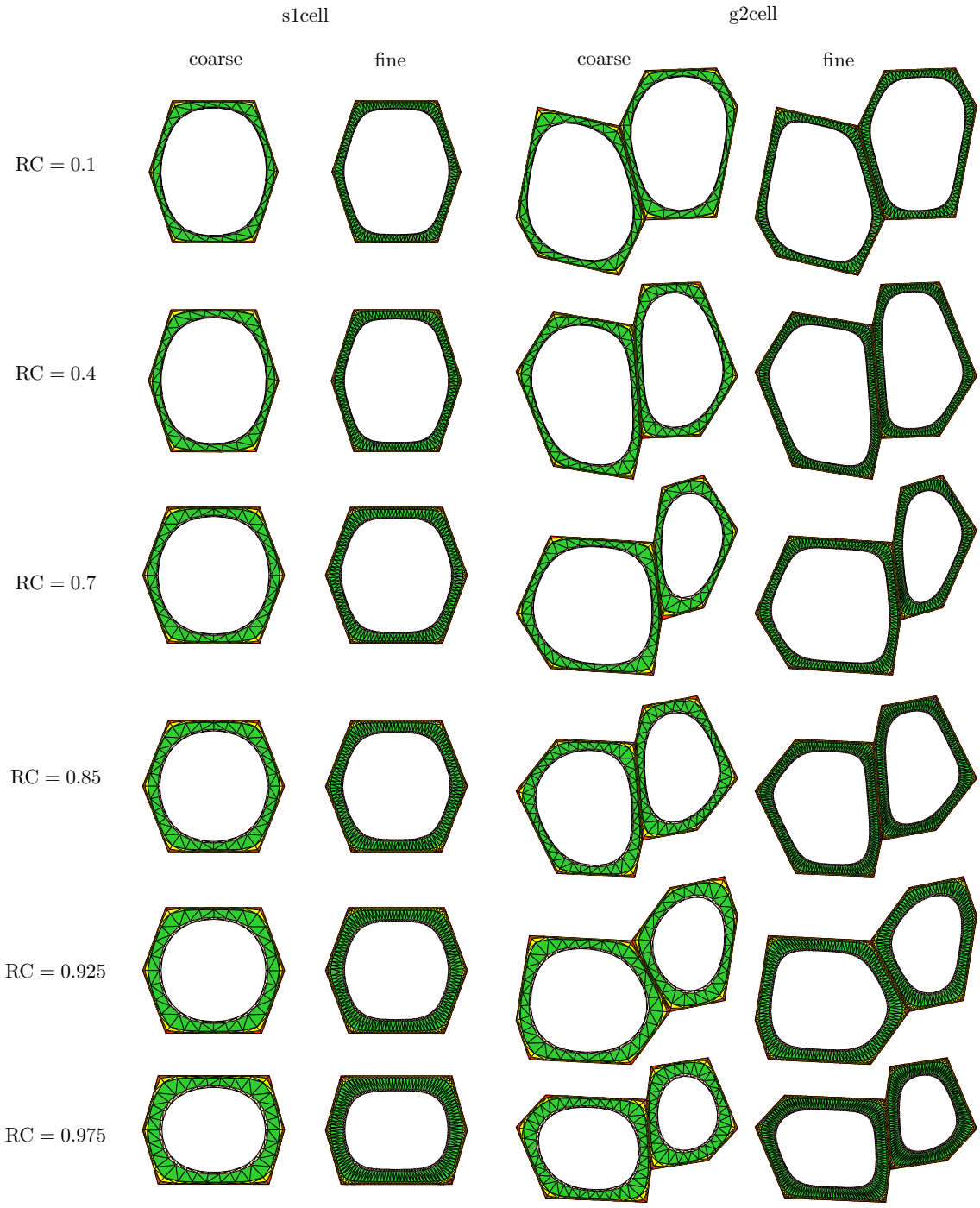

Figure 5.14.: s1cell and g2cell models. Not to scale.

between the idealized and real aggregate models can be made, both coarse and fine meshes of s1cell and g2cells models have been computed.

The effective properties computed appear in tables 5.7–5.11. Results have been calculated for 23 earlywood, 15 middlewood and 15 latewood aggregates, although only ten of each type are tabulated. The summaries presented include all results.

While the g2cell and multicell models are generally anisotropic, only the orthotropic elastic coefficients are tabulated. The other effective coefficients are non zero, but small. For example, for the multicell models the largest stiffness coeffcient not tabulated was less than 3% of the corresponding longitudinal stiffness.

The effective properties computed using uniform stress and uniform strain boundary condition, denoted σ and ϵ in tables 5.9–5.11, do not coincide. This is due to the limited number of cells contained within the these models. According to Vincent (1998), Wegst (1996) determined that 16 cells were sufficient to capture the behaviour. Stol (1996b) on the other hand concluded that at least 50 cells were required. Unfortunately, due to the size limits discussed above, the question of convergence of the effective properties determined using multicell models with stress and strain boundary conditions as the number of cells in these models is increased has not be able to be answered.

Longitudinal modulus E_3 is the hygro-elastic property least sensitive to transverse geometry. The specific longitudinal modulus for all s1cell, g2cell and multicell models is 13.5–14$\times 10^6$ m^2/s^2. As Navi (1988) pointed out this is considerably less than the 21.8$\times 10^6$ m^2/s^2 predicted using classical lamination theory (CLT) assuming the cell-wall cannot twist and somewhat greater than the 12.2$\times 10^6$ m^2/s^2 if twisting is entirely unrestrained. The other longitudinal properties – ν_{13}, ν_{23}, ν_{23}, G_{31}, α_3^w – do depend on the transverse geometry to a degree, the variation amongst all the models being 5–20%.

As expected, the transverse properties are highly dependent on the transverse geometry. In figure 5.16, the directional specific modulus and hygroexpansional coefficient are plotted for the coarse s1cell and g2cell models corresponding to ring coordinates of 0.4, 0.85 and 0.975 as well as the multicell models. These plots encapsulate all the transverse property data for these models. In going from earlywood to latewood the transverse elastic anisotropy, that is the ratio of maximum to minimum transverse modulus, is reduced from 2.0 to 1.4. Similarly the transverse hygroexpansional anisotropy reduces from 1.4 to 1.1.

Unexpectedly, the plots of figure 5.16 indicate that the s1cell rather than g2cell models give better estimates for the effective transverse properties, in the sense that they are more similar to those from the multicell models. These plots also indicate that the uniform strain rather than unifrom stress boundary conditions result in effective properties closer to those determined using periodic boundary conditions.

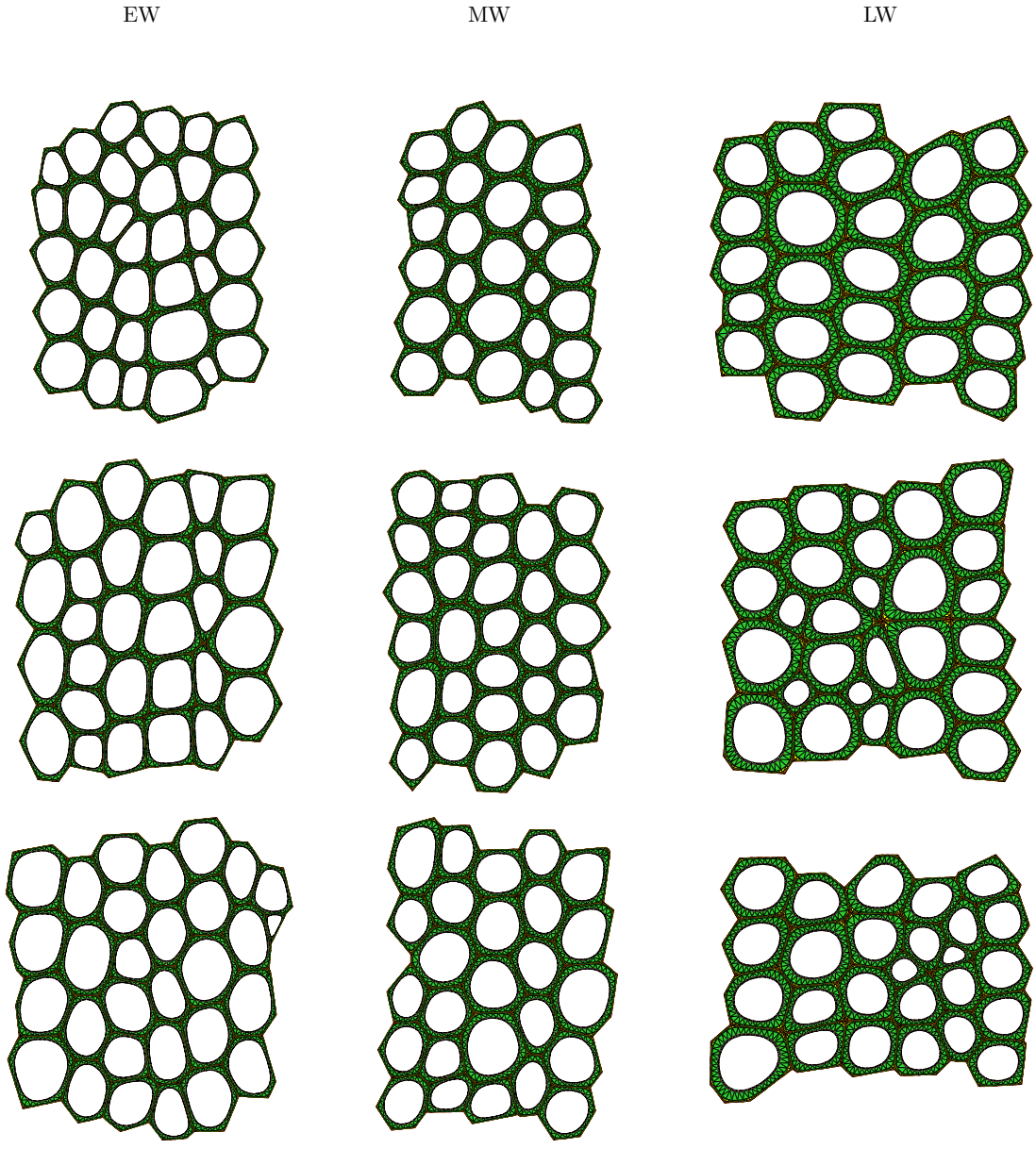

Figure 5.15.: Examples of multicell models. Not to scale.

		E_1 GPa	ν_{12}	ν_{13}	E_2 GPa	ν_{23}	E_3 GPa	G_{23} GPa	G_{31} GPa	G_{12} GPa	α_1^w	α_2^w	α_3^w	
RC = 0.1, $\rho = 0.38$ g/cc	s1c	0.4901	0.9584	0.3472	1.034	0.5111	5.163	1.213	0.9772	0.1798	0.2343	0.09749	0.04244
	s1f	0.4426	1.053	0.3859	1.122	0.4839	5.286	1.275	0.9666	0.1415	0.2308	0.1010	0.03907
	g2c	0.4384	0.9714	0.3613	1.043	0.4950	5.166	1.212	0.9505	0.1582	0.2239	0.1107	0.04169
	g2f	0.4032	1.045	0.3917	1.155	0.4753	5.273	1.312	0.9100	0.1289	0.2209	0.1105	0.03910
RC = 0.4, $\rho = 0.42$ g/cc	s1c	0.6300	0.8797	0.3545	1.247	0.5072	5.660	1.331	1.093	0.2206	0.2369	0.1044	0.04191
	s1f	0.5725	0.9610	0.3882	1.370	0.4806	5.789	1.392	1.077	0.1752	0.2350	0.1072	0.03885
	g2c	0.5226	0.9522	0.3662	1.405	0.4848	5.662	1.389	0.9924	0.1588	0.2437	0.1165	0.04115
	g2f	0.4915	0.9776	0.3920	1.591	0.4670	5.796	1.499	0.9280	0.1371	0.2427	0.1154	0.03851
RC = 0.7, $\rho = 0.47$ g/cc	s1c	1.049	0.6850	0.3965	1.452	0.4923	6.490	1.475	1.348	0.2794	0.2105	0.1272	0.04035
	s1f	0.9685	0.7397	0.4105	1.535	0.4720	6.592	1.499	1.351	0.2358	0.2129	0.1262	0.03821
	g2c	0.7837	0.7938	0.3426	1.582	0.4974	6.349	1.491	1.216	0.2058	0.2614	0.1224	0.04191
	g2f	0.7156	0.8037	0.3820	1.801	0.4679	6.554	1.575	1.187	0.1722	0.2566	0.1260	0.03839

Table 5.7.: Effective properties from s1cell and g2cell models. s1c, s1f, g2c and g2f refer to coarse and fine s1cell and g2cell models respectively.

	E_1 GPa	ν_{12}	ν_{13}	E_2 GPa	ν_{23}	E_3 GPa	G_{23} GPa	G_{31} GPa	G_{12} GPa	α_1^w	α_2^w	α_3^w	
RC = 0.85, $\rho = 0.52$ g/cc	s1c	1.335	0.6299	0.4098	1.661	0.4845	7.221	1.629	1.538	0.3507	0.2072	0.1420	0.03913
	s1f	1.253	0.6729	0.4168	1.734	0.4665	7.307	1.641	1.543	0.3049	0.2102	0.1395	0.03766
	g2c	0.9883	0.7515	0.3951	1.865	0.4711	7.114	1.700	1.374	0.3299	0.2369	0.1426	0.03988
	g2f	0.9334	0.7504	0.4108	2.040	0.4556	7.293	1.794	1.314	0.2793	0.2394	0.1410	0.03742
RC = 0.925, $\rho = 0.59$ g/cc	s1c	1.811	0.5607	0.4132	2.059	0.4774	8.190	1.827	1.781	0.4285	0.2133	0.1583	0.03808
	s1f	1.734	0.5873	0.4162	2.154	0.4638	8.279	1.819	1.806	0.3824	0.2181	0.1539	0.03679
	g2c	1.744	0.5579	0.4223	2.045	0.4636	8.119	1.816	1.736	0.3829	0.2151	0.1667	0.03831
	g2f	1.662	0.5761	0.4248	2.129	0.4532	8.253	1.854	1.728	0.3448	0.2147	0.1643	0.03670
RC = 0.975, $\rho = 0.68$ g/cc	s1c	2.799	0.4345	0.4200	2.547	0.4699	9.320	1.970	2.140	0.4799	0.2136	0.1894	0.03687
	s1f	2.755	0.4386	0.4136	2.602	0.4658	9.465	1.905	2.228	0.4341	0.2220	0.1790	0.03548
	g2c	2.456	0.4760	0.4174	2.660	0.4595	9.230	2.025	2.030	0.4627	0.2268	0.1902	0.03710
	g2f	2.358	0.4643	0.4208	2.753	0.4465	9.433	2.039	2.034	0.4028	0.2320	0.1870	0.03532

Table 5.8.: Effective properties from s1cell and g2cell models. s1c, s1f, g2c and g2f refer to coarse and fine s1cell and g2cell models respectively.

	N_c	BCs	E_1 GPa	ν_{12}	ν_{13}	E_2 GPa	ν_{23}	E_3 GPa	G_{23} GPa	G_{31} GPa	G_{12} GPa	α_1^w	α_2^w	α_3^w
ew1a	29	σ	0.4057	0.9723	0.4074	0.8236	0.4650	5.625	1.271	1.047	0.09830	0.1942	0.1415	0.04203
		ϵ	0.9955	0.6026	0.4346	1.502	0.4563	5.661	1.311	1.089	0.2722	0.1818	0.1417	0.04113
ew1d	25	σ	0.3190	1.008	0.3726	0.8303	0.4768	5.608	1.276	1.023	0.1071	0.2167	0.1320	0.04255
		ϵ	0.9666	0.6243	0.4292	1.530	0.4616	5.668	1.320	1.084	0.2780	0.1893	0.1367	0.04099
ew2a	26	σ	0.3296	1.001	0.3980	0.7308	0.4620	5.610	1.245	1.062	0.1166	0.2025	0.1404	0.04258
		ϵ	0.9796	0.6237	0.4352	1.410	0.4571	5.666	1.292	1.117	0.2783	0.1779	0.1438	0.04114
ew2c	28	σ	0.3457	0.9936	0.4131	0.6058	0.4654	5.621	1.266	1.042	0.1076	0.1880	0.1450	0.04208
		ϵ	0.8974	0.6670	0.4394	1.402	0.4547	5.661	1.308	1.089	0.2989	0.1769	0.1444	0.04105
ew2d	30	σ	0.3334	1.048	0.4041	0.6781	0.4708	5.620	1.268	1.039	0.1043	0.1961	0.1391	0.04211
		ϵ	0.8681	0.6872	0.4389	1.375	0.4553	5.663	1.314	1.086	0.2967	0.1790	0.1428	0.04103
ew3a	27	σ	0.3170	1.073	0.3989	0.6395	0.4804	5.674	1.278	1.075	0.1184	0.2004	0.1312	0.04122
		ϵ	0.9419	0.6457	0.4334	1.394	0.4619	5.706	1.321	1.119	0.3302	0.1827	0.1365	0.04047
ew3d	30	σ	0.3736	1.020	0.3938	0.7141	0.4823	5.675	1.293	1.072	0.1261	0.1993	0.1304	0.04122
		ϵ	0.9075	0.6712	0.4302	1.404	0.4641	5.704	1.328	1.111	0.3072	0.1831	0.1363	0.04052
ew4a	29	σ	0.5912	0.7166	0.4244	0.6502	0.4607	5.668	1.205	1.151	0.09376	0.1774	0.1474	0.04145
		ϵ	1.151	0.5388	0.4360	1.356	0.4601	5.699	1.247	1.187	0.2817	0.1698	0.1461	0.04074
ew4d	36	σ	0.3894	0.9180	0.4059	0.6363	0.4704	5.648	1.249	1.086	0.1121	0.1959	0.1381	0.04174
		ϵ	0.9757	0.6269	0.4330	1.365	0.4609	5.683	1.293	1.127	0.3095	0.1778	0.1420	0.04084
ew5b	29	σ	0.2348	1.227	0.3685	0.6476	0.4840	5.615	1.280	1.013	0.1048	0.2224	0.1272	0.04239
		ϵ	0.8749	0.6865	0.4314	1.403	0.4611	5.671	1.331	1.075	0.3258	0.1875	0.1372	0.04095
min			0.2348	0.5388	0.3685	0.5665	0.4536	5.605	1.205	0.9964	0.08642	0.1698	0.1270	0.04047
mean			0.6545	0.8205	0.4179	1.048	0.4645	5.654	1.287	1.078	0.2083	0.1889	0.1400	0.04141
max			1.151	1.227	0.4407	1.574	0.4840	5.706	1.356	1.187	0.3733	0.2224	0.1474	0.04258
% rnge			140.0	83.82	17.26	96.12	6.548	1.779	11.73	17.72	137.7	27.81	14.60	5.093
s1cell			0.6300	0.8797	0.3545	1.247	0.5072	5.660	1.331	1.093	0.2206	0.2369	0.1044	0.04191
g2cell			0.5226	0.9522	0.3662	1.405	0.4848	5.662	1.389	0.9924	0.1588	0.2437	0.1165	0.04115

Table 5.9.: Effective properties for earlywood tracheid aggregates. $\rho = 0.41$ g/cc.

	N_c	BCs	E_1 GPa	ν_{12}	ν_{13}	E_2 GPa	ν_{23}	E_3 GPa	G_{23} GPa	G_{31} GPa	G_{12} GPa	α_1^w	α_2^w	α_3^w
mw1a	27	σ	0.8513	0.7561	0.4235	1.192	0.4641	7.175	1.589	1.461	0.2076	0.2028	0.1562	0.03947
		ϵ	1.632	0.5157	0.4393	1.937	0.4566	7.206	1.638	1.511	0.4479	0.1900	0.1593	0.03892
mw1b	29	σ	0.8681	0.7604	0.4287	1.182	0.4575	7.159	1.578	1.471	0.2059	0.1954	0.1623	0.03971
		ϵ	1.640	0.5134	0.4427	1.907	0.4528	7.184	1.623	1.515	0.4446	0.1859	0.1635	0.03924
mw1c	26	σ	0.7651	0.7877	0.4188	1.078	0.4625	7.160	1.595	1.451	0.2271	0.2035	0.1589	0.03978
		ϵ	1.468	0.5687	0.4348	1.843	0.4588	7.194	1.645	1.498	0.4814	0.1940	0.1580	0.03912
mw2b	27	σ	0.6398	0.8694	0.4150	1.022	0.4620	7.125	1.596	1.417	0.2475	0.2045	0.1591	0.04015
		ϵ	1.477	0.5714	0.4407	1.848	0.4534	7.168	1.646	1.479	0.5147	0.1895	0.1618	0.03929
mw2d	31	σ	0.7352	0.8042	0.4203	1.092	0.4587	7.137	1.594	1.430	0.2285	0.2018	0.1614	0.03995
		ϵ	1.446	0.5796	0.4427	1.774	0.4525	7.173	1.641	1.483	0.4909	0.1895	0.1622	0.03922
mw3d	25	σ	0.7073	0.8161	0.4074	0.9516	0.4716	7.142	1.575	1.456	0.2512	0.2029	0.1576	0.03995
		ϵ	1.488	0.5682	0.4287	1.792	0.4635	7.176	1.625	1.511	0.5243	0.1940	0.1569	0.03928
mw4a	33	σ	0.8986	0.7328	0.4344	1.116	0.4578	7.180	1.596	1.465	0.2136	0.1941	0.1615	0.03938
		ϵ	1.557	0.5403	0.4403	1.887	0.4556	7.203	1.639	1.507	0.4579	0.1886	0.1604	0.03898
mw4b	30	σ	0.7953	0.7821	0.4254	1.090	0.4601	7.162	1.582	1.469	0.2248	0.1954	0.1638	0.03970
		ϵ	1.566	0.5380	0.4413	1.838	0.4547	7.193	1.628	1.517	0.4674	0.1865	0.1630	0.03910
mw5a	26	σ	0.8515	0.7365	0.4298	0.9344	0.4580	7.172	1.554	1.505	0.2234	0.1905	0.1656	0.03959
		ϵ	1.517	0.5546	0.4410	1.665	0.4539	7.195	1.600	1.545	0.4981	0.1815	0.1680	0.03918
mw5d	29	σ	0.8291	0.7065	0.4335	0.8550	0.4499	7.158	1.543	1.492	0.2249	0.1855	0.1741	0.03979
		ϵ	1.591	0.5256	0.4411	1.732	0.4529	7.188	1.596	1.543	0.5005	0.1812	0.1697	0.03919
min			0.6040	0.4993	0.3978	0.8431	0.4499	7.123	1.538	1.390	0.2059	0.1812	0.1401	0.03879
mean			1.139	0.6770	0.4295	1.428	0.4591	7.173	1.609	1.481	0.3619	0.1949	0.1609	0.03945
max			1.663	0.9709	0.4428	1.943	0.4818	7.214	1.709	1.547	0.5557	0.2249	0.1741	0.04024
% rnge			92.99	69.65	10.48	77.00	6.949	1.271	10.64	10.54	96.65	22.44	21.12	3.680
s1cell			1.335	0.6299	0.4098	1.661	0.4845	7.221	1.629	1.538	0.3507	0.2072	0.1420	0.03913
g2cell			0.9883	0.7515	0.3951	1.865	0.4711	7.114	1.700	1.374	0.3299	0.2369	0.1426	0.03988

Table 5.10.: Effective properties for middlewood tracheid aggregates. $\rho = 0.52$ g/cc.

	N_c	BCs	E_1 GPa	ν_{12}	ν_{13}	E_2 GPa	ν_{23}	E_3 GPa	G_{23} GPa	G_{31} GPa	G_{12} GPa	α_1^w	α_2^w	α_3^w
lw1b	25	σ	1.722	0.6094	0.4328	1.806	0.4469	9.300	2.001	2.026	0.4088	0.2097	0.2036	0.03697
		ϵ	2.765	0.4368	0.4444	2.653	0.4445	9.328	2.055	2.084	0.6821	0.2001	0.2029	0.03652
lw1c	24	σ	2.300	0.4808	0.4480	1.707	0.4339	9.281	1.919	2.108	0.3838	0.1885	0.2249	0.03731
		ϵ	3.063	0.3890	0.4442	2.597	0.4441	9.309	1.970	2.157	0.6023	0.1897	0.2145	0.03687
lw2a	29	σ	1.768	0.5725	0.4474	1.553	0.4308	9.284	1.960	2.053	0.4385	0.1944	0.2200	0.03712
		ϵ	2.731	0.4443	0.4478	2.473	0.4402	9.319	2.015	2.110	0.7277	0.1943	0.2097	0.03655
lw3b	26	σ	1.824	0.5824	0.4384	1.750	0.4430	9.269	2.007	2.000	0.4220	0.2064	0.2061	0.03699
		ϵ	2.648	0.4561	0.4391	2.667	0.4485	9.296	2.059	2.053	0.6725	0.2060	0.1990	0.03657
lw4a	26	σ	2.037	0.5309	0.4382	1.742	0.4400	9.249	1.947	2.048	0.3845	0.2007	0.2134	0.03756
		ϵ	2.874	0.4141	0.4387	2.683	0.4458	9.275	2.003	2.100	0.6800	0.1981	0.2076	0.03714
lw4b	28	σ	1.849	0.5796	0.4381	1.833	0.4431	9.267	1.980	2.039	0.4418	0.2064	0.2066	0.03728
		ϵ	2.720	0.4457	0.4430	2.560	0.4447	9.295	2.028	2.085	0.6632	0.1983	0.2051	0.03684
lw4c	23	σ	1.937	0.5349	0.4391	1.609	0.4297	9.176	1.928	2.019	0.4162	0.2015	0.2165	0.03816
		ϵ	2.702	0.4445	0.4401	2.552	0.4423	9.218	1.989	2.074	0.6775	0.1983	0.2092	0.03740
lw5b	28	σ	2.051	0.5053	0.4548	1.458	0.4203	9.246	1.918	2.071	0.4141	0.1847	0.2322	0.03758
		ϵ	2.816	0.4279	0.4470	2.477	0.4392	9.282	1.978	2.128	0.6824	0.1896	0.2155	0.03694
lw5c	25	σ	2.148	0.4930	0.4527	1.545	0.4256	9.260	1.911	2.087	0.4032	0.1869	0.2292	0.03734
		ϵ	2.836	0.4262	0.4454	2.464	0.4417	9.294	1.971	2.139	0.6679	0.1901	0.2148	0.03678
lw5d	25	σ	1.813	0.5741	0.4519	1.563	0.4285	9.301	1.982	2.053	0.4580	0.1960	0.2175	0.03698
		ϵ	2.588	0.4741	0.4501	2.424	0.4391	9.331	2.035	2.106	0.7340	0.1941	0.2087	0.03645
min			1.667	0.3795	0.4328	1.399	0.4203	9.176	1.909	1.976	0.3415	0.1847	0.1990	0.03644
mean			2.375	0.4892	0.4448	2.119	0.4382	9.285	1.984	2.080	0.5494	0.1961	0.2132	0.03703
max			3.074	0.6094	0.4549	3.071	0.4485	9.334	2.066	2.178	0.7866	0.2097	0.2322	0.03816
% rnge			59.26	47.00	4.968	78.90	6.422	1.693	7.926	9.684	81.01	12.74	15.54	4.629
s1cell			2.799	0.4345	0.4200	2.547	0.4699	9.320	1.970	2.140	0.4799	0.2136	0.1894	0.03687
g2cell			2.456	0.4760	0.4174	2.660	0.4595	9.230	2.025	2.030	0.4627	0.2268	0.1902	0.03710

Table 5.11.: Effective properties for latewood tracheid aggregates. $\rho = 0.68$ g/cc.

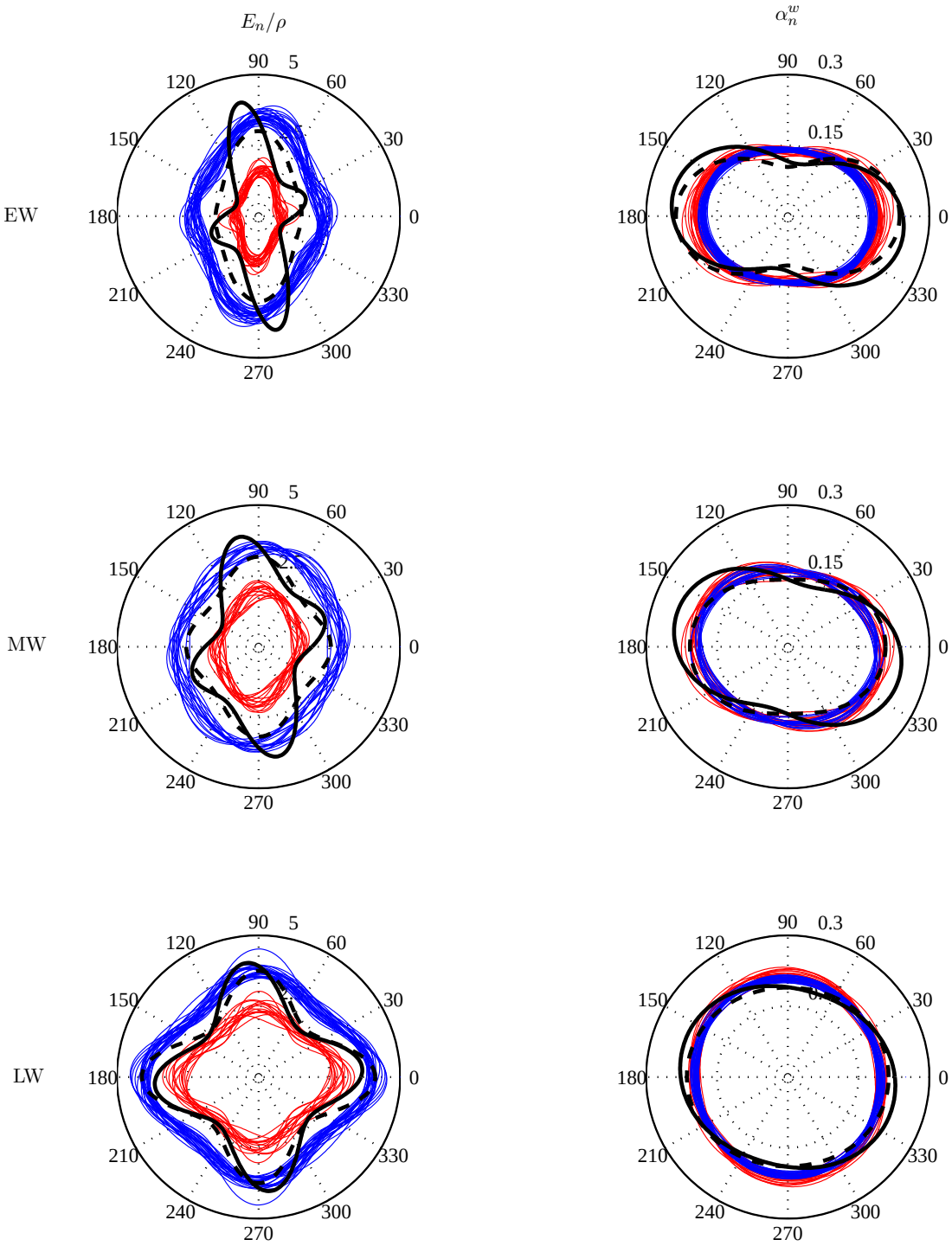

Figure 5.16.: Directional specific modulus and shrinkage coefficient in the transverse plane. Thin lines are for multicell models. Thick dashed line is for the s1cell model and thick solid line is for the g2cell model.

5.7. Summary, discussion and future work

In this chapter, models that incorporate the transverse internal and external geometries as well as the arrangement of tracheids have been developed. Effective properties for idealized and actual transverse tracheid geometries corresponding to various intraring positions have been presented and the results discussed.

A number of structural features have been neglected and assumptions made in the development of the models presented. The most significant of these are the omission of the pits, the neglection of circumferential and longitudinal variation in cell-wall properties and the assumption that the cells are prismatic. In appendix H a highly simplified model of a bordered pit is analyzed and it is concluded that the pits could significantly lower the longitudinal modulus of radial cell-walls. In appendix I, the stiffening effect of tracheid tips on the transverse modulus is estimated and found to be no greater than 7% and probably much less. While longitudinal variation is not explicitly included, the layer smearing process introduced in the preceding chapter implicitly accounts for longitudinal variation in microfibril orientation, and having a variety of cell shapes in a cross section is equivalent to including longitudinal variation in transverse tracheid shape.

In the future, these models could be used to investigate a number of problems in wood technology. For example, how does varying the relative proportions of the secondary wall layer affect the transverse properties, in particular the degree to which cell-wall swelling is accommodated internally and externally?

Future developments to the cellular models could include:

- allowing for different properties and microfibril orientations in radial and tangential walls.
- incorporating the effects of pitting by either using appropriate effective properties within radial cell walls, or by explicitly including a single pit per radial wall in a three dimensional model.
- explicitly treating severe compression wood, including the more rounded transverse tracheid shapes, intercellular spaces and helical cavities as well as the ultrastructural differences in topochemistry.
- allowing for differences in cell wall ultrastructure in different cells.
- computing the properties per element rather than assuming the wall to be layered. This would allow for better representations of the variation in composition and orientation but would require considerably more data, much of which is not currently available.

- removing the prismatic assumption and including rays at a cellular scale. Finding a suitable way to characterise the geometry is the major challenge to doing this.

Chapter 6

Tracheid wall layer solid volume fractions

Solid volume fractions are used in 5 to describe relative proportions of the ML, S1, S2 and S3 layers withn the cell-wall. In this chapter data from the literature are examined and used to relate the total solid volume fraction, itself related to wood microdensity, to the layer solid volume fractions. Such a model is useful in the absence of more specific data.

6.1. Existing data on layer proportions

Measurements of the cell-wall layer proportions have been reported by a number of authors including Wardrop (1957a); Meier and Wilkie (1959); Meier (1961); Stamm and Sanders (1966); Mark (1967); Saiki (1970); Fengel and Stoll (1973); Siddiqui (1976); Boyd (1977b); Saka and Thomas (1982); Grozdits and Ifju (1984). As far as can be ascertained no direct measurements of tracheid cell-wall layer volume fractions have been made. Instead layer thicknesses or area fractions are measured. Usually these measurements are made directly on transverse micrographs although optical birefringence has also been exploited (Page and El-Hosseiny, 1974).

Layer areas have been determined either by direct measurement (planimeter, cutout weighing, grid counting, digital image analysis) or indirectly by combining measurements of layer thickness and perimeters (McIntosh, 1965).

Table 6.1 summarizes ranges for the layer thicknesses, relative thicknesses, solid and total volume fractions reported by:

- Mark (1965) for eastern redcedar,
- Fengel (1969); Fengel and Stoll (1973) for spruce,
- Saiki (1970) for akamatsu, sugi, hinoki, karamatsu and konotegashiwa,
- Saka and Thomas (1982) for loblolly pine,
- Siddiqui (1976) for Douglas fir and redpine,
- and Grozdits and Ifju (1984) for eastern hemlock.

	ML	S1	S2	S3
absolute thickness (μm)	0.03–1.50	0.10–1.05	0.60–10.6	0–0.40
relative thickness	0.01–0.27	0.02–0.22	0.52–0.94	0–0.12
solid volume fraction	0.01–0.18	0.04–0.27	0.51–0.95	0–0.14
total volume fraction	0.01–0.11	0.02–0.20	0.08–0.62	0.03–0.10

Table 6.1.: Summary of data on tracheid cell-wall layer proportions.

The tabulated ML thickness is that associated with a single cell, i.e. half the total ML thickness.

The results of these studies indicate that:

(i) layer thicknesses vary significantly between species (Saiki, 1970; Boyd, 1977b),

(ii) layer thicknesses vary with wood density and position in growth ring, in particular they are different in earlywood and latewood (Saiki, 1970; Fengel, 1969; Fengel and Stoll, 1973; Grozdits and Ifju, 1984),

(iii) layer thicknesses vary between neighbouring tracheids, in particular Singh and Booker (2000) found the S3 thickness in neighbouring radiata pine tracheids could differ by as much as a factor of 5 from 0.06 to 0.3 μm,

(iv) within a single tracheid the wall and wall layer thicknesss vary circumferentially, with the radial walls and wall layers being thinner than their tangential counterparts in earlywood and vice versa in latewood (Saiki, 1970),

(v) within a single tracheid the wall and wall layer thicknesses vary longitudinally; in particular the S2 layer in the radial wall is thicker in the middle of the cell than it is towards the ends of the cell (Wardrop and Dadswell, 1953; Okumura et al., 1974, 1976),

(vi) in compression wood S1 and S2 are thicker than in normal wood, while S3 is reduced or absent (Fujita et al., 1978; Timell, 1986a)

(vii) relative layer thicknesses, as well as the absolute thicknesses, vary with moisture content (Fengel and Stoll, 1973). In particular S3 may swell to a greater extent than the other layers. This may be attributed to compositional differences as well as lesser restraint to swelling.

In figure 6.1 layer thicknesses are plotted against total wall thickness. It is immediately apparent that the S2 layer thickness is highly correlated with total wall thickness. The thickness of the other layers also appear to be positively correlated to total wall thickness, but not as strongly.

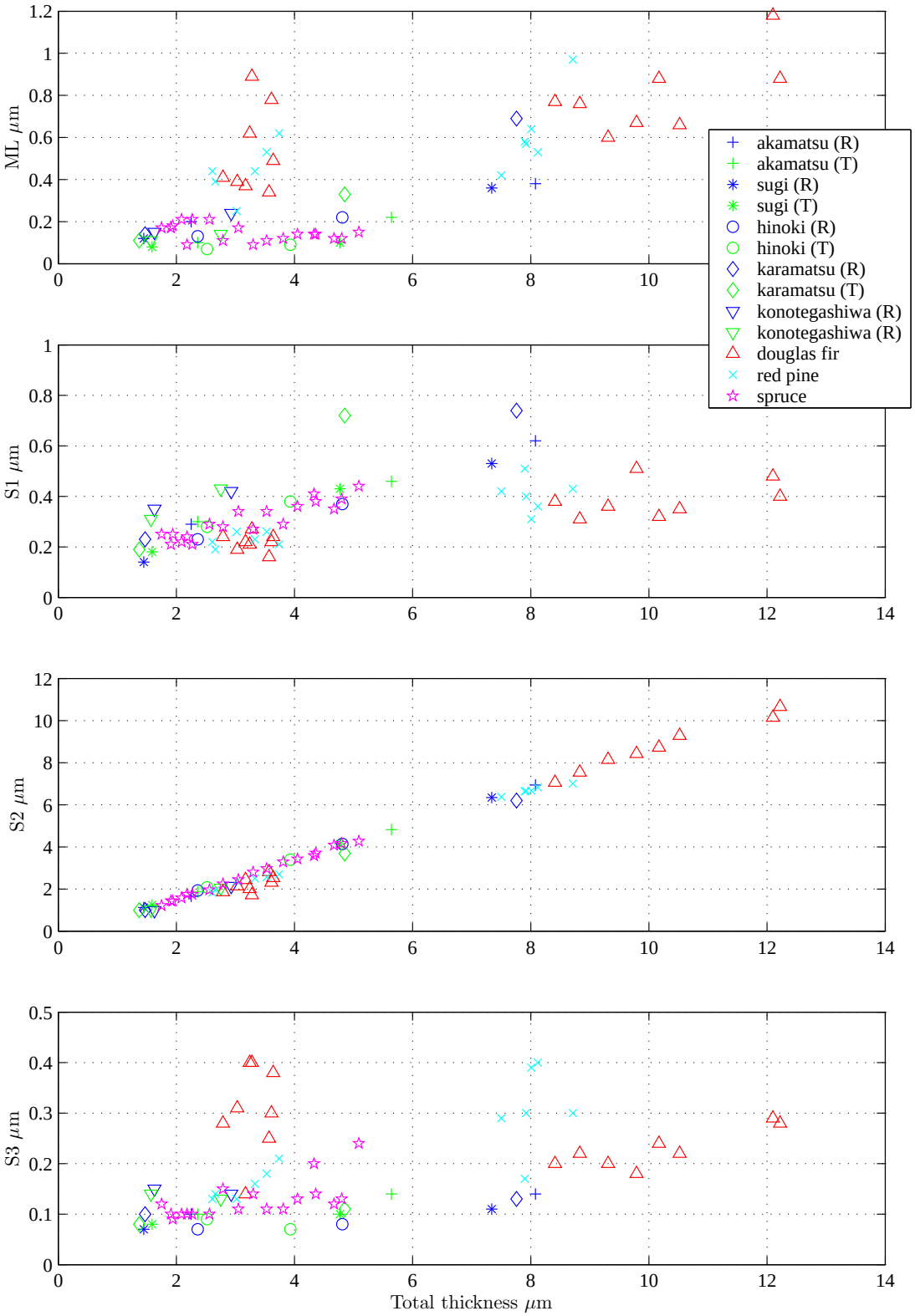

Figure 6.1.: Tracheid cell-wall layer thicknesses plotted against total thickness. Data taken from Saiki (1970), Fengel and Stoll (1973) and Siddiqui (1976) for a variety of softwoods. In the legend (R) and (T) refer to measurements made on radial and tangential walls respectively.

6.2. A model for layer solid volume fractions

A linear model is proposed for the relationship between total solid volume fraction $\hat{v}$ and the layer solid volume fractions $\hat{v}|^l$, i.e.

$$\hat{v}|^l = a_1|^l \hat{v} + a_0|^l. \tag{6.1}$$

Since the layer total volume fractions $v|^l$ are related to the layer solid volume fractions by $v|^l = \hat{v}\hat{v}|^l$ (6.1) gives a quadratic relationship

$$v|^l = a_1|^l \hat{v}^2 + a_0|^l \hat{v} \tag{6.2}$$

between the layer total volume fractions and the total solid volume fraction.

The total volume fraction is related to the cellular density (microdensity) ρ^* and the cell wall layer densities $\rho|^l$ by

$$\rho^* = \hat{v} \sum_l \hat{v}|^l \rho|^l \tag{6.3}$$

and if (6.1) holds then

$$\hat{v}^2 \sum_l a_1|^l \rho|^l + \hat{v} \sum_l a_0|^l \rho|^l - \rho^* = 0. \tag{6.4}$$

Of the studies mentioned both those of Fengel and Stoll (1973) and Grozdits and Ifju (1984) provide sufficient measurements to be able to relate the layer solid volume fractions to cellular solid volume fraction. These datasets and best fit lines, determined using a least-square procedure, are plotted in figure 6.2. Regression parameters and coefficients of determination (r^2) appear in table 6.2.

	Fengel and Stoll (1973)			Grozdits and Ifju (1984)		
layer	a_1	a_0	r^2	a_1	a_0	r^2
CML	-0.0910	0.1147	0.66	-0.0055	0.0831	0.01
S1	-0.0153	0.1242	0.07	-0.0372	0.1675	0.09
S2	0.1462	0.7045	0.62	0.2406	0.5356	0.44
S3	-0.0399	0.0567	0.67	-0.1978	0.2138	0.41

Table 6.2.: Parameters for the layer solid volume fraction model.

While the r^2 values for the proposed linear model indicate that total solid volume fraction can account for only a fraction of the observed variation in the layer solid volume fractions, particularly in the case of the S1 layer, these models do capture the overall trends.

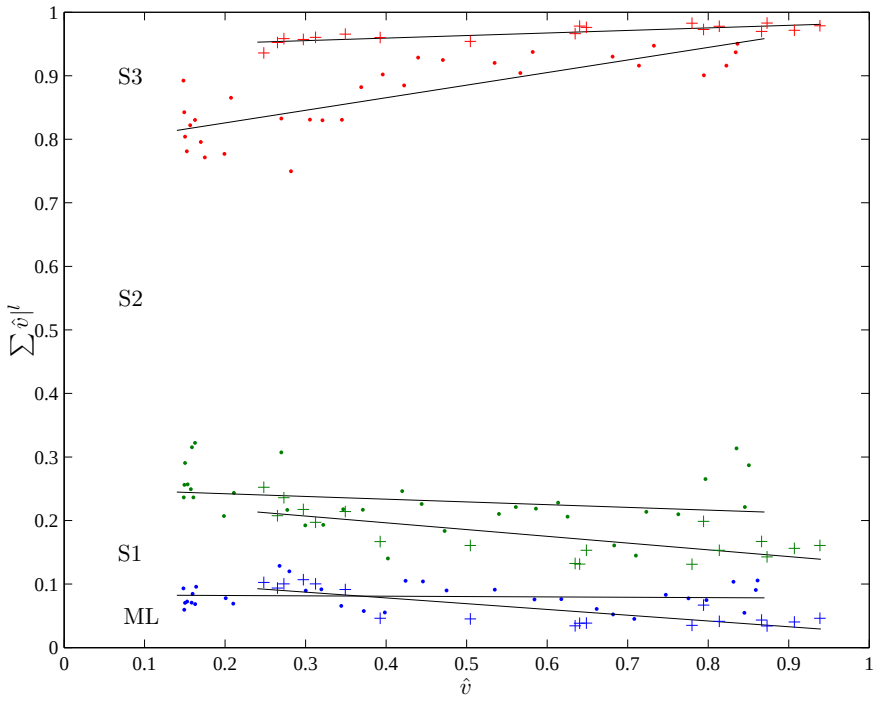

Figure 6.2.: Cumulative layer volume fractions plotted against total solid volume fractition. · Grozdits and Ifju (1984), + Fengel and Stoll (1973). Regression lines are those of table 6.2.

6.3. Dependence on moisture content

The heterogeneous composition of the cell-wall gives rise to heterogeneous expansional strains on the addition or removal of moisture even in the abscence of a macroscopic moisture gradient. Thus the layer volume fractions will change with moisture content, as was observed by Fengel and Stoll (1973).

Because of a lack of data, the present model does not directly include the influence of moisture content. However, moisture content does have an indirect influence on the layer volume fractions by way of the moist cellular ρ^* and layer densities $\rho|^l$. Moist cellular density is presumed to be an exogenous variable, that is to say it is expected that it will be prescribed. The layer densities on the other hand are endogenous variables and, within the current sequence of models, are influenced by the nanophase densities, hygroscopities and volume fractions within each of the cell wall layers. In figure 6.3 the variation in layer volume fractions predicted by the current set of models for a cellular domain having a dry density of 0.4 g/cc are plotted against moisture content. The regressions against the data of Grozdits and Ifju (1984) have been used in computing these results. It is unlikely that the layer density predictions are sufficiently accurate to provide good estimates for the variation in layer volume fractions with moisture content. This claim is supported by the fact that Fengel and Stoll (1973) found the solid volume fraction of the S3 layer to increase with increasing moisture content whereas the current

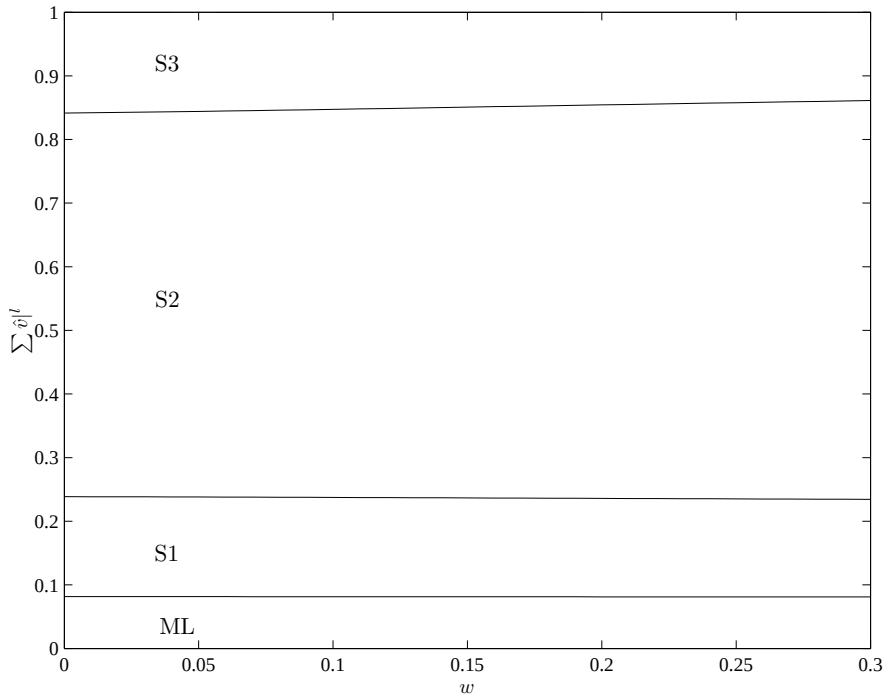

Figure 6.3.: Variation in layer solid volume fractions with moisture content according to the current set of models.

model predicts the opposite.

6.4. Future work

If this work is to be taken further a great deal more data is required. This data should:

- be for a specific species, since the layer proportions have been shown to differ between species,
- retain individual cell measurements so that variation between cells can be investigated,
- include measurements of:
  - microdensity (by either gravitometric or densitometric methods),
  - total solid volume fraction (by image analysis),
  - layer area fractions in TR sections,
  - layer thicknesses at a number of circumferential and axial points and on RL and TL as well as TR sections,
  - cell diameters and shapes,

- note the position within the growth ring and stem of each measurement made, so that spatially and temporally based models for layer volume fractions could be investigated,
- be made on samples at least 3 different moisture contents and the layer volume fractions in these samples should be representative of those in-situ.

As well as being useful in developing the layer volume fraction model the data described above could also be used to validate the internal growth model of chapter 5 and to investigate the differences between direct measurements of cell-wall density and the apparent cell-wall density determined from microdensity and cell-wall volume from image analysis.

Chapter 7

Nanophase volume fractions

7.1. Introduction

The nanostructural models of chapter 3 require nanophase volume fractions as input. These nanophase volume fractions cannot be obtained directly as imaging protocols with sufficient resolution and contrast do not currently exist. Even if such protocols did exist, the variability of the nanophase volume fractions within wood tissue and with moisture content would make their usage prohibitively expensive.

As an alternative to direct measurement, the nanophase volume fractions can be computed from the dry mass fractions, hygroscopicities and densities of the nanophases and the overall moisture content (see §7.5).

The nanophase hygroscopicites and densities are discussed in chapter 8. Obtaining estimates for the dry nanophase mass fractions within any nanoscopic domain is the main subject of this chapter.

7.2. Softwood composition

The principal chemical constituents of the wood cell-wall are celluloses, hemicelluloses (in softwoods principally glucomannans, xylans, galactoglucomannans and galactans) and lignins. Descriptions of these constituents can be found in appendix D.

Overall, softwoods consist of 30–60% cellulose, 17–40% hemicellulose and 19–40% lignin by weight (Timell, 1986a; Sjöström, 1981; Sjöstrøm and Alén, 1999; Fengel and Wegener, 1984; Saka, 1990; Easty and Thompson, 1991; Uprichard, 1991). These compostional ranges are broad. In part, this is due to the constituents being classes of compounds rather than specific substances. Also, summative chemical analysis of wood is a complex undertaking and different analytic techniques yield different results (Tsoumis, 1991). These factors aside, wood composition is inherently variable. Variation in the composition occurs:

- across the cell-wall (Sachs et al., 1963; Fengel, 1969; Fengel and Stoll, 1978; Kibblewhite and Brookes, 1976; Parameswaran and Liese, 1982; Sovari et al., 1983; Takabe et al., 1983, 1989; Meier, 1985; Westermark et al., 1986, 1988; Donaldson,

1987, 1991a; Donaldson et al., 1999; Northcote et al., 1989; Daniel et al., 1991; Downes et al., 1991; Terashima et al., 1993; Baba et al., 1994; Maeda et al., 2000),

- around the cell-wall (particularly between radial and tangential walls) (Preston, 1974),
- between cell types (Hoffmann and Timell, 1972),
- across growth rings (Wilson and Wellwood, 1965; Wellwood et al., 1965; Larson, 1966; Siddiqui, 1976; Sjöström, 1981),
- between normal and compression wood (Watson and Dadswell, 1957; Timell, 1982, 1986a),
- within a stem (in particular between corewood and outerwood) (Larson, 1966; Sjöström, 1981; Zobel and Sprague, 1998),
- between trees,
- and between species (Kollmann and Côté, 1968; Fengel and Grosser, 1975; Sjöström, 1981).

Of these variations the most substantial is that occurring across the cell-wall.

7.3. Dry HS and LM phase mass fractions from dry CF mass fraction

According to Saka (1990), Whiting and Goring analyzed tissue fractions taken from black spruce (*Picea mariana* Mill.) tracheids. They found an approximately linear relationship between the concentration of lignin in the various fractions and the concentration of cellulose, glucomannan, glucuronoarabinoxylan, galactan and arabinan. Byrd et al. (1965) also detected a linear relationship between the constituent fractions of loblolly pine, but concluded that the correlation was too weak to permit the fraction of one to be determined from the fraction of another.

Inspired by Whiting and Goring's results, compositional data for various softwoods and softwood fractions – including normal wood, compression wood, earlywood, latewood and tissue from the cell-wall layers – has been compiled from various sources (Meier, 1961; Timell, 1967, 1982, 1986a,b; Sjöström, 1981; Sjöstrøm and Alén, 1999; Fengel and Wegener, 1984; Saka, 1990; Easty and Thompson, 1991; Uprichard, 1991). This data is plotted in figure 7.1. Note that rather than using lignin content for the independent variable, as Whiting and Goring did, the cellulose content has been used. The amount of cellulose present is particularly important as it is the most prevalent constituent and controls the stiffness in the MF direction, thus it is convenient

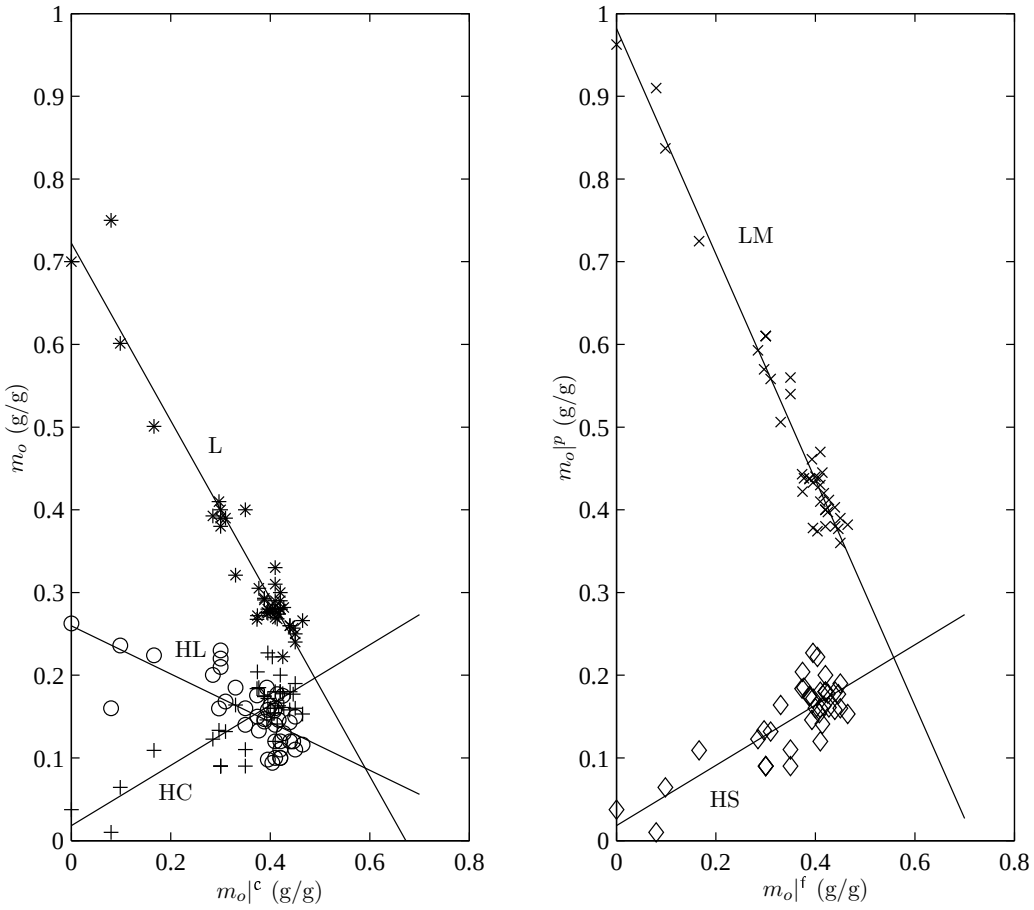

Figure 7.1.: Compositional data and linear models.

to be able to specify it independently and determine the concentration of the other constituents based on this specification.

In compiling this data the constituents have been partitioned in two different ways. The first of these partitions is into four classes of compounds: the celluloses (C), the hemicelluloses associated with celluloses (HC), the hemicelluloses associated with lignins (HL) and the lignins (L). The second partition corresponds to the CF, HS and LM nanophases introduced in chapter 3.

The CF phase and the cellulose class are identical, hence the dry CF mass fraction is equal to the cellulose concentration. In the past it has been suggested that some of the cellulose might be present in a more or less amorphous form. Support for this hypothesis appears to be decreasing. For example, Newman et al. (1993) claim that all the cellulose in wood is contained within the microfibrils and the non-crystalline component in pulp is a product of the pulping process.

The HS phase and the HC compound class are also equivalent and are identified with the glucomannans. In the case of the HS phase, this identification was made on the basis of topochemical information. In the case of the HC compound class, the identification was based on which hemicelluloses increased in concentration with increasing cellulose fraction.

Hemicelluloses whose fraction increases with lignin fraction have been assigned to the HL class, thus the HL class contains all the hemicelluloses except for the glucomannans. These hemicelluloses are believed to be intimately mixed with the lignins and collectively they and the lignins constitute the LM phase.

Linear models,

$$m_o|^p = a_1 m_o|^{\mathsf{f}} + a_0, \tag{7.1}$$

for the dry mass fractions of the members of both partitions, $m_o|^p \; p \in \{\mathfrak{hc}, \mathfrak{hl}, \mathfrak{l}, \mathfrak{s}, \mathfrak{m}\}$, as functions of the cellulose (or CF) dry mass fraction, $m_o|^{\mathsf{f}}$, have been fitted to the data of figure 7.1. The resulting regression coefficients and the coefficients of determination appear in table 7.1 and the regression lines are plotted in figure 7.1. These models are valid in the range $0 \leq m_{\mathfrak{c}}^o < 0.67$, outside this range the dry mass fraction of one of the constituent classes is less than zero which is physically unreasonable.

Uprichard (1991) gives mean compositions for the innerwood (rings 1–10) and outerwood (rings 16+) of radiata pine and claims that these compositions bracket the actual composition anywhere in radiata pine wood. In table 7.2 this compositional data is compared with that predicted using the linear models of (7.1). The agreement is reasonable, though the HS dry mass fraction is overestimated (10%) and the LM dry mass fraction is underestimated (5%).

	a_0	a_1	r^2
HC	0.0182	0.3645	0.6474
HL	0.2596	-0.2907	0.5285
L	0.7222	-1.0738	0.9239
HS	0.0182	0.3645	0.6474
LM	0.9818	-1.3645	0.9626

Table 7.1.: Compositional model parameters.

	Innerwood		Outerwood	
	expt.	model	expt.	model
C, CF	0.393	–	0.439	–
HC, HS	0.146	0.161	0.158	0.178
HL	0.185	0.145	0.143	0.132
L	0.276	0.300	0.260	0.251
LM	0.461	0.445	0.403	0.383

Table 7.2.: Comparison of experimentally determined dry mass fractions in the innerwood and outerwood of radiata pine (Uprichard, 1991) with those predicted by the compositional model of equation (7.1).

7.4. Variation of dry CF mass fraction across the cell-wall

Cellulose content changes across the tracheid cell wall. It is lowest in the primary wall layer and attains a maximum in the S2 layer (Meier, 1961; Fengel, 1969; Parameswaran and Liese, 1982; Takabe et al., 1983; Saka, 1990). Table 7.3 lists a selection of values taken from the literature for the mean cellulose content of the major cell wall layers. The cellulose mass fractions presented in the last row of this table are computed from data for the distribution of polysaccharides and lignin, across the cell walls of *Cryptomeria* and loblolly pine tracheids respectively, presented in Saka (1990). These calculations assume that the CML contains no cellulose. This is not the case, but it is in keeping with the decision to neglect the primary wall.

Fengel and Wegener (1984) suggest that while the overall composition of wood is variable, the compositions of the cell-wall layers is the same. If this is the case, then the compositional variation can be attributed to changes in the relative proportions of the cell-wall layers rather than changes in the composition of the layers themselves.

To test the validity of this idea, data relating wood composition and density were sought. Suprisingly little was found, however Harris and Cown (1991) give typical values for the dry density in the innerwood and outerwood of radiata pine of 0.36

ref.	CML	S1	S2	S3
Cave (1976)	0.16	0.45	0.50	0.44
Fengel and Wegener (1984)	0.14	0.35	0.58	0.58
Panshin and de Zeeuw (1980)	0.13	0.28	0.51	0.50
Sjöström and Westermark (1999)	0.08	0.45	0.45	0.44
Saka (1990)	0	0.43	0.52	0.30

Table 7.3.: Dry cellulose mass fraction in the cell-wall layers.

and 0.53 g/cc[1] corresponding to the compositional data of Uprichard (1991) already employed above (see table 7.2).

In figure 7.2 (a) these data points are compared with the relationship between wood density and composition resulting from the layer volume fraction model of chapter 6, the nanophase density models of chapter 8 and assumed constant layer dry CF mass fractions of 0, 0.43, .52 and .30 in the CML, S1, S2 and S3 layers respectively.

While the implied relationship passes through the outerwood data point and correctly predicts that the total CF mass fraction will increase with density, this effect is underestimated.

Unsuccessful attempts have been made to remedy this failing by adjusting the layer CF mass fractions and the layer volume fraction model. Consequently, a model for CF concentration across the cell wall is proposed. This model assumes that the CF dry mass fraction at a point across the cell-wall is a function of the cellular solid volume fraction of the material lying outside of that point[2]. The assumed functional relationship is piecewise linear,

$$m_o|^{\mathrm{f}}(\hat{v}) = \begin{cases} \min(a_1(\hat{v}-\hat{v}_1)+m_1, m_{\max}, a_2(\hat{v}-\hat{v}_2)+m_2) & \hat{v}_1 \le \hat{v} \le \hat{v}_2 \\ 0 & \text{otherwise} \end{cases}, \tag{7.2}$$

and is illustrated in figure 7.3. Obviously $0 \le \hat{v}_1 < 1$, $0 < \hat{v}_2 \le 1$, $a_1 \ge 0$, $a_2 \le 0$, $0 \le m_1 \le m_{\max}$ and $0 \le m_2 \le m_{\max}$. Less obviously,

$$\hat{v}_1 < \frac{m_2 - m_1 + a_1\hat{v}_1 - a_2\hat{v}_2}{a_1 - a_2} < \hat{v}_2. \tag{7.3}$$

This model is based on two hypotheses:

1. the cellular processes giving rise to the variation in composition change linearly

[1] Actually Harris and Cown (1991) give basic densities of 0.320 and 0.475 g/cc which can be converted to dry densities by assuming a total green-dry volumetric shrinkage of 0.104 (Cown and McConchie, 1980).

[2] Note that the geometry of the surfaces on which points are labelled with the same solid volume fraction are left unspecified. They correspond to surfaces that on which wall deposition was occurring at some particular point in time.

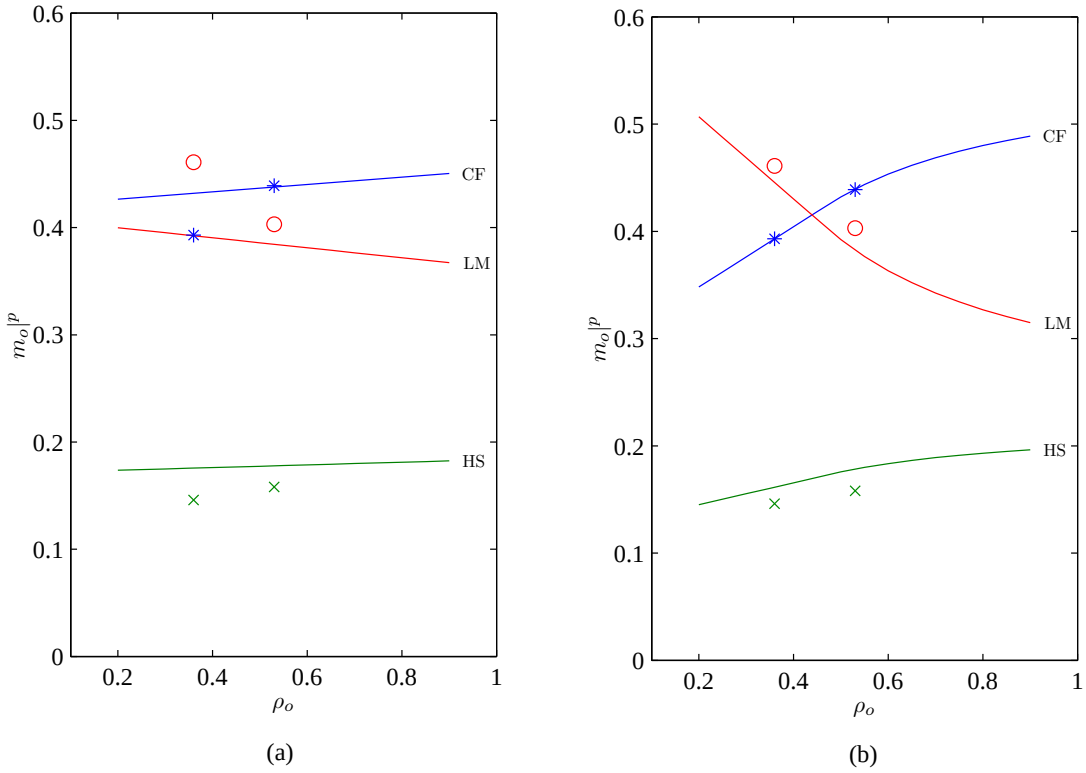

Figure 7.2.: Dry nanophase mass fractions as functions of dry density.

in time (or remain constant),

2. there is an upper limit to the CF mass fraction.

While these hypotheses are speculative and simplified they do not contradict anything known about the variation of cellulose composition across the cell wall and they do predict that the cellulose content increases from the primary wall, reaches a maximum in the S2 layer and decreases thereafter.

The $\hat{v}_1$ and $\hat{v}_2$ parameters in (7.2) are assumed to be the same as the CML total volume fraction and the total solid volume fraction respectively. Using the same dry density and cellulose concentration data as used above to critique the constant layer model, suitable values for the remaining parameters of (7.2) have been determined (see table 7.4). Using these values the relationship between dry density and composition – resulting from the combination of (7.2), the layer volume fraction model of chapter 6 and the nanophase density models of chapter 8 – has been plotted in figure 7.2 (b). The predicted mean layer compositions for three different dry densities appear in table 7.5. These compare favourably with the experimental compositions of table 7.3.

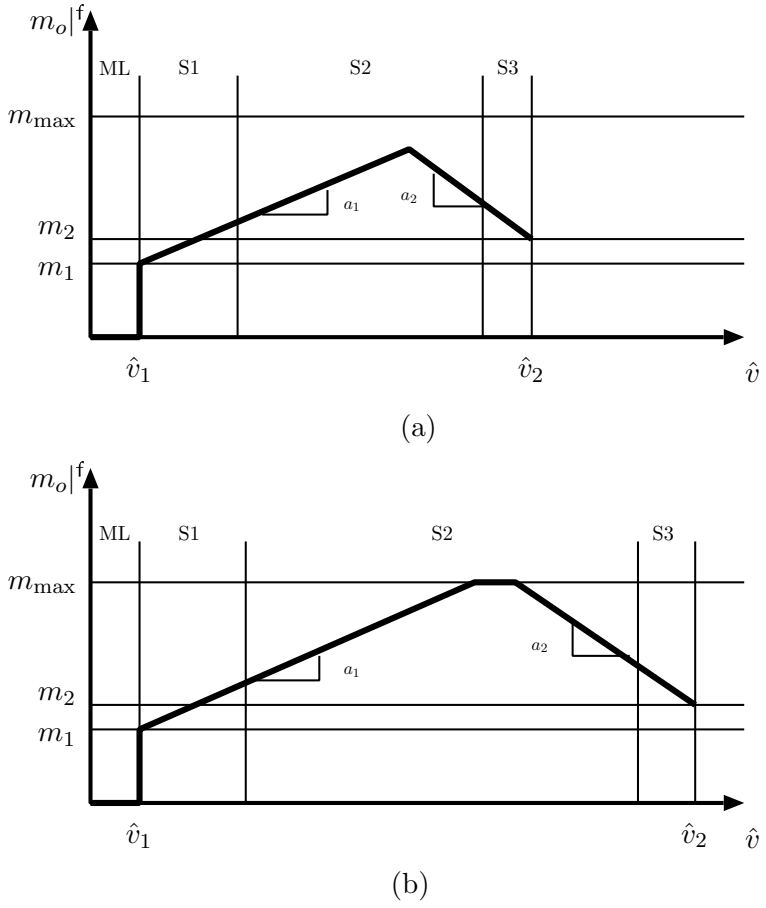

Figure 7.3.: Piecewise linear model for variation in dry CF mass fraction across the cell-wall. (a) EW, low solid volume fraction. (b) LW, high solid volume fraction.

m_1	m_2	$m_{\max}$	a_1	a_2
0.31	0.34	0.60	1.28	-3.27

Table 7.4.: Parameters for use with (7.2).

ρ_o g/cc	$\tilde{\rho}$	$m_o\|^{\mathsf{f}}_{\mathsf{CML}}$	$m_o\|^{\mathsf{f}}_{\mathsf{S1}}$	$m_o\|^{\mathsf{f}}_{\mathsf{S2}}$	$m_o\|^{\mathsf{f}}_{\mathsf{S3}}$
0.2	0.20	0	0.32	0.39	0.38
0.5	0.48	0	0.34	0.51	0.42
0.8	0.76	0	0.36	0.56	0.43

Table 7.5.: Layer dry CF mass fractions from the piecewise linear model for various dry wood densities.

7.5. Moist volume fractions from dry mass fractions

Given the dry phase mass fractions $m_o|^p$, the phase moisture contents $w|^i$, and moist phase specific volumes $\nu|^p = 1/\rho|^p$, in any domain, then the phase volume fractions may be computed using

$$v|^p = \frac{\nu|^p m_o|^p (1 + w|^p)}{\sum_i \nu|^i m_o|^i (1 + w|^i)}. \tag{7.4}$$

In terms of the phase hygroscopicites $\chi|^p$ and the overall moisture content in any domain, (7.4) can be rewritten as

$$v|^p = \frac{\nu|^p m_o|^p \left(\sum_i \chi|^i m_o|^i + \chi|^p\right)}{\left(\sum_i \chi|^i m_o|^i\right)\left(\sum_i \nu|^i m_o|^i\right) + \sum_i \nu|^i m_o|^i \chi|^i} \tag{7.5}$$

Figure 7.4 shows the variation in nanophase densities and volume fractions with moisture content for dry CF mass fractions of 0.3, 0.4 and 0.5 g/g. The HS and LM dry mass fractions are determined using the model described above. The densities are those predicted by the nanophase density models of chapter 8. The CF and HS nanophase hygroscopicities are $\chi|^{\mathrm{f}}_{=} 0$ and $\chi|^{\mathrm{s}}_{=} 1$. The LM phase hygroscopicity depends on the relative proportions of lignin and hemicellulose that constitute the LM phase.

7.6. Summary

In this chapter models have been presented that:

- relate the dry HS and LM phase mass fractions to the dry CF mass fraction,
- determine the dry CF mass fraction in the cell-wall layers,
- relate the moist nanophase volume fractions to the dry nanophase mass fractions, the overall moisture content and the phase hygroscopicities.

Collectively, these models specify the nanophase volume fractions based solely on the wood density and moisture content.

The quality of these models is uncertain as sufficient data, against which they can be tested and refined, have yet to be located. However, in the abscence of more specific information they do provide a rational starting point which is necessary for numerical modelling.

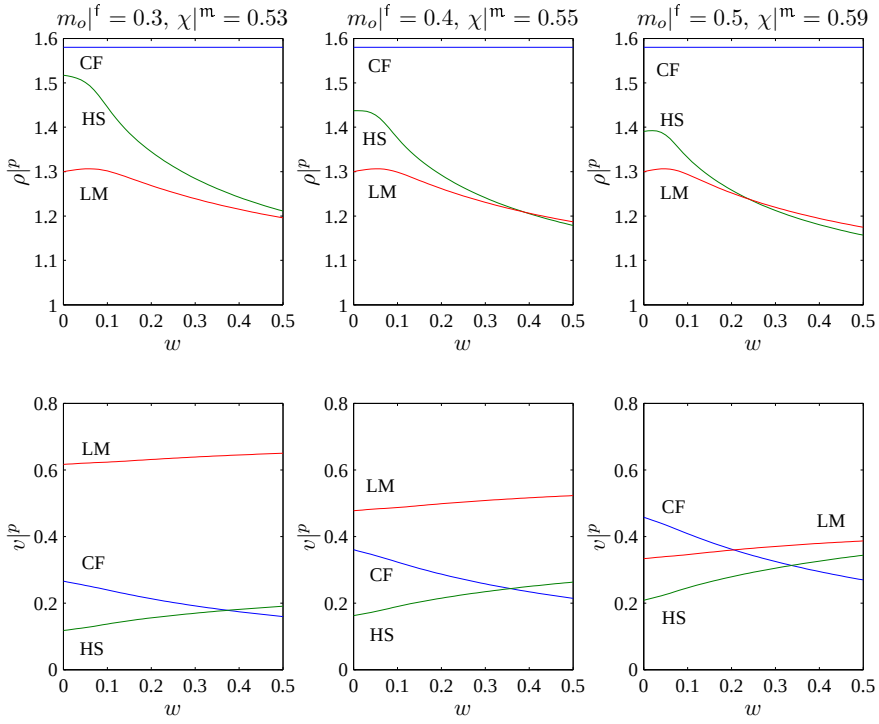

Figure 7.4.: Phase densities and volume fractions as functions of moisture content for three dry CF phase mass fractions.

Chapter 8

Nanophase properties

This chapter describes models that provide estimates for the

1. density,
2. elastic moduli,
3. hygroscopicity,
4. and hygro-expansion coefficients,

of the CF, HS and LM nananophases required by the nanostructual models of chapter 3.

The nanophase properties, and consequently wood properties, are affected by temperature and moisture content. Practical problems in wood technology, particularly wood drying, occur at moisture contents from dry to saturated and temperatures up to 200°C. Since one of the major aims of this thesis is to provide input data for macroscopic finite element models built to address these problems it is desirable for the nanophase property models to operate over these ranges.

8.1. CF phase properties

8.1.1. Elastic moduli

The CF phase is highly anisotropic owing to the differences in nature and magnitude of the attractive forces which give rise to order within the microfibrils: strong covalent bonding, augmented by intramolecular hydrogen bonds, in the chain direction, weaker intermolecular hydrogen bonding in the sheet plane and weaker still non-bonded intermolecular attractions in the sheet-stacking direction.

From the triclinic and monoclinic symmetries of the cellulose I_α and I_β phases respectively, it would be expected that I_α would require 21, and I_β 13, parameters to characterize the elastic behaviour. As the molecular arrangement in I_α is only slightly different to that of I_β it seems reasonable to expect that the possibly non-zero terms introduced by the change from monoclic to triclinic symmetry will be small (and hence negligible).

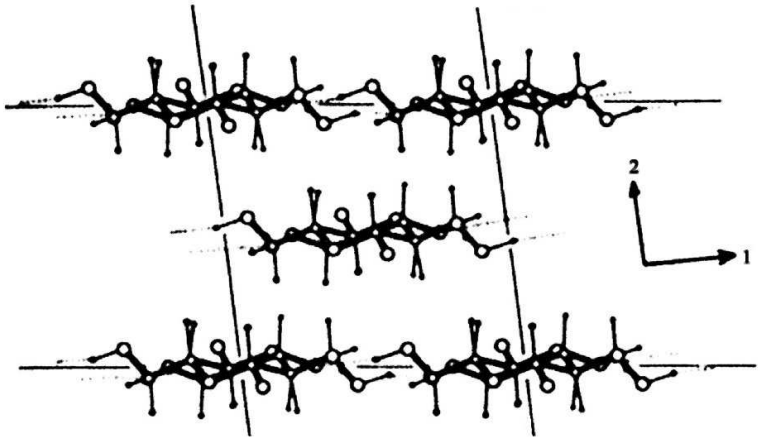

Figure 8.1.: Cellulose I_β crystal structure (projection along the 3-direction i.e. the chain axis). Adapted from Tashiro and Kobayashi (1991).

By most accounts the microfibrils are randomly oriented in the transverse plane (at least within wood overall, though this may have more to do with the arrangement of material at the cellular rather than the nanostructural level) (Sisson, 1935; Okano, 1972; Prud'homme and Noah, 1975), and that equal numbers are present in both the up and down directions and thus it is reasonable to treat the 'average' fibre as being transversely isotropic (hexagonal symmetry). Such an assumption reduces the required number of elastic parameters to only 5.

Table 8.1 lists all known complete sets of elastic parameters that have been calculated for cellulose or a putative fibre phase. Also shown are values adopted in the models of Navi (1988), Koponen et al. (1989), Persson (1997) and Watanabe (1998); Watanabe et al. (1999).

The first full set of elastic parameters was presented by Jawson et al. (1968) and later refined by Gillis (1969). They reasoned that while the crystal structure on which their models were based was monoclinic, it had a symmetry which deviated only slightly from orthorhombic and hence its behaviour would be approximately that of an orthotropic material. Unfortunately the original paper included an error towards the end of the analysis that affected the final values presented. Corrected values can be found in Mark (1972). Like the earlier calculations of Mark (1965) and Mark (1967) the computed values were based on a cellulose crystal structure in which the intermolecular hydrogen bonding pattern is significantly different from that in currently accepted structures.

Cave and Robinson (1969) estimated the CF stiffnesses using the values of Mark (1965) in conjunction with a vanishing transverse Poisson's ratio. Cave (1978a) later proposed a set of elastic constants based on a fit to experimental data along with Cousins (1978) experimentally determined Young's modulus for hemicellulose and as-

Ref.	C_{11} GPa	C_{12} GPa	C_{13} GPa	C_{16} GPa	C_{22} GPa	C_{23} GPa	C_{26} GPa	C_{33} GPa	C_{36} GPa	C_{44} GPa	C_{45} GPa	C_{55} GPa	C_{66} GPa	symmetry
Jawson et al. (1968)	25.45	0	0.94	-	38.05	1.57	-	56.63	-	0.40	-	0.24	3.30	orthorhombic
	25.70	0	0.86	-	16.80	0.69	-	56.58	-	0.18	-	0.25	2.63	orthorhombic
Gillis et al. (1969)	24.92	0	0.92	-	37.27	1.53	-	319.16	-	0.39	-	0.23	3.23	orthorhombic
	25.17	0	0.85	-	16.45	0.67	-	246.47	-	0.12	-	0.24	2.58	orthorhombic
Cave and Robinson (1969)	15.43	0.02	1.55	-	15.43	1.55	-	134.95	-	3.73	-	3.73	7.71	hexagonal
Cave (1978a)	24.00	12.00	12.00	-	24.00	12.00	-	136.00	-	6.00	-	6.00	6.00	hexagonal
Cave (unpublished)	11.50	2.00	10.36	-	11.50	10.36	-	151.89	-	5.89	-	5.89	4.75	hexagonal
Tashiro and Kobayashi (1991)	54.55	1.58	-2.52	-3.23	15.16	1.26	4.31	167.79	0.51	3.53	1.43	8.08	4.53	monoclinic
Koponen et al. (1989)	27.20	14.00	14.00	-	27.20	14.00	-	137.00	-	4.40	-	4.40	4.40	hexagonal
Persson (1997)	27.00	14.00	14.00	-	27.00	14.00	-	137.00	-	6.60	-	6.60	6.60	hexagonal
Watanabe et al. (1999)	27.30	1.15	2.85	-	27.30	2.85	-	134.57	-	4.40	-	4.40	13.08	hexagonal
Navi (1988)	20.80	0.77	0.77	-	20.80	0.77	-	246.50	-	0.20	-	0.20	2.58	hexagonal

Table 8.1.: Complete sets of cellulose stiffnesses from the literature. The 3-direction is parallel to the cellulose chains, and the 2-direction is approximately normal to the h-bonded sheets (see figure 8.1). '-' indicates terms that are required to be zero by the assumed symmetry.

sumed anisotropy ratios. A third estimation due to Cave (unpublished) is also included in table 8.1.

The only set of elastic constants that treat cellulose as monoclinic, those of Tashiro and Kobayashi (1991), are also the most recent, and in all likelihood the best available, though they are still not entirely satisfactory. Based on crystal structure proposed by Gardner and Blackwell (1974) for cellulose I, a structure similar to that currently favoured for I_β, this set of elastic constants were calculated using the so called lattice-dynamical equations (Tashiro et al., 1978) with force field parameters refined against spectroscopic data. The chain modulus of 167.5 GPa is high compared to the experimental values in table 8.2. The authors claimed that this was due to the force field representing the behaviour at low temperatures, and to the underestimation of the true crystalline modulus due to the assumed stress homogeneity as discussed above. The latter explanation has to be viewed somewhat sceptically given the number of calculations which give a chain modulus around 130 GPa.

Srinavasan (1942) provided an estimate of 2.1–4.2 GPa for the transverse modulus of the fibre phase, and appears to have been the first to make such calculations. Subsequently Mark (1965) and Mark (1967) calculated, based on a crystal structure first proposed by Liang and Marchessault (1959), a transverse modulus of 15.4–27.2 GPa, a longitudinal-transverse shear modulus of 3.62–4.40 GPa and a longitudinal-transverse Poisson's ratio of 0.1.

8.1.2. Longitudinal fibre modulus

Of all the elastic parameters, of any of the nanophases, the CF longitudinal modulus is the most significant and has also been the most studied. As the longitudinal fibre direction coincides with the cellulose chain axis, the longitudinal fibre modulus is determined in the first instance by the primary molecular structure (the covalent bonds), in particular by the resistance to stretching and bending around the glycosidic linkage. The primary bonds are augmented along the chain axis by intramolecular hydrogen bonds which also bridge between glucose residues. The frequency of these intramolecular hydrogen bonds has a significant influence on the chain modulus as has been pointed out by Kroon-Batenburg et al. (1986) and Tashiro and Kobayashi (1991).

In table 8.2 theoretical and experimental estimates for the chain modulus of cellulose, in various forms, are presented.

While of historical interest, earlier theoretical estimates of 20–319 GPa for the chain modulus of cellulose (Meyer and Lotmar, 1936; Meyer, 1942; Srinavasan, 1942; Meredith, 1956, 1959; Lyons, 1958, 1959; Treloar, 1960; Mark, 1965, 1967, 1972; Jawson et al., 1968; Gillis, 1969) are of little practical value as they are based on outdated crystal structures and force fields. Likewise, the axial modulus of only 0.140 GPa computed

Ref.	E_l GPa	Notes
	Theoretical	
Tashiro and Kobayashi (1985)	173	low temperature
Kroon-Batenburg et al. (1986)	130–142	room temperature
Pizzi (1989)	0.140	
Tashiro and Kobayashi (1991)	168	low temperature
Tashiro and Kobayashi (1996)	183	
Marhöfer et al. (1996)	162	I_α at 0 K
	128	I_α at 300 K
	148	I_β at 0 and 300 K
Newman (1998)	120	
	Experimental	
Sakurada et al. (1962)	134	
Sakurada et al. (1964)	130	
Northolt and de Vries (1985)	118	dynamic measurement
Nishino et al. (1995)	138	

Table 8.2.: Longitudinal CF modulus. See text for details.

by Pizzi (1989) was based on a structural model ('amorphous', helical conformation) not representative of cellulose as it occurs in wood.

More recently Tashiro and Kobayashi (1985) calculated a modulus in the chain direction of 173 GPa for a crystal structure with two intramolecular hydrogen bonds. Tashiro and Kobayashi (1991) chain modulus of 168 GPa using lattic-dynamical equations and a force field refined against vibrational spectral data thought to represent the behaviour at low temperatures. The same authors also reported a chain modulus of 183 GPa computed using the Dreiding II force field (Tashiro and Kobayashi, 1996).

Kroon-Batenburg et al. (1986, 1990, 1997) calculated a chain modulus of 130–142 GPa for a model of cellobiose with two intramolecular hydrogen bonds using a molecular mechanics approach with a force field that they considered representative of the mechanics at room temperature.

Reiling and Brickmann (1995) and Marhöfer et al. (1996) have considered the cellulose I_α and I_β allomorphs separately. Using both molecular dynamics and molecular mechanics simulations they computed crystal moduli in the chain direction of 162 and 128 GPa for I_α at 0 K and 300 K respectively, and 148 GPa for I_β at both 0 and 300 K.

The cellulose chains on the surface of a microfibril exist in a different environment to that of the internal chains. Fewer intra-chain hydrogen bonds may be present in the external chains thus reducing their stiffness. Consequently Newman (1998), based on a simple rule of mixture average, has suggested a longitudinal microfibril modulus of

120 GPa. As the number of exterior intrachain hydrogen bonds may well depend on the availability of water, this kind of reasoning may also require the CF properties to be treated as functions of moisture content.

Unlike the other CF moduli, the longitudinal modulus has also been measured experimentally. Meyer and Lotmar (1936) reported experimental values ranging from 78 to 108 GPa, but these values were for cellulosic fibres (ramie) rather than cellulose per se. Northolt and de Vries (1985) have reported a dynamic modulus of 118 GPa for a native cellulosic fibre (manila). Values of 130–138 GPa have been determined from X-ray observations of the lattice strain in native cellulosic samples (purified ramie) subjected to a constant applied stress (Sakurada et al., 1962, 1964, 1966; Sakurada and Kaji, 1970; Nishino et al., 1995). It is worth noting that Sakurada et al. (1962) observed a linear relationsip between tensile stress and strain at least up to a stress of 390 MPa (0.3 % strain), indicating that the CF behaviour is well represented by a linear elastic material as would be expected for a highly ordered (crystalline) material. In calculating a modulus from the observed lattice strains a homogenous stress distribution was assumed, and since any heterogeneity in the sample will inevitably lead to higher stress in the crystalline (stiffer) phase, the calculated moduli represent a lower bound on the chain modulus. Futhermore, as the reflections used to evaluate the strain do not distinguish between I_α and I_β structures the experimental values represent an average. Taking a 1:1 ratio between I_α and I_β allomorphs (Newman, 1999b), the theoretical values of Marhöfer et al. (1996) discussed above, and using the rule of mixtures gives an average stiffness of 138 GPa, which is in excellent agreement with experimental values.

8.1.3. Density

Densities of cellulosics have been reported and discussed by, amongst others, Hermans (1949), Treiber (1957), Stamm (1964); Stamm and Sanders (1966), Frey-Wyssling (1964), Fengel (1969, 1970b), Beall (1972), Seifert (1972), and Kellogg et al. (1975). Values range from 1.47–1.63 g/cc, with the variation attributable to the degree of supramolecular order (amorphous to crystalline) and the mode of determination. For crystalline cellulose Sugiyama et al. (1991) calculated densities of 1.582 and 1.599 g/cc for the I_α and I_β allomorphs respectively.

Previous modelling studies (Mark, 1967; Cave, 1973, 1976; Koponen et al., 1987) have used a value of 1.55 for the specific gravity of cellulose; however in keeping with a highly ordered internal fibre structure a value of 1.58 g/cc has been adopted for the density of the CF phase.

8.1.4. Thermal influences

Below 200°C the principal and immediate effect of an increase in temperature on the cellulosic fibres is a decrease in stiffness. Other effects of elevated temperature relate to an increase in the rate of normal aging processes (McGinnis and Shafizadeh, 1991). At temperatures over 80°C the degree of polymerization (DP) drops over time, but the crystalline structure is not altered and may even be improved (Fengel and Wegener, 1984), possibly due to the solid state transformation of I_α to I_β (Yamamoto et al., 1989; Debzi et al., 1991). As changes in DP have been shown to influence strength but not stiffness (Ifju, 1964; Benedict et al., 1994) and I_α and I_β are believed to have similar mechanical properties these effects may be safely ignored.

It appears that no direct quantitative data on the influence of temperature on the elastic properties of cellulose exist other than the theoretical calculations of Marhöfer et al. (1996) mentioned above. Their results were inconclusive with the I_α chain modulus decreasing by 20 GPa between 0 and 300 K, whereas the I_β modulus remained constant.

The glass transition of dry cellulosics is around 230°C (Goring, 1963; Salmén, 1982). For highly crystalline samples no glass transition is detected below the melting point. Semicrystalline polymers in general show a linear decrease in modulus with increasing temperature up to the glass transition with the rate of drop off depending on the degree of crystallinity (Gradin et al., 1989). Batten and Nissan (1987a) developed a theoretical model

$$\frac{d \ln E}{d\vartheta} = -2.4 \times 10^{-3} \quad {}^\circ\mathrm{C}^{-1} \tag{8.1}$$

that relates the modulus E of a hydrogen bond dominated solid to the temperature ϑ. In the region of interest this model is essentially linear and compares favourably with experimental results for cellulosic papers. This model is adopted below, but it should be noted that its applicability to an essentially crystalline material is questionable and it probably overestimates the softening in the chain direction, since in that direction the softening attributable to the intrachain hydrogen bonds is ameliorated by the covalent bonding along the backbone.

For the CF phase a resonable estimate for the volumetric coefficient of thermal expansion is around $100 \times 10^{-6} {}^\circ\mathrm{C}^{-1}$ (Wada and Okano, 1999; Kim et al., 2001) so an increase in temperature of 100°C would decrease the density by only 1%. Consequently, changes in fibre density with temperature are ignored.

8.1.5. Hygral influences

As water is known not to penetrate crystalline cellulosic domains (Clark and Howsman, 1946; Broughton et al., 1955; Cutter and Murphey, 1972), it is assumed that the CF

phase does not swell or shrink as the wood moisture content changes. It is also generally assumed that the CF moduli are unaffected by moisture. This is almost certainly true within the microfibrils. However, the external cellulose chains may interact with water and it is possible that some of the intramolecular hydrogen bonds in the external chains might be broken and replaced with cellulose-water hydrogen bonds, reducing the longitudinal fibre modulus.

8.1.6. Adopted moduli

If the force field parameters used by Tashiro and Kobayashi (1991) were responsible for the chain stiffness being too high then it is likely that all of the moduli would be too high. For the fibre stiffnesses at ambient temperature, the elastic constants of Tashiro and Kobayashi (1991), linearly scaled to give the experimentally determined chain modulus of 136 GPa at 20 °C, have been adopted, i.e.

$$\mathbf{C}(\vartheta = 20°\mathrm{C})|^{\mathrm{f}} = \begin{bmatrix} 44.28 & 1.282 & -2.045 & 0 & 0 & -2.622 \\ & 12.30 & 1.023 & 0 & 0 & 3.498 \\ & & 136.2 & 0 & 0 & 0.4140 \\ & & & 2.865 & 1.161 & 0 \\ & \text{symm.} & & & 6.558 & 0 \\ & & & & & 3.677 \end{bmatrix} \text{ GPa.} \quad (8.2)$$

It is tempting to include the reduction in longitudinal modulus proposed by Newman (1998) and mentioned above, but the fact that Cave (1978a) found a chain modulus of 136 GPa to give the best fit to his experimental data suggests that this might be premature, or it may be that this reduction occurs only at higher water activities. For similar reasons, no attempt has been made to incorporate the possible reduction in longitudinal modulus due to the breaking of intramolecular cellulose-cellulose hygrogen bonds in favour of water-cellulose bonds.

Except in appendix K, the CF phase is treated as being transversely isotropic. In appendix K, it is shown that using the orientational average of the CF compliance tensor over a uniform in-plane distribution leads to results similar to treating the CF phase as monoclinic. Consequently the CF stiffnesses are taken to be

$$\mathbf{C}(\vartheta = 20°\mathrm{C})|^{\mathrm{f}} = \begin{bmatrix} 11.90 & 4.815 & 0.3466 & 0.000 & 0.000 & 0.000 \\ & 11.90 & 0.3466 & 0.000 & 0.000 & 0.000 \\ & & 136.0 & 0.000 & 0.000 & 0.000 \\ & & & 3.702 & 0.000 & 0.000 \\ & \text{symm.} & & & 3.702 & 0.000 \\ & & & & & 3.545 \end{bmatrix} \text{ GPa.} \quad (8.3)$$

At temperatures other than ambient the CF softening is modelled using the thermal softening model of Batten and Nissan (1987a) discussed above, that is

$$\mathbf{C}(\vartheta)|^{\mathsf{f}} = \exp\left(-2.4 \times 10^{-3}(\vartheta - 20)\right) \mathbf{C}(\vartheta = 20)|^{\mathsf{f}}. \tag{8.4}$$

Between 0–200°C this model predicts a 38% decrease in stiffness, with the softening nearly proportional to the change temperature.

8.2. Matrix phase properties

8.2.0.1. Hygroscopicity

The sorption of water by celluloses, hemicelluloses and lignins isolated from wood has been studied and discussed by Runkel (1954); Runkel and Luthgens (1956),Sadoh and Kadita (1957); Sadoh (1959, 1960, 1961a,b, 1962), Christensen and Kelsey (1958), Goring (1963), Cousins (1976, 1978), Ziegler and Beall (1974), Pizzi et al. (1987b,a), Salmén (1997), Anagnost and Smith (1997) and Rawat et al. (1998); Rawat and Khali (1999). These studies are in qualitative agreement and indicate that the hemicelluloses are the most hydrophilic of the constituents and the lignins the least. Quantitatively, considerable variation exists, with the equilibrium moisture content depending on:

- sample preparation,
- the relative humidity,
- the temperature,
- and the sample history (hysteresis).

To obtain a consistent[1] and realistic estimate for the partition of moisture amongst the constituents and nanophases from the existing sorption data it is here assumed that:

- the nature of the celluloses, hemicelluloses and lignins in regard to moisture are the same everywhere within wood,
- the moisture contents of the celluloses capable of sorbing water, the hemicelluloses associated with the celluloses and the hemicelluloses associated with the lignins are the same, i.e. $w|^{\mathsf{c}} = w|^{\mathsf{hc}} = w|^{\mathsf{hl}} = w|^{\mathsf{h}}$,
- *in situ* the sorption behaviour of the lignins is the same as that of the periodate lignin prepared and tested by Cousins (1976),
- hysteresis and temperature do not change the relative hygroscopicities.

[1] Consistent in the sense that the moisture mass is conserved – that is for an average composition appropriate for whole wood the model predicts the correct moisture content.

In any domain, the total moisture content w is taken to be the mass fraction weighted sum of the moisture contents of the celluloses $w|^{\mathsf{c}}$, the hemicelluloses associated with the celluloses $w|^{\mathsf{hc}}$, the hemicelluloses associated with the lignins $w|^{\mathsf{hl}}$ and the lignins $w|^{\mathsf{l}}$, i.e.

$$w = w|^{\mathsf{c}}\alpha m_o|^{\mathsf{c}} + w|^{\mathsf{hc}}m_o|^{\mathsf{hc}} + w|^{\mathsf{hl}}m_o|^{\mathsf{hl}} + w|^{\mathsf{l}}m_o|^{\mathsf{l}}. \tag{8.5}$$

The factor of α ($0 \leq \alpha \leq 1$) is introduced in (8.5) to account for the fraction of cellulose that can interact with water. From NMR studies a reasonable value is $\alpha = 0.5$ (Newman, 1998).

If the overall equilibrium moisture content $w^\star$ in some reference material, the equilibrium moisture content of the lignins $w|^{\mathsf{l}}$ and the corresponding dry constituent mass fractions – $m_o|^{\mathsf{c}}_\star$, $m_o|^{\mathsf{hc}}_\star$, $m_o|^{\mathsf{hl}}_\star$ and $m_o|^{\mathsf{l}}_\star$ – are known, then from (8.5), in conjucntion with the assumption that $w|^{\mathsf{c}} = w|^{\mathsf{hc}} = w|^{\mathsf{hl}} = w|^{\mathsf{h}}$, the moisture content of the hemicelluloses is

$$w|^{\mathsf{h}} = \frac{w^\star - m_o|^{\mathsf{l}}_\star w|^{\mathsf{l}}}{\alpha m_o|^{\mathsf{c}}_\star + m_o|^{\mathsf{hc}}_\star + m_o|^{\mathsf{hl}}_\star}. \tag{8.6}$$

Now, assuming that the constituent moisture contents are the same as in whole wood even though the composition is not, the moisture contents of the CF, HS and LM phases – $w|^{\mathsf{f}}$, $w|^{\mathsf{s}}$, $w|^{\mathsf{m}}$ – in any domain may be determined. The water associated with the cellulose and associated hemicelluloses is attributed to the HS phase. The remaining water is assigned to the LM phase. Thus

$$w|^{\mathsf{f}} = 0, \tag{8.7}$$

$$w|^{\mathsf{s}} = \frac{\alpha m_o|^{\mathsf{c}} + m_o|^{\mathsf{hc}}}{m_o|^{\mathsf{hc}}} w|^{\mathsf{h}}, \tag{8.8}$$

$$w|^{\mathsf{m}} = \frac{m_o|^{\mathsf{hl}} w|^{\mathsf{h}} + m_o|^{\mathsf{l}} w|^{\mathsf{l}}}{m_o|^{\mathsf{hl}} + m_o|^{\mathsf{l}}}. \tag{8.9}$$

The matrix moisture content in this domain is then

$$w|^{\mathsf{M}} = \frac{m_o|^{\mathsf{s}} w|^{\mathsf{s}} + m_o|^{\mathsf{m}} w|^{\mathsf{m}}}{m_o|^{\mathsf{s}} + m_o|^{\mathsf{m}}} \tag{8.10}$$

and the total moisture content is

$$w = m_o|^{\mathsf{s}} w|^{\mathsf{s}} + m_o|^{\mathsf{m}} w|^{\mathsf{m}}. \tag{8.11}$$

If the material used to determine the carbohydrate moisture content using (8.6) is used as the reference material to define the hygroscopicities[2], then the consituent and

[2]Hygroscopicities are defined in chapter 2, §2.1.2.

nanophase hygroscopicities are

$$\chi|^{\mathtt{l}} = \frac{w|^{\mathtt{l}}}{w^\star}, \tag{8.12}$$

$$\chi|^{\mathtt{h}} = \frac{w|^{\mathtt{l}}}{w^\star} = \frac{1 - m_o|^{\mathtt{l}}_\star \chi|^{\mathtt{l}}}{\alpha m_o|^{\mathtt{c}}_\star + m_o|^{\mathtt{hc}}_\star + m_o|^{\mathtt{hl}}_\star}, \tag{8.13}$$

$$\chi|^{\mathtt{f}} = \frac{w|^{\mathtt{f}}}{w^\star} = 0, \tag{8.14}$$

$$\chi|^{\mathtt{s}} = \frac{w|^{\mathtt{s}}}{w^\star} = \frac{\alpha m_o|^{\mathtt{c}} + m_o|^{\mathtt{hc}}}{m_o|^{\mathtt{hc}}} \chi|^{\mathtt{h}}, \tag{8.15}$$

$$\chi|^{\mathtt{m}} = \frac{w|^{\mathtt{m}}}{w^\star} = \frac{m_o|^{\mathtt{hl}} \chi|^{\mathtt{h}} + m_o|^{\mathtt{l}} \chi|^{\mathtt{l}}}{m_o|^{\mathtt{hl}} + m_o|^{\mathtt{l}}} \tag{8.16}$$

and the rates of change of the hygroscopicities with respect to the moisture content of the reference material are

$$\frac{d\chi|^{\mathtt{l}}}{dw^\star} = \frac{1}{w^\star}\frac{dw|^{\mathtt{l}}}{dw^\star} - \frac{w|^{\mathtt{l}}}{w^{\star 2}}, \tag{8.17}$$

$$\frac{d\chi|^{\mathtt{h}}}{dw^\star} = -\left(\frac{m_o|^{\mathtt{l}}_\star}{\alpha m_o|^{\mathtt{c}}_\star + m_o|^{\mathtt{hc}}_\star + m_o|^{\mathtt{hl}}_\star}\right)\frac{d\chi|^{\mathtt{l}}}{dw^\star}, \tag{8.18}$$

$$\frac{d\chi|^{\mathtt{f}}}{dw^\star} = 0, \tag{8.19}$$

$$\frac{d\chi|^{\mathtt{s}}}{dw^\star} = \left(\frac{\alpha m_o|^{\mathtt{c}} + m_o|^{\mathtt{hc}}}{m_o|^{\mathtt{hc}}}\right)\frac{d\chi|^{\mathtt{h}}}{dw^\star}, \tag{8.20}$$

$$\frac{d\chi|^{\mathtt{m}}}{dw^\star} = \left(\frac{m_o|^{\mathtt{hl}}}{m_o|^{\mathtt{hl}} + m_o|^{\mathtt{l}}}\right)\frac{d\chi|^{\mathtt{h}}}{dw^\star} + \left(\frac{m_o|^{\mathtt{l}}}{m_o|^{\mathtt{hl}} + m_o|^{\mathtt{l}}}\right)\frac{d\chi|^{\mathtt{l}}}{dw^\star}. \tag{8.21}$$

Cunningham and Sprott (1984) have published parameters for a Fink-Jackson model (Fink and Jackson, 1973) of the boundary adsorption isotherm of radiata pine. According to Uprichard (1991) typical dry constituent mass fractions for this material are $m_o|^{\mathtt{c}}_= 0.44$, $m_o|^{\mathtt{hc}}_= 0.16$, $m_o|^{\mathtt{hl}}_= 0.14$ and $m_o|^{\mathtt{l}}_= 0.26$. These results, combined with the boundary adsorption data for a periodate lignin preparation reported by Cousins (1976) can be used to relate lignin moisture content, $w|^{\mathtt{l}}$, to the overall moisture content of the reference material (radiata pine in adsorption), $w^\star$, and thus determine $w|^{\mathtt{h}}$ using (8.6).

The Fink-Jackson model for the sorption-isotherm,

$$\ln(w) = A + B\ln\left(h^{-c} - 1\right), \tag{8.22}$$

is invertible and can be used to model the relationship between $w|^{\mathtt{l}}$ and $w^\star$ by eliminating the relative humidity h, i.e.

$$\ln(w|^{\mathtt{l}}) = A + B\ln\left(\left(\exp\left(\frac{\ln(w^\star) - A^\star}{B^\star}\right) + 1\right)^{c/c^\star} - 1\right). \tag{8.23}$$

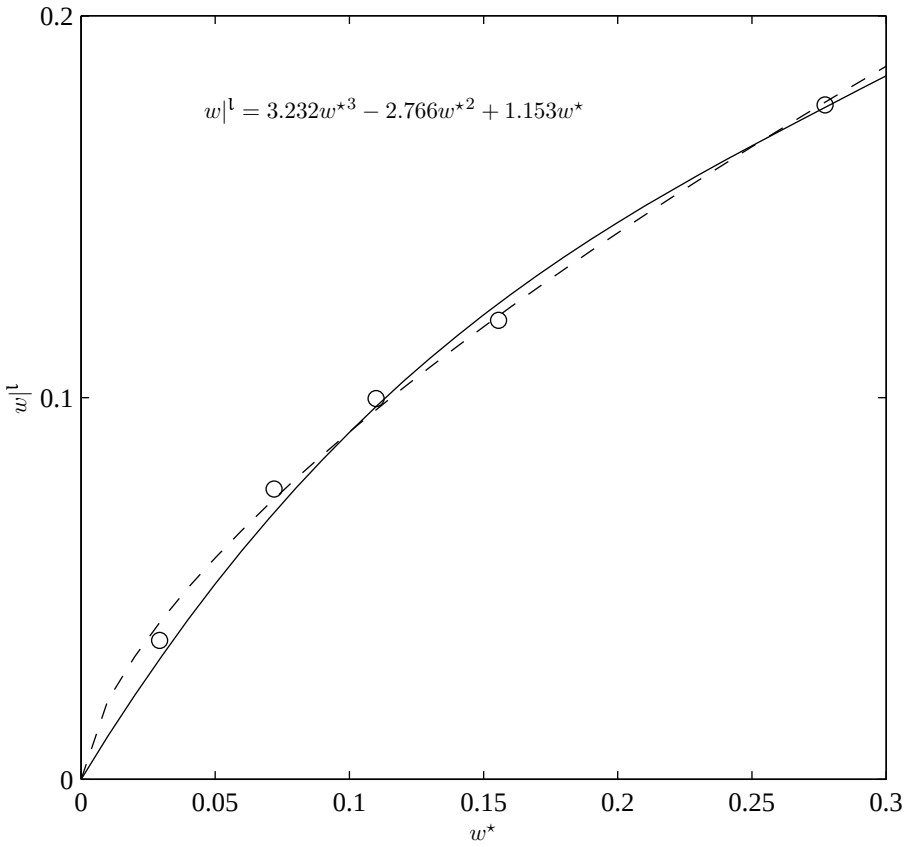

Figure 8.2.: Relationship between the equilibrium moisture content of lignin and radiata pine in boundary adsorption. The dashed line is the model of (8.23). The solid line is the cubic model of (8.24). The data is taken from Cunningham and Sprott (1984) and Cousins (1976).

This model provides a good fit to the data (see figure 8.2), but is somewhat unwieldy and when used in the system of equations (8.6)–(8.11) requires that a numerical method be used to determine $w^\star$ correspodning to a given total moisture content w. Furthermore, at very low moisture contents it produces unrealistic negative values for $w|^{\mathrm{h}}$.

Instead the experimental data, and (eqn:pmdl-wl-wS-model1), can be reasonably represented by a single cubic polynomial,

$$w|^{\mathrm{l}} = a_1 w^\star + a_2 w^{\star 2} + a_3 w^{\star 3} \tag{8.24}$$

with the parameters of table 8.3. This model is also shown in figure 8.2.

a_1	a_2	a_3
1.153	-2.766	3.232

Table 8.3.: Parameters for (8.24).

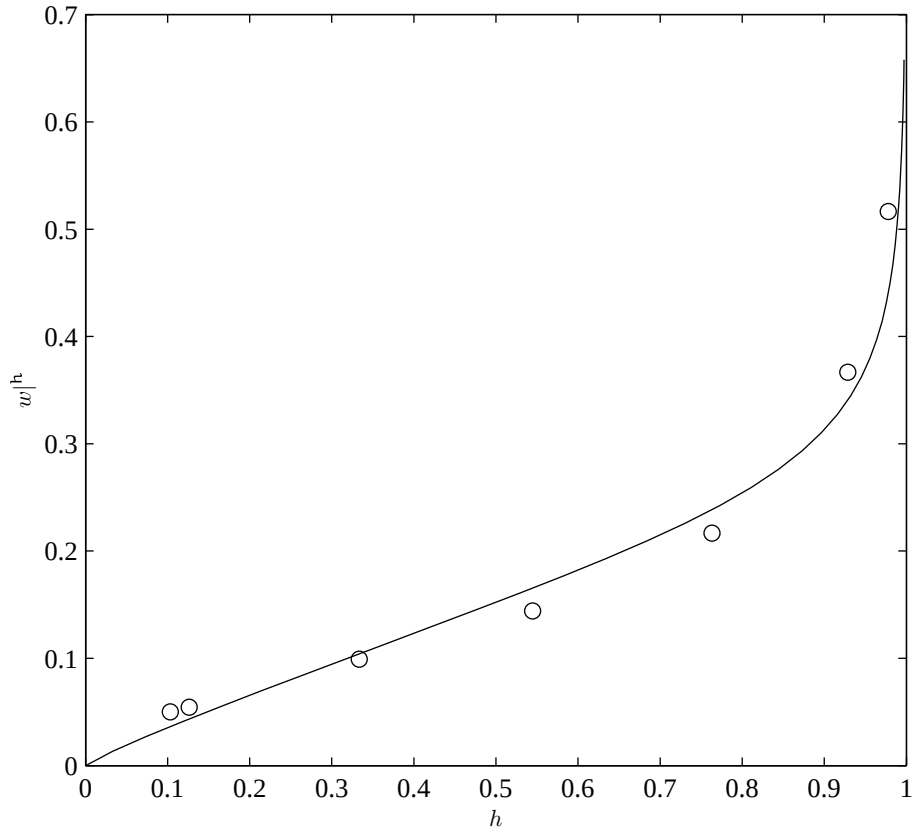

Figure 8.3.: Computed sorption isotherm compared with experimental data from Cousins (1978).

In figure 8.3, the computed carbohydrate sorption isotherm is compared with experimental data for isolated hemicelluloses undergoing boundary adsorption (Cousins, 1978). The model yields acceptable predictions.

In figure 8.4, the ratio of HS to LM hygroscopicity computed from the above equations is plotted for three dry CF mass fractions. The compositional model of chapter 7 was used to fix the values of the other dry consituent mass fractions. The relative hygroscopicity of the HS phase increases with increasing moisture content and the mean value of around 3.3 is significantly higher than the value of 2.6 used in a similar context by Cave (1978a) and Persson (1997).

8.2.1. Density

8.2.1.1. Overall matrix density

Densities for dry, isolated hemicelluloses of between 1.5 and 1.8 g/cc have been reported (Beall, 1972; Seifert, 1972; Kellogg et al., 1975). Lignins in similar conditions have densities of 1.3–1.4 g/cc (Stamm and Sanders, 1966; Stamm, 1969; Seifert, 1972;

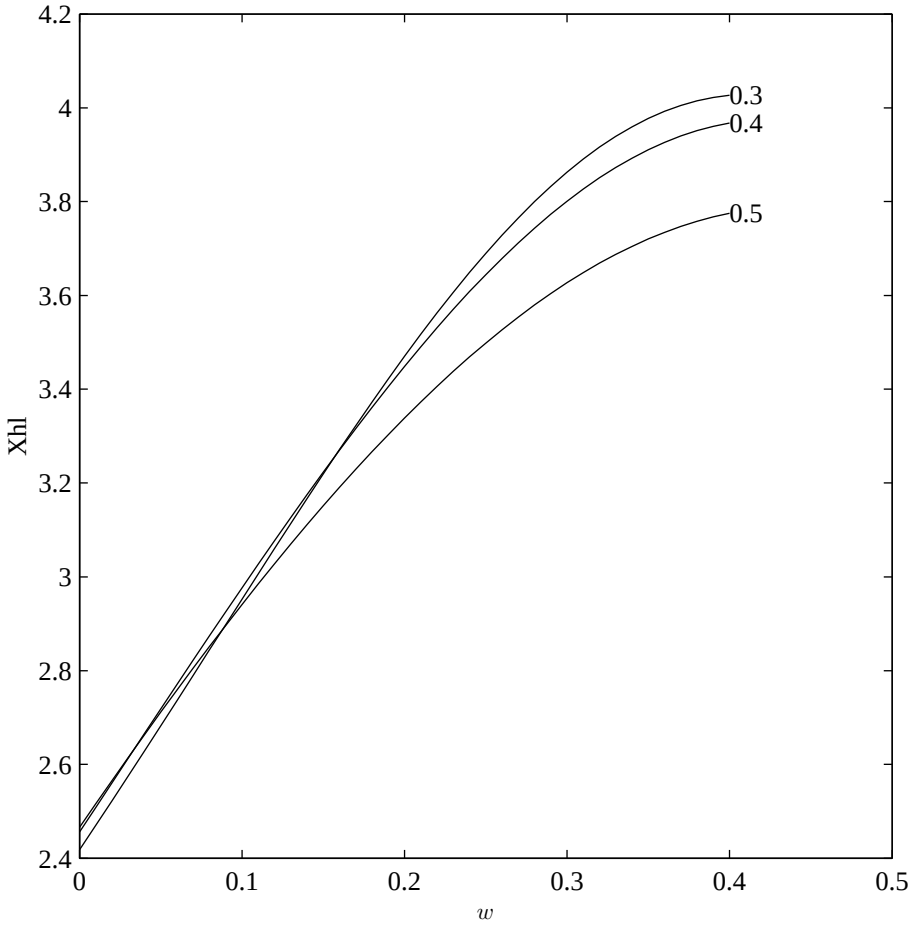

Figure 8.4.: Ratio of HS and LM hygroscopicities vs domain moisture content for various dry CF mass fractions.

Jurasek, 1998a). However, there seems little reason to expect the density of an extracted wall component to be the same as it is *in situ* due to the physical and chemical changes brought about by the extraction process, and while Beall (1972) found good agreement between the extracted constituent densities, the composition and the overall density, Kellogg et al. (1975) has pointed out that this was more than likely fortuitous. Furthermore, while the variation in matrix density with temperature, like the variation in fibre density with temperature, can be neglected, the variation in matrix density with moisture content cannot.

The moist phase densities could be determined by integrating the swelling strains from the dry to the current moist state using the nanostructural hygro-expansional model presented in chapter 3. This approach was taken by Persson (2000). However, in the current context, it has two major drawbacks. Firstly, it neglects the restraint to swelling or shrinkage imposed by structural features at larger scales, for example the resistance to transverse shrinkage in the S2 layer provided by the microfibrils in the S1 and S3 layers[3]. Secondly, as the current nanostructural model considers only linear elastic material behaviour, it neglects strain relaxation due to inelastic mechanisms and the consequent changes in phase densities.

For these reasons it seems preferable not to rely on dry, extracted constituent densities, and instead to take a different approach to the question of matrix density. The mean density of the cell-wall has been determined over a range of moisture contents (Seifert, 1972). If it is assumed that all of wood substance is either matrix or fibre then the mean matrix density can be calculated from the overall density if the mean fibre density and fibre mass fraction are known. This has been done (see appendix L), and as a result the matrix density $\rho|^{\mathsf{M}}$ is modelled as a function of matrix moisture content $w|^{\mathsf{M}}$ by

$$\rho|^{\mathsf{M}} = \frac{1.477(1 + w|^{\mathsf{M}})}{1.058 + w|^{\mathsf{M}} + 0.01382 \ln\left(\exp(34.35 w|^{\mathsf{M}}) + 32.47\right)} \tag{8.25}$$

This result gives the *in situ* overall matrix density and reflects both the nature of the matrix itself, and the degree to which wood structure restrains volumetric changes in the matrix. Obviously it is a mean value and will vary with wood composition and structure. These variations will be small and equation 8.25 provides an acceptable estimate.

8.2.1.2. HS and LM densities

A value of 1.5 g/cc is adopted for the dry HS density $\rho_o|^{\mathsf{hc}} = \rho_o|^{\mathsf{s}}$. This value is in keeping with the values of dry isolated hemicelluloses and is slightly less than the dry

[3]It is possible to include this restraint by iteratively ascending and descending the hierarchical set of models but this is computationally expensive and has not been attempted.

CF density, reflecting the lesser order present in the HS phase.

When dry, the lignins are assumed to have a density of 1.3 g/cc. The dry density of the hemicellulose fraction of the LM phase is then determined such that – for a typical spruce wood composition, $m_o|^{\mathtt{c}} = 0.4$, $m_o|^{\mathtt{hc}} = 0.16$, $m_o|^{\mathtt{hl}} = 0.17$, $m_o|^{\mathtt{c}} = 0.27$ (Sjöström, 1981) – the dry matrix density is that measured by Seifert (1972). This results in $\rho_o|^{\mathtt{hl}} = 1.258$, which is considerably less than the density of isolated hemicelluloses, but not irreconcilable with the notion of the hemicelluloses in the LM phase forming a loose framework upon which the lignins are polymerized (Atalla, 1998). The dry LM specific volume is then

$$\nu_o|^{\mathtt{m}}_{=} \frac{m_o|^{\mathtt{hl}} \nu_o|^{\mathtt{hl}} + m_o|^{\mathtt{l}} \nu_o|^{\mathtt{l}}}{m_o|^{\mathtt{hl}} + m_o|^{\mathtt{hl}}}. \tag{8.26}$$

The moist matrix density can be written as

$$\nu|^{\mathtt{M}} = \frac{\nu_o|^{\mathtt{M}} + w|^{\mathtt{M}} \bar{\nu}|^{w}_{\mathtt{M}}}{1 + w|^{\mathtt{M}}} \tag{8.27}$$

in which $\bar{\nu}|^{w}_{\mathtt{M}}$ is the apparent specific volume of the bound moisture. Assuming that the apparent specific volume of the water held by any constituent fraction is the same, i.e. $\bar{\nu}|^{w}_{\mathtt{M}} = \bar{\nu}|^{w}_{\mathtt{s}} = \bar{\nu}|^{w}_{\mathtt{m}}$, allows the moist specific volumes of the nanophases to be calculated using relations of the same form as (8.27).

Using the compositional model of chapter 7, the nanophase hygroscopicities of §8.2.0.1 and the assumptions and relationships described above, the overall density of a nanostructural cell wall domain, the overall matrix density and the HS and LM phase densities can be related to the dry CF mass fraction and overall moisture content. These relationships are plotted in figure 8.5.

8.2.2. Matrix phase elastic moduli

8.2.2.1. A polymer modulus model

Extracted from wood, hemicelluloses and lignins behave in a manner typical of amorphous polymers (Cousins, 1978; Sakata and Senju, 1975; Salmén and de Ruvo, 1985; Salmén and Olsson, 1998). Broadly speaking the effects of increasing temperature on such materials are:

(i) an increase in the molecular mobility,

(ii) a decrease in the interatomic forces, particularly the nonbonded forces,

(iii) and an increase in the molecular spacing.

Similarly the effects of increasing moisture content are:

(i) an increase in the molecular mobility,

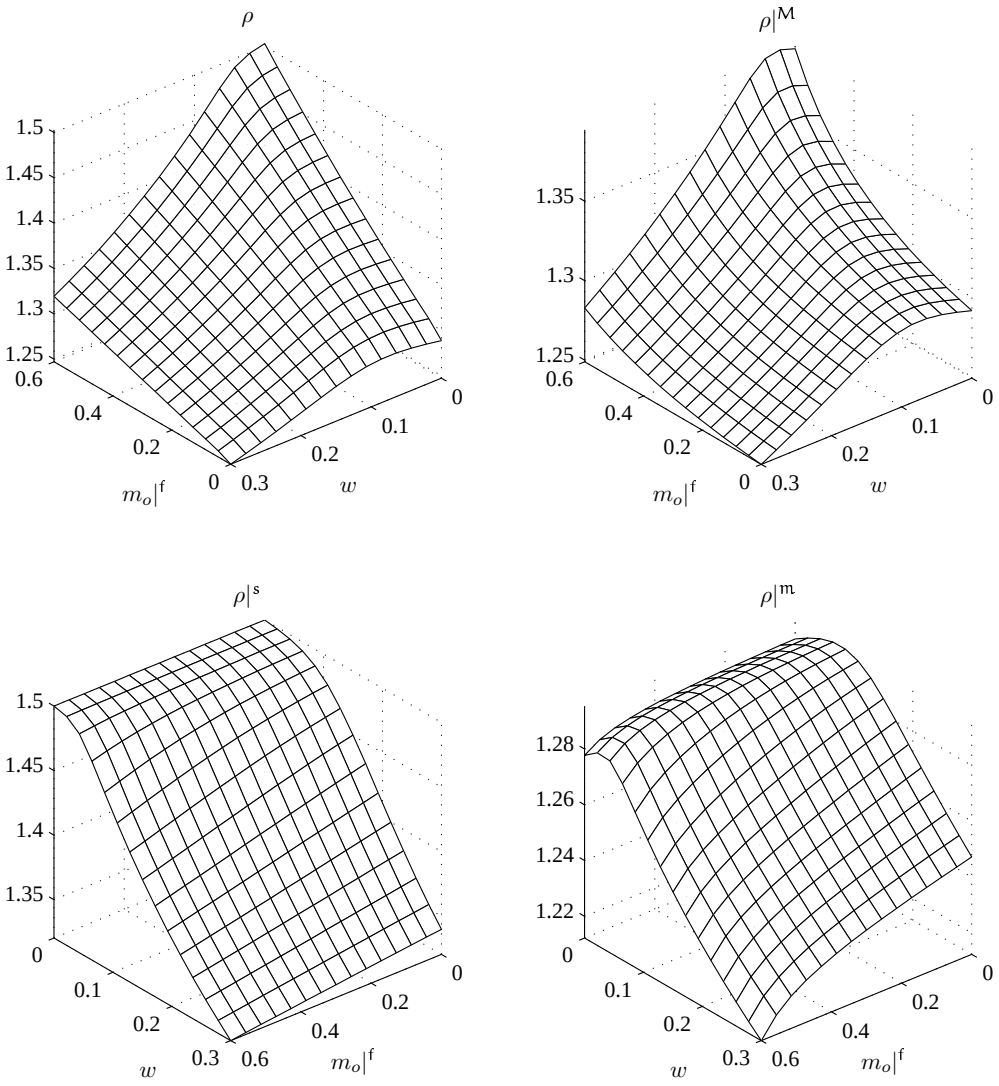

Figure 8.5.: Density of a nanostructural domain and subdomains.

(ii) a dilution of the structure resulting in less load carrying material per unit volume,

(iii) and changes in the non-covalent bond interactions, particulary the replacement of polymer-polymer hydrogen bonds with polymer-water bonds.

Both increasing temperature and increasing moisture content enhance the polymer motility, lessening the time required to attain equilibrium and reducing the apparent modulus. The transition from a glassy to a rubbery state is the most significant consequence of this increasing molecular freedom. In the region of the glass transition the moduli drop dramatically and are strongly time dependent. For linear polymers such as hemicelluloses this drop can be by a factor of 1000 or more (Haward and Young, 1997). For cross-linked polymers such as lignin it is less, usually around a decade (Gibson and Ashby, 1997) and occurs over a broader region (Nielsen and Landel, 1994).

Cousins and colleagues (Cousins et al., 1975; Cousins, 1976, 1977, 1978) determined, by way of tensile, torsion and indentation tests, the elastic modulus of lignin and hemicellulose preparations from radiata pine over a range of relative humidities at ambient temperature.

To make the fullest use of this experimental data, the following model is proposed for the modulus of lignin and hemicellulose extracted from wood,

$$\frac{E(T,w)}{E_o(T)} = \begin{cases} f_g(w) & T \leq T_g(w) \\ f_r(w) & T > T_g(w) \end{cases} \tag{8.28}$$

where E_o, f_g, f_r and T_g are prescribed functions of temperature, T, and moisture content, w. Respectively these functions represent the dry modulus, the moist modulus in the glassy regime and the moist modulus in the rubbery regime as functions of temperature, and the glass transition temperature as a function of moisture content.

In the glassy regime the decrease in the modulus of an amorphous polymer with increasing temperature is approximately linear (Gibson and Ashby, 1997). Once a constituent has entered the rubbery state its contribution to wood stiffness becomes insignificant, and its further variation is of little interest. Hence a crude model for the dry modulus, E_o, as a function of temperature, T is,

$$E_o(T) = \begin{cases} E^0_{g,o} - a\frac{T-T_0}{T_{g,o}} & T \leq T_{g,o} \\ E_{r,o} & T > T_{g,o}. \end{cases} \tag{8.29}$$

$E^0_{g,o}$ is the dry modulus at the reference temperature T_0, and $T_{g,o}$ is the dry glass transition temperature. Gibson and Ashby (1997) suggest that $a \approx 0.5$. The model of Batten and Nissan (1987a) for the variation of modulus of a hydrogen bond dominated solid is available for temperatures below that of the glass transition. It has not been used as the number of hydrogen bonds per unit volume has not been determined.

Like the variation of modulus with temperature in the rubbery regime, the variation with moisture content is of little interest here. Consequently $f_r = 1$.

This model has a physically unrealistic step change in properties across the glass transition; whereas in reality this change is smooth. There are various ways in which the transition from the glassy to rubbery state could be modelled, however, for the moment it is convenient to retain the step change as it makes the phase transitions easy to identify in macroscopic results.

8.2.2.2. Glass transition

The glass transitions of lignins, hemicelluloses and wood have been investigated and discussed by, amongst others, Goring (1963); Sakata and Senju (1975); Salmén and Back (1977); Salmén (1984, 1990); Back and Salmén (1982); Irvine (1984); Kelley et al. (1987); Olsson and Salmén (1997). When dry, the softening temperature is high (130–220°C) for both lignins and hemicelluloses. With increasing moisture content the transition temperatures are depressed and when fully saturated the hemicellulose transition occurs below ambient temperature, and the lignin transition at around 90°C. The temperature at which the softening occurs depends strongly on the characteristic time (or frequency).

Kelley et al. (1987) used dynamic mechanical thermal analysis and differential scanning calorimetry to investigate the viscoelastic properties of spruce wood. They detected two glass transitions, which they assigned to the hemicelluloses and lignins. However, these transitions can also be interpreted as the glass transitions of the HS and LM phases.

A number of models have been developed for the prediction of the effects of a diluent or plasticizer on the glass transition temperature (Nielsen and Landel, 1994; Painter and Coleman, 1997). One such model, which incorporates the effects of secondary interactions between the diluent and polymer, is the Kwei equation (Kwei, 1984) which can be written in the form

$$T_g = \frac{T_{g,o} + kwT_{g,w}}{1 + kw} + q\frac{w}{(1+w)^2} \tag{8.30}$$

where $T_{g,o}$ is the dry glass transition temperature, $T_{g,w}$ is the glass transition temperature of water – taken to be 136°K (Salmén and Back, 1977) – and k and q are parameters. Kelley et al. (1987) found this model gave an excellant fit to their data.

Kelley et al. (1987) fit (8.30) to their T_g data, with total wood moisture content as the independent variable. Herein, the HS and LM phase glass transition temperatures as functions of phase, rather than total, moisture content are desired. These have been obtained by refitting the glass transition temperature data of Kelley et al. (1987) to the phase moisture contents computed using the hygroscopicity models described

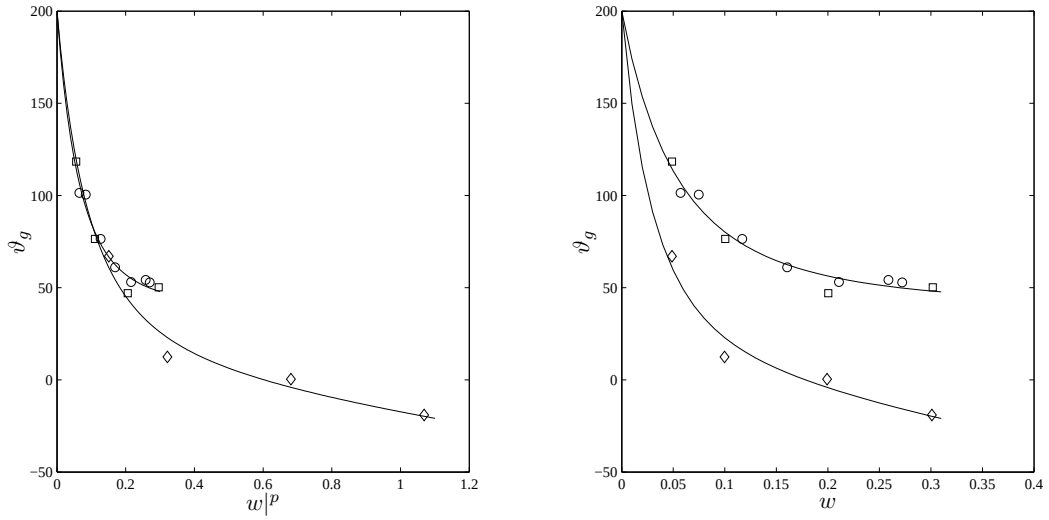

Figure 8.6.: HS and LM glass transition temperatures as functions of total and phase moisture content.

above, assuming a typical composition for spruce wood of $m_o|^{\mathtt{c}} = 0.4$, $m_o|^{\mathtt{hc}} = 0.16$, $m_o|^{\mathtt{hl}} = 0.17$ and $m_o|^{\mathtt{l}} = 0.27$ (Sjöström, 1981). The best fit parameters appear in table 8.4, and the data and models are plotted against phase and total moisture contents in figure 8.6.

	$T_{g,o}$ °K	$T_{g,w}$ °K	k	q °K
HS	473.0	136.0	7.136	313.0
LM	473.0	135.9	8.866	523.2

Table 8.4.: Parameters for use with Kwei equation (8.30).

8.2.2.3. HS elastic moduli

Cousins (1978) measured the Young's modulus of samples prepared from hemicelluloses extracted from radiata pine at various moisture contents and ambient temperature. These measurements are reproduced in figure 8.7.

At ambient temperatures and saturated moisture contents hemicelluloses exist in the rubbery state. Cousins measured a modulus of 0.01 GPa for these conditions, hence $E_{r,o}|^{\mathtt{s}} = 0.01$ GPa.

Batten and Nissan (1987a) proposed that, for materials such as hemicelluloses whose mechanics are dominated by hydrogen bonding, the modulus and moisture con-

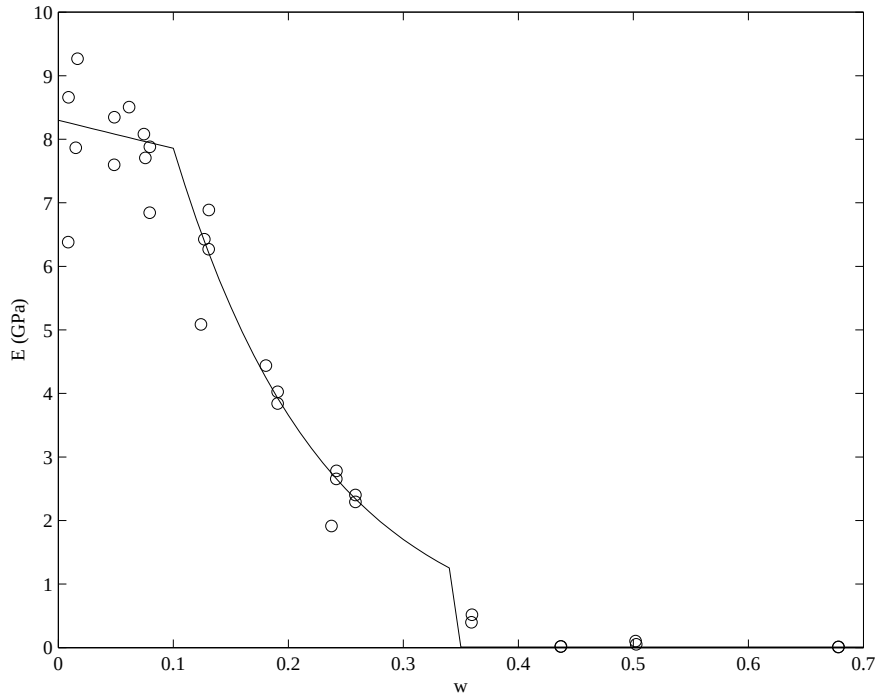

Figure 8.7.: Relationship between Young's modulus and moisture content for hemicellulose preparations at ambient temperature. Data from Cousins (1978).

tent could be related by

$$3a_2 \ln f_g|_{\cdot}^{\mathrm{s}} = \begin{cases} -w & w \leq a_1 \\ a_1(a_3 - 1) - a_3 w|_{\cdot}^{\mathrm{s}} & w > a_1 \end{cases} \tag{8.31}$$

This model, with the parameters given in table 8.5, fits the experimental data of Cousins (1978) well as demonstrated in figure 8.7.

The Poisson's ratio for hemicellulose has not been measured. Generally amorphous glassy polymers have a Poisson's ratio in the range 0.3–0.4 (Nielsen and Landel, 1994). Herein, a value of 0.3 is assumed.

The extracted hemicellulose samples tested by Cousins were believed to be isotropic. *In situ* the hemicelluloses constituting the HS phase are oriented, at least to some extent, in parallel with the microfibrils. The effects of uniaxial orientation on the mechanical behaviour of polymers has been studied extensively as it is the mechanism by which the so-called ultrahigh modulus synthetic fibres are produced as well as being a consequence, often undesirable, of a number of manufacturing processes. According to Nielsen and Landel (1994) the principal effect of orientation is to increase the Young's modulus in the draw direction, E_l, compared to that of the unoriented material, $\bar{E}$. This increase in modulus is due to the increasing contribution of the stiffer intramolecular bonds. The longitudinal-transverse shear modulus, G_{lt}, is also raised for the same

reason, though to a lesser degree. On the other hand, the transverse Young's modulus, E_t, and the transverse shear modulus, G_{tt}, are reduced, though the decrease is less than the associated increase in the draw direction, as while the intra-molecular bond contribution is decreased these moduli remain governed by intermolecular forces. The effect on the Poisson's ratios are not well known, and is probably slight.

In keeping with these facts, it is assumed that the elastic compliance matrix of a hypothetical sample of perfectly oriented hemicelluloses has the form

$$\mathbf{D} = \frac{1}{E_1}\begin{bmatrix} 1 & -\nu_{12} & -\nu_{12} & 0 & 0 & 0 \\ -\nu_{12} & 1 & -\nu_{12} & 0 & 0 & 0 \\ -\nu_{12} & -\nu_{12} & 1/N & 0 & 0 & 0 \\ 0 & 0 & 0 & 2(1+\nu_{12}) & 0 & 0 \\ 0 & 0 & 0 & 0 & 2(1+\nu_{12}) & 0 \\ 0 & 0 & 0 & 0 & 0 & 2(1+\nu_{12}) \end{bmatrix}. \tag{8.32}$$

Then, for the isotropic average compliances (see appendix B) to yield the experimentally determined modulus $\bar{E}$ and assummed Poisson's ratio $\bar{\nu}$, E_1 and ν_{12} must be

$$\begin{aligned} E_1 &= \frac{(4N+1)\bar{E}}{5N} \\ \nu_{12} &= \frac{(12N+3)\bar{\nu} - N + 1}{15N}. \end{aligned} \tag{8.33}$$

The parameter N describes the relative stiffness along the chain direction compared to the stiffness in the plane normal to the hemicellulose chains. Reasonable estimates for N lie between 5 and 15. For the elastic properties of the perfectly oriented material to be positive definite,

$$\begin{aligned} &E_1 > 0, \\ &\nu_{12} > -1, \\ &1 + N(1-\nu_{12}) \pm \sqrt{(9\nu_{12}^2 - 2\nu_{12} + 1)N^2 + 2(\nu_{12}-1)N + 1} > 0. \end{aligned} \tag{8.34}$$

If the degree of orientation of the hemicelluloses were known *in situ*, then one of various models for predicting the properties of uniaxially oriented polymers (Ward, 1997) could be used to determine the properties of the HS phase. No such data is available and hence it is assumed that the HS phase elastic compliances are given by (8.32) and (8.33) with $N = 7$.

8.2.2.4. LM phase elastic moduli

As described in chapter 3, the LM phase is believed to consist of crosslinked ellipsoidal lignin particles polymerized within and chemically bonded to a hemicellulose frame-

T_0 (°K)	$E^0_{g,o}$	a_1	a_2 (°K)	a_3 (GPa)	$E_{r,o}$	ν	n	(GPa)
293	8.1	0.1	0.61	14	0.01	0.3	7	

Table 8.5.: Parameters for the HS phase elastic property model.

T_0 (°K)	$E^0_{g,o}$	a_1 (°K)	a_2 (GPa)	a_3	$E_{r,o}$	ν	(GPa)
293	5.68	4.17	30.8	27.4	0.1	0.4	

Table 8.6.: Parameters for the lignin elastic property model.

work. Previously the LM phase has been treated as heterogenous (Harrington et al., 1998), however, if it is agreed that the observed glass transitions can be attributed to the HS and LM phases, then the lack of a third glass transition that could attributed to the LM hemicelluloses, which exist in a different environment to the HS hemicelluloses and hence should have a different T_g, can be interpreted to mean that, from a mechanical point, the LM phase is homogeneous. Currently, the LM phase is assumed to be isotropic and have properties similar to those of extracted lignins.

The Young's modulus and shear modulus of a number of lignin preparations over a range of moisture contents have been reported by Cousins et al. (1975); Cousins (1976, 1977). The Young's modulus data for periodate lignin, the preparation believed to have properties most similar to those of native lignins, is reproduced in figure 8.8. At room temperature, the variation in Young's modulus with moisture content relative to the dry modulus is well approximated by a function of the form

$$f_g|^{\mathfrak{m}}_{\cdot} = \left(\frac{1}{1 + a_1 w|^{\mathfrak{m}}_{\cdot}}\right)^2 + \frac{a_2 w|^{\mathfrak{m}}_{\cdot}}{\exp(a_3 w|^{\mathfrak{m}}_{\cdot})}. \tag{8.35}$$

This model, with the parameters of table 8.6, is also plotted in figure 8.8.

If the Poisson's ratio is calculated from the Young's modulus and shear modulus measurements determined by Cousins then values of 0.4–0.8 are obtained. Generally glassy polymers have a Poisson's ratio in the range 0.3–0.4 (Nielsen and Landel, 1994), and if a material is isotropic then the Poisson's ratio must be less than 0.5 (Lai et al., 1993). As Cousins pointed out, the computed Poisson's ratio is unreliable as it sensitive to small experimental errors in the moduli. Conversely, if the shear modulus is computed from the Young's modulus its value is little affected by small changes in the Poisson's ratio. A constant Poisson's ratio of 0.4 is assumed for the LM phase, independent of temperature and moisture content.

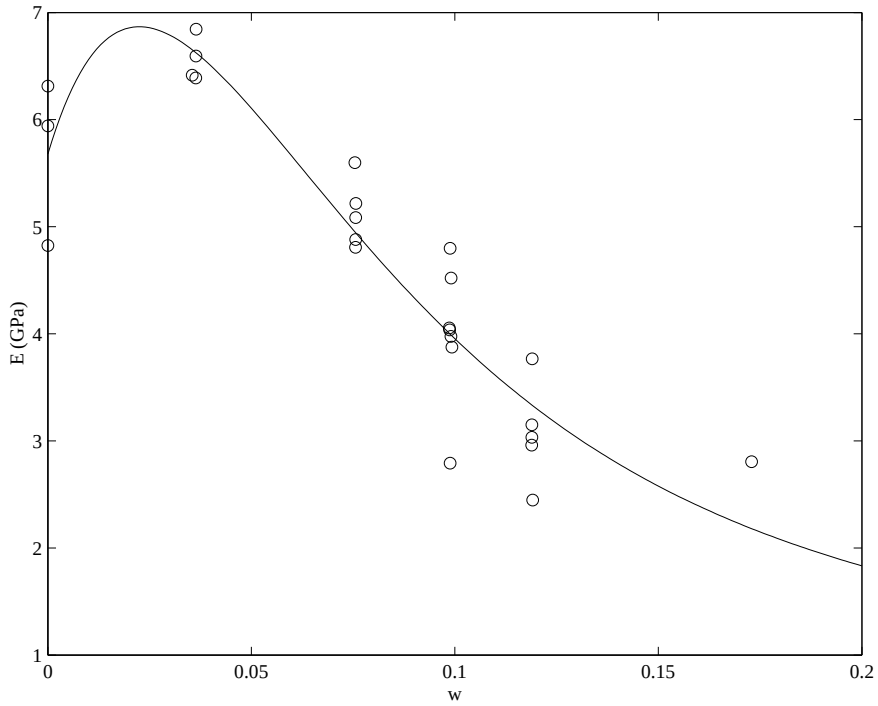

Figure 8.8.: Relationship between Young's modulus and moisture content for periodate lignin preparations at ambient temperature. Data from Cousins et al. (1975); Cousins (1976, 1977).

8.2.3. Hygral expansion coefficients

8.2.3.1. Phase volumetric hygro-expansion coefficients

The change in specific volume of isolated hemicelluloses and lignins with moisture content has been investigated by Christensen and Kelsey (1959) and Seifert (1972). Christensen and Kelsey (1959) found that the swelling of lignin preparations was less than the free volume of the moisture sorbed, with the deficit being greatest at low moisture contents and at moisture contents approaching saturation. Seifert (1972) also found this to be the case at low moisture contents.

The coefficient of volumetric hygral expansion α_V^w is related to the specific volume ν by

$$\alpha_V^w = \frac{1}{1+w} + \frac{1}{\nu}\left(\frac{\partial \nu}{\partial w}\right)_{\boldsymbol{\sigma},\vartheta}. \tag{8.36}$$

If the specific volume is written as

$$\nu = \frac{\nu_o + \int_0^w \nu^w}{1+w} \tag{8.37}$$

where ν_o is the dry specific volume and ν^w is the apparent specific volume of an in-

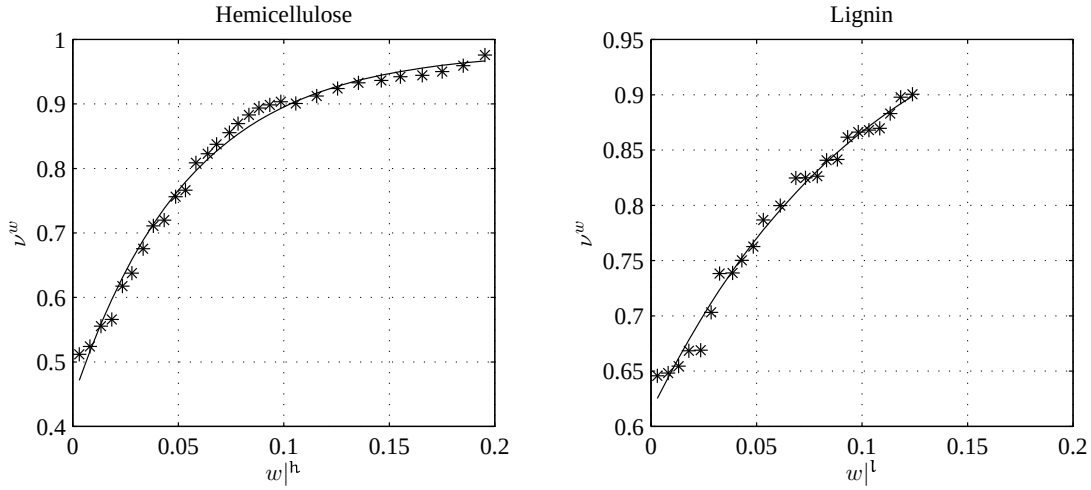

Figure 8.9.: Apparent specific volume of adsorbed water in hemicellulose and lignin. Data from Seifert (1972). Model according to (8.39).

finitesimal increment of water, then

$$\alpha_V^w = \frac{\nu^w}{\nu_o + \int_0^w \nu^w}. \tag{8.38}$$

An exponential model,

$$\nu^w = a_2 - a_1 \exp(-a_3 w), \tag{8.39}$$

with the parameters of table 8.7 provides an adequate fit to the data of Seifert (1972) ν^w for sorption by hemicellulose and lignin (see figure 8.9). With this model,

$$\alpha_V^w = \frac{a_3(a_2 - a_1 \exp(-a_3 w))}{a_3\nu_o + a_2 a_3 w - a_1(1 - \exp(-a_3 w))}. \tag{8.40}$$

	a_1 cc/g	a_2 cc/g	a_3
hemicellulose	0.542	0.990	17.4
lignin	0.440	1.06	8.45

Table 8.7.: Parameters for equations (8.39) and (8.40).

8.2.3.2. Phase linear hygro-expansional coefficients

For small strains

$$\alpha_V^w \approx \alpha_1^w + \alpha_2^w + \alpha_3^w. \tag{8.41}$$

Following Cave (1978a), it is assumed that the swelling of the HS phase – within which the hemicelluloses are assumed to be perfectly aligned – takes place only in the plane normal to the chain direction. Thus, the hygroexpansional strains in the HS phase are given by

$$\boldsymbol{\alpha}^w|^{\mathrm{s}} = \frac{\alpha_V^w|^{\mathrm{s}}}{2}\begin{bmatrix}1 & 1 & 0 & 0 & 0 & 0\end{bmatrix}^{\mathrm{t}}. \tag{8.42}$$

The LM phase is assumed to swell isotropically, thus

$$\boldsymbol{\alpha}^w|^{\mathrm{m}} = \frac{\alpha_V^w|^{\mathrm{m}}}{3}\begin{bmatrix}1 & 1 & 1 & 0 & 0 & 0\end{bmatrix}^{\mathrm{t}}. \tag{8.43}$$

8.3. Summary and future work

In this chapter, models have been presented for the densities, elastic coefficients and hygro-expansional coefficients of the CF, HS and LM nanophases. These models have included, for the first time, the effects of temperature as well as moisture content on the nanophase properties.

The models presented have, for the most part, been based on experimental measurements made on extracted wood components. If this approach is to be taken further it will be necessary to make more of measurements of the

- sorption characteristics,
- elastic properties,
- hygro- and thermo-expansional coefficients,

over the full range of temperatures and moisture contents on samples representing the nanophases. These samples must be prepared in such a way as to minimise the chemical and physical differences between the isolated components and their *in situ* counterparts. It will also be necessary to investigate the time dependent behaviour and the effects of stress. Since these experiments are costly, the models of this thesis could be used to identify those properties which have the most significant influence on macroscopic behaviours of interest.

Possible alternative – and complementary – approaches to determining the nanophase properties that could be investigated in the future include:

- *In-situ* measurements using nanomechanical tools such as scanning-probe microscopes and coupled strain-diffraction and strain-spectroscopic techniques (e.g. the diffraction analysis employed by Kisi and Howard (1998); Howard and Kisi (1999)).

- Refining the parameters of the current models against a comprehensive dataset that included structural and mechanical measurements for particular macroscopic wood samples.

- Molecular modelling of the nanophases and of nanostructural domains. This approach has the added advantage that it would allow the effects of chemical changes on mechanical properties to be considered directly.

In the current work it has been tacitly assumed that the nanophases have the same properties everywhere. This assumption seems quite reasonable for the cellulosic fibre phase but, in light of the known chemical heterogeneity, is more questionable for the matrix phases. In the future, the validity of this assumption could be investigated.

Chapter 9

Results

Except for the finite element homogenization code, PPHMG, and mesh generation tools, the models presented in the preceding chapters have been implemented as Matlab scripts. Collectively these scripts are referred to as WMDL. This implementation is modular, built around a material data structure, and has proved to be flexible and easily maintained. Its only significant drawback is its computational efficiency. To compute the properties of a single cellular domain takes around 12 seconds using WMDL. An alternate fortran 90 implementation requires less than a tenth of this time, although it supports only a subset of WMDL's capabilities.

To demonstrate the use of combined models, and the WMDL toolkit, the variation in the effective hygroelastic properties of homogeneous cellular domains with density, S2 microfibril angle, temperature and moisture content have been computed and the results are presented in figures 9.1–9.14.

These four parameters have been chosen since they are considered to be amongst the most significant, in that wood properties are sensitive to variations in them, and in practice they vary substantially. They are also the model parameters most likely to be known for a particular sample.

In practice moisture content and temperature cannot easily be prescribed independently. Moreover, as the temperature increases, the equilibrium moisture content at any fixed water activity decreases. However, all combinations of temperature and moisture content can occur in non-equilibrium processes, particularly during drying. Hence, moisture content and temperature are treated as being independent, and at all temperatures, moisture content ranges from 0–0.3 g/g (0.3 g/g being the nominal fibre saturation point at ambient temperatures) are considered.

There are a number of points to note regarding the particular combination of models and model parameters employed.

- The HH3 model has been used at the nanostructural level.
- Wall layer volume fractions used are based on the data of Grozdits and Ifju (1984) (see table 6.2).

- The s1cell model with a moderately round internal geometry has been used at the cellular scale. The external tracheid geometric parameters used are those of the intra-ring model (see table 5.1).

- The values of density considered correspond to typical low and high values in each of the six intra-ring zones. These values appear in table 9.1.

	EW					LW
ring coord. (RC)	0.1	0.4	0.7	0.85	0.925	0.975
low density (g/cc)	0.3	0.3	0.35	0.4	0.45	0.5
high density (g/cc)	0.4	0.5	0.6	0.65	0.7	0.85

Table 9.1.: Ring coordinates and densities.

- Ray tissue has not been included.

In general the values and trends of the plots of figures 9.1–9.14 are reasonable. The softening behaviour is not well represented, with the apparent fibre saturation point occuring at values much less than would be expected. This is due to the abrupt transition from the glassy to rubbery state used in the current modulus model for the matrix phases, as well as the choice of hygroscopicity parameters – the values used overemphasizing the HS phase sorption and hence shifting the HS phase glass transition to lower overall moisture contents.

It must be remembered that the purpose of presenting the results of this chapter was to demonstrate the cumulative capabilities of the models and that the results presented correspond to one particular set of parameters. To alter these parameters is a simple matter.

Two major modes of use are envisaged for these models: speculation and simulation. Speculation mode encompasses uses such as identifying significant influences on a particular overall property or determining the effect of a proposed structural modification on the overall properties. Simulation mode involves using the models to predict the properties of a specific sample, perhaps to use as input to a macroscopic finite element model.

Validation is an essential aspect of every modelling study. Validation can be undertaken in two stages. The first stage involves assuring that the models are conceptually correct and that their implementation coincides with their conception. For the models contained herein, conceptual validation equates to demonstrating that they are mathematically correct and physically reasonable. Based on the discussion and results presented in preceding chapters, as well a numerous tests and comparisons not reported, it is believed that the current models meet the requirements of the first stage of validation.

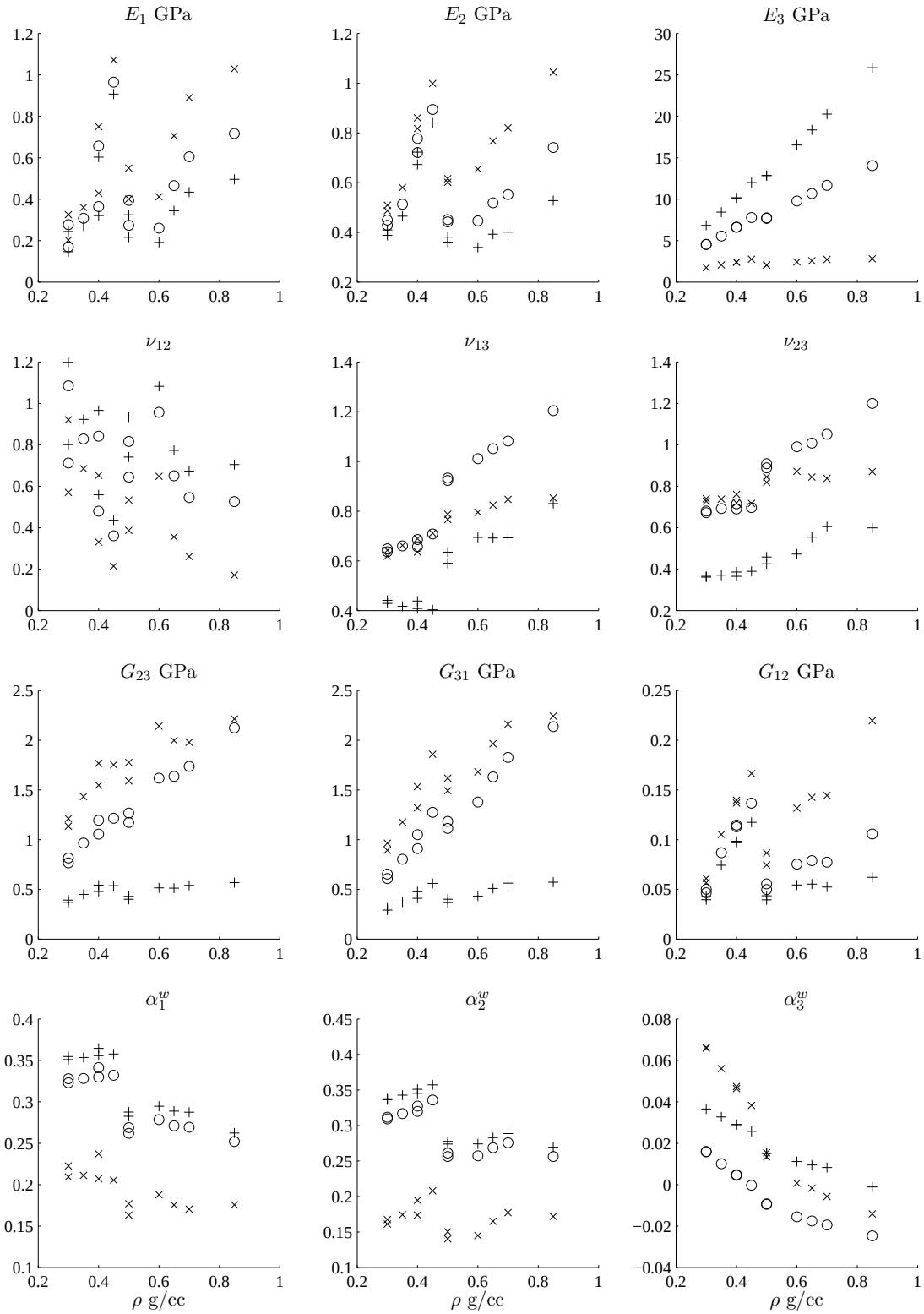

Figure 9.1.: Variation in properties with density ρ. Ambient temperature, air dry conditions ($\vartheta = 22°\mathrm{C}$, $w = 0.1$). S2 MFA: + 5.6°, ∘ 22°, × 39°.

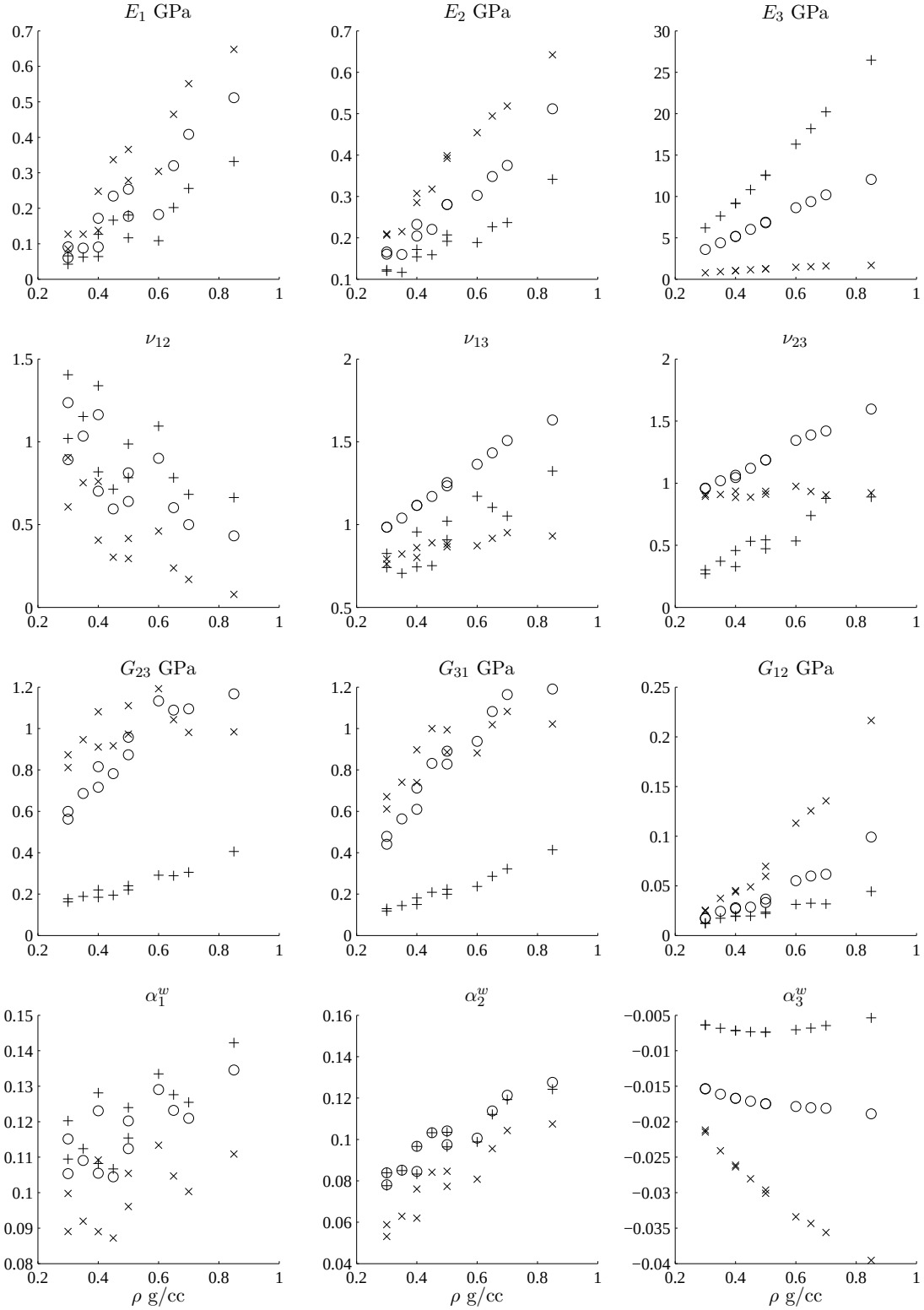

Figure 9.2.: Variation in properties with density ρ. Ambient temperature, saturated conditions ($\vartheta = 22°$C, $w = 0.3$). S2 MFA: + 5.6°, ∘ 22°, × 39°.

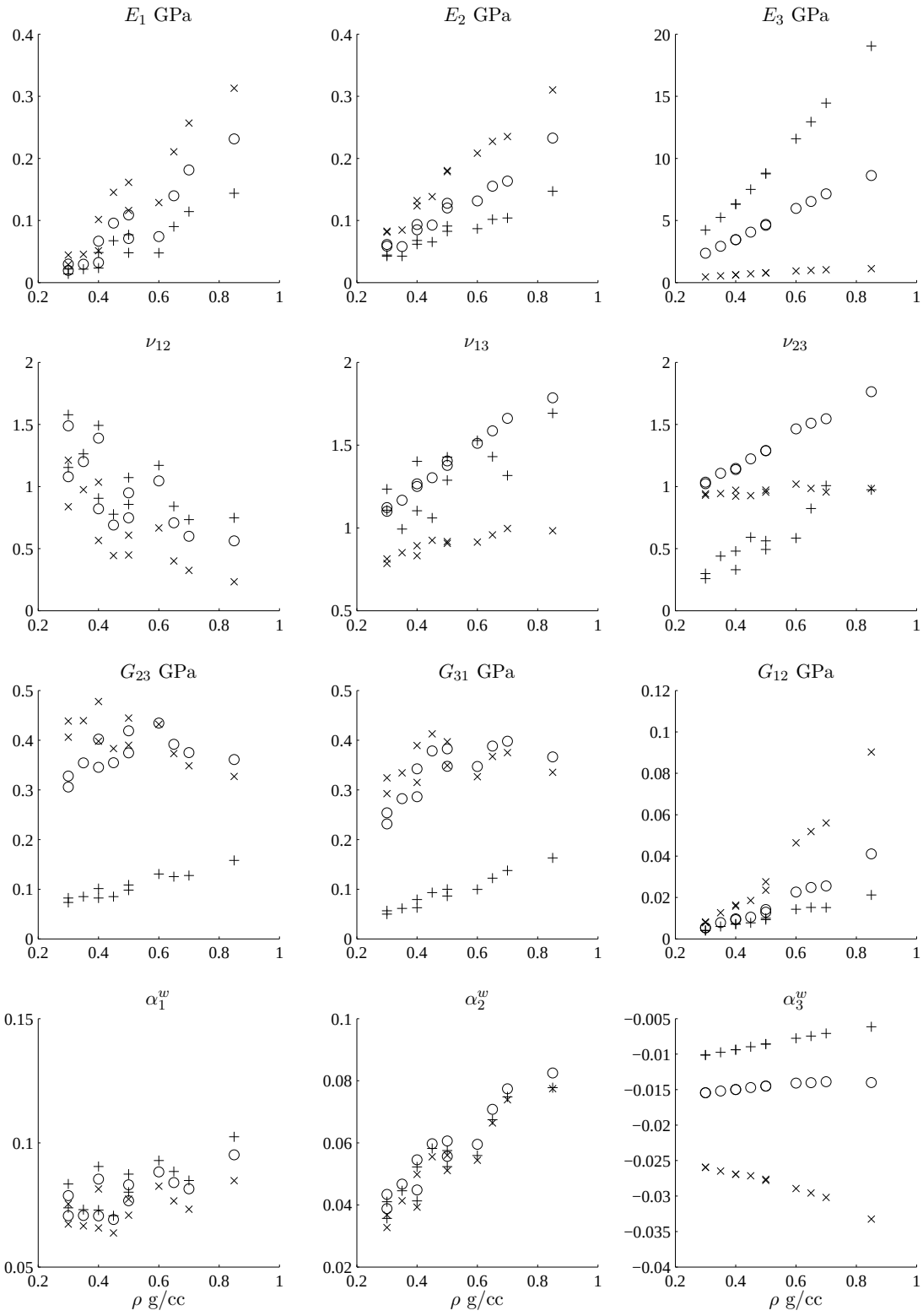

Figure 9.3.: Variation in properties with density ρ. High temperature, saturated conditions ($\vartheta = 110°$C, $w = 0.17$). S2 MFA: + 5.6°, ∘ 22°, × 39°.

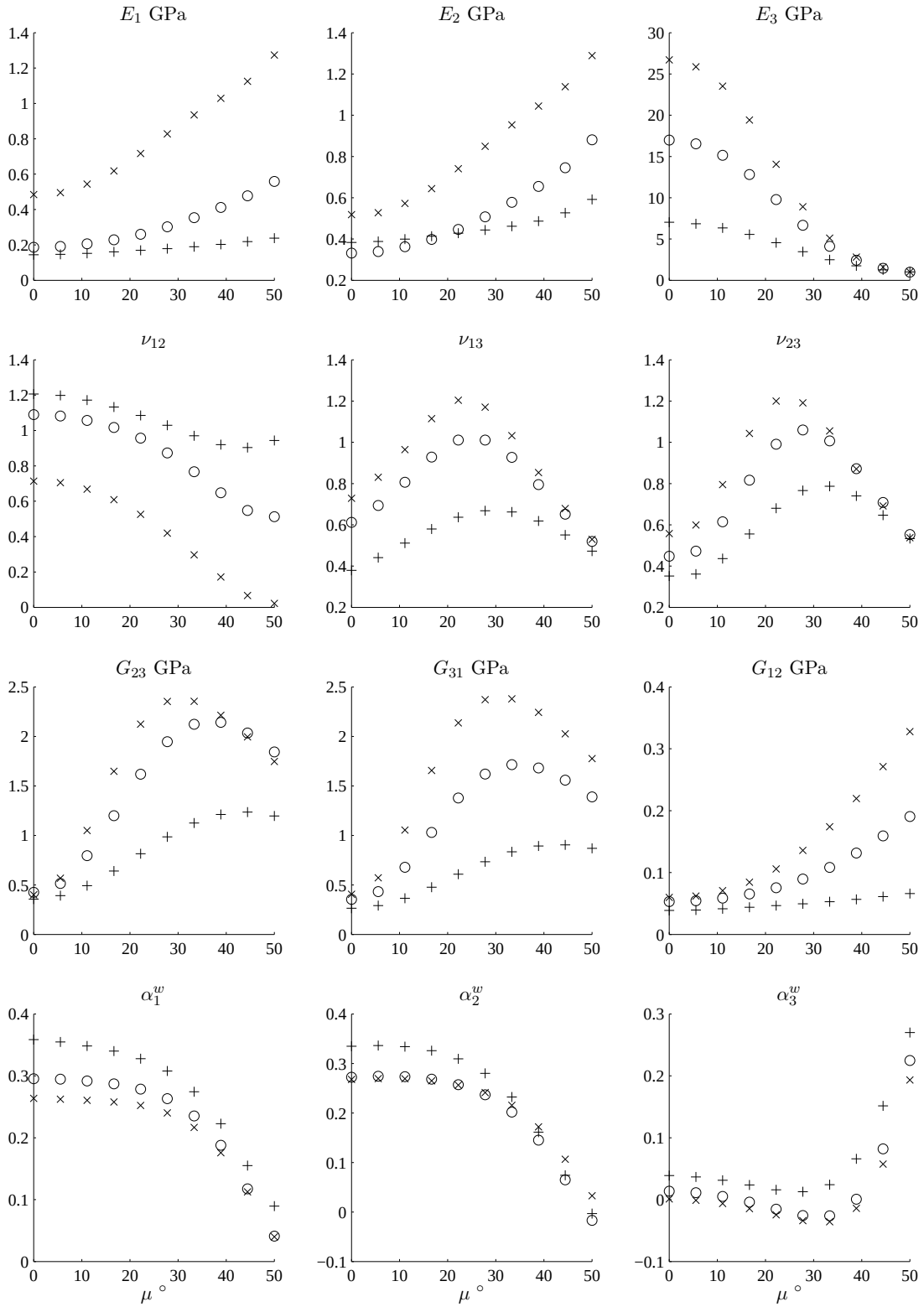

Figure 9.4.: Variation in properties with S2 MFA μ. Ambient temperature, air dry conditions ($\vartheta = 22°$C, $w = 0.1$). + earlywood (RC $= 0.1$, $\rho = 0.3$ g/cc), ∘ middlewood (RC $= 0.7$, $\rho = 0.6$ g/cc), × latewood (RC $= 0.975$, $\rho = 0.85$ g/cc).

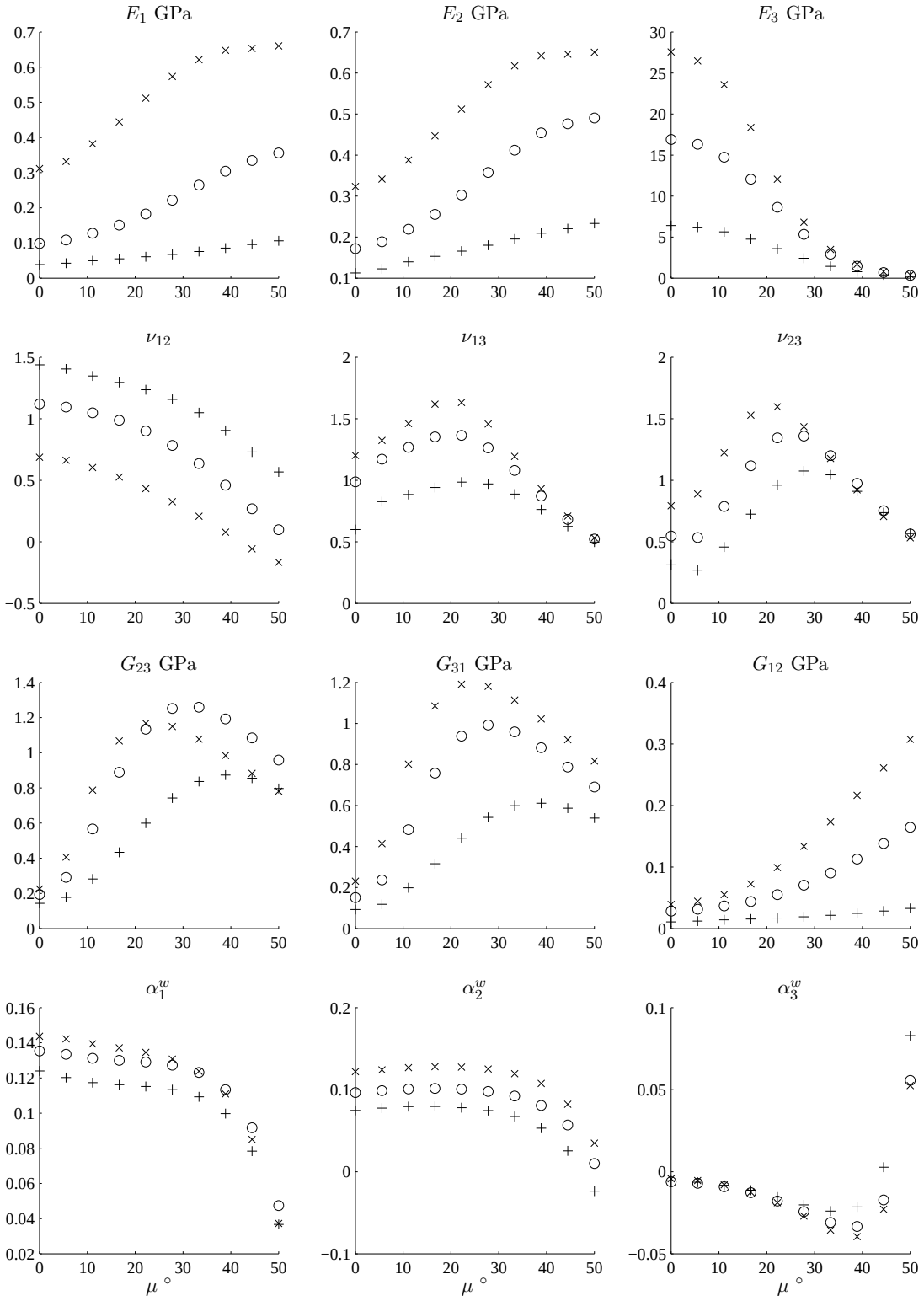

Figure 9.5.: Variation in properties with S2 MFA μ. Ambient temperature, saturated conditions ($\vartheta = 22°$C, $w = 0.3$). + earlywood (RC = 0.1, $\rho = 0.3$ g/cc), ∘ middlewood (RC = 0.7, $\rho = 0.6$ g/cc), × latewood (RC = 0.975, $\rho = 0.85$ g/cc).

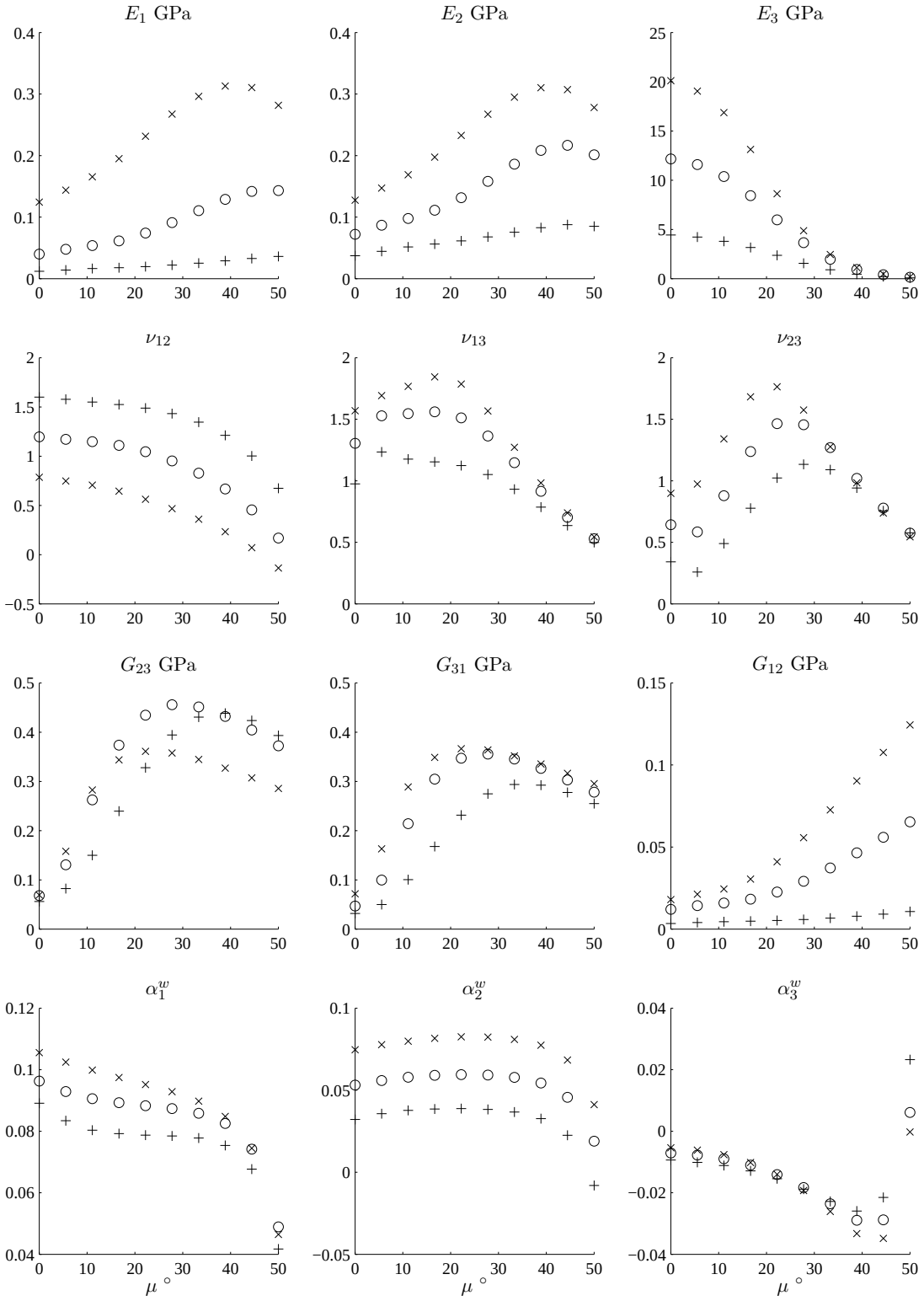

Figure 9.6.: Variation in properties with S2 MFA μ. High temperature, saturated conditions ($\vartheta = 110$°C, $w = 0.17$). + earlywood (RC = 0.1, $\rho = 0.3$ g/cc), ∘ middlewood (RC = 0.7, $\rho = 0.6$ g/cc), × latewood (RC = 0.975, $\rho = 0.85$ g/cc).

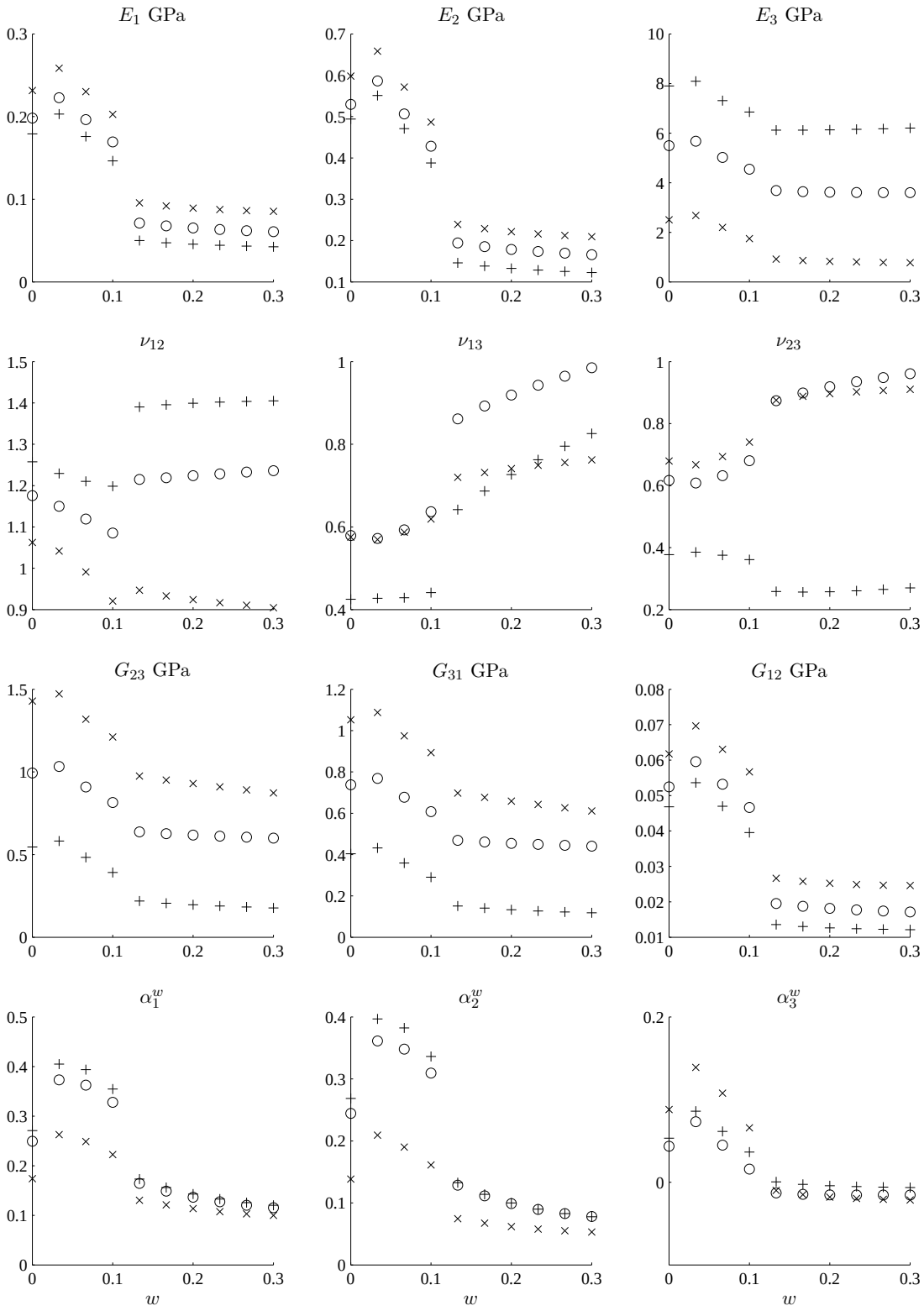

Figure 9.7.: Variation in properties with moisture content w. Earlywood, ambient temperature (RC = 0.1, $\rho = 0.3$ g/cc, $\vartheta = 22°$C). S2 MFA: + 5.6°, ∘ 22°, × 39°.

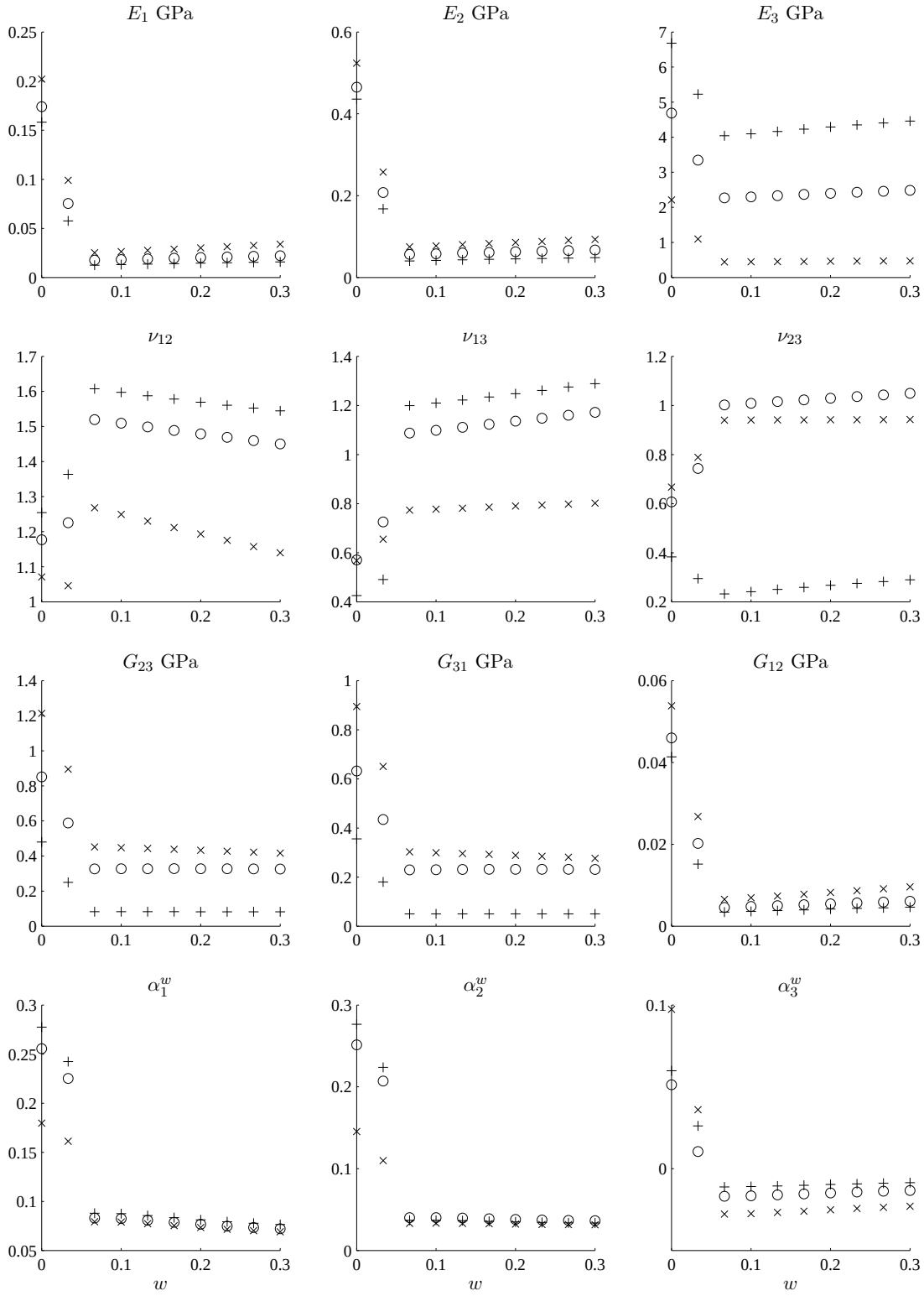

Figure 9.8.: Variation in properties with moisture content w. Earlywood, high temperature (RC = 0.1, $\rho = 0.3$ g/cc, $\vartheta = 110°$C). S2 MFA: + 5.6°, ∘ 22°, × 39°.

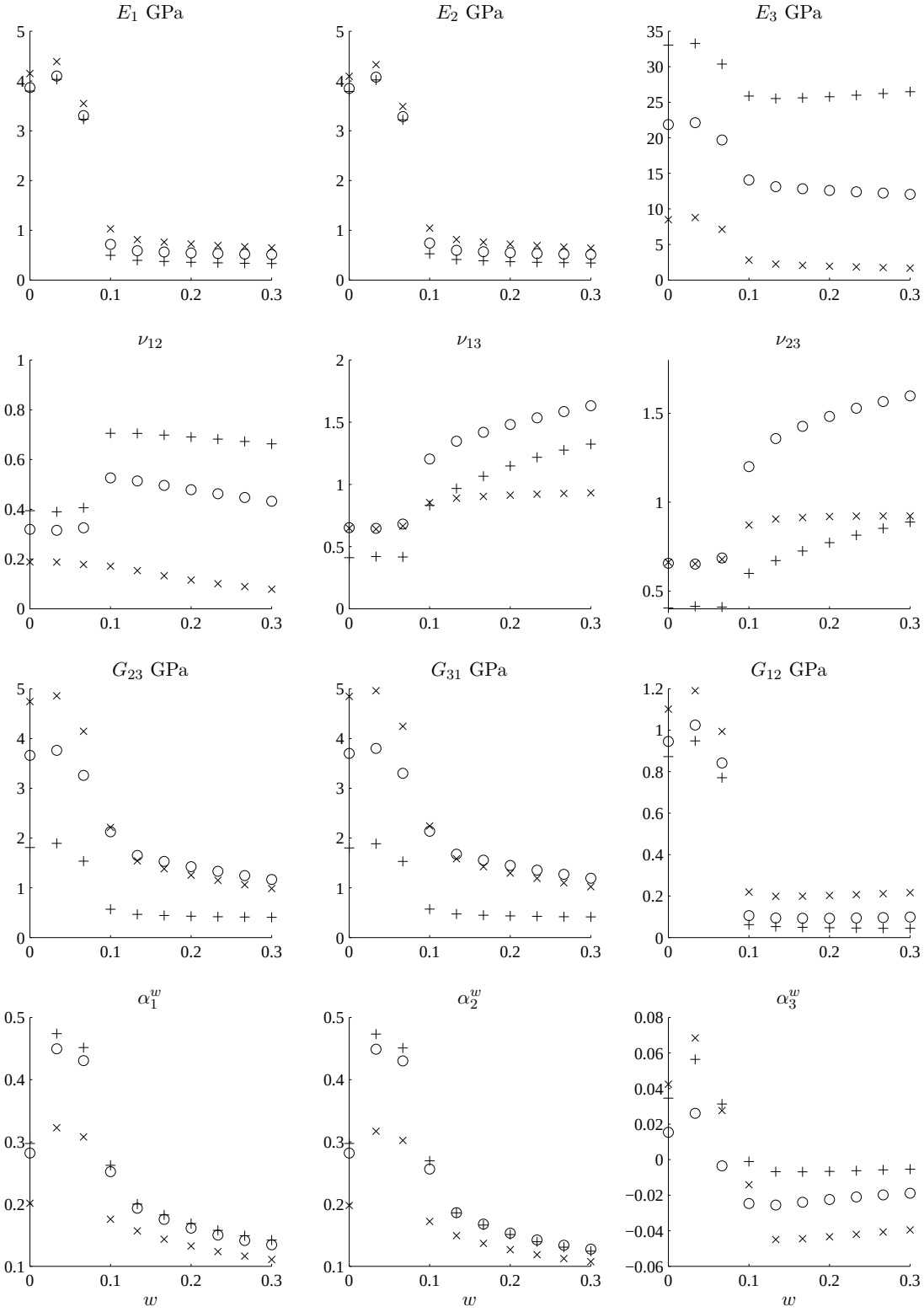

Figure 9.9.: Variation in properties with moisture content w. Latewood, ambient temperature (RC = 0.975, $\rho = 0.85$ g/cc, $\vartheta = 22°$C). S2 MFA: + 5.6°, ∘ 22°, × 39°.

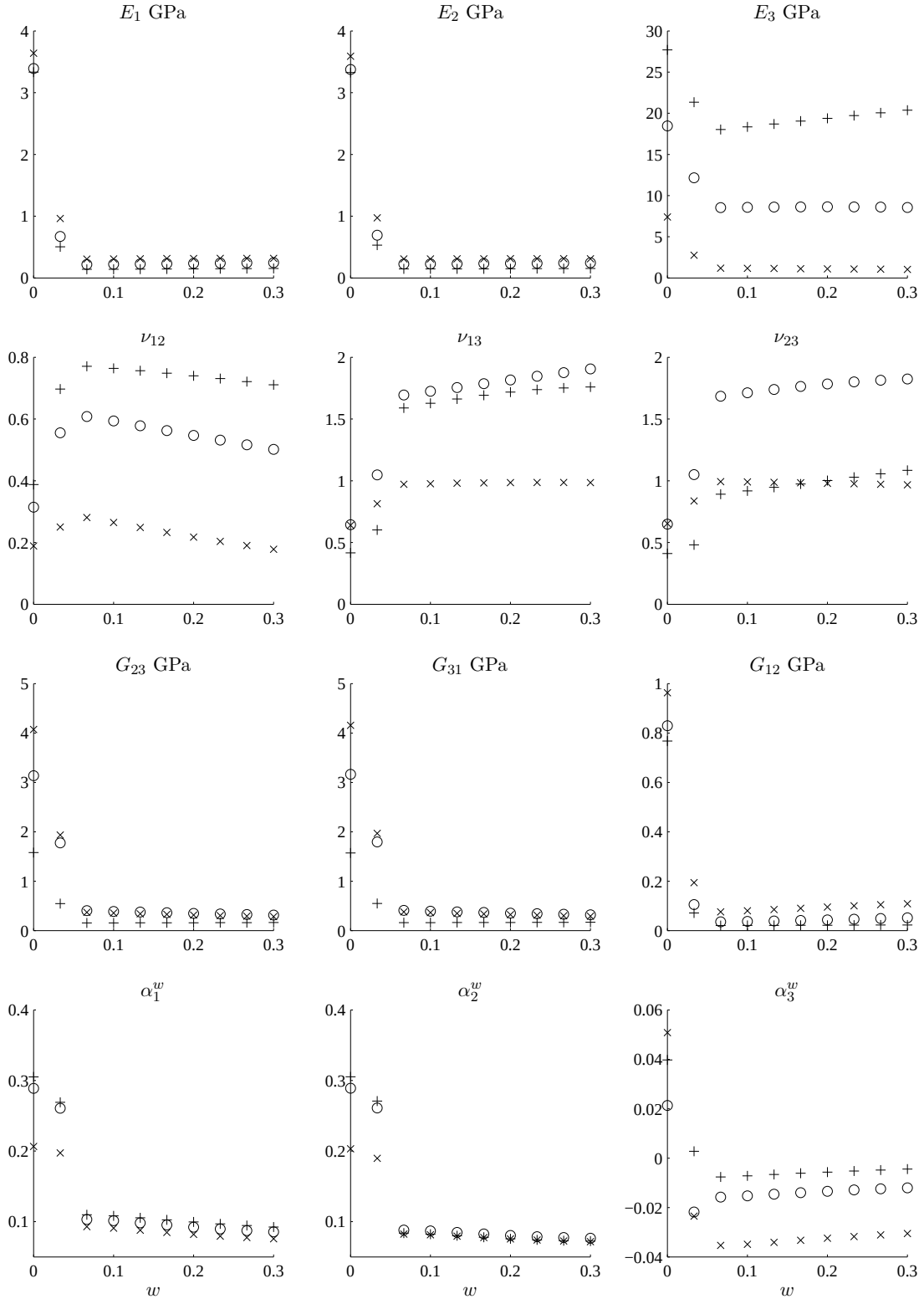

Figure 9.10.: Variation in properties with moisture content w. Latewood, high temperature (RC = 0.975, $\rho = 0.85$ g/cc, $\vartheta = 110°$C). S2 MFA: + 5.6°, ∘ 22°, × 39°.

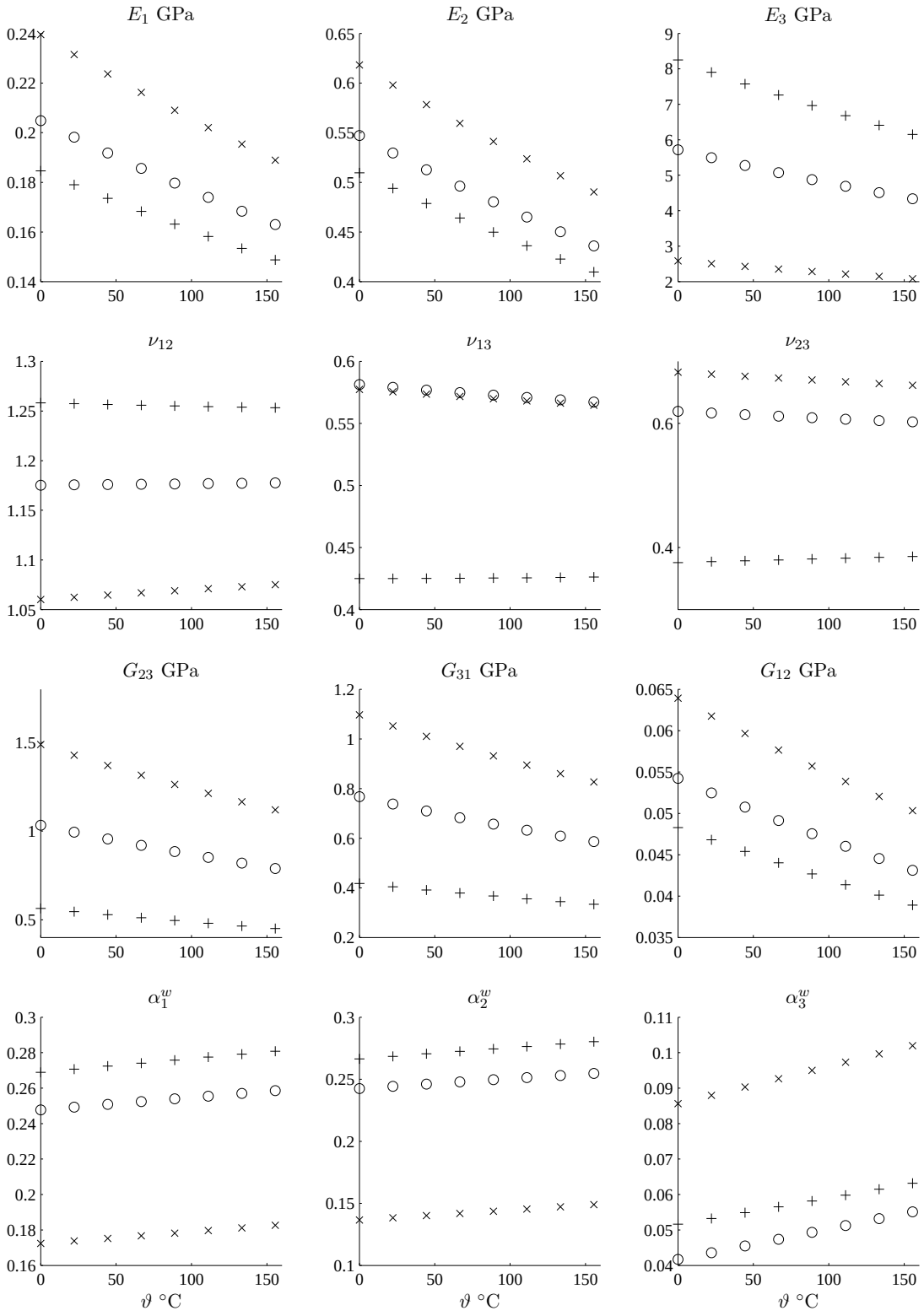

Figure 9.11.: Variation in properties with temperature ϑ. Earlywood, oven dry (RC = 0.1, $\rho = 0.3$ g/cc, $w = 0$). S2 MFA: + 5.6°, ∘ 22°, × 39°.

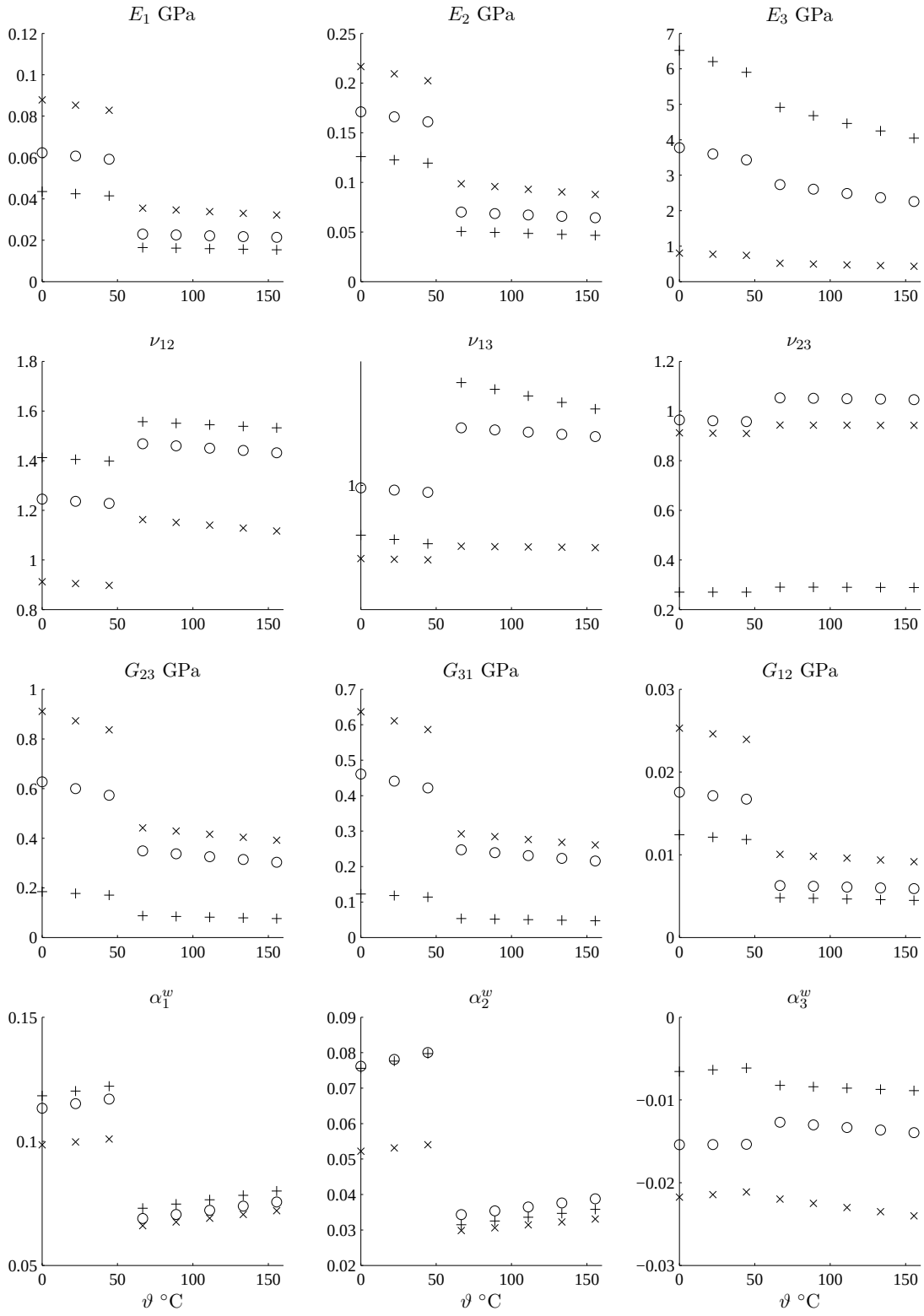

Figure 9.12.: Variation in properties with temperature ϑ. Earlywood, saturated (RC = 0.1, $\rho = 0.3$ g/cc, $w = 0.3$). S2 MFA: + 5.6°, ∘ 22°, × 39°.

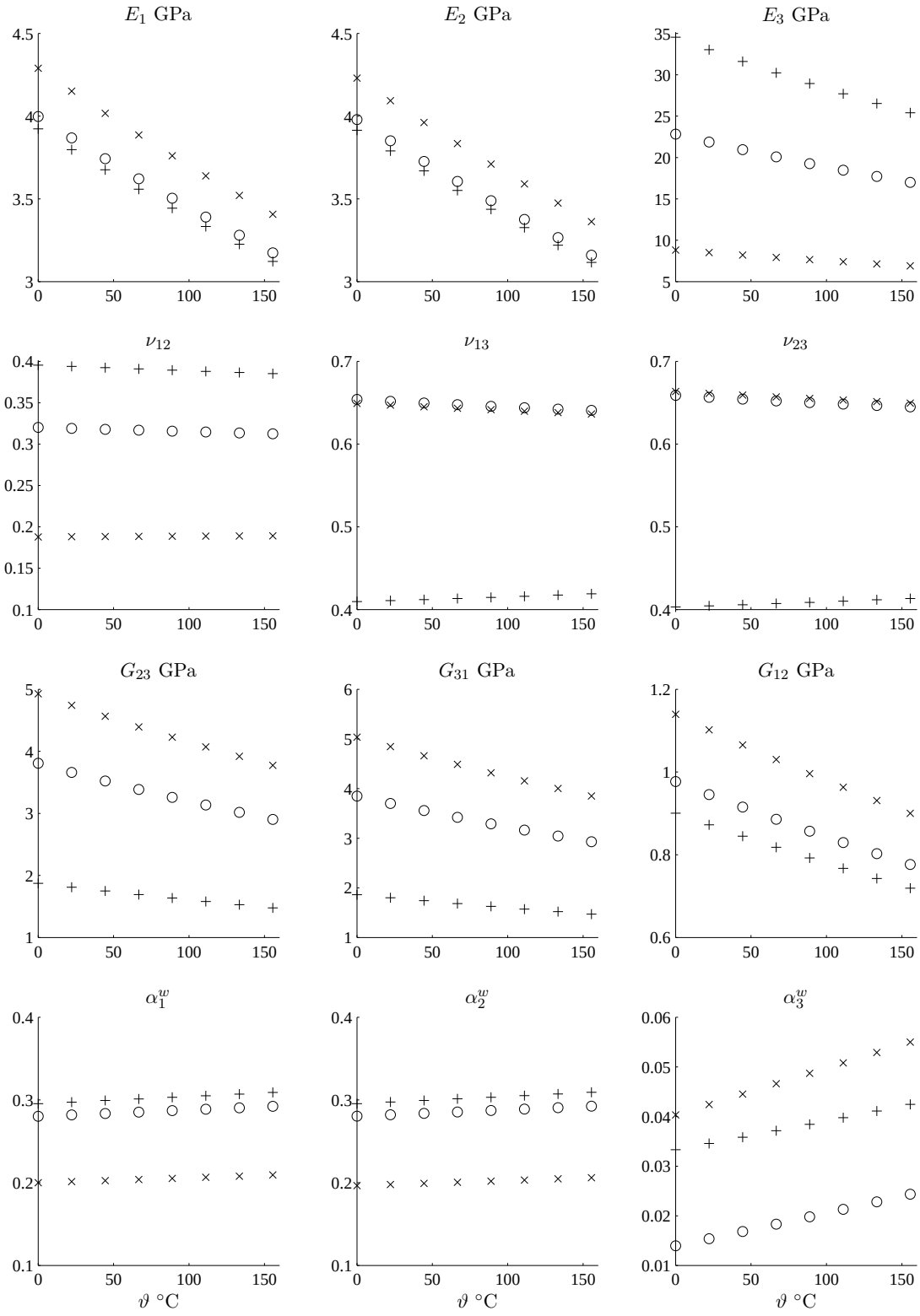

Figure 9.13.: Variation in properties with temperature ϑ. Latewood, oven dry (RC = 0.975, $\rho = 0.85$ g/cc, $w = 0$). S2 MFA: + 5.6°, ∘ 22°, × 39°.

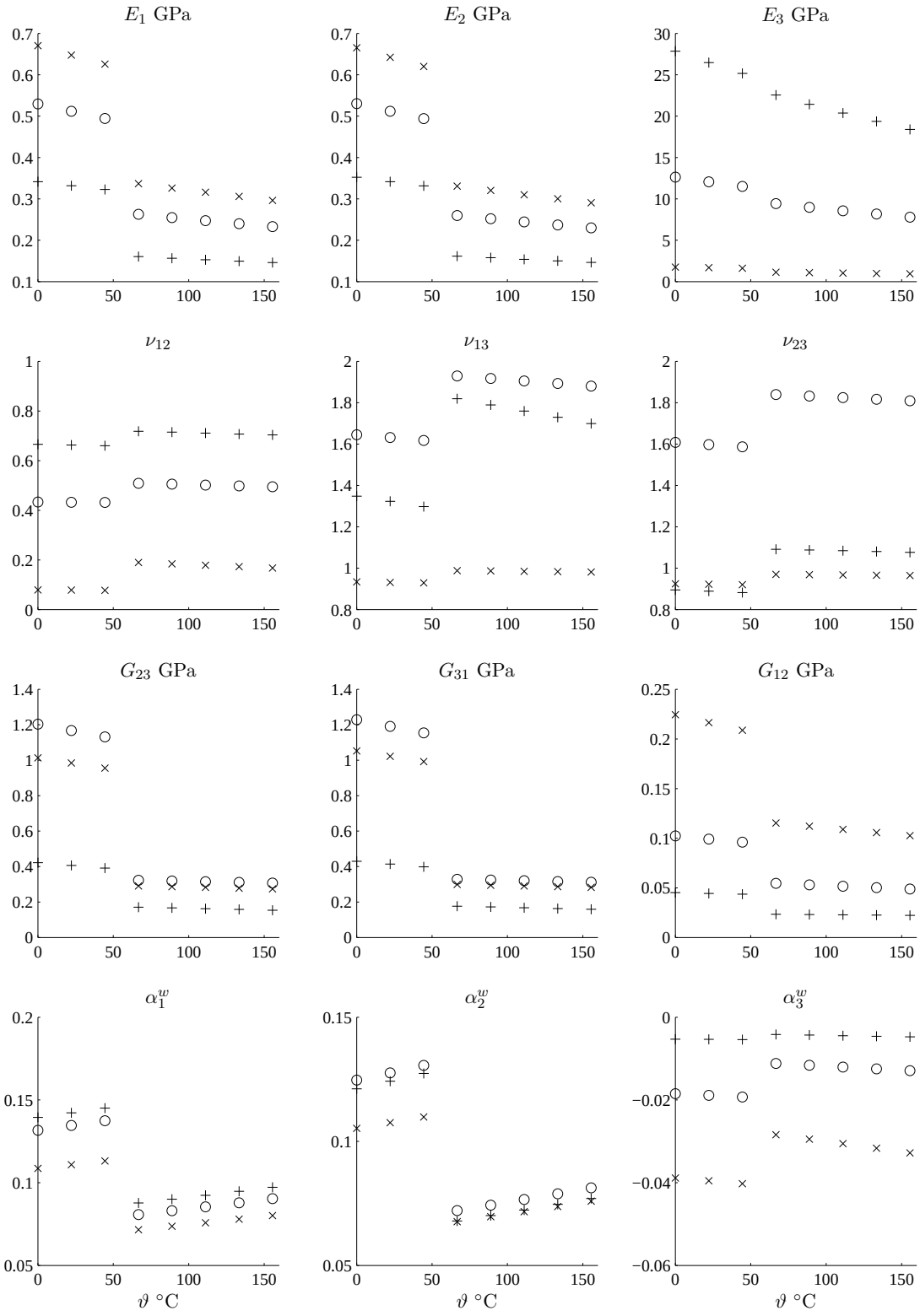

Figure 9.14.: Variation in properties with temperature ϑ. Latewood, saturated (RC = 0.975, $\rho = 0.85$ g/cc, $w = 0.3$). S2 MFA: + 5.6°, ∘ 22°, × 39°.

The second stage in validation involves demonstrating that the models yield results that agree, to a specified accuracy, with empirical data. While it is possible, in a statistical sense, to test the correlation of model predictions with physical observations compiled from the literature, the degree of variation present in wood makes this approach probelmatic. The current models employ a considerable number of parameters; few, if any, of which accompany hygro-elastic data presented in the literature. The effects of many of these parameters on a particular model output are indistinguishable. For example, both increasing density and decreasing microfibril angle lead to an increase in longitudinal modulus. With overlapping degrees of freedom, many having a high intrinsic variability, the critical power of this approach is limited.

An alternate approach to the second stage of validation is to compare the hygro-elastic properties predicted by the models with those measured for a small set of thoroughly characterised specimens. It had been hoped that a concurrent but separate project would provide a dataset of this kind against which the validity of the methodolgy presented could be tested. Unfortunately, this experimental programme has not reached fruition and consequently the second stage of validation has not been completed. The task of assembling a consistent set of hygro-elastically and structurally characterized specimens should be accorded the highest priority if this work is to be continued. Such a dataset could also be used to refine the model input parameters.

While the lack of second stage validation means that the current models cannot be used confidently in simulation mode, their usefulness in speculation mode is less affected. Furthermore, the models presented herein can still serve as a theoretical framework and focus for fundamental experimental work. Truesdell and Noll (1965) state that "without theoretical concepts one would neither know what experiments to perform nor be able to interpret their outcome", and the present set of deterministic models naturally fill both roles of a "theoretical concept". A number of suggestions for future experimental work arising from the construction of these models have already been made in preceding chapters. In the future, a comprehensive sensitivity study could be conducted to identify the degree to which each of the model inputs influences the model outputs. Experimental effort could then be concentrated on characterizing those inputs of greatest significance.

The nanophase property models of chapter 8 deserve special mention. Ultimately, the mechanical behaviour of wood is governed by the mechanical behaviour of its constituents at a molecular level[1], hence any model is only as good as the constituent properties it employs. Put another way, the quality of the overall model is a direct reflection of the quality of the nanophase property models. Currently the matrix phase property models suffer from a number of deficiencies; particularly in regard to the moisture partition and the treatment in the region of the glass transition and of non-

[1] Unless of course mechanics is persued to quantum scales. However, such a pursuit does not appear to offer practical benefit at this time.

equilibrium states. These deficiencies stem from a lack of empirical data for both the *in situ* properties and the properties of isolated constituent preparations.

In recent years, significant advances have been made in the field of computational chemistry. Indeed the prediction of mechanical properties from molecular structure is currently a principal ambition of materials science. Molecular mechanics and molecular dynamics have begun to be applied to wood (Faulon et al., 1994; Faulon and Hatcher, 1994; Houtman and Atalla, 1995; Jurasek, 1995, 1996, 1998b; Russell et al., 2000), although to date no attempt has been made to apply atomistic models to the nanomechanics of the non-cellulosic constituents. In the short term molecular mechanics models could be used to obtain matrix phase properties. In the longer term the current continuum nanostructural model could be replaced with either a fully atomistic model, or a hybrid model containing both discrete and continuum elements.

As well as extending the structurally based modelling to molecular scales, an atomistic approach offers a number of other advantages. It allows for direct incorporation of the effects of genetic modifications, such as those resulting in reduced crosslinking of the lignins, and interactions between the constituents and moisture. It also unifies the treatment of inelastic behaviours including time-dependent mechanisms and fracture.

In chapter 5 a simple growth model was used to describe internal tracheid geometry. Growth models with a physiological basis have also been sucessfully developed at a macroscopic scale (Barthelemy et al., 1995; de Reffye et al., 1997; Fourcaud et al., 1997). In the future, this approach, that is 'growing' the structure rather than using parametric idealized models, has the potential to provide an elegant means for describing wood structure. It would also be a fascinating study in its own right.

Chapter 10

Concluding Remarks

In this thesis a methodology has been developed for predicting the three dimensional hygro-elastic properties of small clearwood domains based on wood structure and constituent properties. This methodology comprises a hierarchical set of structural models, homogenization methods and auxiliary models that provide input to the structural models.

In the future, there are a number of further directions in which this work could be continued.

- Expansional strains directly caused by changes in temperature have been assumed negligible in comparison with the expansional strains due to changes in moisture content associated with changes in temperature. In situations where they are of importance, their inclusion presents no great diffculty as they may be treated in a manner analogous to the hygral stresses and strains. Estimates for the nanophase thermal expansion coefficients are however required.

- Lakes (1995) has shown that the use of micropolar elasticity theories, in which distributed moments as well as forces are postulated, can improve the accuracy of bone modelling. Similar improvements could be expected in wood modelling, particularly at the ultrastructural scale.

- The coupling known to exist between the mechanical (stress and strain) and moisture fields (Barkas, 1949, 1950; Treloar, 1953; Libby and Haygreen, 1967; Cowin, 1985; Negi, 1999) has yet to be included in the modelling. Since moisture movement takes considerable time this coupling is time dependent and intrinsically connected with nonlinear material behaviour such as viscoelastic and mechano-sorptive phenomena.

  To include this effect means replacing the current uncoupled hygro-elastic framework with an analogue of coupled thermo-elasticity and requires the concurrent solution of moisture transport equations as well as the mechanical equations of motion. In many ways this is a natural development as it is also necessary if the deformation of wood during drying is to be addressed.

- Internal stresses, generated during drying or existing within the standing tree as a result of maturation strains, have been neglected in the present study. These stresses can cause considerable technical difficulties during processing.

  By integrating the incremental changes occurring during maturation or drying or both, these stresses could be included. However, as these stresses originate at a molecular level, yet their expression is controlled by macroscopic boundary conditions, performing this integration within a hierarchical framework will not be easy.

- Extending the current models to include inelastic behaviours in far from equilibrium states presents the greatest challenge. At this point it is not even clear how effective properties for some phenomena, such as fracture, can be defined.

Finally, Gibson and Ashby (1997) noted that "wood is complicated stuff". I concur.

Appendix A

Uncoupled hygro-thermo-elasticity

Hygro-elasticity is an analog of thermo-elasticity with moisture content playing the role of temperature. Hygro-thermo-elasticity is a combination of hygro-elasticity and thermo-elasticity.

If the temperature and moisture content fields are treated as being independent of the stress and strain fields then the problem is said to be uncoupled. From the outset it is assumed that the temperature and moisture content fields in the reference state and in the current state (which differs only infinitesimally from the reference state) are fully specified.

In this appendix only a few central results are presented, sufficient for what follows. The fundamentals of continuum mechanics and elasticity can be found in Truesdell and Toupin (1960), Fung (1965), Malvern (1969), Spencer (1980), and Lai et al. (1993). Thermo-elasticity is discussed in detail by Boley and Weiner (1960), Parkus (1968), and by Carlson (1972). Unless stated otherwise the following results are drawn from these sources.

Only cartesian coordinate systems are employed, and tensorial quantities are written either in cartesian component or matrix notation. Unless stated otherwise the summation convention is in effect. Comma notation is used for partial derivatives.

A.1. Governing equations

For small excursions from a reference state the distinction between material (Lagrangian) and spatial (Eulerian) descriptions can be ignored and the deformations of a body may be adequately represented by the infinitesimal strain tensor $\boldsymbol{E}$ whose components are

$$E_{ij} = \frac{1}{2}\left(u_{i,j} + u_{j,i}\right) \tag{A.1}$$

where u_i are the displacement components. By definition $\boldsymbol{E}$ is symmetric, i.e. $E_{ij} = E_{ji}$. From the law of conservation of mass, and to a first order approximation with

respect to E_{ij}, the density ρ is

$$\frac{\rho_0}{\rho} = 1 + E_{ii} \tag{A.2}$$

where ρ_0 is the density in the reference state. Treating a material body as a collection of particles, conservation of linear momentum yields Cauchy's first law of motion

$$T_{ij,i} + \rho b_j = \ddot{u}_j \tag{A.3}$$

where T_{ij} are the components of the Cauchy stress tensor $\boldsymbol{T}$, b_j are the components of the body force per unit mass and $\ddot{u}_j$ are the accelerations. In the absence of substantial accelerations and body forces (A.3) reduces to the equilibrium equation

$$T_{ij,i} = 0. \tag{A.4}$$

If distributed body and surface couples are not postulated then conservation of angular momentum requires the stress tensor to be symmetric, i.e. $T_{ij} = T_{ji}$.

On the boundary of a body the components t_i of the traction vector $\boldsymbol{t}$ are related to the stress components by

$$t_i = T_{ji} n_j \tag{A.5}$$

where n_j are the components of the unit outward normal vector $\boldsymbol{n}$.

The displacements are related to the strains by

$$u_i = E_{ij} x_j \tag{A.6}$$

A constitutive equation for hygroscopic thermoelastic materials may be derived[1] by positing the existence of a caloric equation of state,

$$u = u(s, \boldsymbol{E}, w; \boldsymbol{x}), \tag{A.7}$$

that determines the internal energy density u from the specific entropy s, the infinitesimal strain $\boldsymbol{E}$ and the moisture content w[2]. The thermodynamic temperature ϑ is

[1] The derivation of a linear hygro-thermo-elastic constitutive equation proceeds in an equivalent manner to the derivation presented in Kalamkarov (1992) for a linear thermo-elastic constitutive equation.

[2] Moisture content, that is the ratio of the mass of water held to dry mass, is chosen to represent the moist state as it is more commonplace in wood science than moisture concentration, and unlike water potential or relative humidity is clearly defined at temperatures over 100°C, makes no assumptions regarding equilibrium and avoids some hysteretic effects.

defined by

$$\vartheta \triangleq \left(\frac{\partial u}{\partial s}\right)_{\boldsymbol{E},w} \tag{A.8}$$

and the thermodynamic tension μ conjugate to the moisture content is defined by

$$\mu \triangleq \left(\frac{\partial u}{\partial w}\right)_{s,\boldsymbol{E}}. \tag{A.9}$$

It can also be shown that, for small strains, $\boldsymbol{T}$ is the thermodynamic tension conjugate to $\boldsymbol{E}$ (Malvern, 1969), thus

$$du = \vartheta ds + \frac{1}{\rho} T_{ij} dE_{ij} + \mu dw. \tag{A.10}$$

It is more convenient to treat the temperature rather than the entropy as an independent variable. This may be accomplished by means of a Legendre transformation, by which the specific Helmholz free energy $\psi = u - \vartheta s$ is introduced so that for any real or hypothetical change which proceeds in accordance with (A.7)

$$d\psi = \frac{1}{\rho} T_{ij} dE_{ij} + \mu dw - s d\vartheta. \tag{A.11}$$

For a linear theory, valid for small deformations and small changes in temperature and moisture content, ψ may be expanded as a Taylor series about the reference state ($\vartheta = \vartheta_0$, $\boldsymbol{E} = 0$, $w = w_0$) retaining only the constant, linear and quadratic terms

$$\begin{aligned}\psi =& \psi_0 + \left.\frac{\partial \psi_0}{\partial E_{ij}}\right|_{\psi_0} E_{ij} + \left.\frac{\partial \psi_0}{\partial \vartheta}\right|_{\psi_0} \hat{\vartheta} + \left.\frac{\partial \psi_0}{\partial w}\right|_{\psi_0} \hat{w} + \frac{1}{2} \left.\frac{\partial^2 \psi_0}{\partial E_{ij} \partial E_{kl}}\right|_{\psi_0} E_{ij} E_{kl} \\ &+ \left.\frac{\partial^2 \psi_0}{\partial E_{ij} \partial \vartheta}\right|_{\psi_0} E_{ij} \hat{\vartheta} + \left.\frac{\partial^2 \psi_0}{E_{ij} \partial w}\right|_{\psi_0} E_{ij} \hat{w} + \frac{1}{2} \left.\frac{\partial^2 \psi_0}{\partial \vartheta^2}\right|_{\psi_0} \hat{\vartheta}^2 \\ &+ \frac{1}{2} \left.\frac{\partial^2 \psi_0}{\partial w^2}\right|_{\psi_0} \hat{w}^2 + \left.\frac{\partial^2 \psi_0}{\partial \vartheta \partial w}\right|_{\psi_0} \hat{\vartheta} \hat{w}\end{aligned} \tag{A.12}$$

where $\hat{\vartheta} \triangleq \vartheta - \vartheta_0$, $\hat{\vartheta}/\vartheta_0 \ll 1$, and $\hat{w} \triangleq w - w_0$, $\hat{w}/w_0 \ll 1$. To the same order of approximation as the series expansion of ψ $\rho = \rho_0$, and since (A.11) implies

$$\frac{\partial \psi}{\partial E_{ij}} = \frac{1}{\rho} T_{ij} \tag{A.13}$$

then on differentiating (A.12) with respect to E_{ij} we obtain to second order

$$\frac{1}{\rho_0} T_{ij} = \left.\frac{\partial^2 \psi}{\partial E_{ij} \partial E_{kl}}\right|_{\psi_0} E_{kl} + \left.\frac{\partial^2 \psi}{\partial E_{ij} \partial \vartheta}\right|_{\psi_0} \hat{\vartheta} + \left.\frac{\partial^2 \psi}{\partial E_{ij} \partial w}\right|_{\psi_0} \hat{w} + \left.\frac{\partial \psi}{\partial E_{ij}}\right|_{\psi_0}. \tag{A.14}$$

Define

$$C_{ijkl}(\vartheta, w) \triangleq \rho_0 \frac{\partial^2 \psi(\vartheta, 0, w)}{\partial E_{ij} \partial E_{kl}} \tag{A.15}$$

$$\beta^{\vartheta}_{ij}(\vartheta, w) \triangleq -\rho_0 \frac{\partial^2 \psi(\vartheta, 0, w)}{\partial E_{ij} \partial \vartheta} \tag{A.16}$$

$$\beta^{w}_{ij}(\vartheta, w) \triangleq -\rho_0 \frac{\partial^2 \psi(\vartheta, 0, w)}{\partial E_{ij} \partial w}. \tag{A.17}$$

C_{ijkl}, β^{ϑ}_{ij}, and β^{w}_{ij} can be shown to constitute tensors, respectively referred to as the material stiffness tensor $\boldsymbol{C}$, the thermal stress coefficient tensor $\boldsymbol{\beta}^{\vartheta}$, and the hygral stress coefficient tensor $\boldsymbol{\beta}^{w}$. Equation (A.14) can now be written

$$T_{ij} - T_{0ij} = C_{ijkl} E_{kl} - \beta^{\vartheta}_{ij} \hat{\vartheta} - \beta^{w}_{ij} \hat{w}. \tag{A.18}$$

Solved for the strains (A.18) becomes

$$E_{ij} = D_{ijkl} \left(T_{kl} - T_{0kl} \right) + \alpha^{\vartheta}_{ij} \hat{\vartheta} + \alpha^{w}_{ij} \hat{w}. \tag{A.19}$$

where $\boldsymbol{D} = \boldsymbol{C}^{-1}$ is the material compliance tensor, $\alpha^{\vartheta}_{ij} = D_{ijkl} \beta^{\vartheta}_{kl}$ is the thermal strain coefficient tensor and $\alpha^{w}_{ij} = D_{ijkl} \beta^{w}_{kl}$ is the hygral strain coefficient tensor. Equations (A.18) and (A.19) are the mechanical constitutive equations used throughout this thesis.

Without any loss of generality it may be assumed that

$$C_{ijkl} = C_{jikl} = C_{ijlk} = C_{klij}, \tag{A.20}$$

with similar symmetries present in $\boldsymbol{D}$ (Spencer, 1980). These symmetries reduce the number of independent elastic constants from 81 to 21 in the most generally anisotropic case. Material symmetries further reduce the number of independent constants until, for an isotropic material, only two remain.

As the reference state is one of thermodynamic equilibrium ψ must be strictly increasing for any displacement taking place at constant temperature and moisture content, thus $\boldsymbol{C}$ must be positive-definite, i.e. for arbitrary $\boldsymbol{E}$

$$C_{ijkl} E_{ij} E_{kl} > 0 \tag{A.21}$$

This requirement imposes restrictions on values admissible for the elastic constants.

It is often convenient to treat the non-mechanical strains generated by changes in temperature and moisture content collectively. To this end define

$$E^{\circ}_{ij} \triangleq +\alpha^{\vartheta}_{ij} \hat{\vartheta} + \alpha^{w}_{ij} \hat{w}. \tag{A.22}$$

$\boldsymbol{E}^{\circ}$ is referred to here as the expansional strain, elsewhere it is referred to as the eigenstrain (Mura, 1987).

A.2. Volume averages

Denote the unweighted volume average of some quantity A in some domain Ω by $\langle A \rangle_{\Omega} \triangleq \frac{1}{|\Omega|} \int_{\Omega} A \, d\Omega$.

Consider a body identified with $\Omega \subset \mathbb{R}^N$ subjected to self-equilibrating tractions $\boldsymbol{t}$ on its surface Γ and body forces $\boldsymbol{b}$ on its interior. The volume average stress is

$$\langle T_{ij} \rangle_{\Omega} \triangleq \frac{1}{|\Omega|} \int_{\Omega} T_{ij} \, d\Omega \tag{A.23}$$

$$= \frac{1}{|\Omega|} \int_{\Omega} T_{ik} x_{j,k} \, d\Omega \tag{A.24}$$

since $x_{j,k} = \delta_{jk}$. Integrating by parts gives

$$= \frac{1}{|\Omega|} \int_{\Gamma} T_{ik} x_j n_k \, d\Gamma - \frac{1}{|\Omega|} \int_{\Omega} T_{ik,k} x_j \, d\Omega \tag{A.25}$$

but equilibrium requires $T_{ik,k} = -b_i$ so

$$= \frac{1}{|\Omega|} \int_{\Gamma} T_{ik} x_j n_k \, d\Gamma + \frac{1}{|\Omega|} \int_{\Omega} b_i x_j \, d\Omega \tag{A.26}$$

or, as $T_{ik} n_k = t_i$ on Γ

$$\langle T_{ij} \rangle_{\Omega} = \frac{1}{|\Omega|} \int_{\Gamma} t_i x_j \, d\Gamma + \frac{1}{|\Omega|} \int_{\Omega} b_i x_j \, d\Omega. \tag{A.27}$$

Thus the volume average stress can be determined solely from the boundary tractions and interior body forces.

Again consider the same body but now subjected to compatible displacements $\boldsymbol{u}$ on its boundary. The volume average strain is

$$\langle E_{ij} \rangle_{\Omega} \triangleq \frac{1}{|\Omega|} \int_{\Omega} \frac{1}{2} \left(u_{i,j} + u_{j,i} \right) \, d\Omega \tag{A.28}$$

which on application of the divergence theorem yields

$$\langle E_{ij} \rangle_{\Omega} = \frac{1}{|\Omega|} \int_{\Gamma} \frac{1}{2} \left(n_i u_j + n_j u_i \right) \, d\Gamma. \tag{A.29}$$

Thus the volume average strain is entirely specified by the boundary displacements.

A.3. Coordinate transformation

While tensorial quantities are independent of any coordinate system, tensor components are not.

Consider two rectangular right-handed cartesian coordinate systems orthonormal base vectors $\boldsymbol{e}_i^{(1)}$ and $\boldsymbol{e}_i^{(2)}$ respectively. A vector $\boldsymbol{v}$ has components $v_i^{(1)}$ with respect to the first coordinate system and $v_i^{(2)}$ with respect to the second coordinate system, i.e. $\boldsymbol{v} = v_i^{(1)}\boldsymbol{e}_i^{(1)} = v_i^{(2)}\boldsymbol{e}_i^{(2)}$. Define the direction cosines ω_{ij}, as the cosine of the angle between $\boldsymbol{e}_i^{(2)}$ and $\boldsymbol{e}_j^{(1)}$, i.e.

$$\omega_{ij} = \boldsymbol{e}_i^{(2)} \cdot \boldsymbol{e}_j^{(1)}. \tag{A.30}$$

Now the components of $\boldsymbol{v}$ with respect to the second coordinate system can be expressed in terms of the components in the first system by

$$v_i^{(2)} = v_j^{(1)}\boldsymbol{e}_j^{(1)} \cdot \boldsymbol{e}_i^{(2)} = \omega_{ij}v_j^{(1)}. \tag{A.31}$$

Similarly the components of a cartesian tensor $\boldsymbol{A}$ of order N

$$\boldsymbol{A} = A^{(1)}_{i_1 i_2 \cdots i_N}\boldsymbol{e}^{(1)}_{i_1} \otimes \boldsymbol{e}^{(1)}_{i_2} \otimes \cdots \otimes \boldsymbol{e}^{(1)}_{i_N} = A^{(2)}_{i_1 i_2 \cdots i_N}\boldsymbol{e}^{(2)}_{i_1} \otimes \boldsymbol{e}^{(2)}_{i_2} \otimes \cdots \otimes \boldsymbol{e}^{(2)}_{i_N} \tag{A.32}$$

transform according to

$$A^{(2)}_{j_1 j_2 \cdots j_N} = \omega_{j_1 i_1}\omega_{j_2 i_2} \cdots \omega_{j_N i_N} A^{(1)}_{i_1 i_2 \cdots i_N}. \tag{A.33}$$

A.4. Matrix notation

For computational purposes it is convenient to represent the tensorial quantities introduced above as matrices. This is done by constructing stress $\boldsymbol{\sigma}$ and strain $\boldsymbol{\epsilon}$ matrices from the components of the cartesian stress and strain tensors according to

$$\boldsymbol{\sigma} = \begin{bmatrix} T_{11} & T_{22} & T_{33} & T_{23} & T_{31} & T_{12} \end{bmatrix}^{\mathrm{t}} \tag{A.34}$$

$$\boldsymbol{\epsilon} = \mathbf{W}\begin{bmatrix} E_{11} & E_{22} & E_{33} & E_{23} & E_{31} & E_{12} \end{bmatrix}^{\mathrm{t}}, \tag{A.35}$$

where $\mathbf{W}$, defined as

$$\mathbf{W} \triangleq \begin{bmatrix} 1 & & & & & \\ & 1 & & & & \\ & & 1 & & & \\ & & & \frac{2}{2} & & \\ & & & & \frac{2}{2} & \\ & & & & & \frac{2}{2} \end{bmatrix}, \tag{A.36}$$

is used to make the transition from tensorial to engineering shear strain components, a transition which is convenient as it simplifies the transformation laws in the matrix notation. Since the stress and strain tensors are symmetric only six of the nine

components are retained[3].

In matrix notation, and with respect to a cartesian coordinate system, the strain-displacement relations of equation (A.1) can be written

$$\boldsymbol{\epsilon} = \boldsymbol{\partial}^{\mathrm{t}}\mathbf{u} \tag{A.37}$$

with

$$\mathbf{u} \triangleq \begin{bmatrix} u_1 & u_2 & u_3 \end{bmatrix}^{\mathrm{t}} \tag{A.38}$$

u_i being the components of the displacement vector, and

$$\boldsymbol{\partial} \triangleq \begin{bmatrix} \partial_1 & 0 & 0 & 0 & \partial_3 & \partial_2 \\ 0 & \partial_2 & 0 & \partial_3 & 0 & \partial_1 \\ 0 & 0 & \partial_3 & \partial_2 & \partial_1 & 0 \end{bmatrix} \tag{A.39}$$

where ∂_i denotes $\dfrac{\partial}{\partial x_i}$. In the same fashion the equilibrium equation, in the abscence of body forces, (A.4) can be written

$$\boldsymbol{\partial}\boldsymbol{\sigma} = \mathbf{0}. \tag{A.40}$$

On the boundary the tractions are related to the stresses by

$$\mathbf{t}^{(n)} = \mathbf{n}\boldsymbol{\sigma} \tag{A.41}$$

where

$$\mathbf{n} \triangleq \begin{bmatrix} n_1 & 0 & 0 & 0 & n_3 & n_2 \\ 0 & n_2 & 0 & n_3 & 0 & n_1 \\ 0 & 0 & n_3 & n_2 & n_1 & 0 \end{bmatrix} \tag{A.42}$$

and n_i are the components of the outward normal unit vector.

In matrix notation the constitutive equations are written

$$\boldsymbol{\sigma} = \mathbf{C}(\boldsymbol{\epsilon} - \boldsymbol{\epsilon}^{\circ}) + \boldsymbol{\sigma}_0 \tag{A.43}$$

or as

$$\boldsymbol{\epsilon} = \mathbf{D}(\boldsymbol{\sigma} - \boldsymbol{\sigma}_0) + \boldsymbol{\epsilon}^{\circ} \tag{A.44}$$

[3]This notation is attributed to Voigt by Hearmon (1961). Some authors adopt different contraction orderings, e.g. $(11, 22, 33, 12, 23, 31) \rightarrow (1, 2, 3, 4, 5, 6)$. Other matrix representations for tensorial quantities are discussed by Mehrabadi and Cowin (1990) and by Nowick (1995).

where $\mathbf{C} = \mathbf{D}^{-1}$. The components of the material stiffness $\mathbf{C}$ and compliance $\mathbf{D}$ matrices can be found in terms of their tensor equivalents by comparing the constitutive equations in tensor and matrix notation

$$\mathbf{C} = \begin{bmatrix} C_{1111} & C_{1122} & C_{1133} & C_{1123} & C_{1131} & C_{1112} \\ C_{2211} & C_{2222} & C_{2233} & C_{2223} & C_{2231} & C_{2212} \\ C_{3311} & C_{3322} & C_{3333} & C_{3323} & C_{3331} & C_{3312} \\ C_{2311} & C_{2322} & C_{2333} & C_{2323} & C_{2331} & C_{2312} \\ C_{3111} & C_{3122} & C_{2333} & C_{3123} & C_{3131} & C_{3112} \\ C_{1211} & C_{1222} & C_{1233} & C_{1223} & C_{1231} & C_{1212} \end{bmatrix} \tag{A.45}$$

$$\mathbf{D} = \begin{bmatrix} D_{1111} & D_{1122} & D_{1133} & 2D_{1123} & 2D_{1131} & 2D_{1112} \\ D_{2211} & D_{2222} & D_{2233} & 2D_{2223} & 2D_{2231} & 2D_{2212} \\ D_{3311} & D_{3322} & D_{3333} & 2D_{3323} & 2D_{3331} & 2D_{3312} \\ 2D_{2311} & 2D_{2322} & 2D_{2333} & 4D_{2323} & 4D_{2331} & 4D_{2312} \\ 2D_{3111} & 2D_{3122} & 2D_{3133} & 4D_{3123} & 4D_{3131} & 4D_{3112} \\ 2D_{1211} & 2D_{1222} & 2D_{1233} & 4D_{1223} & 4D_{1231} & 4D_{1212} \end{bmatrix} \tag{A.46}$$

in which use has been made of the symmetries $C_{ijkl} = C_{jikl} = C_{ijlk}$ and $D_{ijkl} = D_{jikl} = D_{ijlk}$. Clearly $\mathbf{C} = \mathbf{C}^{\mathrm{t}}$ and $\mathbf{D} = \mathbf{D}^{\mathrm{t}}$ since $C_{ijkl} = C_{klij}$ and $D_{ijkl} = D_{klij}$.

In matrix notation (A.27) can be written as

$$\langle \boldsymbol{\sigma} \rangle_{\Omega} = \frac{1}{|\Omega|} \int_{\Gamma} \mathbf{W}^{-1} \mathbf{x}^{\mathrm{t}} \mathbf{t} \, d\Gamma = \frac{1}{|\Omega|} \int_{\Gamma} \mathbf{W}^{-1} \mathbf{x}^{\mathrm{t}} \mathbf{n} \boldsymbol{\sigma} \, d\Gamma \tag{A.47}$$

where $\mathbf{x}$ is defined as

$$\mathbf{x} = \begin{bmatrix} x_1 & 0 & 0 & 0 & x_3 & x_2 \\ 0 & x_2 & 0 & x_3 & 0 & x_1 \\ 0 & 0 & x_3 & x_2 & x_1 & 0 \end{bmatrix}. \tag{A.48}$$

Similarly (A.29) can be written as

$$\langle \boldsymbol{\epsilon} \rangle_{\Omega} = \frac{1}{|\Omega|} \int_{\Gamma} \mathbf{n}^{\mathrm{t}} \mathbf{u} \, d\Gamma. \tag{A.49}$$

By expanding (A.33) it can be shown that on changing between cartesian bases the stress, strain, stiffness and compliance matrices transform according to

$$\boldsymbol{\sigma}^{(2)} = \mathbf{T} \boldsymbol{\sigma}^{(1)} \qquad \boldsymbol{\sigma}^{(1)} = \mathbf{T}' \boldsymbol{\sigma}^{(2)} \tag{A.50}$$

$$\boldsymbol{\epsilon}^{(2)} = \mathbf{T}'^{\mathrm{t}} \boldsymbol{\epsilon}^{(1)} \qquad \boldsymbol{\epsilon}^{(1)} = \mathbf{T}^{\mathrm{t}} \boldsymbol{\epsilon}^{(2)} \tag{A.51}$$

$$\mathbf{C}^{(2)} = \mathbf{T} \mathbf{C}^{(1)} \mathbf{T}^{\mathrm{t}} \qquad \mathbf{C}^{(1)} = \mathbf{T}' \mathbf{C}^{(2)} \mathbf{T}'^{\mathrm{t}} \tag{A.52}$$

$$\mathbf{D}^{(2)} = \mathbf{T}'^{\mathrm{t}} \mathbf{D}^{(1)} \mathbf{T}' \qquad \mathbf{D}^{(1)} = \mathbf{T}^{\mathrm{t}} \mathbf{D}^{(2)} \mathbf{T} \tag{A.53}$$

where

$$\mathbf{T} = \begin{bmatrix} \omega_{11}\omega_{11} & \omega_{12}\omega_{12} & \omega_{13}\omega_{13} & 2\omega_{12}\omega_{13} & 2\omega_{11}\omega_{13} & 2\omega_{11}\omega_{12} \\ \omega_{21}\omega_{21} & \omega_{22}\omega_{22} & \omega_{23}\omega_{23} & 2\omega_{22}\omega_{23} & 2\omega_{21}\omega_{23} & 2\omega_{21}\omega_{22} \\ \omega_{31}\omega_{31} & \omega_{32}\omega_{32} & \omega_{33}\omega_{33} & 2\omega_{32}\omega_{33} & 2\omega_{31}\omega_{33} & 2\omega_{31}\omega_{32} \\ \omega_{21}\omega_{31} & \omega_{22}\omega_{32} & \omega_{23}\omega_{33} & \omega_{22}\omega_{33}+\omega_{23}\omega_{32} & \omega_{21}\omega_{33}+\omega_{23}\omega_{31} & \omega_{21}\omega_{32}+\omega_{22}\omega_{31} \\ \omega_{11}\omega_{31} & \omega_{12}\omega_{32} & \omega_{13}\omega_{33} & \omega_{12}\omega_{33}+\omega_{13}\omega_{32} & \omega_{11}\omega_{33}+\omega_{13}\omega_{31} & \omega_{11}\omega_{32}+\omega_{12}\omega_{31} \\ \omega_{11}\omega_{21} & \omega_{12}\omega_{22} & \omega_{13}\omega_{23} & \omega_{12}\omega_{23}+\omega_{13}\omega_{22} & \omega_{11}\omega_{23}+\omega_{13}\omega_{21} & \omega_{11}\omega_{22}+\omega_{12}\omega_{21} \end{bmatrix}, \tag{A.54}$$

and

$$\mathbf{T}' = \mathbf{W}^{-1}\mathbf{T}^{\mathrm{t}}\mathbf{W} = \mathbf{T}^{-1}$$
$$= \begin{bmatrix} \omega_{11}\omega_{11} & \omega_{21}\omega_{21} & \omega_{31}\omega_{31} & 2\omega_{21}\omega_{31} & 2\omega_{11}\omega_{31} & 2\omega_{11}\omega_{21} \\ \omega_{12}\omega_{12} & \omega_{22}\omega_{22} & \omega_{32}\omega_{32} & 2\omega_{22}\omega_{32} & 2\omega_{12}\omega_{32} & 2\omega_{12}\omega_{22} \\ \omega_{13}\omega_{13} & \omega_{23}\omega_{23} & \omega_{33}\omega_{33} & 2\omega_{23}\omega_{33} & 2\omega_{13}\omega_{33} & 2\omega_{13}\omega_{23} \\ \omega_{12}\omega_{13} & \omega_{22}\omega_{23} & \omega_{32}\omega_{33} & \omega_{22}\omega_{33}+\omega_{23}\omega_{32} & \omega_{12}\omega_{33}+\omega_{13}\omega_{32} & \omega_{12}\omega_{23}+\omega_{13}\omega_{22} \\ \omega_{11}\omega_{13} & \omega_{21}\omega_{23} & \omega_{31}\omega_{33} & \omega_{21}\omega_{33}+\omega_{23}\omega_{31} & \omega_{11}\omega_{33}+\omega_{13}\omega_{31} & \omega_{11}\omega_{23}+\omega_{13}\omega_{21} \\ \omega_{11}\omega_{12} & \omega_{21}\omega_{22} & \omega_{31}\omega_{32} & \omega_{21}\omega_{32}+\omega_{22}\omega_{31} & \omega_{11}\omega_{32}+\omega_{12}\omega_{31} & \omega_{11}\omega_{22}+\omega_{12}\omega_{21} \end{bmatrix} \tag{A.55}$$

with the direction cosines ω_{ij} defined by (A.30).

A.5. Material symmetry

The symmetry group of a material is defined as the group of transformations of the material coordinates under which the constitutive equations are invariant Malvern (1969). If, in the reference state, the symmetry group of a material is the full group of orthogonal transformations then the material is said to isotropic, otherwise it is said to be anisotropic or, occasionally, aelotropic.

Material symmetries can arise from an ordered structure, as in crystals for which 32 distinct symmetry groups are recognised, or from disorder in a probabilistic fashion. However they arise, the presence of a symmetry reduces the number of independent components of the material properties, a fact expressed by Neumann's principle which states that *the symmetry of any physical property of a material must include all the symmetry elements of the material.* The connections between symmetries and physical properties are discussed in depth by Nye (1957); Green and Adkins (1960); Hearmon (1961); Mehrabadi and Cowin (1990); Nowick (1995).

By comparing the components of the material tensors under transformations from the materials symmetry group admissible forms for the physical properties may be obtained. Materials having five types of symmetry — monoclinic, orthotropic, square, hexagonal, transversely isotropic, and isotropic — are employed in the current work and the independent material parameters for these material types are addressed below.

A material whose symmetry group contains only a 2-fold axis of rotation or a mirror plane or both (with the mirror plane normal parallel to the axis of rotation) is said to have monoclinic symmetry. Taking the axis of rotation or the normal of the mirror

plane to be the 3-axis then such a material will have properties of the form

$$\mathbf{C} = \begin{bmatrix} C_{11} & C_{12} & C_{13} & 0 & 0 & C_{16} \\ & C_{22} & C_{23} & 0 & 0 & C_{26} \\ & & C_{33} & 0 & 0 & C_{36} \\ & & & C_{44} & C_{45} & 0 \\ & \text{symm.} & & & C_{55} & 0 \\ & & & & & C_{66} \end{bmatrix}, \tag{A.56}$$

$$\boldsymbol{\alpha}^w = \begin{bmatrix} \alpha_1^w & \alpha_2^w & \alpha_3^w & 0 & 0 & \alpha_6^w \end{bmatrix}^{\mathrm{t}}.$$

A material possessing at two orthogonal mirror planes, or two orthogonal 2-fold axes of rotation or a plane of symmetry and an axis of 2-fold rotation perpendicular to the mirror plane normal has at least orthotropic or orthorhombic symmetry. Taking the mirror plane normals or axes of rotation to be the 1- and 2-directions, an orthotropic material has properties of the form

$$\mathbf{C} = \begin{bmatrix} C_{11} & C_{12} & C_{13} & 0 & 0 & 0 \\ & C_{22} & C_{23} & 0 & 0 & 0 \\ & & C_{33} & 0 & 0 & 0 \\ & & & C_{44} & 0 & 0 \\ & \text{symm.} & & & C_{55} & 0 \\ & & & & & C_{66} \end{bmatrix}, \tag{A.57}$$

$$\boldsymbol{\alpha}^w = \begin{bmatrix} \alpha_1^w & \alpha_2^w & \alpha_3^w & 0 & 0 & 0 \end{bmatrix}^{\mathrm{t}}.$$

Generally orthotropy is claimed for wood as a consequence of its possessing three mutually perpendicular planes of symmetry having normals parallel to the three principal axes, that is in the radial, tangential and longitudinal directions (Bodig and Jayne, 1982). Even at macroscopic level the radial plane is not a plane of symmetry due to the directed intra-ring property variations. The longitudinal and tangential symmetry planes are present at least on average and within a suitably small volume. However, the helical nature of the cell walls, and the fact that these helices have a uniform sense (Meylan and Butterfield, 1978), prohibit any reflectional symmetry, be it statistical or not. Put another way, wood is non-centrosymmetric. In fact the only defensible symmetry for wood is a 2-fold rotational symmetry about the radial axis, making wood monoclinic, and even this symmetry disappears with grain deviation. Having said this, just because symmetry arguments do not require a component to disappear in the principal axes system does not mean that these components need be substantial, and it is in this sense that wood is approximately orthotropic, an assumption that is supported empirically (Goodman and Bodig, 1970; Dinwoodie, 1981; McEwan et al., 1998; Yang et al., 1998) though evidence to the contrary has also been presented (Goodman and

Bodig, 1970; Oudjehane and Raclin, 1995).

If a 4-fold axis of symmetry is present, about the 3-axis say, along with either a perpendcular plane or 2-fold axis symmetry, then the material is said to possess square symmetry and its properties take on the forms

$$\mathbf{C} = \begin{bmatrix} C_{11} & C_{12} & C_{13} & 0 & 0 & 0 \\ & C_{11} & C_{13} & 0 & 0 & 0 \\ & & C_{33} & 0 & 0 & 0 \\ & & & C_{44} & 0 & 0 \\ & \text{symm.} & & & C_{44} & 0 \\ & & & & & C_{66} \end{bmatrix}, \qquad \boldsymbol{\alpha}^w = \begin{bmatrix} \alpha_1^w & \alpha_1^w & \alpha_3^w & 0 & 0 & 0 \end{bmatrix}^{\mathrm{t}}. \tag{A.58}$$

Any material with a 6-fold axis of symmetry is said to possess hexagonal symmetry. Taking the axis of rotation to be the 3-direction, such a material has properties of the form

$$\mathbf{C} = \begin{bmatrix} C_{11} & C_{11}-2C_{66} & C_{13} & 0 & 0 & 0 \\ & C_{11} & C_{13} & 0 & 0 & 0 \\ & & C_{33} & 0 & 0 & 0 \\ & & & C_{44} & 0 & 0 \\ & \text{symm.} & & & C_{44} & 0 \\ & & & & & C_{66} \end{bmatrix}, \qquad \boldsymbol{\alpha}^w = \begin{bmatrix} \alpha_1^w & \alpha_1^w & \alpha_3^w & 0 & 0 & 0 \end{bmatrix}^{\mathrm{t}}. \tag{A.59}$$

Materials for which the constitutive equations are invariant for any rotation about a single axis are said to be transversely isotropic. Taking the axis of rotation as the 3-axis such a material has properties of the same form as a material having the 3-axis as a 6-fold axis of symmetry.

For an isotropic material all possible point symmetries are present and the properties are of the form

$$\mathbf{C} = \begin{bmatrix} C_{11} & C_{11}-2C_{44} & C_{11}-2C_{44} & 0 & 0 & 0 \\ & C_{11} & C_{11}-2C_{44} & 0 & 0 & 0 \\ & & C_{11} & 0 & 0 & 0 \\ & & & C_{44} & 0 & 0 \\ & \text{symm.} & & & C_{44} & 0 \\ & & & & & C_{44} \end{bmatrix}, \qquad \boldsymbol{\alpha}^w = \begin{bmatrix} \alpha_1^w & \alpha_1^w & \alpha_1^w & 0 & 0 & 0 \end{bmatrix}^{\mathrm{t}}. \tag{A.60}$$

Unlike the transversely isotropic case, none of the crystallographic point groups give rise to properties of an equivalent form to those of an isotropic material.

A.6. Engineering Constants

In practice the stiffness or compliance of materials possesing at least orthtropic symmetry are rarely specified in tensorial or matrix form. Used instead are the Young's moduli, E_i, the shear moduli, G_{ij}, and the Poisson's ratios, ν_{ij}, collectively known as the technical or engineering constants.

While various definitions are in use, here, with respect to the natural material coordinate system, the compliance matrix for an orthotropic material is specified in terms of the engineering constants by

$$\mathbf{D} \triangleq \begin{bmatrix} 1/E_1 & -\nu_{12}/E_2 & -\nu_{13}/E_3 & 0 & 0 & 0 \\ -\nu_{21}/E_1 & 1/E_2 & -\nu_{23}/E_3 & 0 & 0 & 0 \\ -\nu_{31}/E_1 & -\nu_{32}/E_2 & 1/E_3 & 0 & 0 & 0 \\ 0 & 0 & 0 & 1/G_{23} & 0 & 0 \\ 0 & 0 & 0 & 0 & 1/G_{31} & 0 \\ 0 & 0 & 0 & 0 & 0 & 1/G_{12}. \end{bmatrix} \tag{A.61}$$

By this definition ν_{ij} is the ratio of the compressive strain in the j direction to the tensile strain in the i direction resulting from a uniaxial tensile stress applied in the i direction. As $\mathbf{D} = \mathbf{D}^{\mathrm{t}}$ only three of the six Poisson's ratios are independent.

While specifying the stiffness of a material by way of the stiffness coefficients is unique and unambiguous it is not commonplace and the engineering constants are are thought by many to be more physically intuitive, though this might simply be a matter of familiarity. More importantly, states of approximately uniaxial stress are more commonly employed in the experimental characterization of a material and consequently compliance coefficients (or engineering constants) rather than stiffness coefficients are determined. For anisotropic materials it is rare for all the stiffness coefficients to be determined in any single experimental programme and so it may not be possible to determine the stiffness tensor by inverting the compliances. Thus if data are to be compared between studies the engineering constants are to be preferred.

Appendix B

Orientational averages

Consider a set of anisotropic domains constituting a material body. All the domains have the same properties but may be variously oriented. Describe the orientation of the material axes for a particular domain with respect to the body axes by a means of the Euler angles θ_1, θ_2, θ_3 defined as shown in figure B.1. The direction cosine matrix is then (Hughes, 1986)

$$[\omega_{ij}] = \begin{bmatrix} c_1c_3 - s_1c_2s_3 & c_1s_3 + s_1c_2c_3 & s_1s_2 \\ -s_1c_3 - c_1c_2s_3 & -s_1s_3 + c_1c_2c_3 & c_1s_2 \\ s_2s_3 & -s_2c_3 & c_2 \end{bmatrix} \tag{B.1}$$

with $c_i \triangleq \cos\theta_i$ and $s_i \triangleq \sin\theta_i$.

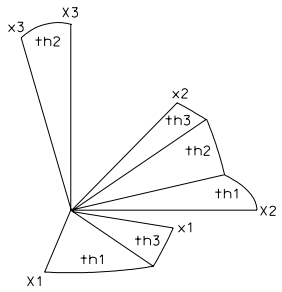

Figure B.1.: 3-1-3 Euler angles.

Suppose that the orientations of the domains with respect to the body coordinate system are distributed according to some orientation density function $n(\theta_1, \theta_2, \theta_3)$, normalized such that

$$\int_0^{2\pi}\int_0^{\pi}\int_0^{2\pi} n(\theta_1, \theta_2, \theta_3) \sin\theta_2 \, d\theta_1 \, d\theta_2 \, d\theta_3 = 1. \tag{B.2}$$

Then with respect to the body axes the expected value of a component $A_{ij\ldots k}$ of an

nth order tensor is

$$\begin{aligned}\bar{A}_{ij\ldots k} &\triangleq \mathrm{E}(A_{ij\ldots k}) \\ &= \int_0^{2\pi}\int_0^{\pi}\int_0^{2\pi} n(\theta_1,\theta_2,\theta_3)\,\omega_{pi}\omega_{qj}\ldots\omega_{rk}A'_{pq\ldots r}\sin\theta_2\,d\theta_1\,d\theta_2\,d\theta_3\end{aligned} \tag{B.3}$$

where $A'_{pq\ldots r}$ are the components of $\boldsymbol{A}$ with respect to the material coordinate system and R denotes the range over which θ_i vary. It is easily shown that the $\bar{A}_{ij\ldots k}$ constitute a tensor, $\bar{\boldsymbol{A}}$, which shall be called the orientational average of $\boldsymbol{A}$ over n.

In matrix notation the orientational averages, or the expected values, over n of the stress, strain, stiffness and compliance matrices are

$$\bar{\boldsymbol{\sigma}} = \int_0^{2\pi}\int_0^{\pi}\int_0^{2\pi} n\mathbf{T}'\boldsymbol{\sigma}'\sin\theta_2\,d\theta_1\,d\theta_2\,d\theta_3 \tag{B.4}$$

$$\bar{\boldsymbol{\epsilon}} = \int_0^{2\pi}\int_0^{\pi}\int_0^{2\pi} n\mathbf{T}^{\mathrm{t}}\boldsymbol{\epsilon}'\sin\theta_2\,d\theta_1\,d\theta_2\,d\theta_3 \tag{B.5}$$

$$\bar{\mathbf{C}} = \int_0^{2\pi}\int_0^{\pi}\int_0^{2\pi} n\mathbf{T}'\mathbf{C}'\mathbf{T}'^{\mathrm{t}}\sin\theta_2\,d\theta_1\,d\theta_2\,d\theta_3 \tag{B.6}$$

$$\bar{\mathbf{D}} = \int_0^{2\pi}\int_0^{\pi}\int_0^{2\pi} n\mathbf{T}^{\mathrm{t}}\mathbf{D}'\mathbf{T}\sin\theta_2\,d\theta_1\,d\theta_2\,d\theta_3 \tag{B.7}$$

with $\mathbf{T}$ and $\mathbf{T}'$ as defined in appendix A.

B.1. Uniaxial distribution

A uniaxial distribution about the 3−-axis is one for which θ_1 and θ_3 are random and hence $n = n(\theta_2)$. For such a distribution the 3-axis is always an axis of six fold symmetry. For a generally anisotropic fundamental domain the independent, non-zero average stiffnesses depend only on the nine orthorhombic components and are given by

$$\bar{\mathbf{c}} = \left(\mathbf{A}_C^{\phi_4}\phi_4 + \mathbf{A}_C^{\phi_2}\phi_2 + \mathbf{A}_C^{1}\right)\mathbf{c} \tag{B.8}$$

with

$$\bar{\mathbf{c}} = \begin{bmatrix} \bar{C}_{11} & \bar{C}_{12} & \bar{C}_{13} & \bar{C}_{33} & \bar{C}_{44} \end{bmatrix}^{\mathrm{t}},$$

$$\mathbf{c} = \begin{bmatrix} C_{11} & C_{12} & C_{13} & C_{22} & C_{23} & C_{33} & C_{44} & C_{55} & C_{66} \end{bmatrix}^{\mathrm{t}},$$

$$\mathbf{A}_C^{\phi_4} = \frac{1}{80}\begin{bmatrix} 9 & 6 & -24 & 9 & -24 & 24 & -48 & -48 & 12 \\ 3 & 2 & -8 & 3 & -8 & 8 & -16 & -16 & 4 \\ -12 & -8 & 32 & -12 & 32 & -32 & 64 & 64 & -16 \\ 24 & 16 & -64 & 24 & -64 & 64 & -128 & -128 & 32 \\ -12 & -8 & 32 & -12 & 32 & -32 & 64 & 64 & -16 \end{bmatrix},$$

$$\mathbf{A}_C^{\phi_2} = \frac{1}{48}\begin{bmatrix} 3 & 2 & 8 & 3 & 8 & -24 & 16 & 16 & 4 \\ 1 & 22 & -8 & 1 & -8 & -8 & 16 & 16 & -20 \\ 4 & -8 & -8 & 4 & -8 & 16 & -32 & -32 & 16 \\ -24 & -16 & 32 & -24 & 32 & 0 & 64 & 64 & -32 \\ 4 & 8 & -16 & 4 & -16 & 16 & -24 & -24 & 0 \end{bmatrix},$$

$$\mathbf{A}_C^{1} = \frac{1}{15}\begin{bmatrix} 3 & 2 & 2 & 3 & 2 & 3 & 4 & 4 & 4 \\ 1 & 4 & 4 & 1 & 4 & 1 & -2 & -2 & -2 \\ 1 & 4 & 4 & 1 & 4 & 1 & -2 & -2 & -2 \\ 3 & 2 & 2 & 3 & 2 & 3 & 4 & 4 & 4 \\ 1 & -1 & -1 & 1 & -1 & 1 & 3 & 3 & 3 \end{bmatrix}.$$

and

$$\phi_2 = \frac{1}{2}\left(3\int_0^{\pi} N(\theta)\cos^2\theta\sin\theta\, d\theta - 1\right), \tag{B.9}$$

$$\phi_4 = \frac{1}{4}\left(5\int_0^{\pi} N(\theta)\cos^4\theta\sin\theta\, d\theta - 1\right) \tag{B.10}$$

When all the domains are aligned then $\phi_2 = \phi_4 = 1$. When there is no preferred orientation then $\phi_2 = \phi_4 = 0$.

Likewise the independent, non-zero average compliances are given by

$$\bar{\mathbf{d}} = \left(\mathbf{A}_D^{\phi_4}\phi_4 + \mathbf{A}_D^{\phi_2}\phi_2 + \mathbf{A}_D^{1}\right)\mathbf{d} \tag{B.11}$$

with

$$\bar{\mathbf{d}} = \begin{bmatrix} \bar{D}_{11} & \bar{D}_{12} & \bar{D}_{13} & \bar{D}_{33} & \bar{D}_{44} \end{bmatrix}^{\mathrm{t}},$$

$$\mathbf{d} = \begin{bmatrix} D_{11} & D_{12} & D_{13} & D_{22} & D_{23} & D_{33} & D_{44} & D_{55} & D_{66} \end{bmatrix}^{\mathrm{t}},$$

$$\mathbf{A}_D^{\phi_4} = \frac{1}{80}\begin{bmatrix} 9 & 6 & -24 & 9 & -24 & 24 & -12 & -12 & 3 \\ 3 & 2 & -8 & 3 & -8 & 8 & -4 & -4 & 1 \\ -12 & -8 & 32 & -12 & 32 & -32 & 16 & 16 & -4 \\ 24 & 16 & -64 & 24 & -64 & 64 & -32 & -32 & 8 \\ -48 & -32 & 128 & -48 & 128 & -128 & 64 & 64 & -16 \end{bmatrix},$$

$$\mathbf{A}_D^{\phi_2} = \frac{1}{48}\begin{bmatrix} 3 & 2 & 8 & 3 & 8 & -24 & 4 & 4 & 1 \\ 1 & 22 & -8 & 1 & -8 & -8 & 4 & 4 & -5 \\ 4 & -8 & -8 & 4 & -8 & 16 & -8 & -8 & 4 \\ -24 & -16 & 32 & -24 & 32 & 0 & 16 & 16 & -8 \\ 16 & 32 & -64 & 16 & -64 & 64 & -24 & -24 & 0 \end{bmatrix},$$

and

$$\mathbf{A}_D^{1} = \frac{1}{30}\begin{bmatrix} 6 & 4 & 4 & 6 & 4 & 6 & 2 & 2 & 2 \\ 2 & 8 & 8 & 2 & 8 & 2 & -1 & -1 & -1 \\ 2 & 8 & 8 & 2 & 8 & 2 & -1 & -1 & -1 \\ 6 & 4 & 4 & 6 & 4 & 6 & 2 & 2 & 2 \\ 8 & -8 & -8 & 8 & -8 & 8 & 6 & 6 & 6 \end{bmatrix}.$$

Also the independent, non-zero average strains are

$$\bar{\mathbf{e}} = \left(\mathbf{A}_\epsilon^{\phi_2}\phi_2 + \mathbf{A}_\epsilon^{1}\right)\mathbf{e} \tag{B.12}$$

with

$$\bar{\mathbf{e}} = \begin{bmatrix} \bar{\epsilon}_1 & \bar{\epsilon}_3 \end{bmatrix}^{\mathrm{t}},$$

$$\mathbf{e} = \begin{bmatrix} \epsilon_1 & \epsilon_2 & \epsilon_3 \end{bmatrix}^{\mathrm{t}},$$

$$\mathbf{A}_\epsilon^{\phi_2} = \frac{1}{6}\begin{bmatrix} 1 & 1 & -2 \\ -2 & -2 & 4 \end{bmatrix},$$

and

$$\mathbf{A}_\epsilon^{1} = \frac{1}{3}\begin{bmatrix} 1 & 1 & 1 \\ 1 & 1 & 1 \end{bmatrix}.$$

B.2. Postscript

A presentation very similar to the above can be found in Wu and McCullough (1977). Advani and III. (1987) define a set of even ordered tensors that describe constituent orientation distributions and can be used to evaluate effective properties. In the context of partially oriented polymers, a more sophisticated approach is commonplace, see for example Roe and Krigbaum (1964) or Bower (1997). This approach expands the orientation distribution function, n, in terms of generalized spherical harmonic functions, i.e.

$$n(\theta_1, \theta_2, \theta_3) = \sum_{l=1}^{\infty} \sum_{m=-l}^{l} \sum_{n=-l}^{l} P_{lmn}\, Z_{lmn}(\cos\theta_2)\, e^{-im\theta_1} e^{-in\theta_3} \tag{B.13}$$

where Z_{lmn} is a generalized Legendre polynomial. As these spherical harmonics are orthogonal the coefficients, P_{lmn}, are, to within a normalization factor, equal to the average values of the corresponding function taken over the distribution.

Appendix C

Periodic layered media

Chou et al. (1972) have presented a mechanics of materials analysis for the effective elastic properties of periodic layered composites. A similar analysis, undertaken within the framework of asymptotic homogenization, can be found in Kalamkarov (1992) and the references cited therein. Here the approach of Chou et al. (1972) is generalized to include expansional strains and to permit completely anisotropic lamellae properties.

Consider a periodic laminate composed of repeating units, each unit having M layers (see figure C.1). The macroscopic stress $\boldsymbol{\sigma}$ and strain $\boldsymbol{\epsilon}$ are related by

$$\boldsymbol{\sigma} = \mathbf{C}\left(\boldsymbol{\epsilon} - \boldsymbol{\epsilon}^{\circ}\right). \tag{C.1}$$

where $\mathbf{C}$ is the effective stiffness and $\boldsymbol{\epsilon}^{\circ}$ the effective expansional strain. In layer m, with respect to the laminate co-ordinate system, the stresses and strains are related by

$$\boldsymbol{\sigma}^{(m)} = \mathbf{C}^{(m)}\left(\boldsymbol{\epsilon}^{(m)} - \boldsymbol{\epsilon}^{\circ(m)}\right). \tag{C.2}$$

If it is assumed that within each layer the stresses and strains are homogenous, and that

$$\epsilon_i^{(m)} = \epsilon_i \qquad i = 1,3,5 \tag{C.3}$$

$$\sum_{n=1}^{(m)} v^{(m)} \epsilon_i^{(m)} = \epsilon_i \qquad i = 2,4,6 \tag{C.4}$$

$$\sum_{n=1}^{(m)} v^{(m)} \sigma_i^{(m)} = \sigma_i \qquad i = 1,3,5 \tag{C.5}$$

$$\sigma_i^{(m)} = \sigma_i \qquad i = 2,4,6 \tag{C.6}$$

then the overall stiffness, $\mathbf{C}$, and expansional strain, $\boldsymbol{\epsilon}^{\circ}$, can be determined. In doing so the symmetry of equations (C.3)–(C.6) can be better exploited by defining

$$\boldsymbol{\epsilon}_a \triangleq \begin{bmatrix} \epsilon_1 & \epsilon_3 & \epsilon_5 \end{bmatrix}^{\mathrm{t}} \tag{C.7}$$

$$\boldsymbol{\epsilon}_b \triangleq \begin{bmatrix} \epsilon_2 & \epsilon_4 & \epsilon_6 \end{bmatrix}^{\mathrm{t}} \tag{C.8}$$

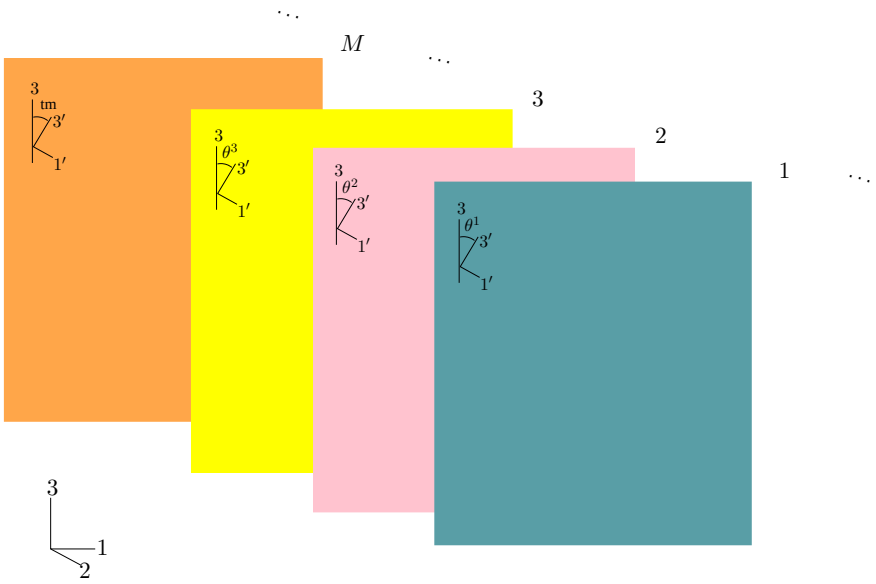

Figure C.1.: Periodic laminate.

$$\boldsymbol{\sigma}_a \triangleq \begin{bmatrix} \sigma_1 & \sigma_3 & \sigma_5 \end{bmatrix}^{\mathrm{t}} \tag{C.9}$$

$$\boldsymbol{\sigma}_b \triangleq \begin{bmatrix} \sigma_2 & \sigma_4 & \sigma_6 \end{bmatrix}^{\mathrm{t}} \tag{C.10}$$

$$\mathbf{C}_{aa} \triangleq \begin{bmatrix} C_{11} & C_{13} & C_{15} \\ C_{13} & C_{33} & C_{35} \\ C_{15} & C_{35} & C_{55} \end{bmatrix} \tag{C.11}$$

$$\mathbf{C}_{ab} \triangleq \mathbf{C}_{ba}^{\mathrm{t}} \triangleq \begin{bmatrix} C_{12} & C_{14} & C_{16} \\ C_{32} & C_{34} & C_{36} \\ C_{52} & C_{54} & C_{56} \end{bmatrix} \tag{C.12}$$

$$\mathbf{C}_{bb} \triangleq \begin{bmatrix} C_{22} & C_{24} & C_{26} \\ C_{24} & C_{44} & C_{46} \\ C_{26} & C_{46} & C_{66} \end{bmatrix} \tag{C.13}$$

$$\boldsymbol{\epsilon}_a^{\circ} \triangleq \begin{bmatrix} \epsilon_1^{\circ} & \epsilon_3^{\circ} & \epsilon_5^{\circ} \end{bmatrix}^{\mathrm{t}} \tag{C.14}$$

$$\boldsymbol{\epsilon}_b^{\circ} \triangleq \begin{bmatrix} \epsilon_2^{\circ} & \epsilon_4^{\circ} & \epsilon_6^{\circ} \end{bmatrix}^{\mathrm{t}}. \tag{C.15}$$

Since $\boldsymbol{\sigma}_b^{(m)} = \boldsymbol{\sigma}_b$

$$\mathbf{C}_{ba}^{(m)} \left(\boldsymbol{\epsilon}_a - \boldsymbol{\epsilon}_a^{\circ(m)} \right) + \mathbf{C}_{bb}^{(m)} \left(\boldsymbol{\epsilon}_b{}^{(m)} - \boldsymbol{\epsilon}_b^{\circ(m)} \right) = \mathbf{C}_{ba} \left(\boldsymbol{\epsilon}_a - \boldsymbol{\epsilon}_a^{\circ} \right) + \mathbf{C}_{bb} \left(\boldsymbol{\epsilon}_b - \boldsymbol{\epsilon}_b^{\circ} \right)$$

where use has also been made of the relation $\boldsymbol{\epsilon}_a^{(m)} = \boldsymbol{\epsilon}_a$, so

$$\begin{aligned}\boldsymbol{\epsilon}_b^{(m)} = \boldsymbol{\epsilon}_b^{\circ(m)} + \left(\mathbf{C}_{bb}^{(m)}\right)^{-1} \big[&\mathbf{C}_{ba}\left(\boldsymbol{\epsilon}_a - \boldsymbol{\epsilon}_a^{\circ}\right) + \mathbf{C}_{bb}\left(\boldsymbol{\epsilon}_b - \boldsymbol{\epsilon}_b^{\circ}\right) \\ &- \mathbf{C}_{ba}^{(m)}\left(\boldsymbol{\epsilon}_a - \boldsymbol{\epsilon}_a^{\circ(m)}\right)\big]\end{aligned} \tag{C.16}$$

Also,

$$\begin{aligned}\boldsymbol{\sigma}_a^{(m)} &= \mathbf{C}_{aa}^{(m)}\left(\boldsymbol{\epsilon}_a^{(m)} - \boldsymbol{\epsilon}_a^{\circ(m)}\right) + \mathbf{C}_{ab}^{(m)}\left(\boldsymbol{\epsilon}_b^{(m)} - \boldsymbol{\epsilon}_b^{\circ(m)}\right) \\ &= \mathbf{C}_{aa}^{(m)}\left(\boldsymbol{\epsilon}_a - \boldsymbol{\epsilon}_a^{\circ(m)}\right) + \mathbf{C}_{ab}^{(m)}\Big[\left(\mathbf{C}_{bb}^{(m)}\right)^{-1}\big[\mathbf{C}_{ba}\left(\boldsymbol{\epsilon}_a - \boldsymbol{\epsilon}_a^{\circ}\right) \\ &\quad + \mathbf{C}_{bb}\left(\boldsymbol{\epsilon}_b - \boldsymbol{\epsilon}_b^{\circ}\right) - \mathbf{C}_{ba}^{(m)}\left(\boldsymbol{\epsilon}_a - \boldsymbol{\epsilon}_a^{\circ(m)}\right)\big] - \boldsymbol{\epsilon}_b^{\circ(m)}\Big]\end{aligned} \tag{C.17}$$

First consider the case of no expansional strain (i.e. $\boldsymbol{\epsilon}^{\circ(m)} = 0$, $\forall m$; $\boldsymbol{\epsilon}^{\circ} = 0$), then from (C.1) and (C.3)–(C.6)

$$\begin{bmatrix} \sum_{n=1}^{(m)} v^{(m)}\boldsymbol{\sigma}_a^{(m)} \\ \boldsymbol{\sigma}_b \end{bmatrix} = \begin{bmatrix} \mathbf{C}_{aa} & \mathbf{C}_{ab} \\ \mathbf{C}_{ba} & \mathbf{C}_{bb} \end{bmatrix} \begin{bmatrix} \boldsymbol{\epsilon}_a \\ \sum_{n=1}^{(m)} v^{(m)}\boldsymbol{\epsilon}_b^{(m)} \end{bmatrix} \tag{C.18}$$

Putting (C.16) and (C.17) in (C.18) and eliminating $\boldsymbol{\epsilon}_a$ and $\boldsymbol{\epsilon}_b$ yields four matrix equations whose solution gives

$$\mathbf{C}_{bb} = \left(\sum_{n=1}^{(m)} v^{(m)}\left(\mathbf{C}_{bb}^{(m)}\right)^{-1}\right)^{-1} \tag{C.19}$$

$$\mathbf{C}_{ab} = \sum_{n=1}^{(m)} v^{(m)}\mathbf{C}_{ab}^{(m)}\left(\mathbf{C}_{bb}^{(m)}\right)^{-1}\mathbf{C}_{bb} \tag{C.20}$$

$$\mathbf{C}_{ba} = \mathbf{C}_{bb}\sum_{n=1}^{(m)} v^{(m)}\left(\mathbf{C}_{bb}^{(m)}\right)^{-1}\mathbf{C}_{ba}^{(m)} = \left(\mathbf{C}_{ab}\right)^{\mathrm{t}} \tag{C.21}$$

$$\mathbf{C}_{aa} = \sum_{n=1}^{(m)} v^{(m)}\left(\mathbf{C}_{aa}^{(m)} - \mathbf{C}_{ab}^{(m)}\left(\mathbf{C}_{bb}^{(m)}\right)^{-1}\mathbf{C}_{ba}^{(m)}\right) + \mathbf{C}_{ab}\left(\mathbf{C}_{bb}\right)^{-1}\mathbf{C}_{ba}. \tag{C.22}$$

Having determined the overall stiffness, the overall expansional strains can be found by setting $\boldsymbol{\sigma} = 0$, that is by considering the case of unrestrained expansion. Since $\boldsymbol{\sigma} = 0$, $\boldsymbol{\epsilon} = \boldsymbol{\epsilon}^{\circ}$, then from (C.16)

$$\boldsymbol{\epsilon}_b^{(m)} = \boldsymbol{\epsilon}_b^{\circ(m)} - \left(\mathbf{C}_{bb}^{(m)}\right)^{-1}\mathbf{C}_{ba}^{(m)}\left(\boldsymbol{\epsilon}_a - \boldsymbol{\epsilon}_a^{\circ(m)}\right) \tag{C.23}$$

and from (C.17)

$$\boldsymbol{\sigma}_a^{(m)} = \left(\mathbf{C}_{aa}^{(m)} - \mathbf{C}_{ab}^{(m)}\left(\mathbf{C}_{bb}^{(m)}\right)^{-1}\mathbf{C}_{ba}^{(m)}\right)\left(\boldsymbol{\epsilon}_a^{\circ} - \boldsymbol{\epsilon}_a^{\circ(m)}\right). \tag{C.24}$$

As $\boldsymbol{\sigma}_a = \sum v^{(m)} \boldsymbol{\sigma}_a^{(m)} = 0$

$$\sum_{n=1}^{(m)} v^{(m)} \left(\mathbf{C}_{aa}^{(m)} - \mathbf{C}_{ab}^{(m)} \left(\mathbf{C}_{bb}^{(m)} \right)^{-1} \mathbf{C}_{ba}^{(m)} \right) \left(\boldsymbol{\epsilon}_a^{\circ} - \boldsymbol{\epsilon}_a^{\circ(m)} \right) = 0 \tag{C.25}$$

so

$$\begin{aligned} \boldsymbol{\epsilon}_a^{\circ} = & \left(\mathbf{C}_{aa} - \mathbf{C}_{ab} \left(\mathbf{C}_{bb} \right)^{-1} \mathbf{C}_{ba} \right)^{-1} \\ & \cdot \sum_{n=1}^{(m)} v^{(m)} \left(\mathbf{C}_{aa}^{(m)} - \mathbf{C}_{ab}^{(m)} \left(\mathbf{C}_{bb}^{(m)} \right)^{-1} \mathbf{C}_{ba}^{(m)} \right) \boldsymbol{\epsilon}_a^{\circ(m)} \end{aligned} \tag{C.26}$$

And since $\boldsymbol{\epsilon}_b = \sum v^{(m)} \boldsymbol{\epsilon}_b^{(m)} = \boldsymbol{\epsilon}_b^{\circ}$ then from (C.23)

$$\begin{aligned} \boldsymbol{\epsilon}_b^{\circ} &= \sum_{n=1}^{(m)} v^{(m)} \left[\boldsymbol{\epsilon}_b^{\circ(m)} - \left(\mathbf{C}_{bb}^{(m)} \right)^{-1} \mathbf{C}_{ba}^{(m)} \left(\boldsymbol{\epsilon}_a^{\circ} - \boldsymbol{\epsilon}_a^{\circ(m)} \right) \right] \\ &= \sum_{n=1}^{(m)} v^{(m)} \left[\boldsymbol{\epsilon}_b^{\circ(m)} + \left(\mathbf{C}_{bb}^{(m)} \right)^{-1} \mathbf{C}_{ba}^{(m)} \boldsymbol{\epsilon}_a^{\circ(m)} \right] - \left(\mathbf{C}_{bb} \right)^{-1} \mathbf{C}_{ba} \boldsymbol{\epsilon}_a^{\circ}. \end{aligned} \tag{C.27}$$

C.1. Sublaminates — continuous orientation distribution

The M layers may themselves be laminates. In particular the mth-layer may be composed of lamellae of the same anisotropic material but with various orientations. Indeed, since the order of the layers in the above analysis is unimportant, layers composed of the same material, but intercalated with layers of different materials, may be conceptually grouped together.

Now, if the orientation of the lamellae within layer m, are described by a normalized orientation distribution function $w^{(m)} = w^{(m)}(\theta)$ for $-\pi \leq \theta < \pi$ so that $w^{(m)}\, d\theta$ is the fraction of material m having an orientation between θ and $\theta + d\theta$, then equations (C.19)–(C.22), (C.26) and (C.27) can be written as

$$\mathbf{C}_{bb} = \left(\sum_{m=1}^{(m)} v^{(m)} \int_{-\pi}^{\pi} w^{(m)} \mathbf{T}_{bb}' \left(\mathbf{C}_{bb}^{\prime(m)} \right)^{-1} \left(\mathbf{T}_{bb}' \right)^{\mathrm{t}} \, d\theta \right)^{-1} \tag{C.28}$$

$$\mathbf{C}_{ab} = \left(\sum_{m=1}^{(m)} v^{(m)} \int_{-\pi}^{\pi} w^{(m)} \mathbf{T}_{aa}' \mathbf{C}_{ab}^{\prime(m)} \left(\mathbf{C}_{bb}^{\prime(m)} \right)^{-1} \left(\mathbf{T}_{bb}' \right)^{\mathrm{t}} \, d\theta \right) \mathbf{C}_{bb} \tag{C.29}$$

$$\begin{aligned} \mathbf{C}_{ba} &= \mathbf{C}_{bb} \left(\sum_{m=1}^{(m)} v^{(m)} \int_{-\pi}^{\pi} w^{(m)} \left(\mathbf{T}_{bb}' \right)^{\mathrm{t}} \left(\mathbf{C}_{bb}^{\prime(m)} \right)^{-1} \mathbf{C}_{ba}^{\prime(m)} \mathbf{T}_{aa}' \, d\theta \right) \\ &= \left(\mathbf{C}_{ab} \right)^{\mathrm{t}} \end{aligned} \tag{C.30}$$

$$\mathbf{C}_{aa} = \sum_{m=1}^{(m)} v^{(m)} \int_{-\pi}^{\pi} w^{(m)} \mathbf{T}'_{aa} \left(\mathbf{C}'^{(m)}_{aa} - \mathbf{C}'^{(m)}_{ab} \left(\mathbf{C}'^{(m)}_{bb} \right)^{-1} \mathbf{C}'^{(m)}_{ba} \right) \left(\mathbf{T}'_{aa} \right)^{\mathrm{t}} \, d\theta + \mathbf{C}_{ab} \left(\mathbf{C}_{bb} \right)^{-1} \mathbf{C}_{ba} \tag{C.31}$$

$$\boldsymbol{\epsilon}^{\circ}_{a} = \left(\mathbf{C}_{aa} - \mathbf{C}_{ab} \left(\mathbf{C}_{bb} \right)^{-1} \mathbf{C}_{ba} \right)^{-1} \cdot \sum_{m=1}^{(m)} v^{(m)} \int_{-\pi}^{\pi} w^{(m)} \mathbf{T}'_{aa} \left(\mathbf{C}'^{(m)}_{aa} - \mathbf{C}'^{(m)}_{ab} \left(\mathbf{C}'^{(m)}_{bb} \right)^{-1} \mathbf{C}'^{(m)}_{ba} \right) \boldsymbol{\epsilon}^{\circ\prime(m)}_{a} \, d\theta \tag{C.32}$$

$$\boldsymbol{\epsilon}^{\circ}_{b} = \sum_{m=1}^{(m)} v^{(m)} \int_{-\pi}^{\pi} w^{(m)} \mathbf{T}'_{bb} \left(\boldsymbol{\epsilon}^{\circ\prime(m)}_{b} + \left(\mathbf{C}'^{(m)}_{bb} \right)^{-1} \mathbf{C}'^{(m)}_{ba} \boldsymbol{\epsilon}^{\circ\prime(m)}_{a} \right) \, d\theta - \left(\mathbf{C}_{bb} \right)^{-1} \mathbf{C}_{ba} \boldsymbol{\epsilon}^{\circ}_{a}. \tag{C.33}$$

in which $\mathbf{C}'^{(m)}_{ij}$ and $\boldsymbol{\epsilon}^{\circ\prime(m)}_{a}$ are the material properties of lamellae m with respect to the lamellae coordinate system, and the transformation from lamella to laminate coordinate systems is accomplished using

$$\mathbf{T}'_{aa} = \begin{bmatrix} \cos^2\theta & \sin^2\theta & 2\cos\theta\sin\theta \\ \sin^2\theta & \cos^2\theta & -2\cos\theta\sin\theta \\ -\cos\theta\sin\theta & \cos\theta\sin\theta & \cos^2\theta - \sin^2\theta \end{bmatrix}$$

and

$$\mathbf{T}'_{bb} = \begin{bmatrix} 1 & 0 & 0 \\ 0 & \cos\theta & -\sin\theta \\ 0 & \sin\theta & \cos\theta \end{bmatrix}.$$

The coefficients of the integrands in equations (C.28)–(C.33) are products of w and fourth order polynomials in $\sin\theta$ and $\cos\theta$ or alternatively, by applying the multiple angle formulas, products of w and first order polynomials in $\sin(n\theta)$ and $\cos(n\theta)$ for $n = 1 \ldots 4$. Thus the integrals are linear combinations of the orientation integrals I_p defined by

$$I_0 \triangleq \int_{-\pi}^{\pi} w \, d\theta \triangleq 1$$

$$\begin{aligned} I_1 &\triangleq \int_{-\pi}^{\pi} w \sin(\theta) \, d\theta & I_2 &\triangleq \int_{-\pi}^{\pi} w \cos(\theta) \, d\theta \\ I_3 &\triangleq \int_{-\pi}^{\pi} w \sin(2\theta) \, d\theta & I_4 &\triangleq \int_{-\pi}^{\pi} w \cos(2\theta) \, d\theta \\ I_5 &\triangleq \int_{-\pi}^{\pi} w \sin(3\theta) \, d\theta & I_6 &\triangleq \int_{-\pi}^{\pi} w \cos(3\theta) \, d\theta \\ I_7 &\triangleq \int_{-\pi}^{\pi} w \sin(4\theta) \, d\theta & I_8 &\triangleq \int_{-\pi}^{\pi} w \cos(4\theta) \, d\theta \end{aligned} \tag{C.34}$$

It is worth noting that in order to determine the effective hygro-elastic properties a complete knowledge of w is unecessary, all that is required are the orientation integrals.

In the general case the explicit forms of equations (C.28) to (C.33) in terms of the orientation integrals are too cumbersome to include. They have been evaluated and can be computed.

C.1.1. Isotropic orientation distribution

If there is only one distinct material, and this material is isotropic in the $1'2'$-plane, and if the orientation distribution is isotropic in the plane of layers, i.e. $w = 1/(2\pi)$ and $I_i = 0$, then the overall properties of the periodic laminate are isotropic in the 13-plane. For this case the explicit solution is manageable, the non-zero stiffness coefficients are

$$C_{11} = C_{33} = \left(2C'_{11} + 4C'_{13} + 3C'_{33} + 4C'_{44} + 4C'_{66}\right)/8 - A \tag{C.35}$$

$$C_{22} = C'_{11} \tag{C.36}$$

$$C_{12} = C_{23} = (C'_{11} + C'_{13})/2 - C'_{66} \tag{C.37}$$

$$C_{13} = \left(2C'_{11} + 4C'_{13} + C'_{33} - 4C'_{44} - 4C'_{66}\right)/8 + A \tag{C.38}$$

$$C_{44} = C_{66} = 2\left(C'_{44}C'_{66}\right) / \left(C'_{66} + C'_{44}\right) \tag{C.39}$$

$$C_{55} = (C_{11} - C_{13})/2 = \left(C'_{33} + 4C'_{44} + 4C'_{66}\right)/8 - A \tag{C.40}$$

where

$$A = \left({C'_{13}}^2 + 4C'_{13}C'_{66} + 4{C'_{66}}^2\right)/8C'_{11},$$

and the non-zero expansional strain coefficients are

$$\begin{aligned}\epsilon_1^\circ = \epsilon_3^\circ = &\left(-4C'_{11} - 2C'_{13} + 4C'_{66}\right)C'_{66}\epsilon_1^{\circ\prime}/B \\ &+ \left[\left(C_{13} - 2C_{66}\right)C_{13} - C_{33}C_{11}\right]\epsilon_3^{\circ\prime}/B\end{aligned} \tag{C.41}$$

$$\begin{aligned}\epsilon_2^\circ = &\left[\left(4C'_{66} - 2C'_{13} + 2C'_{33} - 4C'_{11}\right)C'_{66} - 2C'_{11}C'_{33} + 2{C'_{13}}^2\right]\epsilon_1^{\circ\prime}/B \\ &+ \left(-2C_{66}C_{33} - 2C_{13}C_{66} + C_{33}C_{11} - {C_{13}}^2\right)\epsilon_3^{\circ\prime}/B\end{aligned} \tag{C.42}$$

where

$$B = 4\left(C'_{66} - C'_{11} - C'_{13}\right)C'_{66} + {C'_{13}}^2 - C'_{33}C'_{11}.$$

C.1.2. Gaussian orientation distribution

Following Cave (1968) consider the orientation function

$$w(\theta) = \sum_m g(\theta + 2m\pi), \tag{C.43}$$

where $g(\theta)$ is the gaussian distribution with mean $\bar{\theta}$ and standard deviation s, i.e.

$$g(\theta) = \frac{1}{s\sqrt{2\pi}} \exp\left(-\frac{(\bar{\theta}-\theta)^2}{2s^2}\right) \tag{C.44}$$

Obviously $w(\theta)$ is periodic, with period 2π, and may be expanded as a Fourier series whose coefficients are

$$a_n = \int_{-\pi}^{\pi} w\cos(n\theta)\,d\theta = \int_{-\infty}^{\infty} g\cos(n\theta)\,d\theta = \exp(-n^2s^2/2)\cos(n\bar{\theta}) \tag{C.45}$$

$$b_n = \int_{-\pi}^{\pi} w\sin(n\theta)\,d\theta = \int_{-\infty}^{\infty} g\sin(n\theta)\,d\theta = \exp(-n^2s^2/2)\sin(n\bar{\theta}). \tag{C.46}$$

see Cave (1968) for the derivation. Thus

$$\begin{aligned} I_1 &= \exp(-s^2/2)\sin(\bar{\theta}) & I_2 &= \exp(-s^2/2)\cos(\bar{\theta}) \\ I_3 &= \exp(-2s^2)\sin(2\bar{\theta}) & I_4 &= \exp(-2s^2)\cos(2\bar{\theta}) \\ I_5 &= \exp(-9s^2/2)\sin(3\bar{\theta}) & I_6 &= \exp(-9s^2/2)\cos(3\bar{\theta}) \\ I_7 &= \exp(-8s^2)\sin(4\bar{\theta}) & I_8 &= \exp(-8s^2)\cos(4\bar{\theta}). \end{aligned} \tag{C.47}$$

Appendix D

Molecular components

Dry wood is composed of celluloses, hemicelluloses and lignins as well varying quantities of extractives and small amounts of pectins, proteins and inorganic elements. These constituents are not precisely defined chemically, but rather are classes of similar compounds.

D.0.3. Celluloses

Cellulose is the predominant component of wood, making up 30–50% of the overall mass, and is a linear homopolymer of (1→4)-linked β-D-glucopyranose residues (fig. D.1). Cellulose is ubiquitous within the plant kingdom, and is also produced by some fungi, bacteria, and is even found in animal tissue (Richmond, 1991). Introductions to cellulose structure, chemistry and biosynthesis can be found in Fengel and Wegener (1984); Timell (1986a); Okamura (1990); McGinnis and Shafizadeh (1991); Atalla (1999a).

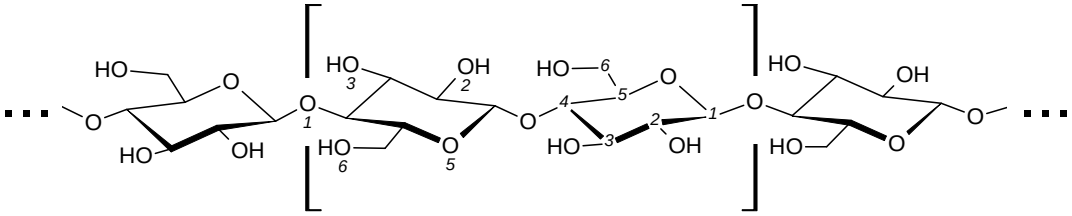

Figure D.1.: Cellulose structure. Conventional carbon and oxygen numberings are shown along with the cellobiose unit.

Native celluloses have a very high molecular weight. The degree of polymerization (DP) reported ranges widely, up to 40,000, depending on:

(i) the source of the cellulose; algal celluloses having the highest DP

(ii) the preparation techniques employed

(iii) and the method of determining molecular weight or DP.

Careful studies of celluloses from wood result in DP measurements of 9000–12000 (Goring and Timell, 1962; Patscheke and Poller, 1980). Celluloses from the secondary wood wall appear to be monodisperse, whereas primary wall celluloses, which have lower

molecular weights, are also polydisperse. All things considered, it seems safe to assume that in undegraded wood the cellulose chains consist of at least 10,000 glucose residues and have a length of around 5000 nm.

Glucopyranose in the equatorial chair form, the most stable conformation, has all the bulky side groups lying in the same plane as the ring. This, combined with the β-glycosidic linkages give cellulose a flat, ribbon-like shape. In contrast, amylose, one component of starch and another polyglucan, with (1→4)-α-glycosidic links adopts a helical conformation. A cellulose chain has a transverse aspect ratio of around 2:1 and a cross sectional area of 0.319 nm^2(Nishino et al., 1995).

A half twist between sucessive glucosides results in a more favourable chain conformation by admitting two intramolecular hydrogen bonds (O2H..06 and 03H..05). In this conformation the (1→4)-β-D-glucose dimer, cellobiose, is the true translational repeat unit. Amongst the wood cell wall polysaccharides such a secondary structure appears unique to cellulose and significantly stiffens the cellulose chains.

In solution, cellulose exhibits a highly extended conformation and can be regarded as a semi-rigid polymer (Sarko, 1976). Cellulose also exhibits liquid crystal properties, a characteristic of rigid chain polymers (Chanzy et al., 1980).

D.0.4. Hemicelluloses

Like the celluloses, the hemicelluloses are polysaccharides constructed from the monosaccharides shown in figure D.2. Unlike the celluloses the hemicelluloses are heteropolymers, have a much lower degree of polymerization and are not strictly linear, though the sidechains rarely exceed several sugar residues in length. Meier (1964) pointed out that hemicellulose is something of a misnomer since these polysaccharides are not 'half-cellulose' in any sense, though he still preferred the term over the older alternatives: cellulosanes, polyuronides or polyosanes. Fengel and Wegener (1984) argue forcefully against the using the term hemicellulose, preferring instead polyose. Unfortunately, while the latter may be more correct the former is overwhelmingly prevalent.

Introductions to hemicellulose structures, chemistry and biosynthesis can be found for example in Fengel and Wegener (1984); Timell (1986a); Shimizu (1990); Whistler and Chen (1991); Gregory and Bolwell (1999). Hemicelluloses in radiata pine are reviewed by Uprichard (1991).

Within the hemicelluloses further classification can be made. These subgroups have names built from the names of the component monosaccharides ordered, by convention, from the least to the most prevalent. In softwoods the galactoglucomannans are the most abundant group of hemicelluloses with arabinoglucuronoxylans present in lesser concentration. Compression wood also contains galactans and (1→3)-linked β-D-glucans, sometimes referred to as laricinans.

Aldopentoses

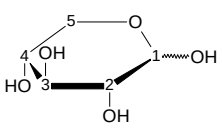

D-xylopyranose
(D-Xyl*p*)

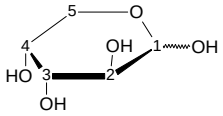

D-arabinopyranose
(D-Ara*p*)

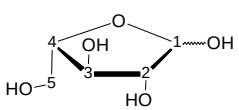

L-arabinofuranose
(L-Ara*f*)

Uronic acids

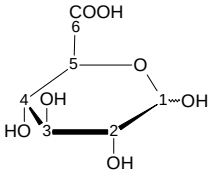

D-glucuronic acid
(D-GlcA)

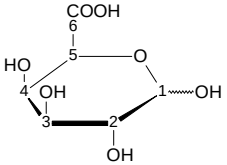

D-galacturonic acid
(D-GalA)

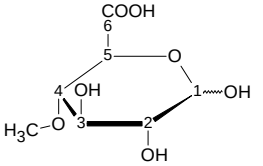

4-O-methyl-D-glucuronic acid
(4-O-Me-α-D-Glc*p*)

Aldohexoses

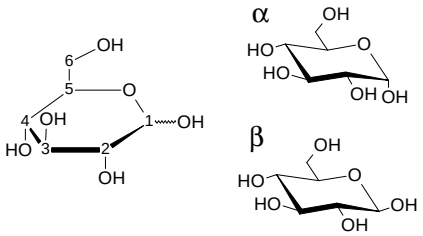

D-glucopyranose
(D-Glc*p*)

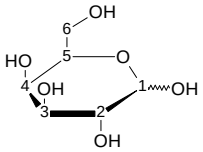

D-galactopyranose
(D-Gal*p*)

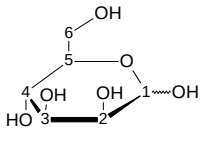

D-mannopyranose
(D-Man*p*)

Deoxy sugars

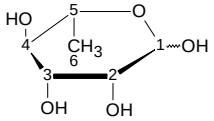

L-rhamnose
(6-deoxy-L-mannose)

Figure D.2.: Monosaccharides present in wood.

D.0.4.1. Galactoglucomannans and Glucomannans

O-acetyl-galactoglucomannan (figure D.3), also referred to as galactoglucomannan, is the principle hemicellulose in the normal wood of most softwoods where it constitutes 15–22% of the whole mass. Notable exceptions to this rule include incense cedar and some larches. In compression wood the proportion of this polysaccharide is lower, generally only 8–9%. Galactoglucomannans are only lightly branched and have a main chain of 50–100 (1→4)-linked β-D-glucopyranose and β-D-mannopyranose units, with side groups of (1→6)-linked α-D-galactopyranose. The Glc residues occupy 20–50% of the backbone positions, but are not contiguous (Gregory and Bolwell, 1999). The C2 and C3 positions on the mannose and glucose units are partially (DS of 0.17–0.36) acetylated. Galactoglucomannans can be roughly divided into two fractions having different galactose contents; very approximately the the sugar residues are found in each of these fractions are in proportions Gal:Glu:Man of 0.1:1:3 and 1:1:3. The low galactose fraction is often referred to as simply glucomannan. While the total amount of galactoglucomannan present is relatively constant the ratio of these two fractions and the ratios of the monosaccharides varies from species to species (Timell, 1961; Fengel and Wegener, 1984). In radiata pine the total Gal:Glc:Man ratio is taken as 0.13:1:3.7 and the DP is at least 45 (Harwood, 1973). The high galactan fraction is relatively easily removed from deliginifed wood. The glucomannan fraction on the other hand is much harder to extract and is assumed to be tightly bound to the cellulose.

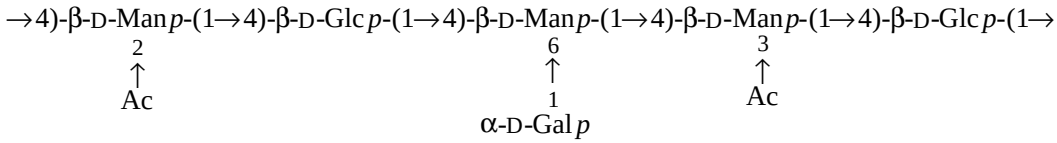

Figure D.3.: Partial structure of an O-acetyl-galactoglucomannan. After Shimizu (1990).

Extracted from the cell wall glucomannans can be crystallized (Millane and Hendrixson, 1994), but there appears to be no evidence for any long range order *in vivo*.

D.0.4.2. Xylans

Arabino-(4-O-methylglucurono)xylans (figure D.4), also referred to as arabinoglucuronoxylans or simply as xylans, are also common in softwoods, constituting 8–12% of the mass of normal wood. Compression wood usually contains a similar or slightly larger amount. Xylans are moderately branched with 5–10 branches per macromolecule and have a main chain of 50–200 (1→4)-linked β-D-xylopyranose units with 4-O-methyl α-D-glucuronic acid groups attached mainly at C2, but also at C3, and α-L-arabinofuranose groups attached at predominantly at the C3 position. Branch points probably also

occur at the C2 position. The arabinofuranose side chains often consist of only a single unit, but they may be longer. The ratio of xylose to arabinose residue is reported as being between 5:1 and 12:1. Arabinose and 4-O-methyl-glucuronic-acid residues are present in numerically equal amounts. Separation of xylan and galactoglucomannan is often difficult.

Pentosan content is an approximate measure of xylan content since wood contains signficantly more xylose than arabinose and the other sugars present, glucose, galactose, and mannose, are hexoses.

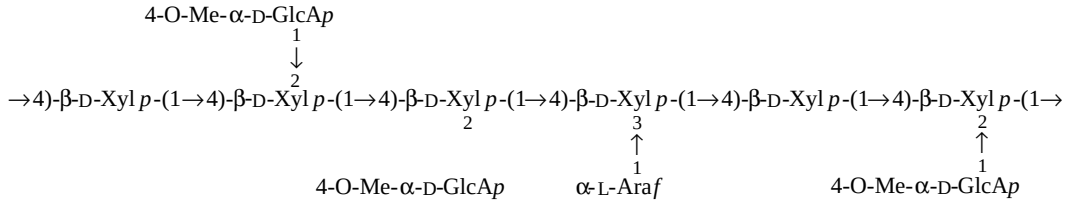

Figure D.4.: Partial structure of an arabino-(4-O-methylglucurono)xylan. After Shimizu (1990).

D.0.4.3. Galactans

Galactan (figure D.5) makes up 9–10% of pronounced compression wood, but little or none is found in normal wood. Galactan has a backbone of 200–300 (1→4)-linked *β*-D-galactopyranose residues, with galacturonic and glucuronic acids present as sidechains and terminal residues. One in twenty galactose residues carries a single terminal residue of *β*-D-glucuronic acid attached at C6. A large portion (80%) of the galactan present is not associated with the cellulose and numerous chemical links with lignin almost certainly exist. The remainder is very tightly bound to the microfibrils, even more so than glucomannan. Most of the galactan is located in the S1 and outer S2 wall layers. Galactan is slightly branched with 4–6 branches per macromolecule.

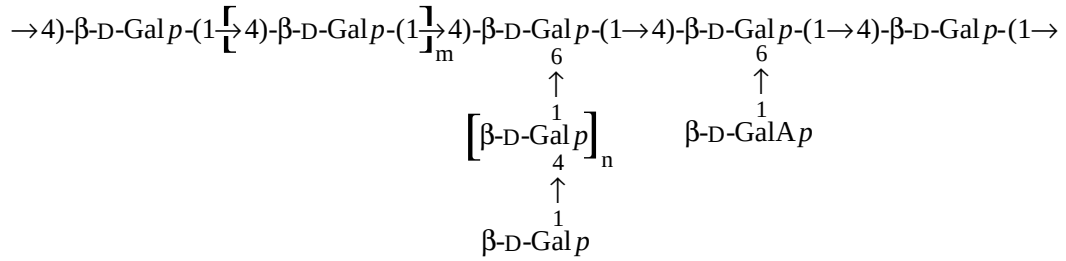

Figure D.5.: Partial structure of a galactan. After Shimizu (1990).

D.0.4.4. Laricinans

Laricinan concentrations of 2–4% are thought to exist in compression wood, but only trace amounts are found in normal wood. Like callose, laricinan has a main chain of around 200–300 primarily (1→3)-linked *β*-D-glucopyranose residues, but 6–7% of the linkages are (1→4). Galacturonic and glucuronic residues are also present, probably as single unit side chains. The ease with which laricinans may be removed from deliginified wood indicate that these hemicelluloses are not strongly associated with the cellulose microfibrils.

Wloch and Hejnowicz (1983) report finding laricinan in the helical cavities in the S2 layer of compression wood and have proposed a role for laricinan in the mechanism of compression wood. Boyd (1978) on the other hand claims that laricinan is not the main factor in the generation of reorientation forces in compression wood.

D.0.4.5. Arabinogalactans

Arabinogalactan (figure D.6) is found in large quantities (5–40%) only in species og the *Larix* genus, but is present in small amounts (<2%) in a number, if not all conifers, including radiata pine (Brasch and Wise, 1956a,b; Brasch et al., 1959). Arabinogalactans are highly branched, with nearly every residue carrying a branch at C-6, and as a consequence are water soluble. They are found only in the heartwood, concentrated at the sapwood/heartwood boundary, and unlike other hemicelluloses are extracellular and non-structural (Cote, Jr. et al., 1966; Jr. and Timell, 1967).

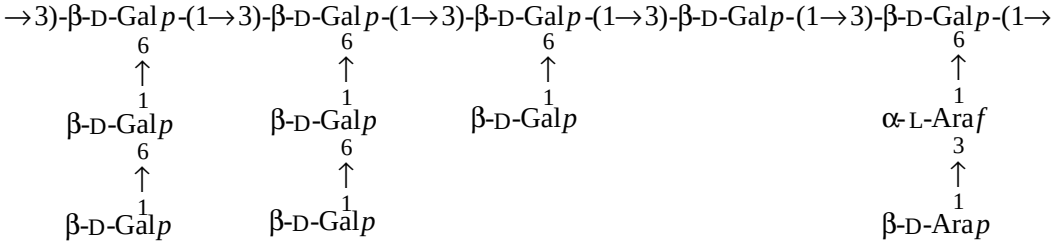

Figure D.6.: Partial structure of an arabinogalactan. After Shimizu (1990).

D.0.4.6. Arabinans

Arabinans have been reported in Scotch pine (*Pinus sylvestris*) and maritime pine (*Pinus pinaster*) (Whistler and Chen, 1991), but only in trace amounts and they are probably found only in the primary wall.

D.0.5. Lignins

Lignins are chemically very different to the polysaccharides discussed so far. They are considered to be evolutionarily more advanced and, setting aside the controversial moss 'lignins', are found only in plants with vascular tissues. Reviews of lignin structure, chemistry and biosynthesis can be found in Freudenberg and Neish (1968); Sarkanen and Ludwig (1971); Fengel and Wegener (1984); Glasser and Sarkanen (1989); Sakakibara (1990); Chen (1991); Lewis and Sarkanen (1998); Lewis (1999); Lewis et al. (1999); Davin and Lewis (2000).

In softwoods lignin content varies between 20 and 40% by mass. The primary structure of lignins are still to a large degree uncertain. What is known is that lignin is a crosslinked polymer constructed from the phenylpropane monolignols: p-coumaryl, coniferyl and sinapyl alcohols (figure D.7). Softwood lignins are mostly composed of guiacyl units (G) originating from coniferyl alcohol, but syringyl (S) from sinapyl alcohol and p-hydroxyphenyl (H) units from p-coumaryl are also present in a G:S:H ratio of around 60:1:6. The preponderance of guiacyl units in softwood lignins means they are classed as G-lignins. Based on known connections and substructures various model lignins have been proposed Fengel and Wegener (1984). A portion of one of these is shown in figure D.8. Lignins are known to be heterogenous, varying between taxa and tissue types, as well as within cell walls (Fengel and Wegener, 1984; Ruel et al., 1999). In particular, compression wood lignins and lignins from the compound middle lamella have a higher proportion of H units, and are consequently classified as GH-lignins.

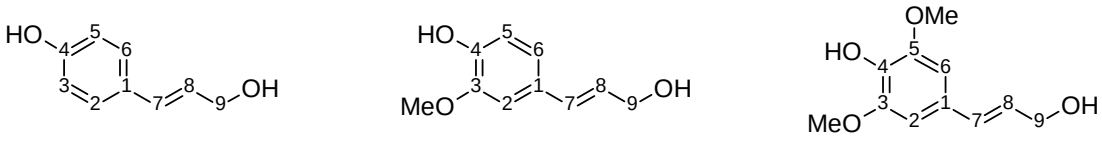

Figure D.7.: Monolignols.

Isolated lignins are highly polydisperse, and it would appear that the same is true *in vivo*. Weight average molecular masses of upwards of 80,000 have been recorded for lignins from softwood. Assuming a compact form and an average density of around 1.3 g/cc such a molecule would occupy around 100 nm^3, and would be built from more than 400 monolignols.

Erins et al. (1976) deduced a model for the structure of the wood cell wall based on various chemical extraction techniques. They concluded that lignin has a globular structure, with hemicellulose chains linking several globules together. Each globule consists of about 20 tightly crosslinked phenylpropane units and has a molecular weight

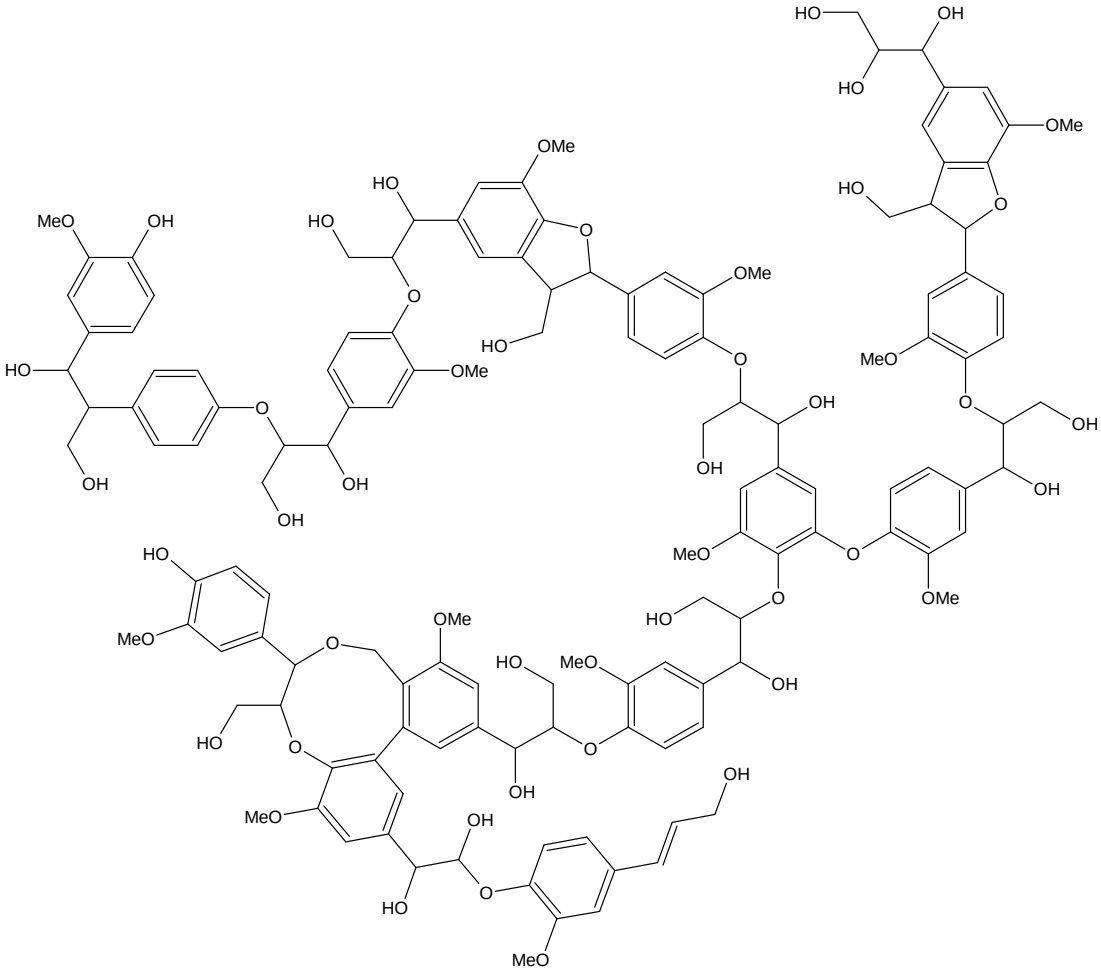

Figure D.8.: Structure scheme for a fragment of softwood lignin. After Brunow et al. (1998).

of around 4000. They also suggested that many of these globules could be found in association, forming aggregations with molecular weights of up to 100,000.

Secondary structure is also uncertain, but lignins can form inter- and intra-molecular hydrogen bonds. Electron microscopic investigations show lignins to adopt globular shapes (Fengel and Wegener, 1984), and Favis et al. (1984) characterized extracted lignins as being disc-like with a spherical diameter of between 5 and 10 nm. In molceular dynamics studies of model lignins Faulon et al. (1994) found a helical configuration was favoured and Russell et al. (2000) describe a compact conformation.

D.0.6. Pectins and proteins

Pectins, another class of polysaccharides, and glycoproteins occur in the middle lamella and primary wall. In cambial tissue they can make up well over 50% of the mass, but in mature wood they account for less than 2% (Simson and Timell, 1978; Selvendran, 1985; Westermark et al., 1986).

Exactly what distinguishes pectins from hemicelluloses is unclear. For example, Fengel and Wegener (1984) class arabinans as pectins; indeed they define pectins as comprising the galacturonans, galactans and arabinans. On the other hand Rogers and Perkins (1968) define pectin to be a partially methylated polygalacturonic acid. That is, a (1→4)-linked D-galacturonic acid whose carboxyl groups are in the majority esterified by methyl groups.

Westermark et al. (1986) studied the pectins and proteins found in the middle lamella and primary wall of *Picea abies* . They found a much lower pectin content in the lignified wall compared to that previously found in unlignified tissue, and concluded that the pectin content is largely removed after the cell stops enlarging and prior to lignification. Alternatively it has also been suggested that the pectic substances are incorporated into lignin-like compounds.

D.0.7. Extractives

Extractives, so called because they can be removed (at least partially) with water or various non-polar organic solvents, generally make up 1–10% by weight, though extractive contents of upwards of 20% are not unheard of. They are often concentrated in heartwood and in the butt of the stem. Typically the extractive content of radiata pine is around 2.5% (Uprichard, 1991).

The chemical nature of the extractive fraction is species specific and varies widely with gums, fats, resins, sugars, oils, starches, alkaloids, tannins and lignans (non-lignin phenolic substances) all occurring. Extractives are not part of the wood structural substance, however they may alter the hygroscopicity of the cell wall and impede water movement and thus indirectly influence the mechanical behaviour. However Meylan

and Butterfield (1972) reported that there was no difference in longitudinal shrinkage between extracted and unextracted small clear radiata pine samples. On the other hand, Cown (1992) claims that in radiata pine the volumetric shrinkage of heartwood is around 1% less than that of the sapwood of the same basic density.

D.0.8. Inorganic matter

Inorganic elements, primarily Ca, K, Mg, and Mn, are distributed throughout the cell wall (Chatters, 1963) and make up 0.1–1.0% of softwood by weight (Fengel and Wegener, 1984), though 5% or more may be found in tropical wood (Browning, 1963). Wood from radiata pine has an average ash content of only 0.2% (Uprichard, 1991).

Inorganic elements are found randomly dispersed within the cell-wall (Chatters, 1963) where they may act to crosslink other wall polymers. Inorganic matter may also occur as mineral deposits within the cell lumina.

Appendix E

Microfibrillar orientation from oblique sections

E.1. Introduction

A description of the variation in microfibrillar orientation across tracheid cell-walls is required for a detailed stress analysis. The analysis of oblique sections, imaged by transmission electron microscopy, provides a potential method for obtaining such a description. This appendix presents the theoretical basis for the determination of microfibril angle from oblique sections, and applies the method to sections cut from *Pinus radiata* earlywood tracheids. Results are presented and the method is critically discussed.

In transmission electron micrographs of oblique sections of stained tracheid cell walls, the microfibrillar alignment produces the appearance of arcs in regions of rearrangement and line segments in regions of constant orientation (Roland and Mosiniak, 1983; Roland et al., 1987; Neville and Levy, 1985; Neville, 1993). These arcs can be seen in E.1 and their origin is illustrated in figure E.2.

By measuring the apparent orientation of the microfibrils in the images it is possible to determine the true orientation of the microfibrils in the cell-wall. Fujita and Harada (1990) suggest that a method to do this has been developed previously by Yamanaka (1969). Such a method is developed again here.

E.2. Theory

Within the cell wall the orientation of the microfibrils can be described by a unit vector field, $\boldsymbol{u}(\boldsymbol{x})$.

Introduce two cartesian coordinate systems, the wall coordinate system with base vectors $\boldsymbol{e}_i^w$ whose 3-axis is oriented parallel to the longitudinal axis of the cell and whose 1-axis lies in the plane tangent to the central surface of the middle lamella, and the section coordinate system with base vectors $\boldsymbol{e}_i^s$ whose 3-axis is normal to the sectioning plane and whose 1-axis also lies in the plane tangent to the central middle lamella surface.

The microfibrillar orientation function has components u_i^w in the wall coordinate

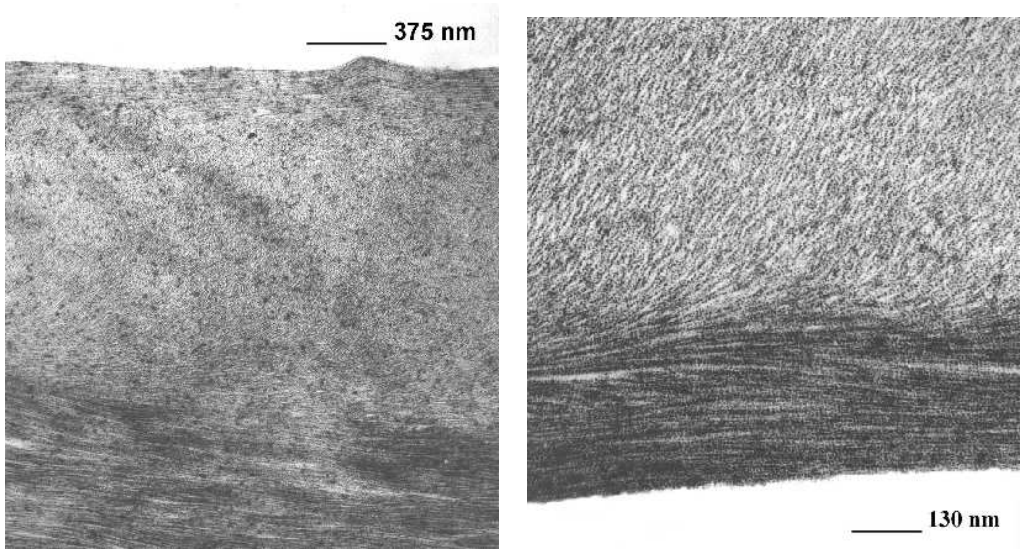

Figure E.1.: Oblique micrographs (TEM) of the cell wall of radiata pine tracheids. Courtesy of Dr Lloyd Donaldson, Forest Research, Rotorua.

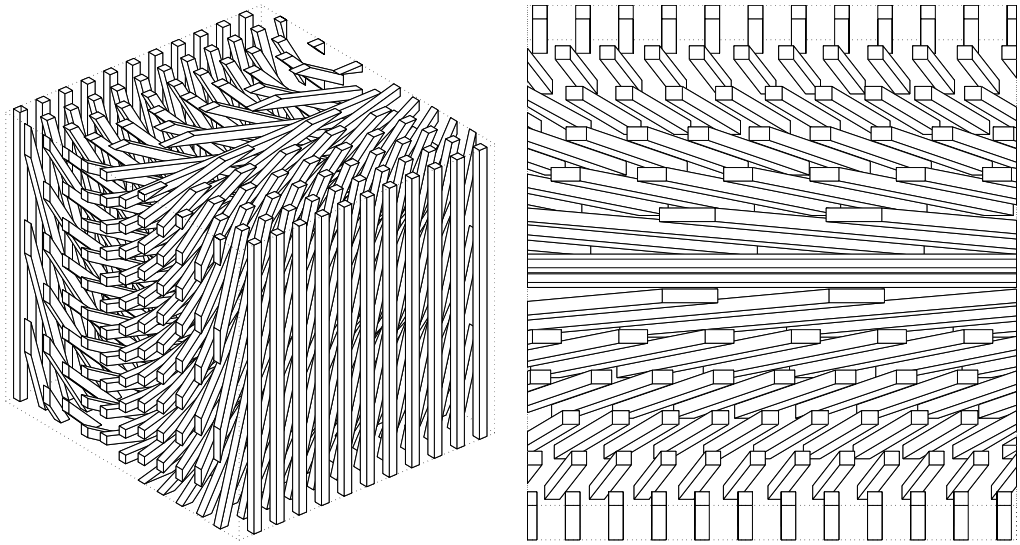

Figure E.2.: Origin of arcs in oblique sections.

system and u_i^s in the section coodinate system, i.e.

$$\boldsymbol{u} = u_i^w \boldsymbol{e}_i^w = u_i^s \boldsymbol{e}_i^s. \tag{E.1}$$

The u_i^s are related to the u_i^w by

$$u_i^s = Q_{ij}^{sw} u_j^w, \tag{E.2}$$

where

$$Q_{ij}^{sw} = \boldsymbol{e}_i^s \cdot \boldsymbol{e}_j^w. \tag{E.3}$$

The transformation from the wall to section coordinate systems is by a rotation through the sectioning angle ψ about an axis lying in the sectioning plane and normal to the cutting direction. The axis of rotation lies in the wall 12-plane, and makes an angle γ with the 1-axis of both the wall and the section coordinate systems. The direction cosine matrix corresponding to this transformation is

$$\mathbf{Q}^{sw} = \begin{bmatrix} \cos\psi + (1-\cos\psi)\cos^2\gamma & (1-\cos\psi)\cos\gamma\sin\gamma & -\sin\psi\sin\gamma \\ (1-\cos\psi)\cos\gamma\sin\gamma & \cos\psi + (1-\cos\psi)\sin^2\gamma & \sin\psi\cos\gamma \\ \sin\psi\sin\gamma & -\sin\psi\cos\gamma & \cos\psi \end{bmatrix}. \tag{E.4}$$

Given the coordinate systems described above the microfibril angle, θ, can be defined as

$$\tan\theta \triangleq \frac{u_1^w}{u_3^w}, \tag{E.5}$$

and if it is assumed that the microfibrils lie in concentric lamellae then $u_2^w = 0$.

Define ϕ to be the angle made between the 2-axis of the section coordinate system and the apparent orientation of the microfibrils in the section plane, i.e.

$$\tan\phi \triangleq \frac{u_1^s}{u_2^s}. \tag{E.6}$$

So from (E.2), (E.5) and (E.6)

$$\tan\phi = \frac{\left(\cos^2\gamma(\cos\psi - 1) - \cos\psi\right)\tan\theta + \sin\psi\sin\gamma}{\cos\gamma\left((-\sin\gamma + \sin\gamma\cos\psi)\tan\theta - \sin\psi\right)} \tag{E.7}$$

from which the microfibril angle θ can be determined as

$$\tan\theta = \frac{\sin\psi\left(\sin\gamma + \tan\phi\cos\gamma\right)}{\cos\psi + \cos^2\gamma(1-\cos\psi) + \tan\phi(\cos\psi - 1)\cos\gamma\sin\gamma}. \tag{E.8}$$

In practice it is convenient to set $\gamma = 0$ by measuring only cell walls whose normal

is parallel to the sectioning direction. When this is the case equation E.8 reduces to

$$\tan\theta = \sin\psi \tan\phi \tag{E.9}$$

and the error in θ is

$$d\theta = \frac{\sin\psi\, d\phi + \cos\psi \sin\phi \cos\phi\, d\psi + \sin\psi(1 - \cos\psi \sin^2\phi)\, d\gamma}{1 - \cos^2\psi \sin^2\phi}. \tag{E.10}$$

Using equation E.9 if the sectioning angle ψ is known then the microfibril angle can be determined along lines parallel to the sectioning direction and perpendicular to the cell wall layers from measurements of the angle, ϕ, between the radial cell-wall direction and the apparent microfibril direction in the images. Equation E.10 then gives an indication of the likely error in the microfibril angle so determined.

E.3. Results and discussion

A small block ($1\times1\times1$ mm) of *Pinus radiata* earlywood was stained with uranyl acetate and lead citrate and embedded in resin. Thin sections (60–100 nm) were prepared using an ultramicrotome. These sections were cut obliquely, with the knife-edge making an angle, ψ, with the specimen's transverse plane. Two sets of specimens were prepared, the first with $\psi = 20°$, the second with $\psi = 40°$. The sections were imaged in a transmission electron microscope at a magnification of between 7500 and 40,000 times, 80kV[1]. Knife marks on the section were used to find portions of the cell wall where the radial wall direction was parallel to the cutting direction. In these regions $\gamma = 0$. Two sequences of images across a cell wall (one for each specimen set) were prepared.

Only the sequence of images of sections cut at 20° had sufficient contrast to permit the measurement of ϕ. These images were made at a magnification of 40,000× and several were required to cover the cell wall. Fortuitously there were sufficient distinct features to permit the montage shown in figure E.3(a) to be constructed. The ϕ angles were measured manually at 27 positions across the secondary cell wall. The calculated microfibril angles are shown in figure E.4. The error bars shown are based on estimated absolute errors in γ of ±5°, in ψ of ±2° and in ϕ of ±5°.

A quartic spline model for the variation in θ across the cell wall has been fitted to the experimental data and is also plotted in figure E.4. Using this model for θ, a 20° oblique section has been simulated (see figure E.3(b)). The micrograph montage and the simulation can be seen to be similar. Based on the spline model, the mean MFA, the standard deviation of the MFA and the orientation integrals defined in appendix C

[1]Specimen preparation and ultarmicrotomy were performed by Manfred Ingerfeld in the Department of Plant and Microbial Science, University of Canterbury.

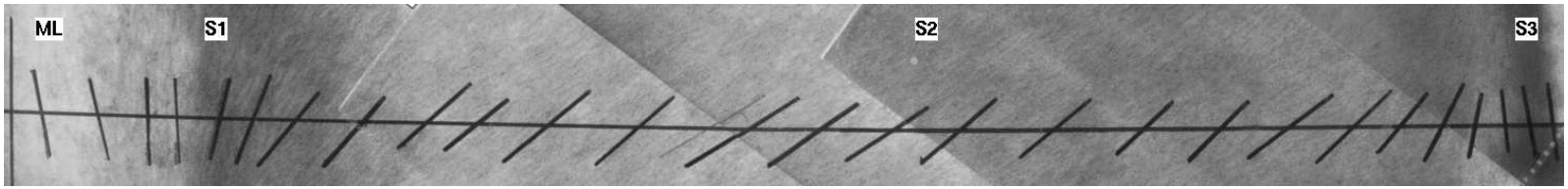

(a) Montage of micrographs

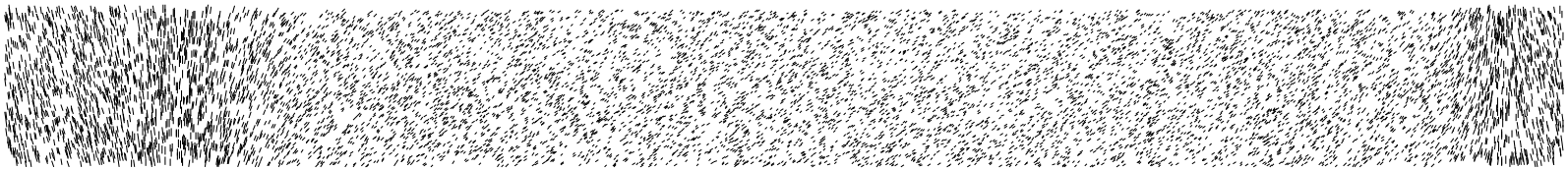

(b) Simulation

Figure E.3.: Tracheid cell wall sectioned at 20°. ML on the left.

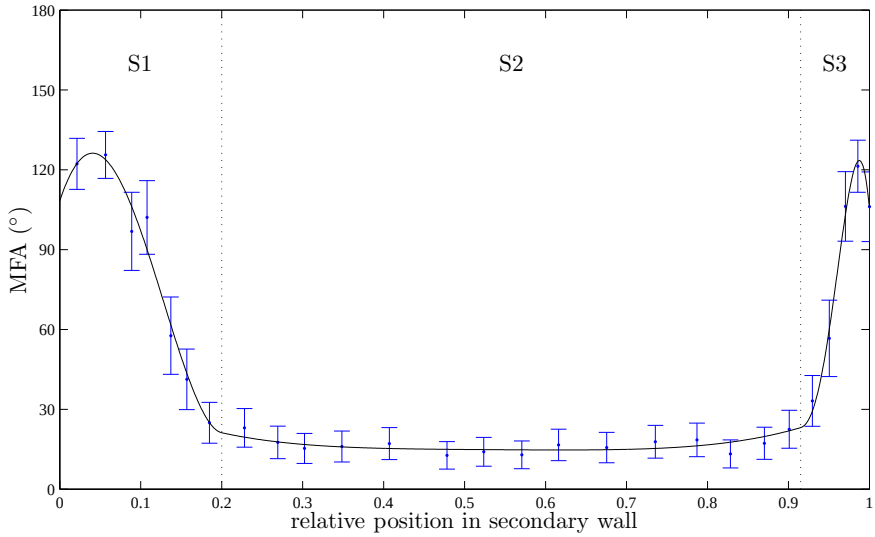

Figure E.4.: Microfibril angles across the secondary wall of a single tracheid.

	mean	std. dev.	I_1	I_2	I_3	I_4	I_5	I_6	I_7	I_8
S1	85	37	0.80	0.048	-0.063	-0.35	0.052	0.29	0.43	-0.23
S2	16	2.0	0.28	0.96	0.54	0.84	0.75	0.65	0.90	0.41
S3	74	37	0.77	0.21	0.15	-0.28	0.12	0.16	0.42	-0.20

Table E.1.: Mean, standard deviation and orientation integrals for secondary wall layers.

have been calculated for each of the major wall layers. The results of these calculations are reported in table E.1.

The variation in θ across the cell wall of a *Pinus radiata* tracheid shown in figure E.4 is similar to that presented by Fujita and Harada (1990) for *Pinus densiflora* and the mean microfibrillar angles in the layers compare well with those from the literature.

A mean MFA in the S2 layer of 20°was measured, using iodine staining and X-ray methods, in material taken from a similiar position in the same tree as the sample used in this study (K. Winkelmann, private communication).

Appendix F

Tracheid shape database

F.1. Introduction

Parametric polygonal models for the transverse shape of tracheids, such as those proposed in chapter 5, are used in the description of prismatic cellular models. To determine appropriate values for the parameters of these models a database of actual tracheid cross sectional shapes is required. Applications for such a database can also be found in other areas of wood science, for example in determining the microfibril angle from x-ray scattering experiments (Entwistle and Navaranjan, 2001). This appendix describes a database of this type, the method by which it has been constructed and a summary of the data it contains.

F.2. Method

Frequency space or spectral methods for the characterization of tracheid shape have been developed and applied by Fujita et al. (1989, 1991, 1996); Maekawa et al. (1993); Watanabe (1998); Watanabe et al. (1998a,b). These methods provide an elegant and compact representation for the transverse cell shape, but require a significant amount of preprocessing before they can be applied.

In the present work a direct approach has been taken. Individual tracheid transverse shapes have been manually digitised from images and stored as polygons. A manual procedure was adopted since it provided the greatest flexibility, required the shortest development time and because it is tolerant of poor quality images.

It is well known that the transverse shape of tracheids varies considerably across growth rings. The position of a tracheid within a growth ring is described using the ring coordinate, denoted RC and defined as the relative position within a growth ring with RC = 0 corresponding to the boundary separating the latewood of the previous growth ring from the earlywood of the current ring, and RC = 1 corresponding to the boundary separating the latewood of the current ring from the earlywood of the next ring,

A Matlab script, getcells.m, was written to perform the shape digitization. This script loads the requested image, prompts the operator to define the true radial direction

then randomly selects and marks points within the image. If the operator judges the marked point to be suitable, the cell that contains the point is enlarged and the operator picks whatever they consider to be the vertices of the cell. If the point is rejected a new point is selected and so on. After a set number of cells have been digitized getcells.m saves the image along with the traced cell outlines, corrects the vertex coordinates for the radial misalignment of the image and saves a list of vertex coodinates and cell vertices. Having done this getcells.m exits.

To minimise the variation in digitization technique in time and across operators, and to avoid bias in the sampling, the following protocols were established:

1. skip a sample point if it is not clear which cell has been selected,
2. skip a sample point if it is associated with a cell adjacent to a cell that has already been digitised,
3. skip a sample point if it lies outside of the ring being processed,
4. skip a sample point if the cell geometry is not clearly defined,
5. do *not* skip cells with ray boundaries.

It should be emphasized that rejection criterion 4 must be applied sparingly and only in situations where the information contained within the image is insufficient to permit the cell shape to be made out.

Having collected a set of polygonal shapes, wall length and orientation statistics can be computed, along with statistics describing the coordination number (number of neighbours), cell diameters, cell area and perimeter and the fraction of non-convex polygons.

F.3. Materials

Images of tracheids from radiata pine wood samples of unknown provenance, captured by SilviScan-1 (Evans, 1994), have been used in this study. While the quality and resolution of these images is less than ideal, they cover entire growth rings and are cross indexed against microdensity, microfibril angle and automatically measured transverse diameters against which the results of the method described above can be compared. Figure F.1 shows a growth ring reconstructed from the SilviScan-1 images. Figure F.2 shows a typical frame after processing using getcells.m. On average each SilviScan-1 image contains around 1200 whole cells, of which 30 are digitized.

Given the low resolution of the SilviScan-1 images, the question of errors in the measured lengths and orientations is of concern. It is reasonable to assume that the error in finding the 'true' location of any vertex is isotropic and independent of the

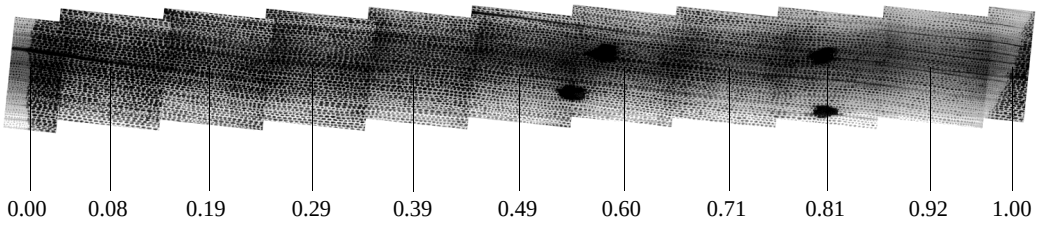

Figure F.1.: Reconstructed ring with frame ring coordinates

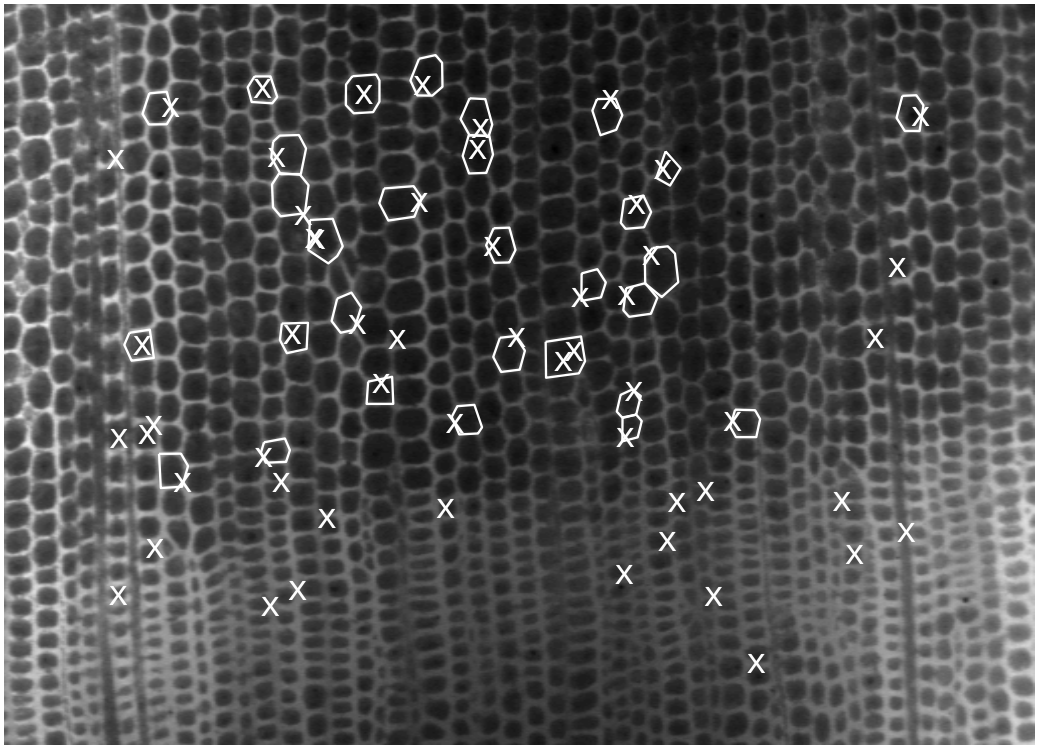

Figure F.2.: Example frame after processing with getcells.m.

vertex location. Referring to figure F.3, it is clear that if, to some prescribed confidence level, the true location lies within a disc of radius Δ centered on the chosen location, then the true edge length lies in the interval $L \pm 2\Delta$ and the true orientation lies in the interval $\theta \pm \sin^{-1}(2\Delta/L)$, which, if $\Delta \ll L$, can be approximated as $\theta \pm 2\Delta/L$.

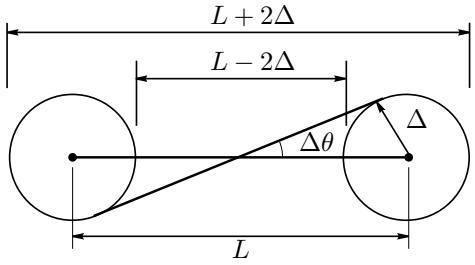

Figure F.3.: Error analysis. See text for details.

A set of 30 repeated digitizations were made on a typical six sided cell. Assuming that the mean of the vertex locations is a good estimator for the true vertex location, then, from the cumulative distribution of the distance between chosen locations and the mean, at a confidence level of 90% $\Delta = 1.5$ μm. Thus, the error estimate for edge lengths is $L \pm 3.0$ μm, and for the edge orientation $\theta \pm 3.0/L$. This means approximately 17% and 26% of the edges in the current database might have length errors of greater than 10% or orientation errors in excess of 10°(those edges less than 30 and 17 μm in length respectively).

F.4. Results

F.4.1. Database summary

To date, 3300 tracheid cross sections, from 10 growth rings in 4 different radiata pine boards, have been processed. Digitizing these tracheid shapes took around 40 hours of labour.

Over 99.8% of the cells in the database have convex polygonal outlines. The coordination number, that is the number of neigbours a tracheid has in a given cross section, ranges between 4 and 10 with 6 being the most common (see figure F.4). Only 4 out of 3300 of the cross sectional shapes have more than 8 edges, and they are all large cells, having areas in greater than 95% of the cross-sections measured.

In figure F.5 frequency distributions for the transverse area, perimeter and circularity are shown. The circularity, defined as $P^2/(4\pi A)$ where P and A are the perimeter and area respectively, of a circle is 1, of a regular hexagon is 1.103 and of a square is 1.273. The circularity frequency distribution indirectly supports descriptions of tracheid shapes as being between hexagonal and square since 85% of the circularity

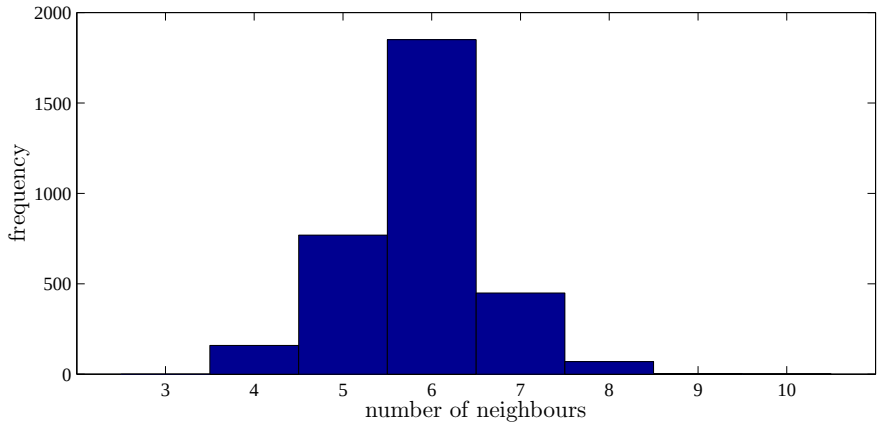

Figure F.4.: Frequency distribution for number of neighbours.

measurements lie between 1.103 and 1.273. Note that having a circularity within these limits is a necessary, but not sufficent, condition for a cell to have a shape intermediate to a regular hexagon or square.

The frequency distribution for edge length and orientations are plotted in figure F.6. Edge orientation is defined as the angle made by the edge relative to the tangential axis. Edge orientation is between -90° and 90° as the edges are not directed. The length weighted orientation frequency distribution is plotted in figure F.6.

The orientation distributions are slightly asymmetric. Whether or not this asymmetry is statistically significant has not been tested. The peak in the orientation distributions at 90° is due primarily to the presence of rays which induce a local preferential alignment of the tangential walls of adjacent tracheids with the radial-longitudinal plane. This effect was noted by Kahle and Woodhouse (1994), who also pointed out its mechanical significance.

F.4.2. Variation with ring coordinate

Based on intra-ring profiles of radial diameter and density, the growth ring has been divided into six zones and the tracheid shapes analyzed in each of these zones. Figure F.7 shows how the coordination number decreases from earlywood to latewood. In figure F.8 the edge length and orientation distributions in each of the growth ring zones are plotted. Differences between zones are evident, although the statistical significance of these differences has not been tested.

F.4.3. Transverse diameters: comparison with SilviScan-1

In figure F.9 the radial and tangential cell diameters computed from the measurements described above are compared with the equivalent measurements made by SilviScan-1

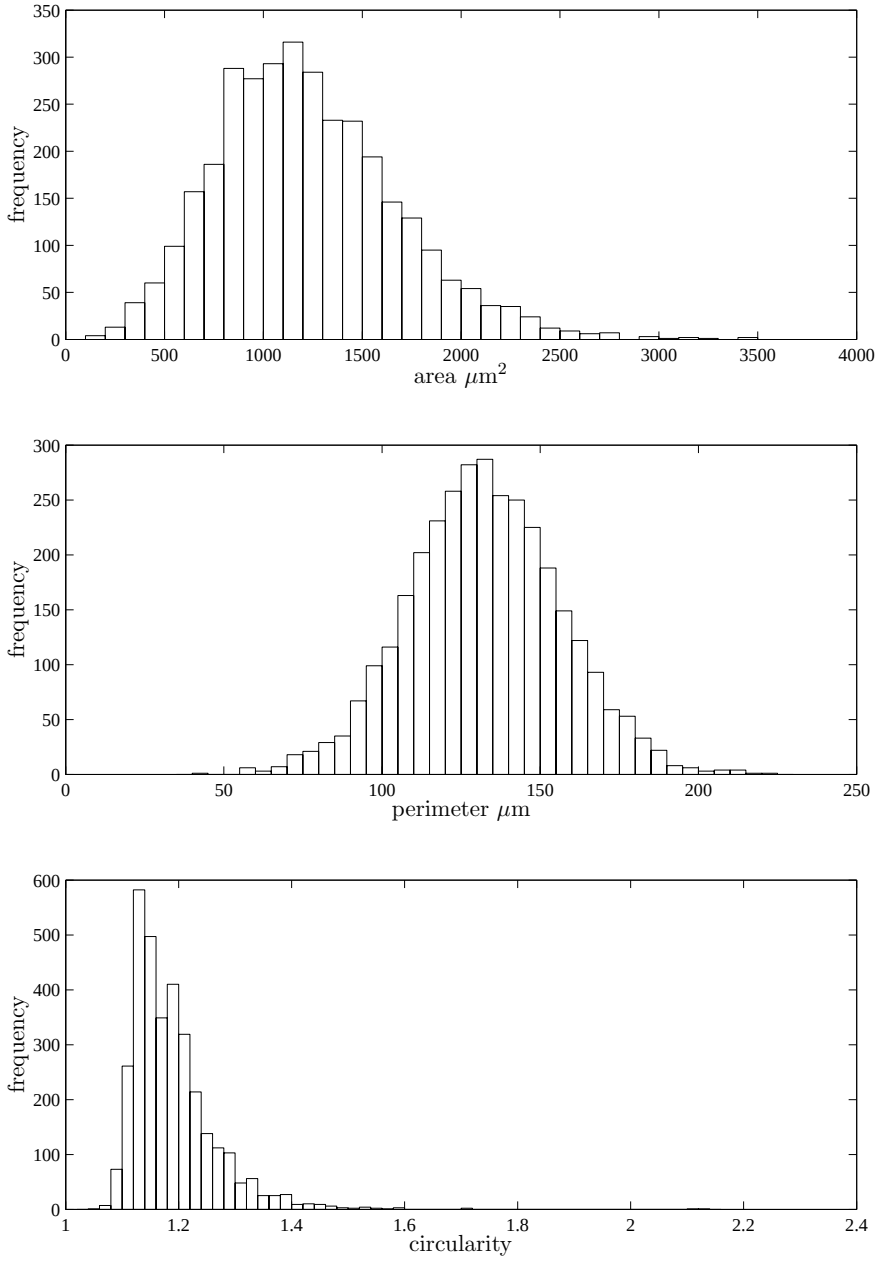

Figure F.5.: Frequency distributions for transverse area, perimeter and circularity.

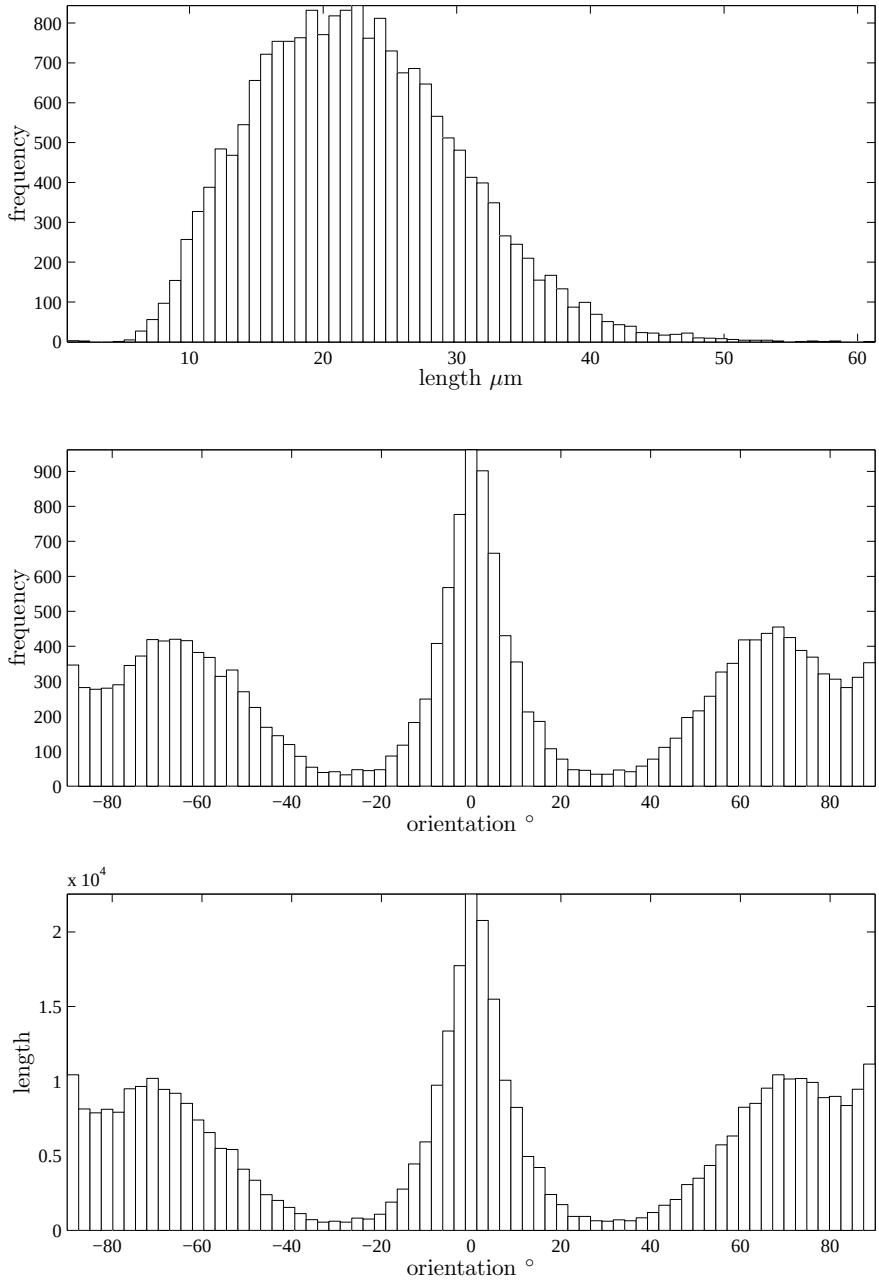

Figure F.6.: Frequency distributions for transverse edge length, orientation and length weighted orientation.

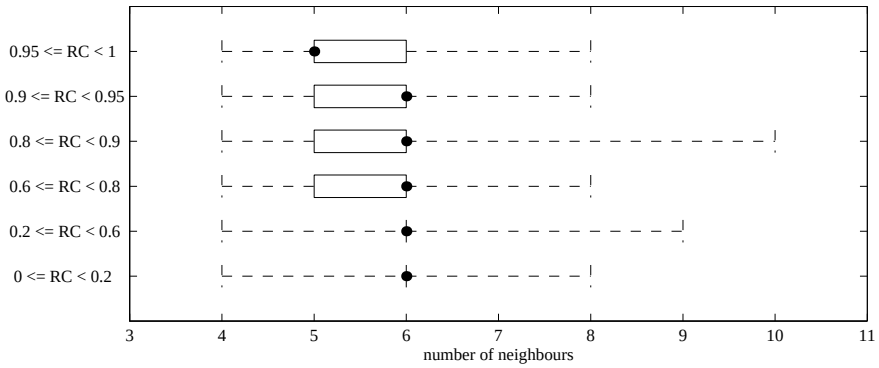

Figure F.7.: Distribution of number of neighbours in different growth ring zones.

for a single growth ring.

The observed trends across the growth ring are similar, as are the mean values for the radial diameter. The tangential diameters from the current study are considerably greater than those measured by SilviScan-1. It may be that a consistent bias towards wider tracheids exists in the manually measured tracheid cross-sections, or it may be that the SilviScan-1 measurements are lower because they include measurements of the tangential width of ray cells.

F.4.4. Wall orientation: comparison with Entwistle and Navaranjan (2001)

In figure F.10 the length weighted edge orientation probability distributions from the current study is compared with part of the dataset used by Entwistle and Navaranjan (2001). The distributions are similar although the spike at 90° discussed already above, is more prominent in the Entwistle and Navaranjan (2001) distribution. This may be because the manual procedure employed in the current study was biased against tracheid cross sections adjacent to rays.

F.5. Summary and future work

A tracheid shape database has been described, a summary of its contents presented and comparison with other measurements made.

The current estimated errors in the length and orientation of short edges are unacceptably large. If this database is to be extended, then the accuracy of the vertex location process must be improved. Using higher resolution images is one possible way to do this.

The manual method used is somewhat time consuming and, despite the precautions taken, possibly prone to sampling bias. Application of a pruned medial axis transform (skeletonisation) (Ogniewicz, 1992) to binary digital images, followed by an automated

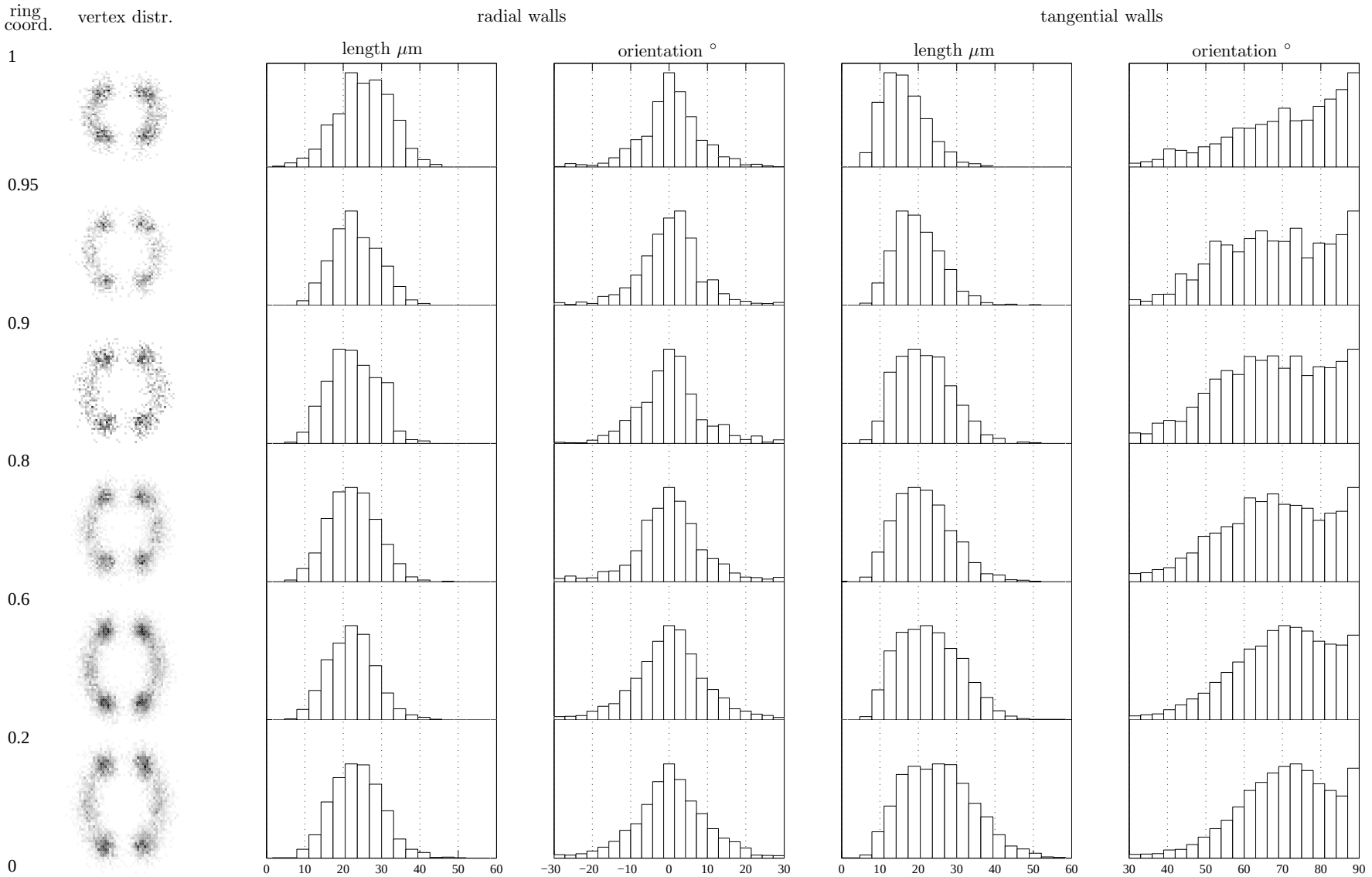

Figure F.8.: Wall lengths, orientations and vertex distributions in different growth ring zones.

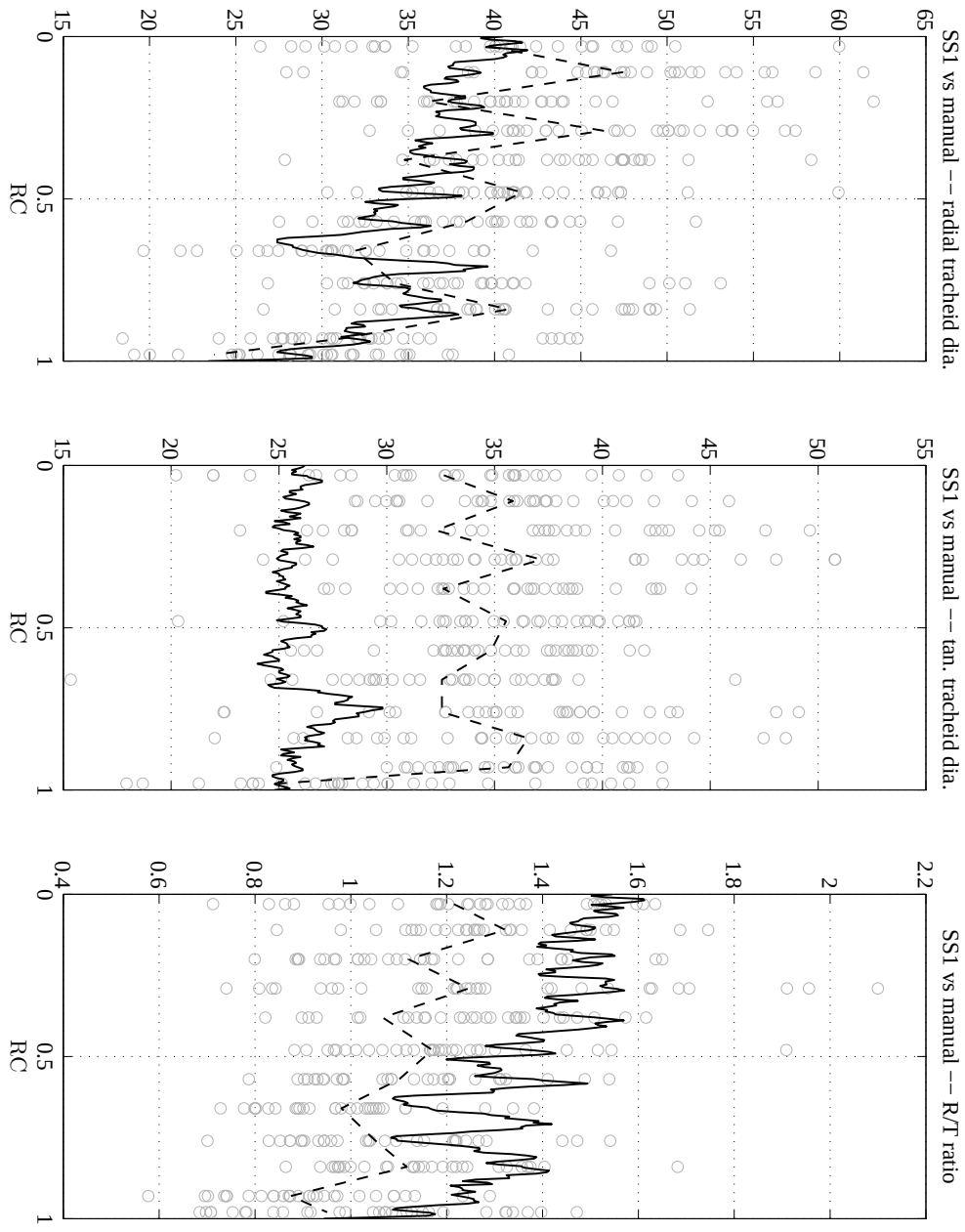

Figure F.9.: Comparisons between transverse tracheid diameters measured by SilviScan-1 (solid line) and those measured manually (data points, mean value dashed line).

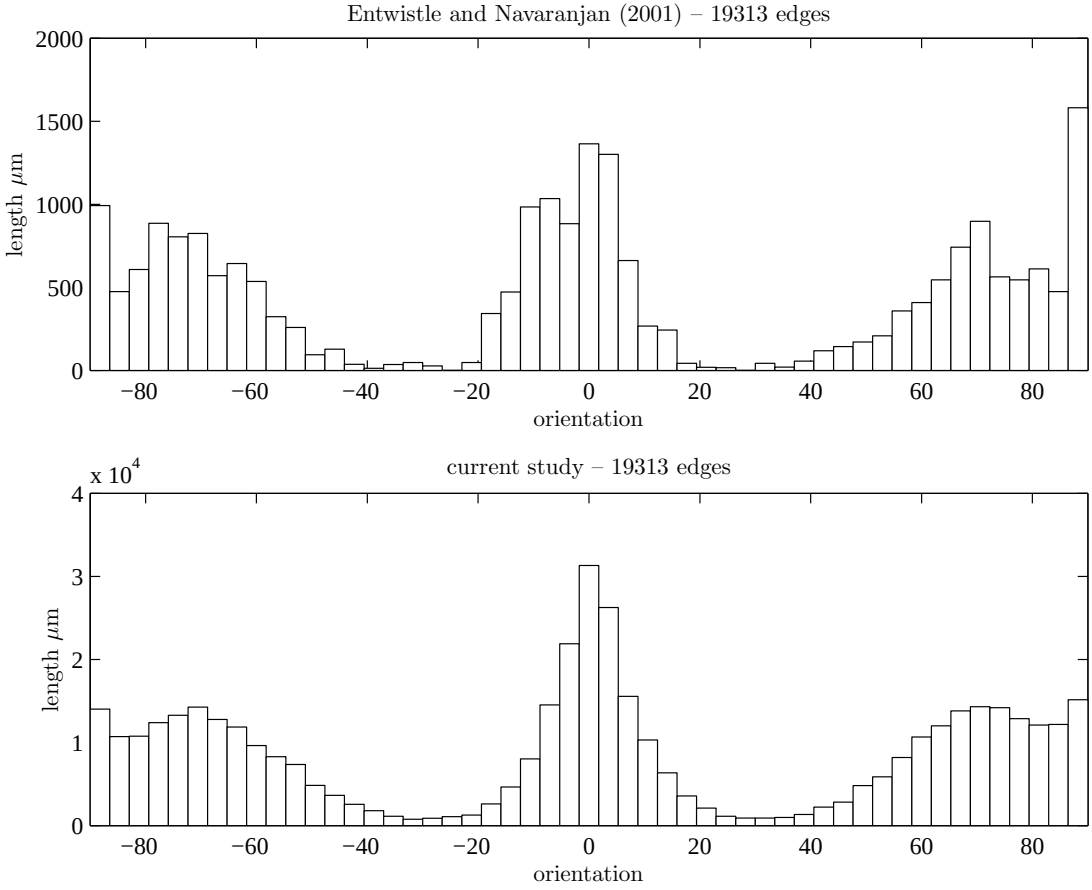

Figure F.10.: Comparison of length-weighted wall orientation distributions.

procedure to extract of polygonal cell shapes, can be used to collect very large numbers of cell shapes in a short amount of time. This process has been trialed and works well as long as the images used are of sufficient resolution and the cell walls are unbroken, particularly along ray boundaries. Development of imaging protocols to obtain such images should be accorded a high priority. It should be noted that, if quality images are available, the main drawback of the spectral methods mentioned above is removed, and these techniques might be more effective than the direct approach taken herein.

To date the tracheid shapes captured correspond only to wood in the air dry condition. While Donaldson and Lausberg (1998) note that the transverse shape of radiata pine tracheids changes little with changes in moisture content, the results of Watanabe et al. (1998b) suggest otherwise and in any case the tracheid size certainly varies with moisture content. By extending the database to include measurements made at varying moisture contents, this question could be addressed, along with other questions relating to the transverse shrinkage anisotropy. Measured shapes at varying moisture contents could also be used to indirectly validate the hygro-elastic modelling procedure.

A fundamental deficiency in the current database is that nothing is known about the cells adjacent to a given cell (except in an average sense). In particular, the distances from the centre of a given cell to the centres of that cells neighbours are not recorded. In the future it would be advantageous to incorporate this information.

Appendix G

Cell growth model

G.1. Introduction

The secondary cell wall develops by appositional growth taking place on its inner surface. Modelling this growth starting from the convex prismatic polygonal surface used for the external geometry is one approach to describing the internal tracheid geometry. Using this approach, it is a simple matter to include variable packing density in different wall regions. Furthermore, the growth surface and the paths of points on that surface through time define a coordinate system that can be used to locate points within the cell wall and to generate a finite element mesh.

G.2. Analytic treatment

If a cell is treated as being prismatic then the internal cell surface at time t can be described by the parametric vector function

$$\boldsymbol{C}(\xi, t) = C_1(\xi, t)\hat{\boldsymbol{x}} + C_2(\xi, t)\hat{\boldsymbol{y}}. \tag{G.1}$$

Assume that growth takes place normal to the surface and that the growth rate is a function of the curvature, κ, as well as the position on the surface and time. Then the evolution of $\boldsymbol{C}$ in time from a prescribed initial shape is governed by

$$\frac{\partial}{\partial t}\ (\boldsymbol{C} \cdot \hat{\boldsymbol{n}}) = g(\xi, \kappa(\xi), t) \tag{G.2}$$

with the initial condition

$$\boldsymbol{C}^0 = \boldsymbol{C}(\xi, 0) \tag{G.3}$$

where $\hat{\boldsymbol{n}} = \hat{\boldsymbol{n}}(\xi)$ is a unit vector normal to the surface and κ is the curvature at ξ.

The function g is the instantaneous surface velocity or the instantaneous growth rate. For the sake of simplicity take

$$g = \alpha + \beta\kappa. \tag{G.4}$$

Denoting $\dfrac{\partial}{\partial\xi}(\cdot)$ by $(\cdot)'$ we have

$$\hat{\boldsymbol{n}} \equiv \frac{-C_2'(\xi,t)\hat{\boldsymbol{x}} + C_1'(\xi,t)\hat{\boldsymbol{y}}}{\sqrt{{C_1'}^2 + {C_2'}^2}} \tag{G.5}$$

$$\kappa \equiv \frac{d\phi}{ds} = \frac{C_1'C_2'' - C_1''C_2'}{\left(\sqrt{{C_1'}^2 + {C_2'}^2}\right)^3} \tag{G.6}$$

where ϕ is the tangential angle. Then equation G.2 can be written

$$\frac{\partial}{\partial t}\left(\frac{C_1'C_2 - C_1C_2'}{\sqrt{{C_1'}^2 + {C_2'}^2}}\right) = \alpha + \beta\frac{C_1'C_2'' - C_1''C_2'}{\left({C_1'}^2 + {C_2'}^2\right)^{3/2}}. \tag{G.7}$$

Since the parameterization of $\boldsymbol{C}$ is not unique we can arbitrarily fix C_1, so long as a suitable function for $C_2 = C$ can be found to satisfy the initial condition G.3. Note that the growth direction is determined by the sense of $\boldsymbol{C}$.

Planar growth Let $C_1 = h(t)$ and $C_2 = -\xi$ then equation G.2 beomes

$$\frac{dh}{dt} = \alpha \tag{G.8}$$

This represents planar growth on a flat surface in the positive x-direction.

Cylindrical growth Let $C_1 = r(t)\cos\xi$, $0 < \xi \leq 2\pi$, and set $C = C_2$. Then equation G.2 becomes

$$-\frac{\partial}{\partial t}\left(r\frac{C\sin\xi + C'\cos\xi}{\sqrt{r^2\sin^2\xi + C'^2}}\right) = \alpha + \beta r\frac{C'\cos\xi - C''\sin\xi}{\left(r^2\sin^2\xi + C'^2\right)^{3/2}}. \tag{G.9}$$

If $C = r(t)\sin\xi$ then equation G.9 becomes

$$-\frac{dr}{dt} = \alpha + \frac{\beta}{r} \tag{G.10}$$

as it should since $C_1 = r\cos\xi$ and $C_2 = r\sin\xi$ are parametric equations for a circle, and if $\boldsymbol{C}^0$ is a circle $\boldsymbol{C}(t)$ should be a circle $\forall t > 0$.

G.3. Numerical treatment

Unfortunately, while (G.7) requires both C_1 and C_2 to have continuous first and second partial derivatives with respect to ξ, the initial curves of interest presently are closed

convex polygons for which, at vertices, these derivative are undefined. Furthermore, finding a general analytical solution to (G.7) is not an easy task.

Instead, a numerical scheme is used to 'grow' a cell using a finite version of equation G.2

$$\delta\left(\boldsymbol{C}\cdot\hat{\boldsymbol{n}}\right)=\delta h=\left(\alpha+\beta\kappa\right)\delta t \tag{G.11}$$

with $\boldsymbol{C}^0$ taken as an arbitrary simple polygon. The inital surface is discretized then stepped forward in time.

Essentially the algorithm employed to generate the internal geometry is:

Algorithm 1 Modelling the inward growth of a closed, initially polygonal, curve.

1: establish initial total area A^0 and target layer areas A_l
2: establish initial mesh ξ_i and $\boldsymbol{x}_i^0$
3: **for** $l=1$ to N_s **do**
4: establish initial $\hat{\boldsymbol{n}}_i^0$ and κ_i^0
5: **end for**
6: **for** $l=1$ to N_r **do**
7: $A\leftarrow 0$
8: **while** $A<A_l$ **do**
9: set the time increment for this step δt
10: **for** $i=1$ to N_s **do**
11: $\delta h_i\leftarrow(1+\gamma\kappa_i)\delta t$
12: $\boldsymbol{x}_i^l\leftarrow\boldsymbol{x}_i^l+\delta h\boldsymbol{n}$
13: **end for**
14: respace mesh points
15: **for** $i=1$ to N_s **do**
16: update $\boldsymbol{n}_i$, κ_i
17: **end for**
18: update layer volume A
19: **end while**
20: **end for**

The N_r cell wall layers employed are subdomains of the CML, S1, S2 and S3 layers used in the cell wall model. N_r and N_s can be looked upon as control parameters which govern the mesh in the radial and circumferential directions respectively. The γ parameter determines how strongly the curvature influences the growth rate.

A linear interpolation is used to respace nodes at step 14 since it can be quickly computed and guarantees that the new nodes will lie between the old nodes, maintaining the convexity of the curve representing the current surface. This interpolation serves to stabilise the mesh by avoiding node 'collisions'.

G.4. Postscript

The model and numerical algorithm described above was developed without reference to the literature. As it happens, Sethian (1999) discusses this type of problem and clearly explains the deficiencies of the numerical approach taken in the preceding section. Sethian (1999) advances level set methods as a better alternative and demonstartes them to be more robust and accurate. In the future, it is intended that the current formulation be replaced.

Appendix H

Bordered pit model

To assess the influence of bordered pits on the elasticity of radial cell walls the highly idealized model shown in figure H.1 has been investigated using finite element analysis. The model considers a portion of cell-wall containing a single bordered pit. The cell-wall is treated as being homogeneous and transversely isotropic, with the xz-plane as the plane of isotropy. This implies that the microfibrils in the wall lie parallel to the y-axis and, since the microfibril direction is the same in both halves of the cell-wall, a zero microfibril angle. Each half of the pit is treated as having two layers; an inner layer (shown in gray) in which the microfibrils run concentrically and an outer layer in which the microfibrils lie in the planes parallel to the yz-plane but follow the contours of the pit. Consequently the microfibrils in the inner layer form circles and those in the outer layer form hyperbolas. The material properties of both the outer and inner layers are the same as those of the wall with the local plane of isotropy normal to the microfibril direction. The material properties used appear in table H.1. These are derived from the phase property and nanostructural models of chapters 8 and 3 and correspond to air-dry wood at ambient temperature.

Based on micrographs of softwood bordered pits the dimensions of table H.2 were selected as being representative. The overall dimensions, X and Y, were selected based on the typical values for the width of a radial wall and the distance between bordered pits towards the middle of an earlywood, *Pinus radiata* tracheid (Jinxing, 1989; Harris, 1991).

Exploiting the symmetries present, a finite element model of one eighth of a bordered pit, consisting of approximately 200 20-node, quadratic displacement elements, was constructed using Ansys 6.0. Appropriate symmetry boundary conditions were applied and displacements normal to both of the free edges were constrained to be uni-

E_t GPa	ν_{tl}	E_l GPa	G_{tl} GPa	G_{tt} GPa
3.2	0.30	47	1.4	1.1

Table H.1.: Material properties used in the bordered pit model.

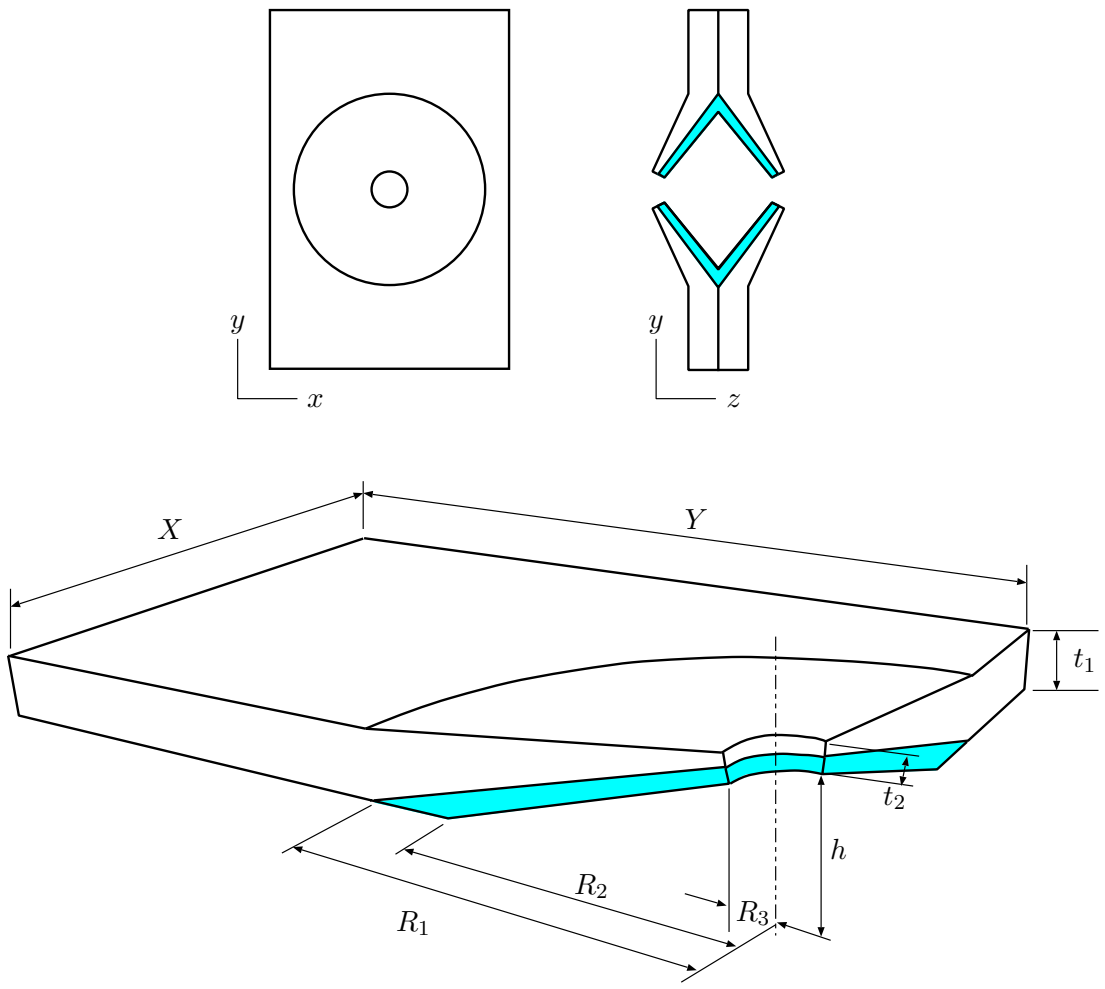

Figure H.1.: Idealized bordered pit model.

R_1 μm	R_2 μm	R_3 μm	t_1 μm	t_2 μm	h μm	X μm	Y μm
15	10	2	3	2	3	20	30

Table H.2.: Geometric dimensions used in the bordered pit model.

	E_x^* GPa	E_y^* GPa	ν_{xy}^*	ν_{yx}^*
with pit	3.5104	31.1545	0.1982	0.0223
without pit	3.2	47	.30	.020

Table H.3.: Wall moduli with and without a pit being present.

form along that edge. Unit normal loads were applied to the free edges as two separate load cases. From displacements along the free edges resulting from a linear elastic small displacement analysis, the 'effective' elastic moduli were calculated. These appear in table H.3.

As required by the symmetry of the stiffness tensor $\nu_{xy}^*/{E_y}^* = \nu_{yx}^*/{E_x}^*$. The effective transverse wall modulus E_x^* is increased by 10% due to the presence of the pit. The effective longitudinal wall modulus on the other hand is reduced by approximately 35%. If it is assumed that the proposed model is a reasonable representation of a bordered pit structure, then, since *in situ* the portion of wall modelled is suported by adjacent radial and tangential cell-walls, this reduction in stiffness can be expected to be an upper limit.

Appendix I

Effect of tracheid tips on the transverse modulus

Assume that the tracheids are all the same length and aligned as shown in figure I.1.

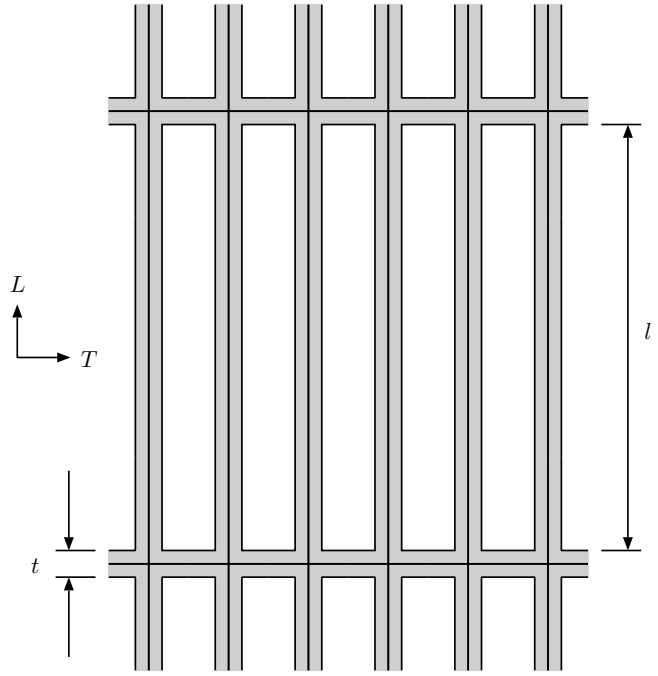

Figure I.1.: Tracheid model including cell tips.

If it is assumed that the mean transverse strain is the same in all transverse planes, the transverse modulus E including the tracheid end walls is

$$E = v_e E_e + (1 - v_e) E_c \tag{I.1}$$

where E_e is the transverse modulus of the tracheid end walls, and E_c is the transverse modulus of tissue lying between the end wall planes and v_e is the volume fraction occupied by tracheid tip walls.

From the s1cell model described in chapter 5, $E_c = 0.4$ GPa for ambient conditions, a dry density of 0.35 g/cc and an S2 MFA of 10°. Using the corresponding longitudinal

wall modulus for the modulus of the tip walls gives $E_e = 30$ GPa. Taking $l = 3$ mm and $t = 3$ μm, appropriate for earlywood, then, $v_e = 0.001$. Thus, $E = 0.43$ GPa, which is an increase of around 7%.

In reality, the tracheid ends are tapered rather than blunt and are not perfectly aligned. The proposed model neglects the wall bending that would occur, hence the calculated 7% increase represents an upper limit on the influence of tracheid tips on the transverse modulus.

Appendix J

Influence of ray tissue

J.1. Ray anatomy

Ray tissue makes up 5–15% of softwood volume (Sjöström, 1981; Bodig and Jayne, 1982; Fengel and Wegener, 1984). In radiata pine stem wood, the rays are generally uniseriate (one cell wide) and 1–26 cells in height and composed of parenchyma and ray tracheids; occasionally the rays are fusiform, containing a radial resin canal lined with epithelium cells (Patel, 1971). Ray anatomy is illustrated in figures J.1 and J.2.

J.2. Modelling

J.2.1. Continuum models

Rays can be included in a hygroelastic model for wood by treating them as homogeneous inclusions in a axial tissue matrix. This continuum approach has been adopted previously; for example by Koponen et al. (1991) who treated the ray and axial tissue as intercalated layers (see the layered model in figure J.3) and used the layered media method of Chou et al. (1972) (see appendix C) to compute the effective properties.

A more realistic continuum model treats rays as having a finite longitudinal extent. The prismatic model of figure J.3 is such a model. This model is periodic and its effective properties can be computed using the finite element method described in chapter 2.

Other continuum models can be devised that include the random dispersion of rays in the TL planes and the variation in ray height.

Low and high estimates of ray stiffness, denoted Rlo and Rhi respectively, have been computed using the s1cell model of chapter 5. The cellular geometries are shown in figure J.4 and the ray properties appear in table J.1.

These ray properties have been combined with typical axial tissue properties for earlywood and latewood. The earlywood (EW) and latewood (LW) properties in table J.1 were computed also using the s1cell model of chapter 5.

The effective properties including ray tissue have been calculated using both the layered and prismatic continuum models of figure J.3 for the four combinations of

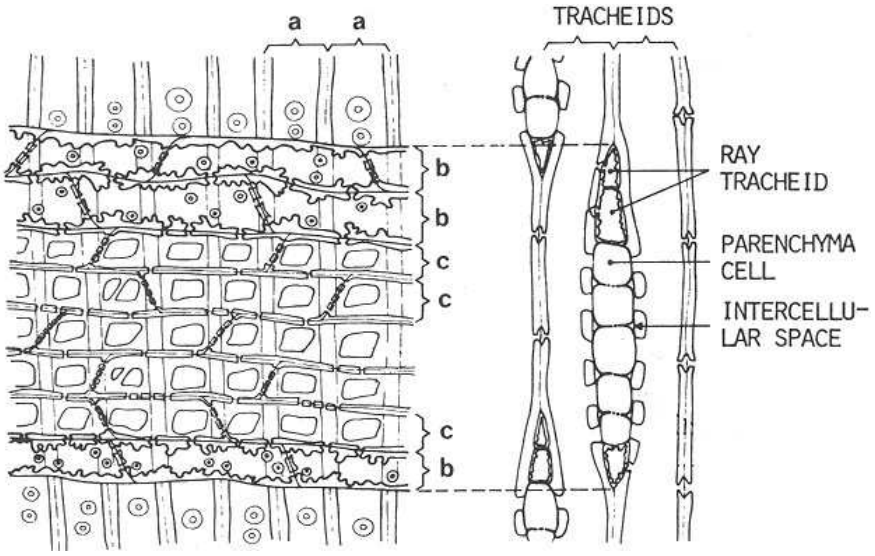

Figure J.1.: Pine ray anatomy. From Sjöström (1981). (a) longitudinal tracheids. (b) ray tracheids. (c) ray parenchyma.

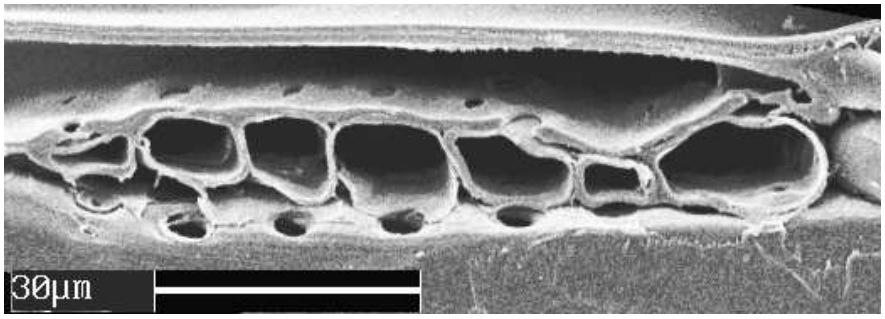

Figure J.2.: SEM micrograph of a portion of a ray in radiata pine.

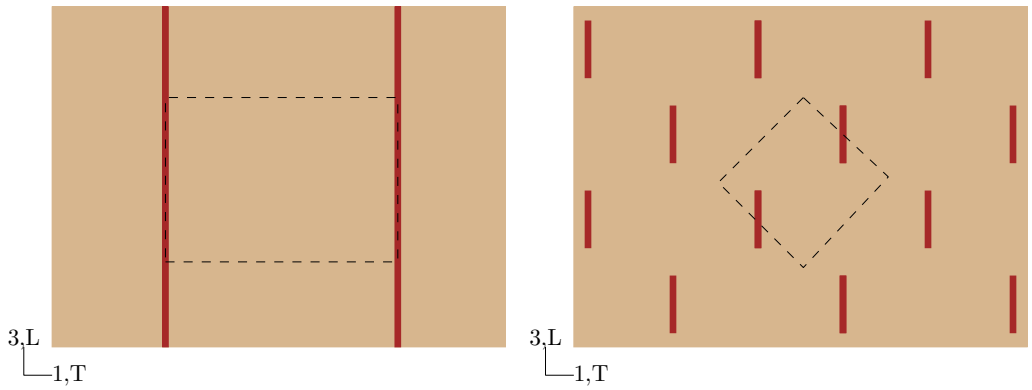

(a) Layered model **(b)** Prismatic model

Figure J.3.: Ray models.

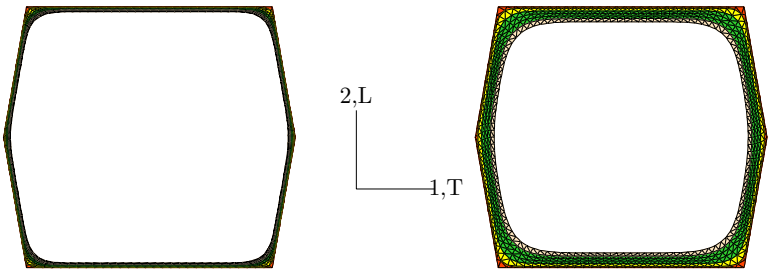

Figure J.4.: Ray cellular geometries.

earlywood and latewood axial properties and high and low stiffness ray properties. For the prismatic model a ray aspect ratio of 10:1 was chosen. Results corresponding to ray volume fractions of 5% and 10% appear in table J.1. In figure J.5, the change in effective properties with increasing ray volume fraction are plotted for the earlywood, low stiffness ray combination.

The presence of rays reduces the longitudinal modulus E_3, the longitudinal shear moduli G_{23} and G_{31} and the Poissons ratio in the radial-longitudinal plane ν_{23} while raising the Poissons ratio in the tangential-longitudinal plane ν_{13}. The transverse moduli E_1 and E_2, the transverse shear modulus G_{12} and the transverse Poissons ratio ν_{12} may be raised or lowered depending on the relative stiffness of the ray tissue compared to the axial tissue.

Rays increase the tangential hygroexpansional coefficient ϵ_1^w while reducing the radial coefficient ϵ_2^w. The longitudinal hygroexpansional coefficient is raised for the earlywood properties considered whereas it is decreased for the latewood.

Both the continuum properties give similar results for the radial modulus E_2, the transverse shear modulus G_{12} and the hygroexpansional coefficients. Compared to the more realistic prismatic model, the layered model underestimates the influence of rays on the longitudinal modulus E_3 and the shear modulus in the radial-longitudinal plane G_{23}, and overestimates the effects on the tangential modulus E_3 and the shear modulus in the tangential longitudinal plane G_{31}. The difference between the two models is particularly marked for this last property. Compared to the longitudinal shear modulus of axial tissue, the low shear modulus of ray tissue in planes normal to the ray cell axes causes the ray tissue to dominate the shear behaviour in the tangential-longitudinal plane when a continuous ray 'layer' is present. This effect is an artifact of the layer model and does not represent the physical behaviour.

J.2.2. Cellular model

Continuum models neglect the interaction at a cellular scale between the ray cells and tracheids. The highly simplified cellular finite element model illustrated in figure J.6

	ρ g/cc	E_1 GPa	ν_{12}	ν_{13}	E_2 GPa	ν_{23}	E_3 GPa	G_{23} GPa	G_{31} GPa	G_{12} GPa	α_1^w $\times 10^{-3}$	α_2^w $\times 10^{-3}$	α_3^w $\times 10^{-3}$
Ray tissue													
Rlo	0.107	0.0320	1.87	0.203	0.160	0.157	1.04	0.0808	0.0721	1.67×10^{-3}	199	130	160
Rhi	0.321	0.261	0.714	0.534	0.520	0.564	6.14	0.475	0.448	0.0211	382	320	11.6
Axial tissue													
EW	0.322	0.180	1.08	0.611	0.461	0.649	4.93	0.746	0.562	0.0557	335	301	15.1
LW	0.865	2.38	0.315	0.741	2.08	0.744	18.6	2.24	2.59	0.512	374	370	-19.8
layered model, 5% ray volume fraction, % difference from no rays													
EW+Rlo	-3.3	-0.94	-3.2	20	6.3	-9.9	-4.5	-4.5	-94	1.2	4.7	-4.9	7.0
EW+Rhi	-0.011	22	-1.1	43	63	-38	-3.1	-1.8	-56	4.6	37	-38	54
LW+Rlo	-4.4	-52	0.41	6.2	-2.5	-2.3	-4.8	-4.8	-99	-23	0.47	-1.5	-2.5
LW+Rhi	-3.1	-23	9.0	0.56	10	-12	-4.1	-3.9	-86	-0.71	3.2	-13	-21
prismatic model, 5% ray volume fraction, % difference from no rays													
EW+Rlo	-3.3	-0.56	-2.7	22	6.5	-12	-6.2	-5.8	-29	1.2	4.7	-4.9	7.4
EW+Rhi	-0.011	22	-1.2	41	63	-38	-4.5	-2.0	-24	6.0	37	-38	56
LW+Rlo	-4.4	-28	0.13	5.5	-2.5	-4.0	-6.4	-6.0	-28	-14	0.44	-1.5	-2.6
LW+Rhi	-3.1	-16	5.9	2.8	10	-14	-5.7	-4.6	-27	-0.69	3.5	-13	-22
layered model, 10% ray volume fraction, % difference from no rays													
EW+Rlo	-6.7	-2.6	-6.5	37	13	-19	-9.0	-8.9	-97	2.3	8.6	-9.3	13
EW+Rhi	-0.022	36	-2.2	59	130	-55	-7.1	-3.6	-72	9.6	52	-55	84
LW+Rlo	-8.8	-68	0.81	12	-5.0	-4.8	-9.6	-9.6	-99	-38	0.96	-3.0	-5.2
LW+Rhi	-6.3	-37	18	0.93	20	-22	-8.5	-7.9	-92	-1.4	6.4	-23	-39
prismatic model, 10% ray volume fraction, % difference from no rays													
EW+Rlo	-6.7	-1.9	-5.5	41	13	-22	-12	-11	-49	2.4	8.6	-9.3	14
EW+Rhi	-0.022	36	-2.3	56	130	-55	-9.5	-3.9	-41	12	52	-56	90
LW+Rlo	-8.8	-48	0.30	11	-5.0	-7.7	-12	-12	-48	-25	0.91	-3.0	-5.4
LW+Rhi	-6.3	-30	13	4.4	20	-25	-11	-9.0	-46	-1.4	6.6	-23	-40

Table J.1.: Axial, ray and combined properties.

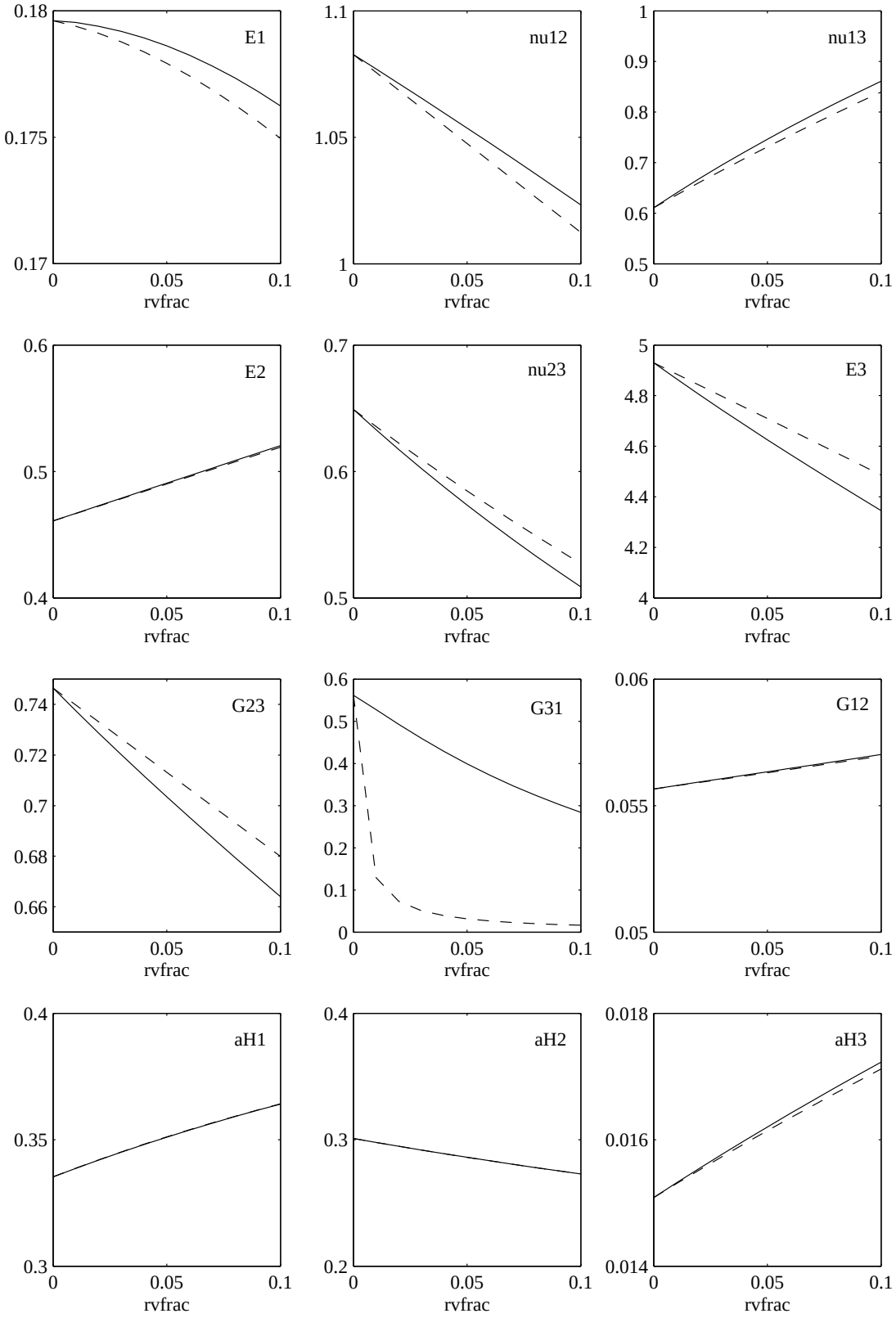

Figure J.5.: Influence of ray volume fraction on wood properties. EW and Rlo properties. ——prismatic continuum model, – –layered continuum model.

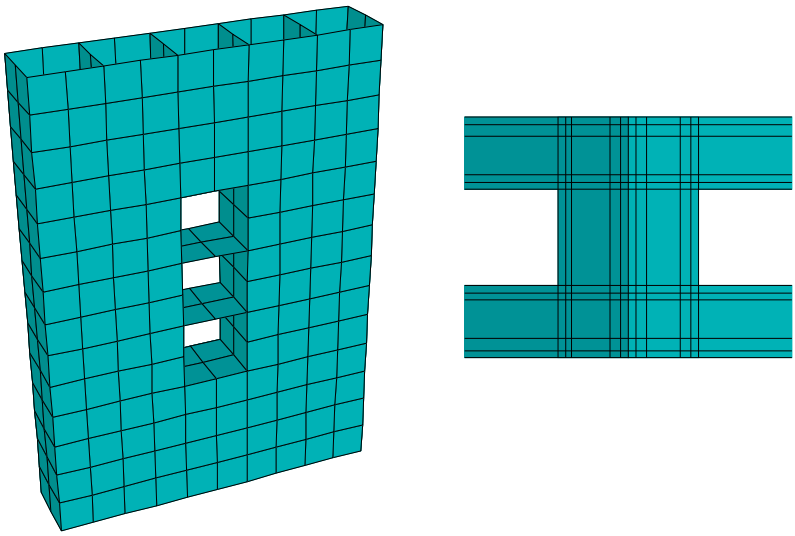

Figure J.6.: Cellular ray model

has been used to investigate the significance of these interactions.

In this model both the axial tracheids and ray cells are treated as having square cross-sectional shapes of uniform size, wall thickness and ultrastructure. This model employs layered shell elements and is homogenized under periodic boundary conditions.

In table J.2 the effective properties of isolated, axial or ray, tissue and the combination computed using this model are presented. Also tabulated are the effective properties computed from the isolated tissue properties using the prismatic continuum model described above.

There are significant differences between the effective moduli computed by these two ray models. In particular, E_1 and G_{12} predicted by the cellular model are around 20% less than predicted by the prismatic continuum model and E_3 and G_{31} are around 10% greater.

J.2.3. Other models

Persson (2000) included ray tissue in his prismatic cellular models by adding an extra outer wall layer to cells walls at a ray boundary. The microfibrils in the layer were radially oriented and the layer total stiffness was assumed to be the same as that of the S2 layer. Because this model treats rays as continuous layers in the RL plane it can be expected to suffer from the same deficiencies as the layered continuum model discussed above.

E_1 GPa	ν_{12}	ν_{13}	E_2 GPa	ν_{23}	E_3 GPa	G_{23} GPa	G_{31} GPa	G_{12} GPa	α_1^w $\times 10^{-3}$	α_2^w $\times 10^{-3}$	α_3^w $\times 10^{-3}$
Separate ray and axial tissue properties											
1.737	-0.04867	0.5466	1.737	0.5466	10.66	0.9888	0.9888	0.01787	61.81	61.81	17.08
Combined ray and axial tissue properties, cellular model											
1.489	-9.911×10^{-3}	0.4820	2.462	0.3748	9.419	0.9620	0.7293	0.02361	59.20	47.64	19.35
Combined ray and axial tissue properties, prismatic continuum model											
1.749	2.024×10^{-3}	0.3957	2.551	0.3663	8.583	0.9888	0.6356	0.02847	59.62	45.55	19.98

Table J.2.: Comparison between cellular and prismatic continuum ray models

J.3. Summary and future work

These results indicate that rays can exert significant influence on the hygroelastic properties of wood. Rays can act to stiffen or soften wood and to restrain or promote shrinkage depending on the direction of interest and on the relative stiffness of the ray tissue compared to the adjoining axial tissue.

The layered continuum model is physically unrealistic and should not be used. The prismatic continuum model is offered as a substitute.

For models including the influence of rays on wood properties to be taken further, quantitative data on ray anatomy, including ray cell populations (numbers of ray tracheids compared to parenchyma) and ray cell ultrastructure, are required.

The differences between continuum and cellular models need further investigation. It may be that rays need to be included in the cellular models of chapter 5 directly rather than being treated as homogeneous inclusions.

The lenticular shape of the rays and the deviations they cause in the surrounding tracheids make rays natural sources of stress concentration. Detailed stress analysis, particularly around ray tips, may shed light on the microscale fracture mechanics of wood.

Appendix K

Average and monoclinic CF properties

In planes perpendicular to the chain axis, the type and strength of the attractive forces between cellulose chains are anisotropic. In one direction, relatively stronger hydrogen bonds create sheets of cellulose molecules. These sheets are then bound together by relatively weaker secondary forces. Consequently, the directional elastic modulus varies considerably in the transverse plane (see figure K.1).

Within a nanoscopic cell-wall domain it is thought that the CMFs are randomly distributed and randomly oriented in planes normal to the chain axes and that equal numbers of CMFs are directed 'up' and 'down'. If this is the case then on average the CMF properties should be isotropic in the transverse plane. Using the orientational averaging apparatus of appendix B transversely isotropic average properties can be computed from the anisotropic properties of a single CMF. This averaging process could be applied to either the stiffness tensor (Cav) or the compliance tensor (Dav). Depending on which tensor is used the average, transversely isotropic, stiffnesses of the CMFs (the CF phase) are very different (see table K.1). When combined in an HH3 model (see chapter 3) with the HS and LM phase properties of table K.1 the effective nanoscale properties based on the compliance and stiffness tensor averages are also different (see table K.1). The question is, does the compliance or stiffness based average give results more like the those resulting from a collection of randomly oriented CMFs?

To answer this question a series of models – referred to as NHH3 models, the first three of which are illustrated in figure K.2 – have been homogenized using the periodic prismatic finite elemnt homogenization process described in chapter 2. These models are similar to the HH3 models but contain multiple CMFs. In an NHH3 model each CMF has anisotropic properties but a random orientation. As the number of CMFs included in the NHH3 models is increased it is expected that the effective properties will converge to a transversely isotropic material.

Originally the orientation of each CMF was chosen at random. This gave very poor results as the uniform angular distribution was not well represented by a few samples. Instead, angles evenly distributed between 0 and 360° were assigned randomly to each CMF. Each CMF was also randomly assigned an 'up' or 'down' direction.

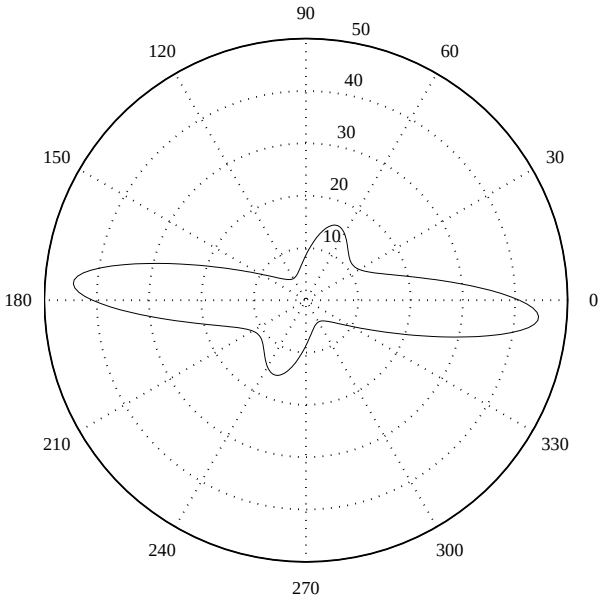

Figure K.1.: Variation in directional modulus of crystalline cellulose in the transvserse plane. Based on the the monoclinic stiffness coefficients of Tashiro and Kobayashi (1991), scaled as described in chapter 8.

	C_{11}	C_{13}	C_{33}	C_{44}	C_{66}
Average CF properties					
Cav	23.35	-0.5107	136.0	4.706	8.580
Dav	11.90	0.3466	136.0	3.702	3.545
Matrix phase properties					
HS	1.113	0.9813	7.767	0.5922	0.2411
LM	6.158	4.105	6.158	1.026	1.026
Effective nanoscale properties					
Cav	4.069	1.564	59.08	1.441	1.034
Dav	3.772	1.570	59.13	1.364	0.9263

Table K.1.: Stiffness coefficients.

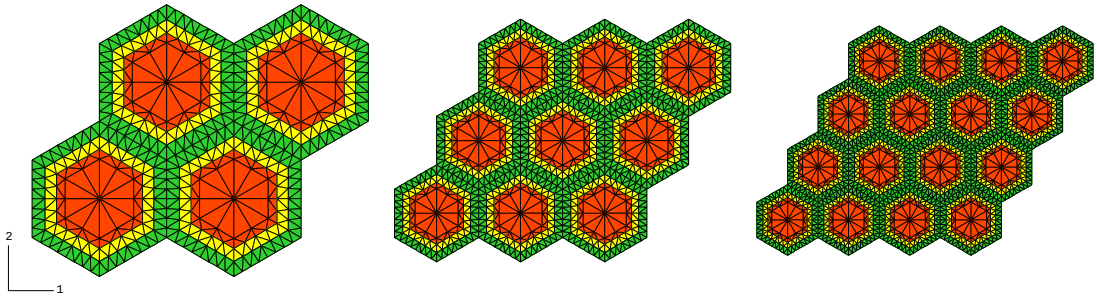

Figure K.2.: The first 3 models in the NHH3 series.

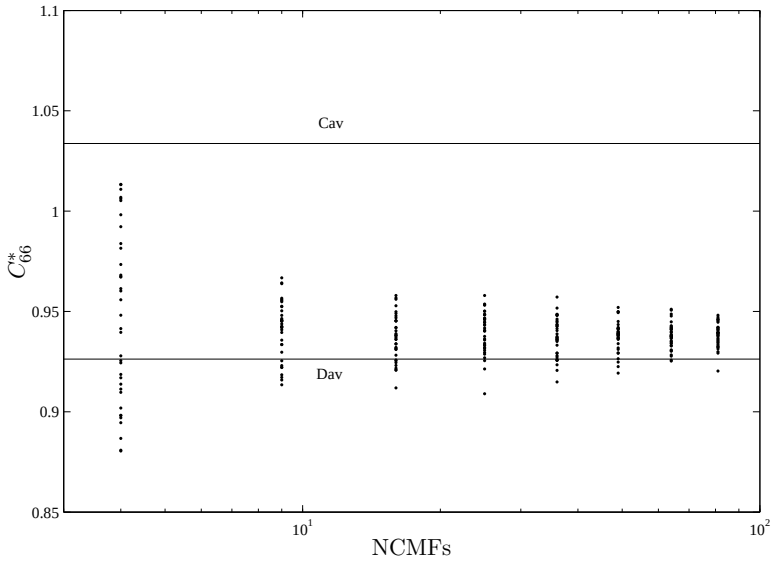

Figure K.3.: Comparison of C^*_{66} for HH3 and NHH3 models.

Effective properties for NHH3 models containing from 4–81 CMFs have been computed using the HS and LM properties of table K.1. Thirty-six different sets of CMF orientations for each NHH3 model were considered. The same discretization was used for the each CMF unit in the NHH3 models as was used with the HH3 models. In figure K.3 the results for the effective property most sensitive to the choice of averaging procedure, C_{66}, are plotted against the number of CMFs (NCMFs) included in the NHH3 model.

The observed rate of convergence of the NHH3 results to a unique value for C_{66} was typical of all the effective stiffness coeficients. Convergence appears suprisingly slow. Even with 81 CMFs different sets of random orientations give different effective properties. It is considered that this is due, at least in part, to the FE discretization being insufficient. Unfortunately no mesh refinement can be considered as an NHH3 model with 81 CMFs has $> 100,000$ degrees of freedom and this is close to the current limit for the PPHMG homogenizer.

Clearly, for C_{66}, using the compliance based average CF properties gives results closer to those of the NHH3 models. This is true for the other effective properties as well. This result is not unexpected as the compliance average is essentially equivalent to assuming that the average stress in each CMF is the same and independent of the CMF orientation, an assumption which seems reasonable.

Appendix L

Matrix density

Within the hygroscopic range, the density of the cell-wall changes with moisture content. As the fibre density is assumed to be unaffected by moisture, then, if the average cell-wall density as a function of cell-wall moisture content is known, the average matrix density as a function of matrix moisture content can be calculated.

If it is assumed that all of the cell wall is either matrix or fibre and that in the hygroscopic range all of the moisture is bound moisture then the average matrix moisture content $w|^{\mathsf{M}}$ is related to the average total moisture content w by

$$w|^{\mathsf{M}} = \frac{w}{1 - m_o|^{\mathsf{f}}} \tag{L.1}$$

where $m_o|^{\mathsf{f}}$ is the mean dry fibre mass fraction.

A change in the matrix moisture content implies a change in matrix mass and also leads to a change in matrix volume. Obviously the combination of these two effects results in a change in matrix density.

The simplest assumption that could be made regarding the change in volume would be to assume that it was equal to the free volume of the moisture gained or lost. However, a 'volume contraction' associated with the sorption of water by wood, cellulosics and lignin is well known (Stamm and Seborg, 1935; Christensen and Kelsey, 1959; Seifert, 1972; Alince, 1989).

In part, this apparent volume contraction is due to the molecular level interactions between sorbate, water, and substrate, the cell-wall polymers. Some sorption sites are interstitial and their occupation generates no swelling, sorption on other sites initiates rearrangement of the local molecular configuration. Restraint imposed *in situ* on the swelling or shrinking of the matrix by the rest of the system also leads to an apparent volume contraction.

In a study of the volume contraction in the wood-water system during sorption Seifert (1972) determined the cell-wall density of spruce shavings using a buoyant-force technique with xylol as the immersion fluid. These measurements were made at 25°C over a range of total moisture contents from dry to just over 0.18 g/g. The densities determined are reproduced in figure L.1. The experimental technique employed would

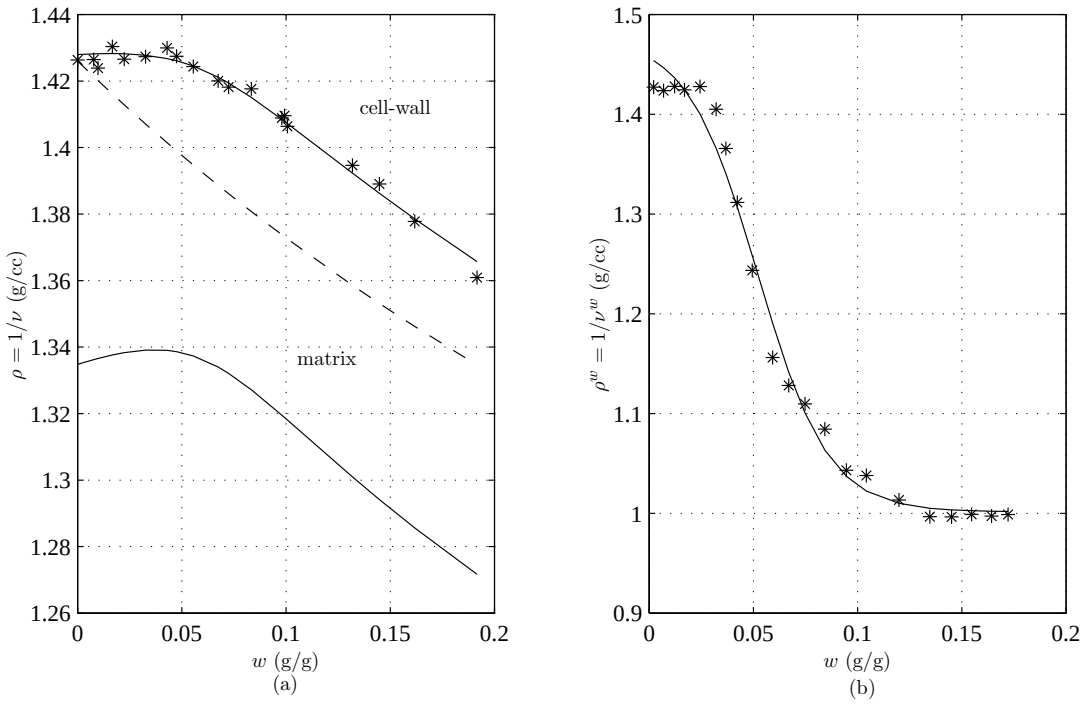

Figure L.1.: (a) Cell-wall and matrix densities as functions of total moisture content. The dashed curve is the cell wall density if the apparent density of the sorbed moisture is constant and equal to that of free liquid water (1.0 g/cc at 25°C). The solid curves are those predicted by equations (L.4) and (L.5). (b) Apparent density of sorbed water. The curve is that predicted by equation (L.3) with the parameters of table L.1. The data points are taken from Seifert (1972).

have included the effect of capillary water held outside of the cell-wall, in tracheid tips and pit membranes for example, if this type of water was present. However, the maximum moisture content for which density was determined was only $w = 0.18$, corresponding to a relative humidity of $h = 0.87$ and a maximum capillary radius of 7.5 nm, so it can be safely assumed that no free water would have been present. Thus the measured density truly reflects the cell-wall density.

The specific volume of the cell wall, ν, can be written as

$$\nu = \frac{\nu_o + \int_0^w \nu^w \, dw}{1 + w} \tag{L.2}$$

in which ν_o is the specific volume of the dry cell-wall and ν^w is the incremental apparent specific volume of the sorbed water. Inspection of Seifert's data for ν^w suggests modelling it using the simple exponential form

$$\nu^w = a_2 + \frac{a_1 - a_2}{1 + a_3 \exp(-a_4 w)}. \tag{L.3}$$

After integrating (L.3) and substituting into (L.2) the cell-wall specific volume is mod-

a_1	a_2	a_3	a_4	ν_o	$\rho\|^{\mathsf{f}}$ cc/g	$m_o\|^{\mathsf{f}}$ g/cc
0.9985	0.6770	32.47	59.23	0.7003	1.58	0.42

Table L.1.: Parameters used to estimate the matrix specific volume.

elled as a function of cell-wall moisture content by

$$\nu = \frac{\nu_o + a_2 w}{1+w} + \frac{a_1 - a_2}{a_4(1+w)} \ln\left(\frac{\exp(a_4 w) + a_3}{1+a_3}\right). \tag{L.4}$$

Using a nonlinear regression procedure a_1, a_2, a_3, a_4 and ν_o have been evaluated and the values appear in table L.1. The corresponding curves are shown in figure L.1.

Now the cell-wall, CF and matrix specific volumes are related via

$$\nu = \frac{\nu|^{\mathsf{f}} m_o|^{\mathsf{f}} + \nu|^{\mathsf{M}}(1 - m_o|^{\mathsf{f}} + w)}{1+w} \tag{L.5}$$

so, in terms of the cell-wall moisture content, the matrix density $\rho|^{\mathsf{M}}$ is

$$\rho|^{\mathsf{M}} = \frac{1 - m_o|^{\mathsf{f}} + w}{\nu(1+w) - m_o|^{\mathsf{f}}/\rho|^{\mathsf{f}}}, \tag{L.6}$$

or, expressed in terms of the matrix moisture content,

$$\rho|^{\mathsf{M}} = \frac{(1 - m_o|^{\mathsf{f}})(1 + w|^{\mathsf{M}})}{\nu(1 + w|^{\mathsf{M}}(1 - m_o|^{\mathsf{f}})) - m_o|^{\mathsf{f}}/\rho|^{\mathsf{f}}}. \tag{L.7}$$

Combining (L.4) and (L.7) with the adopted fibre density, $\rho|^{\mathsf{f}} = 1.58$ g/cc (§8.1.3), and a dry fibre mass fraction of $m_o|^{\mathsf{f}} = 0.42$ appropriate for spruce wood[1] permits the average *in situ* matrix density to be computed as a function of matrix moisture content.

[1] Sjöström (1981) claims an overall cellulose content of 41% for spruce, which when corrected for an extractive content of 1.7% gives $m_o|^{\mathsf{f}}_{\mathsf{W}} = 0.42$.

References

Abe, H., J. Ohtani, and K. Fukazawa (1991). FE-SEM Observations on the Microfibrillar Orientation in the Secondary Wall of Tracheids. *IAWA Bulletin*, 12(4):431–438.

— (1992). Microfibrillar Orientation of the Innermost Surface of Conifer Tracheid Walls. *IAWA Bulletin*, 13(4):411–417.

Aboudi, J. (1991). *Mechanics of Composite Materials-A Unified Micromechanical Approach*. Elsevier, Amsterdam.

Advani, S. G. and C. L. T. III. (1987). The Use of Tensors to Describe and Predict Fiber Orientation in Short Fiber Composites. *J. Rheology*, 31(8):751–784.

Akiva, U., H. D. Wagner, and S. Weiner (1998). Modelling the three-dimensional elastic constants of parallel-fibred and lamellar bone. *Journal of Materials Science*, 33(6):1497–1509.

Alince, B. (1989). Volume contraction of cellulose-water system. In: Shuerch, C. (ed.), *Cellulose and Wood: Chemistry and Technology*, pages 379–388. John Wiley & Sons, Inc., New York.

Anagnost, S. E., R. E. Mark, and R. B. Hanna (1999). Utilization of soft rot cavity formation as a tool for understanding the relation between microfibril angle and mechanical properties of cellulosic fibers. *ASME Proceedings – Mechanics of Cellulosic Materials*, AMD-Vol. 231/MD-Vol. 85:43–62.

— (2000). Utilization of soft-rot cavity orientation for the determination of microfibril angle. Part I. *Wood and Fiber Science*, 32(1):81–87.

Anagnost, S. E. and W. B. Smith (1997). Hygroscopicity of decayed wood: Implications for weight loss determinations. *Wood Fiber Sci.*, 29(3):299–305.

Andersson, S., R. Serimaa, M. Torkkeli, T. Paakkari, P. Saranpaa, and E. Pesonen (2000). Microfibril angle of Norway spruce [Picea abies (L.) Karst.] compression wood: comparison of measuring techniques. *Journal of Wood Science*, 46(5):343–349.

Astley, R. J., K. A. Stol, and J. J. Harrington (1998). Modelling the elastic properties of softwood. Part II. the cellular microstructure. *Holz als Roh- und Werkstoff*, 56:43–50.

Atalla, R. H. (1998). Cellulose and the hemicelluloses: patterns for the assembly of lignin. In: Lewis and Sarkanen (1998), chapter 13, pages 172–179.

— (1999a). Celluloses. In: Pinto (1999), chapter 3.16, pages 529–598.

— (1999b). The individual structures of native celluloses. In: *10th international symposium on wood and pulping chemistry*, volume 1, pages 608–614. TAPPI Press.

— (1999c). The structures of native celluloses, and the origin of their variability. In: *Proceedings of the MIE Bioforum 98, 1999 September 07–11; Suzuka, Japan*, pages 1–13.

Atalla, R. H. and U. P. Agarwal (1985). Raman microprobe evidence of lignin orientation in cell walls of native woody tissue. *Science*, 227:636–638.

Atalla, R. H., J. M. Hackney, I. Uhlin, and N. S. Thompson (1993). Hemicelluloses as structure regulators in the aggregation of native cellulose. *International Journal of Biological Macromolecules*, 15(2):109–112.

Atalla, R. H. and D. L. van der Hart (1984). Native cellulose: a composite of two distinct crystalline forms. *Science*, 223:283–285.

Avellaneda, M. (1987). Iterated homogenization, differential effective medium theory and applications. *Commun. Pure Appl. Math.*, 40:527–554.

— (1991). Bounds on the Effective Elastic Constants of Two-phase Composite Materials. In: *Nonlinear Partial Differential Equations and their Applications. College de France Seminar, Vol. X*. Longman Science Tech., Harlow, UK.

Baba, K., Y. Sone, H. Kaku, A. Misaki, N. Shibuya, and T. Itoh (1994). Localization of hemicelluloses in the cell walls of some woody plants using immuno-gold electron microscopy. *Holzforschung*, 48:297–300.

Babuška, I. (1976). Solution of interface problems by homogenization. Part I & II. *SIAM J. Math. Anal.*, 7:603–645.

— (1977). Solution of interface problems by homogenization. Part III. *SIAM J. Math. Anal.*, 8:923–931.

Back, E. and L. Salmén (1982). Glass transitions of wood components hold implications for molding and pulping processes. *Tappi*, 65(7):107–110.

Bailey, I. W. and E. E. Berkley (1942). The significance of X-rays in studying the orientation of cellulose in the secondary wall of tracheids. *Am. J. Bot.*, 29:231–241.

Bailey, I. W. and I. Kerr (1935). The visible structure of the secondary wall and its significance in physical and chemical investigations of tracheary cells and fibers. *J. Arnold Arboretum*, 16:273–300.

Bailey, I. W., I. Kerr, and M. R. Vestal (1937). The orientation of cellulose in the secondary wall of tracheary cells. *J. Arnold Arboretum*, 18:185–195.

Baird, W. M., R. A. Parham, and M. A. Johnson (1974a). Development and composition of the warty layer in balsam fir. I. Development. *Wood and Fiber*, 6(2):114–125.

— (1974b). Development and composition of the warty layer in balsam fir. II. Composition. *Wood and Fiber*, 6(3):211–222.

Baker, A. A., W. Helbert, J. Sugiyama, and M. J. Miles (1997). High resolution atomic

force microscopy of native Valonia cellulose I microcrystals. *Journal of Structural Biology*, 119(2):129–138.

— (1998). Surface structure of native cellulose microcrystals by AFM. *Applied Physics A*, 66(1):S559–S563.

Bakhvalov, B. and G. Panasenko (1984). *Homogenization: Averaging Processes in Periodic Media*. Kluwer Academic Publ., Dordrecht.

Barber, N. F. and M. C. Probine (1969). Microfibril angle as a parameter in timber quality assessment. *Forest Products Journal*, 19(4):30–34.

Barkas, W. W. (1949). *The Swelling of Wood under Stress : A Discussion of its Hygroscopic, Elastic and Plastic Properties*. H.M.S.O, London.

— (1950). Swelling Stresses in Gels. Forest Products Research Special Report 6, His Majesty's Stationery Office, London.

Barrett, J. D. and A. P. Schniewind (1973). Three-dimensional Finite Element Models of Cylindrical Wood Fibers. *Wood and Fiber*, 5(3):215–225.

Barthelemy, D., F. Blaise, T. Fourcaud, E. Nicolini, and F. le Tacon (1995). Modelling and simulating tree architecture - assessment and outlook. *Revue Forestiere Francaise*, 48:71–96.

Batchelor, W. J., A. B. Conn, and I. H. Parker (1997). Measuring the fibril angle of fibres using confocal microscopy. *Appita*, 50(5):377–380.

Batten, G. L. and A. H. Nissan (1987a). Unified theory of the mechanical properties of paper and other H-bond-dominated solids - Part I. *Tappi*, 70(9):119–123.

Batten, Jr., G. L. and A. H. Nissan (1987b). Unified theory of the mechanical properties of paper and other H-bond-dominated solids - Part III. *Tappi*, 70(11):137–140.

Beall, F. C. (1972). Density of Hemicelluloses and their Relationship to Wood Substance Density. *Wood and Fiber*, 4(2):114–116.

Beall, F. C. and W. K. Murphy (1970). Speculation on cellulose microfibril structure. *Wood and Fiber*, 2:282–284.

Bendtsen, B. A. and J. Senft (1986). Mechanical and anatomical properties in individual growth rings of plantation-grown eastern cottonwood and loblolly pine. *Wood and Fiber Science*, 18(1):23–38.

Benedict, C. R., R. J. Kohel, and G. M. Jividen (1994). Crystalline Cellulose and Cotton Fiber Strength. *Crop Science*, 34(1):147–151.

Bensoussan, A., J. L. Lions, and G. Papanicolaou (1978). *Asymptotic Analysis for Periodic Structures*. North-Holland.

Benveniste, Y. (1987). A new approach to the application of Mori-Tanaka's theory in composite materials. *Mech. Mater.*, 6:147–157.

Bergander, A. and L. Salmén (2000). Variations in transverse fibre wall properties: relations between elastic properties and structure. *Holzforschung*, 54(6):654–660.

Berryman, J. G. (1997). Explicit schemes fo estimating elastic properties of multiphase

composites. Report 79, Stanford Exploration Project.

Bodig, J. and J. R. Goodman (1973). Prediction of Elastic Parameters for Wood. *Wood Science*, 5(4):249–264.

Bodig, J. and B. A. Jayne (1982). *Mechanics of Wood and Wood Composites*. Van Nostrand Reinhold Company, New York.

Boley, B. A. and J. H. Weiner (1960). *Theory of thermal stresses*. Wiley, New York.

Bond, J. S. and R. H. Atalla (1999). A Raman microprobe investigation of the molecular architecture of loblolly pine tracheids. In: *10th international symposium on wood and pulping chemistry*, volume 1, pages 96–101. TAPPI Press.

Bower, D. I. (1997). Infrared dichroism, polarized fluorescence and Raman spectroscopy. In: Ward (1997), chapter 4, pages 181–233.

Boyd, J. D. (1973). Appraising methods of measuring microfibril angles. *Wood Science*, 6(1):95–96.

— (1974). Relating lignification to microfibril angle differences between tangential and radial faces of all wall layers in wood cells. *Drevarsky Vyskum*, 19(2):41–54.

— (1977a). Interpretation of X-ray diffractograms of wood for assessments of microfibril angles in fibre cell walls. *Wood Science and Technology*, 11(2):93–114.

— (1977b). Relationship Between Fibre Morphology and Shrinkage of Wood. *Wood Science and Technology*, 11(1):3–22.

— (1978). Significance of laricinan in compression wood tracheids. *Wood Science and Technology*, 12(1):25–35.

— (1982). An Anatomical Explanation for Viscoelastic and Mechano-sorptive Creep in Wood, and Effects of Loading Rate on Strength. In: Baas, P. (ed.), *New Perspectives in Wood Anatomy*, Forestry Sciences, pages 171–222. Martinus Nijhoff / Dr W. Junk Publishers, The Hague.

Boyd, J. D. and R. C. Foster (1975). Microfibrils in primary and secondary wall growth develop trellis configurations. *Can. J. Bot.*, 53:2687–2701.

Boylston, E. K. and J. J. Hebert (1995). The primary wall of cotton fibers. *Textile Research Journal*, 65:429–431.

Brändström, J. (2001). Micro- and ultrastructural aspects of Norway spruce tracheids: a review. *IAWA Journal*, 22(4):333–353.

Brasch, D. J. and L. E. Wise (1956a). The chemistry of New Zealand grown Pinus radiata. I. Summative analyses and preliminary studies on the hemicelluloses. *Tappi*, 39(8):581–8.

— (1956b). The chemistry of New Zealand grown Pinus radiata. II. Two aldobiuronic acids from the hemicelluloses. *Tappi*, 39(11):768–74.

Brasch, D. J. et al. (1959). Structure of some water-soluble polysaccharides from wood. *Pulp and Paper Magazine of Canada*, 60(11):342–5.

Brett, C. T. (2000). Cellulose microfibrils in plants: Biosynthesis, deposition, and

integration into the cell wall. *International Review of Cytology - A Survey of Cell Biology*, 199:161–199.

Broughton, G., R. E. Heeks, and C. Johnnes (1955). Methods for cellulose accessibility determination. *Tappi*, 38(8):498–502.

Brown, R. M. (1999). Cellulose structure and biosynthesis. *Pure and Applied Chemistry*, 71(5):767–775.

Brown, R. M. and I. M. Saxena (2000). Cellulose biosynthesis: a model for understanding the assembly of biopolymers. *Plant Physiology & Biochemistry*, 38(1-2):57–67.

Browning, B. L. (1963). *The Chemistry of Wood*. Wiley-Interscience.

Brunow, G., I. Kipeläinen, J. Sipilä, K. Syrjänen, P. Karhunen, H. Setälä, and P. Rummakko (1998). Oxidative coupling of phenols and the biosynthesis of lignin. In: Lewis and Sarkanen (1998), chapter 10, pages 131–147.

Budiansky, B. (1965). On the elastic moduli of some heterogenous materials. *J. Mech. Phys. Solids*, 13:223–227.

Buryachenko, V. A. (1996). The overall elastoplastic behavior of multiphase materials with isotropic components. *Acta Mechanica*, 119:93–117.

Butterfield, B. G. (1993). The structure of wood: an overview. In: *Primary Wood Processing: Principles and Practice*, chapter 1, pages 1–22. Chapman & Hall Ltd., London.

Butterfield, B. G. (ed.) (1998). *Microfibril Angle in Wood*. IAWA/IUFRO. Published in conjunction with the IAWA and IUFRO. Printed by University of Canterbury Press, Christchurch, New Zealand.

Butterfield, B. G. and B. A. Meylan (1980). *Three dimensional structure of wood: an ultrastructural approach*. Chapman & Hall, London, New York, 2nd edition.

Byrd, V. L. et al. (1965). Wood characteristics and kraft paper properties of four selected Loblolly Pines. Part II: Wood chemical constituents and their relationship to fiber morphology. *Forest Products Journal*, 15(8):313–20.

Carlson, D. E. (1972). Linear Thermoelasticity. In: *Handbuch der Physik*, volume VIa/2, pages 297–346. Springer-Verlag, Berlin.

Carpita, N. C. (1996). Structure and Biogenesis of the Cell-Walls of Grasses. *Annual Review of Plant Physiology and Plant Molecular Biology*, 47(445-476).

Carpita, N. C. and D. M. Gibeaut (1993). Structural models of primary cell walls in flowering plants: consistency of molecular structure with the physical properties of walls during growth. *Plant J.*, 3:1–30.

Cave, I. and W. Robinson (1998). Interpretation of (002) diffraction arcs by means of a minimalist model. In: Butterfield, B. G. (ed.), *Microfibril Angle in Wood*. IAWA/IUFRO.

Cave, I. D. (1966). Theory of X-ray Measurement of Microfibril Angle in Wood. *Forest Products Journal*, 16(10):37–42.

— (1968). The anisotropic elasticity of the plant cell wall. *Wood Science and Technology*, 2(4):268–278.

— (1973). *Mechanical properties of fibre-reinforced materials: the wood-water system*. Ph.D. thesis, Victoria University of Wellington, New Zealand.

— (1974). Optical Properties of The Wood Cell Wall. Technical Report 451, PEL. This report is in error on page 4. It does not follow that since Mn is unitary it can be represented by the first equation on p4.

— (1976). Modelling the Structure of the Softwood Cell Wall for Computation of Mechanical Properties. *Wood Science and Technology*, 10(1):19–28.

— (1978a). Modelling moisture-related mechanical properties of wood. Part I: properties of wood constituents. *Wood Science and Technology*, 12:75–86.

— (1978b). Modelling moisture-related mechanical properties of wood. Part II: computation of properties of a model of wood and comparison with experimental data. *Wood Science and Technology*, 12:127–139.

— (1997a). Theory of X-ray measurement of microfibril angle in wood. Part 1. The condition for reflection. *Wood Science and Technology*, 31:143–152.

— (1997b). Theory of X-ray measurement of microfibril angle in wood. Part 2. The diffraction diagram. *Wood Science and Technology*, 31:225–234.

Cave, I. D. and W. H. Robinson (1969). A Model for the Mechanical Damping in Wood. In: *Proceedings of a Conference on the Science of Materials, University of Auckland, 17-21 August 1969*, Information Series No. 71, pages 209–215. NZ DSIR.

Chamis, C. C. and G. P. Sendeckjy (1968). Critique on theories predicting thermoelastic properties of fibrous composites. *J. Composite Materials*, 1(2):152–165.

Chanzy, H., A. Peguy, S. Chaunis, and P. Monzie (1980). Oriented cellulose films and fibers from a mesophase system. *Journal of Polymer Science, Polymer Physics Edition*, 18(5):1137–44.

Chatters, R. M. (1963). Siliceous skeletons of wood fibres. *Forest Products Journal*, 13(9):368–72.

Chen, C.-L. (1991). Lignins: occurence in woody tissues, isolation, reactions, and structure. In: Lewin and Goldstein (1991), chapter 5, pages 183–261.

Chou, P. C., J. Carleone, and C. M. Hsu (1972). Elastic constants of layered media. *Journal of Composite Materials*, 6:80.

Christensen, G. N. and K. E. Kelsey (1958). The sorption of water vapour by the constituents of wood: determination of sorption isotherms. *Australian Journal of Applied Science*, 9(3):265–282.

— (1959). The sorption of water vapour by the constituents of wood. III. The swelling of lignin. *Aust. J. Appl. Sci.*, 10(3):284–293.

Christensen, R. M. (1979). *Mechanics of composite materials*. Wiley, New York.

Christensen, R. M. and K. H. Lo (1979). Solutions for effective shear properties in

three phase sphere and cylinder models. *J. Mech. Phys. Solids*, 27:315.

— (1990). A critical evaluation for a class of micromechanics models. *J. Mech. Phys. Solids*, 38:379.

Cioranescu, D. and J. S. J. Paulin (1998). *Homogenization of Reticulated Structures*, volume 136 of *Applied Mathematical Sciences*. Springer.

Clark, G. L. and J. A. Howsman (1946). Swollen, impregnated, and compressed wood samples: X-ray diffraction studies. *Industr. & Engng. Chem. (Industr. Ed.)*, 38(12):1257–62.

Cleary, M. P., L.-W. Chen, and S.-M. Lee (1980). Self-consistent techniques for heterogenous media. *ASCE J. Engng. Mech.*, 106:861–887.

Core, H. A., W. A. Côté, and A. C. Day (1976). *Wood structure and identification*. Syracuse Univ. Press, Syracuse, N.Y.

Cosgrove, D. J. (1997). Assembly and Enlargement of the Primary-Cell Wall in Plants. *Annual Review of Cell and Developmental Biology*, 13(171-201).

— (1999). Enzymes and other agents that enhance cell wall extensibility. *Annu. Rev. Plant Physiol. Plant Mol. Biol.*, 50:391–417.

Côté, W. A. (ed.) (1965). *Cellular Ultrastructure of Woody Plants*. Syracuse University Press, Syracuse, NY.

Côté, W. A. (1967). *Wood ultrastructure: an atlas of electron micrographs*. University of Washington Press, Seattle.

— (1977). Wood Ultrastructure in Relation to Chemical Composition. In: Loewus and Runeckles (1977).

Cote, W. A., A. C. Day, and T. E. Timell (1968). Studies on compression wood-Part VII. Distribution of lignin in normal and compression wood of Tamarack (Larix laricina (Du Roi) K. Koch). *Wood Science and Technology*, 2(1):13–37.

Cote, Jr., W. A., A. C. Day, B. W. Simson, and T. E. Timell (1966). Studies on larch arabinogalactan. I. The distribution of arabinogalactan in larch wood. *Holzforschung*, 20(6):178–92.

Cousins, W. J. (1972). Measurement of mean microfibril angles of wood tracheids. *Wood Science and Technology*, 6(1):58.

— (1976). Elastic Modulus of Lignin as Related to Moisture Content. *Wood Science and Technology*, 10(1):9–17.

— (1977). Elasticity of isolated lignin: Young's modulus by a continuous indentation method. *New Zealand Journal of Forestry Science*, 7(1):107–112.

— (1978). Young's Modulus of Hemicellulose as Related to Moisture Content. *Wood Science and Technology*, 12(3):161–167.

Cousins, W. J., R. W. Armstrong, and W. H. Robinson (1975). Young's modulus of lignin from a continuous indentation test. *J. Mat. Science*, 10:1655–1658.

Cowdrey, D. R. and R. D. Preston (1966). Elasticity and Microfibrillar Angle in the

Wood of Sitka Spruce. *Proceedings of the Royal Society, London*, B166(1004):245–272.

Cowin, S. C. (1985). Modelling shrinkage mechanisms in porous elastic solids. *Journal of Applied Mechanics*, 52:351–355.

Cown, D. J. (1975). Variation in tracheid dimensions in the stem of a 26-year-old radiata pine tree. *Appita*, 28(4):237–245.

— (1992). New Zealand Radiata Pine and Douglas Fir: Suitability for Processing. *FRI-Bulletin*, No. 168:74 pp. The author given is the Compiler/Principal-author.

Cown, D. J. and D. L. McConchie (1980). Wood property variations in an old crop stand of radiata pine. *New Zealand Journal of Forestry Science*, 10(3):508–520.

Crolet, J. M., B. Aoubiza, and A. Meunier (1993). Compact bone: numerical simulation of mechanical characteristics. *J. Biomechanics*, 26(6):677–687.

Crosby, C. M., C. de Zeeuw, and R. Marton (1972). Fibrillar angle variation in Red Pine determined by Senarmont compensation. *Wood Science and Technology*, 6(3):185–195.

Crosby, C. M. and R. E. Mark (1974). Precise S2 angle determination in pulp fibers. *Svensk Papperstidning*, 17:636–642.

Cunningham, M. J. and T. J. Sprott (1984). Sorption properties of New Zealand building materials. Research Report 43, Building Research Association of New Zealand.

Cutter, B. E. and W. K. Murphey (1972). X-ray measurement of crystallite size in wood. *Wood and Fiber*, 4(1):43–44.

Daniel, G. and I. Duchesne (1998). Revealing the surface ultrastructure of spruce pulp fibres using Field Emission-SEM. In: *7th Int. Conference on Biotechnology in the Pulp and Paper Industry, 1998*.

Daniel, G. and T. Nilsson (1984). Studies on the S2 Layer of *Pinus sylvestris*. Rapport 154, Institutionen for Virkeslara, Sveriges Lantbruksuniversitet.

Daniel, G., T. Nilsson, and B. Pettersson (1991). Poorly and non-lignified regions in the middle lamella cell corners of birch (Betula verrucosa) and other wood species. *IAWA Bulletin n.s.*, 12:70–83.

Dasgupta, A. and S. M. Bhandarkar (1992). A generalized self-consistent Mori-Tanaka scheme for fiber composites with multiple inter-phases. *Mechanics of Materials*, 14:67–82.

Davies, G. W. and H. D. Ingle (1966). Wall thickening in *Callitris glauca* R. Br. *Nature, Lond.*, 209(5025):826–7.

Davin, L. B. and N. G. Lewis (2000). Dirigent proteins and dirigent sites explain the mystery of specificity of radical precursor coupling in lignan and lignin biosynthesis. *Plant Physiology*, 123(2):453–461.

de Reffye, P., T. Fourcaud, F. Blaise, D. Barthelemy, F. Houllier, and P. De-Reffye (1997). A functional model of tree growth and tree architecture. *Silva Fennica*,

31(3):297–311.

Debzi, E. M., H. Chanzy, J. Sugiyama, P. Tekely, and G. Excoffier (1991). The I_α to I_β transformation of highly crystalline cellulose by annealing in various mediums. *Macromolecules*, 24:6816–6822.

Delmer, D. P. (1999). Cellulose biosynthesis: exciting times for a difficult field of study. *Annual Review of Plant Physiology & Plant Molecular Biology*, 50:245–276.

Dimitrienko, Y. I. (1999). Modelling of carbon-carbon composite manufacturing process. *Composites: Part A*, 30:221–230.

Dinwoodie, J. M. (1981). *Timber, its nature and behaviour*. Van Nostrand Reinhold.

— (1989). *Wood : nature's cellular, polymeric, fibre-composite*. Institute of Metals, Brookfield, Vermont.

Donaldson, L. A. (1987). S3 Lignin Concentration in Radiata Pine Tracheids. *Wood Science and Technology*, 21(3):227–234.

— (1991a). Seasonal Changes in Lignin Distribution During Tracheid Development in Pinus Radiata D. Don. *Wood Science and Technology*, 25(1):15–24.

— (1991b). The Use of Pit Apertures as Windows to Measure Microfibril Angle in Chemical Pulp Fibers. *Wood and Fiber Science*, 23(2):290–295.

— (1992). Within and Between Tree Variation in Microfibril Angle in Pinus Radiata. *New Zealand Journal of Forestry Science*, 22(1):77–86.

— (1993). Variation in Microfibril Angle Three Genetic Groups of *Pinus radiata* Trees. *New Zealand Journal of Forestry Science*, 23(1):90–100.

— (1994). Mechanical Constraints on Lignin Deposition During Lignification. *Wood Science and Technology*, 28(2):111–118.

— (1998). Between-tracheid variability of microfibril angles in radiata pine. In: Butterfield, B. G. (ed.), *Microfibril Angle in Wood*. IAWA/IUFRO.

— (2001a). Lignification and lignin topochemistry - an ultrastructural view. *Phytochemistry*, 57(6):859–873.

— (2001b). Measurement of cell wall ultrastructural features of wood cell walls by Fourier analysis. Poster.

— (2001c). A three-dimensional computer model of the tracheid cell wall as a tool for interpretation of wood cell wall ultrastructure. *IAWA Journal*, 22(3):213–233.

Donaldson, L. A. and R. D. Burdon (1995). Clonal variation and repeatability of microfibril angle in *Pinus radiata*. *New Zealand Journal of Forestry Science*, 25(2):164–74.

Donaldson, L. A. and M. J. F. Lausberg (1998). Comparison of conventional transmitted light and confocal microscopy for measuring wood cell dimensions by image analysis. *IAWA Journal*, 19(3):321–336.

Donaldson, L. A., A. P. Singh, A. Yoshinaga, and K. Takabe (1999). Lignin distribution in mild compression wood of Pinus radiata. *Can. J. Bot.-Rev. Can. Bot.*, 77:41–50.

Downes, G. M., J. V. Ward, and N. D. Turvey (1991). Lignin distribution across tracheid cell walls of poorly lignified wood from deformed copper deficient Pinus radiata (D. Don). *Wood Science and Technology*, 25(1):7–14.

Duchesne, I. and G. Daniel (1999). The ultrastructure of wood fibre surfaces as shown by a variety of microscopical methods - a review. *Nord. Pulp Paper Res.*, 14(2):129–139.

Dunning, C. E. (1968). Cell-wall Morphology of Longleaf Pine Latewood. *Wood Science*, 1(2):65–76.

— (1969). The Structure of Longleaf Pine Latewood. I. Cell Wall Morphology and the Effect of Alkaline Extraction. II. Intertracheid Membranes and Pit Membranes. *Tappi*, 52(7):1326–41.

Easty, D. B. and N. S. Thompson (1991). Wood Analysis. In: Lewin, M. and I. S. Goldstein (eds.), *Wood Structure and Composition*, volume 11 of *International fiber science and technology series*. Marcel Dekker, Inc., New York.

Echols, R. M. (1965). Linear Relationship of Fibrillar Angle to Tracheid Length and the Genetic Control of Tracheid Length in Slash Pine. *Tropical Woods*, 102:11–22.

El-Hosseiny, F. and D. H. Page (1973). The measurement of fibril angle of wood fibers using polarized light. *Wood and Fiber*, 5(3):208–214.

El-Osta, M. L. M., R. M. Kellogg, R. O. Foschi, and R. G. Butters (1973). A direct X-ray technique for measuring microfibril angle. *Wood and Fiber*, 5(2):118–128.

El-Osta, M. L. M., R. W. Wellwood, and R. G. Butters (1972). An improved x-ray technique for measuring microfibril angle of coniferous wood. *Wood Science*, 5(2):113–117.

Entwistle, K. M. and N. Navaranjan (2001). X-ray diffraction from cellulose microfibrils in the S2 layers of structurally characterised softwood specimens. *J. Matls. Sci.*, 36:3855–3863.

Entwistle, K. M. and N. J. Terrill (2000). The measurement of the micro-fibril angle in soft-wood. *Journal of Materials Science*, 35:1675–1684.

Erikson, Ö., D. A. I. Goring, and B. O. Lindgren (1980). Structural studies on the chemical bonds between lignins and carbohydrates in spruce wood. *Wood Science and Technology*, 14(4):267–279.

Erins, P., V. Cinite, M. Jakobson, and J. Gravitis (1976). Wood as a multicomponent crosslinked polymer system. *Journal of Applied Polymer Science: Applied Polymer Symposium*, 28:1117–1138.

Eshelby, J. D. (1957). The determination of the elastic field of an ellipsoidal inclusion and related problems. *Proc. R. Soc. Lond. A*, 241:376–396.

Evans, R. (1994). Rapid measurement of the transverse dimensions of tracheids in radial wood sections from Pinus radiata. *Holzforschung*, 48(2):168–172.

— (1998). Rapid scanning of microfibril angle in increment cores by x-ray diffractom-

etry. In: Butterfield, B. G. (ed.), *Microfibril Angle in Wood*. IAWA/IUFRO.

— (1999). A variance approach to the X-ray diffractometric estimation of microfibril angle in wood. *Appita*, 52(4):283–289,294.

Evans, R., M. Hughes, and D. Menz (1999). Microfibril angle variation by scanning X-ray diffractometry. *Appita*, 52(5):363–367.

Evans, R., S.-A. Stuart, and J. van der Touw (1996). Microfibril angle scanning of increment cores by x-ray diffractometry. *Appita*, 49(6):411–414.

Farruggia, F. and P. Perré (1997). An explanation of the mechanical behaviour of early wood (*Picea abies* in the transverse plane based only on the arrangement of the cells. In: Jeronimidis, G. and J. F. V. Vincent (eds.), *Plant Biomechanics 1997: Conference Proceedings I*, pages 215–221. Centre for Biomimetics, University of Reading.

Faulon, J. L., G. A. Carlson, and P. G. Hatcher (1994). A three-dimensional model of lignocellulose from gymnospermous wood. *Organic Geochemistry*, 21(12):1169–1179.

Faulon, J.-L. and P. G. Hatcher (1994). Is there any order in the structure of lignin? *Energy and Fuels*, 8:402–407.

Favis, B. D., W. Q. Yean, and D. A. I. Goring (1984). Molecular weight of lignin fractions leached from unbleached Kraft pulp. *J. Wood Chem. Technol.*, 4(3):313–320.

Fengel, D. (1969). The ultrastructure of cellulose from wood. Part I: Wood as the basic material for the isolation of cellulose. *Wood Science and Technology*, 3(3):203–217.

— (1970a). Ultrastructural behaviour of cell wall polysaccharides. *Tappi*, 53(3):497–503.

— (1970b). The ultrastructure of cellulose from wood. Part 2. Problems of the isolation of cellulose. *Wood Science and Technology*, 4(1):15–35.

Fengel, D. and D. Grosser (1975). Chemical composition of softwoods and hardwoods. A literature review. *Holz als Roh- und Werkstoff*, 33(1):32–34 + 2 tab.

Fengel, D. and M. Stoll (1973). Variation in cell cross-sectional area, cell-wall thickness and wall layers of Spruce tracheids within an annual ring. *Holzforschung*, 27(1):1–7.

— (1978). Studies on holocellulose and alpha-cellulose from spruce wood using cryo-ultramicrotomy. Part 2: The influence of heavy metal salt impregnation and the dimensions of delignified cell wall layers. *Wood Science and Technology*, 12(4):261–269.

Fengel, D. and G. Wegener (1984). *Wood: chemistry, ultrastructure, reactions*. Walter de Gruyter, Berlin.

Fenwick, K. M., M. C. Jarvis, and D. C. Apperley (1997). Estimation of polymer rigidity in cell-walls of growing and nongrowing celery collenchyma by solid-state nuclear-magnetic-resonance in-vivo. *Plant Physiology*, 115(2):587–592.

Fink, D. H. and R. D. Jackson (1973). An equation for describing water vapor adsorp-

tion isotherms of soils. *Soil Science*, 116(4):256–261.

Fourcaud, T., F. Blaise, D. Barthelemy, F. Houllier, P. de Reffye, and G. Nepveu (1997). A physiological approach for tree growth modelling in the software AMAPpara. In: *IUFRO WP S5.01-04. Proceedings, second workshop: Connection between silviculture and wood quality through modelling approaches and simulation software, Berg-en-Dal, Kruger National Park, South Africa, August 26-31, 1996*, pages 321–334. Institut National de le Recherche Agronomique (INRA), Departement d'Economie et de Sociologie Rurales, Laboratoire d' Economie Forestere et Agricole; Nancy; France.

Franciosi, P. and R. Gaertner (1998). On phase connectivity descriptions in modeling viscoelasticity of fiber or sphere reinforced composites. *Polymer Composites*, 19(1):81–95.

Freudenberg, K. (1932). The relationship of cellulose to lignin in wood. *J. Chem. Educ.*, 9:1171–1180.

Freudenberg, K. J. and A. C. Neish (1968). *Constitution and biosynthesis of lignin*. Number 2 in Molecular biology, biochemistry and biophysics. Springer-Verlag.

Frey-Wyssling, A. (1964). Ultraviolet and fluorescent optics of lignified cell walls. In: Zimmermann (1964).

Fujino, T. and T. Itoh (1998). Changes in the three dimensional architecture of the cell wall during lignification of xylem cells in *Eucalyptus tereticornis*. *Holzforschung*, 52(2):111–116.

Fujita, M. and H. Harada (1990). Ultrastructure and formation of wood cell wall. In: Hon and Shiraishi (1990).

Fujita, M., S. Hata, and H. Saiki (1989). Application of optical Fourier transformation and FFT to the quantitative analysis of wood structures. *IAWA Bulletin*, 10(3):336–337.

— (1991). Periodic analysis of wood structure. IV. Characteristics of the power spectral pattern of wood sections and application of non-microscopic wood pictures. *Memoirs of the College of Agriculture, Kyoto University*, 138:11–23.

Fujita, M., M. Ohyama, and H. Saiki (1996). Characterisation of vessel distribution by Fourier transform image analysis. In: Donaldson, L. A. et al. (eds.), *Recent advances in wood anatomy. Proceedings of the Third Pacific Regional Wood Anatomy Conference, Rotorua, 20-24 November, 1994*. New Zealand Forest Research Institute; Rotorua; New Zealand.

Fujita, M. and H. Saiki (1990). Section-splitting method for fibril angle measurement of cell wall layers. *Bulletin of the Kyoto University Forests*, 62:270–274.

Fujita, M., H. Saiki, and H. Harada (1978). The secondary wall formation of compression wood tracheids. II. Cell wall thickening and lignification. *Mokuzai Gakkaishi*, 24(3):158–163.

Fung, Y. C. (1965). *Foundations of Solid Mechanics*. Prentice-Hall, Inc., Englewood

Cliffs, N.J.

Fushitani, M. (1973). Study of molecular orientation in wood by fluorescence method. *Mokuzai Gakkaishi*, 19(1):35–40.

Gardner, K. H. and J. Blackwell (1974). The structure of native cellulose. *Biopolymers*, 13:1975–2001.

Gerhards, C. C. (1982). Effect of moisture content and temperature on the mechanical properties of wood: an analysis of immediate effects. *Wood and Fiber*, 14(1):4–36.

Ghosh, S., K. Lee, and S. Moorthy (1995). Multiple scale analysis of heterogeneous elastic structures using homogenization theory and Voronoi cell finite element method. *Int. J. Solids Structures*, 32(1):27–62.

Gibson, L. J. (1981). Ph.D. thesis, Engineering Department, Cambridge University, Cambridge.

Gibson, L. J. and M. F. Ashby (1988). *Cellular Solids: Structure & Properties*. Pergamon Press, Oxford.

— (1997). *Cellular Solids: Structure and Properties*. Cambridge University Press, second edition.

Gillis, P. P. (1969). Effect of Hydrogen Bonds on the Axial Stiffness of Crystalline Native Cellulose. *Journal of Polymer Science: Part A-2*, 7:783–794.

Gillis, P. P., R. E. Mark, and R. C. Tang (1969). Elastic stiffness of crystalline cellulose in the folded-chain state. *J. Mater. Science*, 4:1003–1007.

Glasser, W. G. and S. Sarkanen (eds.) (1989). *Lignin : properties and materials*. Number 397 in ACS symposium series. American Chemical Society, Washington, DC.

Goodman, J. R. and J. Bodig (1970). Orthotropic Elastic Properties of Wood. *Journal of the Structural Division, Proceedings of the American Society of Civil Engineers*, 96(ST11):2301–2319.

Goring, D. A. I. (1963). Thermal Softening of Lignin, Hemicellulose and Cellulose. *Pulp and Paper Magazine of Canada*, 64(12):T517–T527.

Goring, D. A. I. and T. E. Timell (1962). Molecular weight of native celluloses. *Tappi*, 45(6):454–60.

Gorisek, Z., N. Torelli, and H. Guttenberger (1999). Microfibril angle in juvenile, adult and compression wood of spruce and silver fir. *Phyton Horn*, 39(3):129–132.

Gradin, P., P. G. Howgate, R. Seldén, and R. A. Brown (1989). Dynamic-mechanical properties. In: Allen, G., J. C. Bevington, C. Booth, and C. Price (eds.), *Comprehensive Polymer Science. Volume 2: Polymer Properties*, chapter 16, pages 533–569. Pergamon Press.

Green, A. E. and J. E. Adkins (1960). *Large elastic deformations and nonlinear continuum mechanics*. Clarendon Press, Oxford.

Green, D. W., J. W. Evans, J. D. Logan, and W. J. Nelson (1999). Adjusting modulus of

elasticity of lumber for changes in temperature. *Forest Products Journal*, 49(10):82–94.

Gregory, A. and G. P. Bolwell (1999). Hemicelluloses. In: Pinto (1999), chapter 3.17, pages 599–615.

Greguss, P. (1955). *Identification of living gymnosperms on the basis of xylotomy*. Akadémiai Kiado, Budapest.

— (1972). *Xylotomy of the living conifers*. Akademiai Kiado, Budapest. Translated by Balint Balkay.

Grosser, D. (1986). On the occurrence of trabeculae with special consideration of diseased trees. *IAWA Bulletin*, 7(4):319–341.

Grozdits, G. A. and G. Ifju (1984). Differentiation of tracheids in developing secondary xylem of *Tsuga canadensis* L. Carr. Changes in morphology and cell wall structure. *Wood and Fiber Science*, 16(1):20–36.

Grünbaum, B. and G. C. Shephard (1986). *Tilings and Patterns*. W. H. Freeman, New York.

Gustafsson, S. I. (1997). Optimising ash wood chairs. *Wood Science and Technology*, 31(4):291–301.

Ha, M. A., D. C. Apperley, and M. C. Jarvis (1997). Molecular Rigidity in Dry and Hydrated Onion Cell-Walls. *Plant Physiology*, 115(2):593–598.

Hafreén, J., T. Fujino, U. Westermark, and N. Terashima (2000). Ultrastructural changes in the compound middle lamella of *Pinus thunbergii* during lignification and lignin removal. *Holzforschung*, 54(3):234–240.

Hafren, J., T. Fujino, and T. Itoh (1999). Changes in cell wall architecture of differentiating tracheids of Pinus thunbergii during lignification. *Plant Cell Physiol.*, 40(5):532–541.

Halpin, J. C. (1984). *Primer on Composite Materials: Analysis*. Technomic, 2nd edition (revised) edition.

Hanley, S. J., J.-F. Revol, L. Godbout, and D. G. Gray (1997). Atomic force microscopy and transmission electron microscopy of cellulose from *Micrasterias denticulata*; evidence for a chiral helical microfibril twist. *Cellulose*, 4(3):209–220.

Hansson, J.-Å. (1970). Sorption of Hemicelluloses on Cellulose Fibres. Pt. 2. Sorption of Glucomannan. *Holzforschung*, 24(3):77–83.

Harada, H. (1965). Ultrastructure and organization of gymnosperm cell walls. In: Côté, W. (ed.), *Cellular Ultrastructure of Woody Plants*, pages 215–234. Syracuse University Press, Syracuse, N. Y.

— (1982). The structure of cellulose microfibrils in *Valonia*. In: *Cellulose and other natural polymer systems, biogenesis, structure and degradation*, pages 383–401. Plenum Press, New York.

Harada, H. and J. Sugiyama (1985). Morphological Structure of Cellulose Microfibrils.

In: Kucera, L. J. (ed.), *Xylorama*, pages 105–112. Birkhauser Verlag, Basel.

Harada, H. and J. W. A. Côté (1985). Structure of Wood. In: Higuchi, T. (ed.), *Biosynthesis and biodegradation of wood components*, pages 1–42. Academic Press, Orlando, FL.

Harada, H. and A. B. Wardrop (1960). Cell wall structure of ray parenchyma cells of a softwood. *Mokuzai Gakkaishi*, 6(1):34–41.

Harlow, W. M. (1970). *Inside Wood: Masterpiece of Nature*. The American Forestry Assoc., Washington D.C.

Harrington, J. J., R. E. Booker, and R. J. Astley (1998). Modelling the elastic properties of softwood. Part I: the cell-wall lamellae. *Holz als Roh- und Werkstoff*, 56:37–41.

Harris, J. M. (1991). Structure of wood and bark. In: Kininmonth and Whitehouse (1991), chapter 2, pages 2.1–2.16.

Harris, J. M. and D. J. Cown (1991). Basic wood properties. In: Kininmonth and Whitehouse (1991), chapter 6, pages 6.1–6.28.

Harwood, V. D. (1973). Studies on the cell wall polysaccharides of *Pinus radiata*. II. Structure of a glucomannan. *Svensk Papperstidning*, 76(10):377–379.

Hashin, Z. (1962). The elastic moduli of heterogenous materials. *J. Appl. Mech.*, 29:143.

— (1983). Analysis of composite materials. A survey. *J. Appl. Mech.*, 50:483–505.

Hashin, Z. and B. W. Rosen (1964). The elastic moduli of fiber-reinforced materials. *J. Appl. Mech.*, 31:223.

Hashin, Z. and S. Shtrikman (1963). A variational approach to the theory of the elastic behaviour of multiphase materials. *J. Mech. Phys. Solids*, 11:127–140.

Hashin, Z. and T. Shtrikman (1962). A variational approach to the elastic behavior of polycrystals. *J. Mech. Phys. Solids*, 10:343–352.

Haward, R. N. and R. J. Young (eds.) (1997). *The physics of glassy polymers*. Chapman & Hall, 2nd edition.

Heady, R. (1997). *The wood anatomy of CallitrisVent. (Cupressaceae): an SEM Study*. Ph.D. thesis, Dept. of Forestry, Australian National University.

Hearle, J. W. S. (1963). The fine structure of fibers and crystalline polymers. III. Interpretation of the mechanical properties of fibers. *J. Appl. Polymer Science*, 7:1207–1223.

Hearmon, R. F. S. (1961). *An Introduction to Applied Anisotropic Elasticity*. Oxford University Press.

Hepworth, D. G. and J. F. V. Vincent (1998). Modelling the mechanical properties of xylem tissue from tobacco plants (*Nicotiana tabacum*'Samsun') by considering the importance of molecular and micromechanisms. *Annals of Botany*, 81:761–770.

Herman, M., P. Dutilleul, and T. Avella-Shaw (1999). Growth rate effects on intra-ring and inter-ring trajectories of microfibril angle in Norway spruce (Picea abies). *IAWA Journal*, 20(1):3–21.

Hermans, P. H. (1949). *Physics and chemistry of cellulose fibres : with particular reference to rayon*. Elsevier's polymer series ; 2. Elsevier Pub. Co., New York.

Heyn, A. N. (1955). Small particle X-ray scattering by fibers, size and shape of microcrystallites. *J. Appl. Phys.*, 26(5):519–526.

Hill, R. (1964). Theory of the Mechanical Properties of Fibre Strengthened Materials. Part II. Inelastic Behavior. *J. Mech. Phys. Solids*, 12:213–218. Bound together with Part I [Hill64].

— (1965). Mechanical Theory of Fiber Strengthened Materials, III Self Consistent Model. *J. Mech. Phys. Solids*, 13:189–198.

Hiller, C. H. (1964). Pattern of variation of fibril angle within annual rings of Pinus X attenu-radiata.

Hiller, C. H. and R. S. Brown (1967). Comparison of dimension and fibril angles of Loblolly Pine tracheids formed in wet or dry growing seasons. *Amer. J. Bot.*, 54(4):453–60.

Hoffmann, G. C. and T. E. Timell (1972). Polysaccharides in ray cells of normal wood of Red Pine (Pinus resinosa). *Tappi*, 55(5):733–736.

Hollister, S. J., D. P. Fyhrie, K. J. Jepsen, and S. A. Goldstein (1991). Application of homogenization theory to the study of trabecular bone mechanics. *J. Biomechan.*, 24:825–839.

Hollister, S. J. and N. Kikuchi (1992). A comparison of homogenization and standard mechanics analyses for periodic porous composites. *Computational Mechanics*, 10:73–95.

— (1994). Homogenization theory and digital imaging: a basis for studying the mechanics and design principles of bone tissue. *Biotechnology and Bioengineering*, 43:586–596.

Holmberg, S., K. Persson, and H. Petersson (1999). Nonlinear mechanical behaviour and analysis of wood and fibre materials. *Computers and Structures*, 72(4–5):459–480.

Hon, D. N.-S. and N. Shiraishi (eds.) (1990). *Wood and Cellulosic Chemistry*. Marcel Dekker, Inc., New York.

Hopkins, D. A. and C. C. Chamis (1988). A unique set of micromechanics equations for high temperature metal matrix composites. In: DiGiovanni, P. R. and N. R. Adsit (eds.), *Testing Technology of Metal Matrix Composites*, volume 964 of *ASTM STP*, pages 159–176. American Society for Testing and Materials, Philadelphia, PA.

Hori, M. and S. Nemat-Nasser (1993). Double-inclusion model and overall moduli of multi-phase composites. *Mech. Mater.*, 14:189–206.

— (1999). On two micromechanics theories for determining micro-macro relations in heterogenous solids. *Mechanics of Materials*, 31:667–682.

Hotchkiss, Jr., A. T. (1989). Cellulose biosynthesis. In: Lewis and Paice (1989),

chapter 17, pages 232–247.

Houtman, C. J. and R. H. Atalla (1995). Cellulose-lignin interactions: a computational study. *Plant Physiology*, 107:977–984.

Howard, C. J. and E. H. Kisi (1999). Measurement of single-crystal elastic constants by neutron diffraction from polycrystals. *Journal of Applied Crystallography*, 32(4):624–633.

Hu, G. K. and G. J. Weng (2000). The connections between the double-inclusion model and the Ponte Castaneda-Willis, Mori-Tanaka, and Kuster-Toksoz models. *Mechanics Of Materials*, 32:495–503.

Huang, C.-L. (1995). Revealing Fibril Angle in Wood Sections by Ultrasonic Treatment. *Wood and Fiber Science*, 27(1):49–54.

Huang, C.-L., N. P. Kutscha, G. J. Leaf, and R. A. Megraw (1998). Comparison of microfibril angle measurement techniques. In: Butterfield, B. G. (ed.), *Microfibril Angle in Wood*. IAWA/IUFRO.

Hughes, P. C. (1986). *Spacecraft Attitude Dynamics*. John Wiley & Sons, Inc., New York.

Hult, J. and F. G. Rammerstorfer (eds.) (1994). *Engineering Mechanics of Fibre Reinforced Polymers and Composite Structures*. Number 348 in International Centre for Mechanical Sciences. Courses and Lectures. Springer Verlag.

Ifju, G. (1964). Tensile Strength Behavior as a Function of Cellulose in Wood. *Forest Products Journal*, 14(8):366–372.

Iiyama, K., T. B. T. Lam, and B. A. Stone (1994). Covalent cross-links in the cell wall. *Plant Physiol.*, 104:315–320.

Imamura, Y., H. Harada, and H. Saiki (1972). Electron microscopic study on the formation and organization of the cell wall in coniferous tracheids : crisscrossed and transition structures in the secondary wall. *Bulletin of the Kyoto University Forests*, (44):183–193.

Irvine, G. M. (1984). The glass transition temperature of lignin and hemicellulose and their measurement by differential thermal analysis. *Tappi*, 67(5):118–121.

Ivanov, V. and M. Trubetskov (1995). *Handbook of conformal mapping with computer-aided visualization*. CRC Press.

Jakob, H. F., D. Fengel, S. E. Tschegg, and P. Fratzl (1995). The elementary cellulose fibril in Picea abies: comparison of transmission electron microscopy, small-angle X-ray scattering, and wide-angle X-ray scattering results. *Macromolecules*, 28(26):8782–8787.

Jakob, H. F., P. Fratzl, and S. E. Tschegg (1994). Size and Arrangement of Elementary Cellulose Fibrils in Wood Cells: A Small-Angle X-Ray Scattering Study of *Picea abies*. *Journal of Structural Biology*, 113:13–22.

Jane, F. W. (1970). *The Structure of Wood*. Adam & Charles Black, London, second

edition.

Jang, H. F. (1998). Measurement of fibril angle in wood fibres with polarization confocal microscopy. *Journal of Pulp and Paper Science*, 24(7):224–230.

Jansen, S., E. Smets, and P. Baas (1998). Vestures in woody plants: a review. *IAWA Journal*, 19(4):347–382.

Jawson, M. A., P. P. Gillis, and R. E. Mark (1968). The Elastic Constants of Crystalline Native Cellulose. *Proceedings of the Royal Society, London*, A306:389–412.

Jinxing, L. (1989). Distribution, Size and Effective Aperture Area of the Inter-tracheid Pits in the Radial Wall of Pinus Radiata Tracheids. *IAWA Bulletin n.s.*, 10(1):53–58.

Jones, R. M. (1999). *Mechanics of composite materials*. Taylor & Francis, second edition.

Jr., W. A. C. and T. E. Timell (1967). Studies on Larch arabinogalactan. III. Distribution of arabinogalactan in Tamarack. *Tappi*, 50(6):285–9.

Jurasek, L. (1995). Toward a three-dimensional model of lignin structure. *Journal of Pulp and Paper Science*, 21(8):J274–J279.

— (1996). Morphology of Computer-Modeled Lignin Structure - Fractal Dimensions, Orientation and Porosity. *Journal of Pulp and Paper Science*, 22(10):J376–J380.

— (1998a). Experimenting with virtual lignins. In: Lewis and Sarkanen (1998), chapter 19, pages 276–293.

— (1998b). Molecular modelling of fibre walls. *Journal of Pulp and Paper Science*, 24(7):209–212.

Kahle, E. and J. Woodhouse (1994). The Influence of Geometry on the Elasticity of Softwood. *Journal of Materials Science*, 29:1250–1259.

Kalamkarov, A. L. (1992). *Composite and reinforced elements of construction*. Wiley, New York.

Kalamkarov, A. L. and A. G. Kolpakov (1997). *Analysis, Design and Optimization of Composite Structures*. John Wiley & Sons, Chichester.

Kamiński, M. and M. Kleiber (2000). Numerical homogenization of N-component composites including stochastic interface defects. *International Journal for Numerical Methods in Engineering*, 47:1001–1027.

Kantola, M. and H. Kähkönen (1963). Small-angle X-ray investigations of the orientation of crystallites in Finnish coniferous and deciduous wood fibres. *Annales Academique Scientarium Fennicae Series A VI Physica*, 137:1–14.

Kataoka, Y. and T. Kondo (1998). FT-IR microscopic analysis of changing cellulose crystalline-structure during wood cell-wall formation. *Macromolecules*, 31(3):760–764.

Kataoka, Y., H. Saiki, and M. Fujita (1992). Arrangement and superimposition of cellulose microfibrils in the secondary walls of coniferous tracheids. *Mokuzai Gakkaishi*, 38(4):327–335.

Keegstra, K., K. W. Talmadge, W. D. Bauer, and P. Albersheim (1973). The structure of plant cell walls. III. A model of the walls of suspension-cultured Sycamore cells based on the interconnections of the macromolecular components. *Plant Physiology*, 51(1):188–196.

Keith, C. T. (1971). Observations on the anatomy and fine structure of the trabeculae of Sanio. *IAWA Bulletin*, (3):3–11.

— (1975). Tangential wall thickenings in conifer tracheids at ray-contact areas. *Wood and Fiber*, 7:129–135.

Kelley, S. S., T. G. Rials, and W. G. Glasser (1987). Relaxation behaviour of the amorphous components of wood. *J. Mater. Sci.*, 22:617–624.

Kellogg, R. M., C. B. R. Sastry, and R. W. Wellwood (1975). Relationships Between Cell-wall Composition and Cell-wall Density. *Wood and Fiber*, 7(3):170–177.

Kerr, A. J. and D. A. I. Goring (1975). The ultrastructural arrangement of the wood cell wall. *Cellulose Chemistry and Technology*, 9:563–573.

Khalili, S., T. Nilsson, and G. Daniel (2001). The use of soft rot fungi for determining the microfibrillar orientation in the S2 layer of pine tracheids. *Holz als Roh- und Werkstoff*, 58(6):439–447.

Kibblewhite, R. P. and D. Brookes (1976). Distribution of Chemical Components in the Walls of Kraft and Bisulphite Pulp Fibres. *Wood Science and Technology*, 10:39–46.

Kibblewhite, R. P. and N. S. Thompson (1973). The Ultrastructure of the Middle Lamella Region in Resin Canal Tissue Isolated from Slash Pine Holocellulose. *Wood Science and Technology*, 7:112–126.

Kim, D. Y., Y. Nishiyama, M. Wada, S. Kuga, and T. Okano (2001). Thermal decomposition of cellulose crystallites in wood. *Holzforschung*, 55(5):521–524.

Kininmonth, J. A. and L. J. Whitehouse (eds.) (1991). *Properties and Uses of New Zealand Radiata Pine. Volume One - Wood Properties*. Forest Research Institute, Rotorua, New Zealand.

Kisi, E. H. and C. J. Howard (1998). Elastic constants of tetragonal zirconia measured by a new powder diffraction technique. *Journal of the American Ceramic Society*, 81(6):1682–1684.

Kobayashi, Y. (1952). A simple method for the preparation of samples for measurement of inclination of micelle in the wood cell wall. *J. Jap. For. Society*, 34(12).

Kollmann, F. F. P. and W. A. Côté (1968). *Principles of Wood Science and Technology. Vol 1: Solid Wood*. Springer-Verlag, Berlin.

Koponen, S., T. Toratti, and P. Kanerva (1987). Puun mekaanisten ominaisuuksien mallittamisen perusteet (Modelling mechanical properties of wood). Talonrakennustekniikan Laboratorio, Julkaisu/Report 4, Helsinki University of Technology, Espoo, Finland.

— (1989). Modelling longitudinal elastic and shrinkage properties of wood. *Wood*

Science and Technology, 23(1):55–63.

— (1991). Modelling elastic and shrinkage properties of wood based on cell structure. *Wood Science and Technology*, 25(1):25–32.

Koran, Z. (1977). Tangential pitting in Black Spruce tracheids. *Wood Science and Technology*, 11(2):115–123.

Kröner, E. (1972). *Statistical continuum mechanics*. Springer, Berlin.

— (1981). Linear properties of random media – the systematic theory. In: Huet, C. and A. Zaoui (eds.), *Rheological behaviour and structure of materials*, pages 15–40. Presses EPNC.

Kroon-Batenburg, L. M. J., J. Kroon, and M. G. Northolt (1986). Chain modulus and intramolecular hydrogen bonding in native and regenerated cellulose fibres. *Polymer Communications*, 27:290–192.

— (1990). Theoretical studies on $\beta(1rightarrow4)$ glucose oligomers as models for native and regenerated cellulose fibres. *Das Papier*, 44:640–647.

Kroon-Batenburg, L. M. J., P. H. Kruiskamp, J. F. G. Vliegenthart, and J. Kroon (1997). Estimation of the persistence length of polymers by MD simulations on small fragments in solution - application to cellulose. *Journal of Physical Chemistry B*, 101(42):8454–8459.

Kubler, H. (1973). Role of moisture in hygrothermal recovery of wood. *Wood Science*, 5(3):198–204.

Kuo, M. L. and F. G. Manwiller (1986). Morphological and Chemical Characteristics of the Warty Layer in Red Pine (Pinus resinosa Ait). *Wood and Fiber Science*, 18(2):239–247.

Kuster, G. T. and M. N. Toksöz (1974). Velocity and attenuation of seismic waves in two-phase media: I. Theoretical formulation. *Geophysics*, 39:587–606.

Kwei, T. K. (1984). The effect of hydrogen bonding on the glass transition temperatures of polymer mixtures. *J. Polymer Sci., Polym. Lett.*, 22:307–313.

Ladell, J. L. (1967). Ray thickenings in the walls of conifer tracheids. *Nature, Lond.*, 213(5075):470–3.

Lai, W. M., D. Rubin, and E. Krempl (1993). *Introduction to Continuum Mechanics*. Pergamon Press Ltd., Oxford, 3rd edition.

Lakes, R. (1993). Materials with structural hierarchy. *Nature*, 361(6412):511–515.

— (1995). On the torsional properties of single osteons. *J. Biomechanics*, 28:1409–1410.

Laming, P. B. and B. J. H. ter. Welle (1971). Anomalous tangential pitting in *Picea abies*[Karst.] (European spruce). *IAWA Bulletin*, (4):3–10.

Larsen, M. J., J. E. Winandy, and F. G. III (1995). A proposed model of the tracheid cell wall of southern yellow pine having an inherent structure in the S2 layer. *Material und Organismen*, 29:197–210.

Larson, P. R. (1966). Changes in chemical composition of wood cell walls associated

with age in Pinus resinosa. *Forest Products Journal*, 16(4):37–45.

Lawrence, E. (1989). *Henderson's dictionary of biological terms*. Longman Scientific & Technical, Longman Group UK Ltd., Longman House, Burnt Mill, Harlow, Essex CM20 2JE, England, 10th edition.

Leney, L. (1981). A technique for measuring fibril angle using polarised light. *Wood and Fiber*, 13(1):13.

Levin, V. M. (1967). ? *Mech. Solids*, 2:58.

Lewin, M. and I. S. Goldstein (eds.) (1991). *Wood structure and composition*. Marcel Dekker, Inc., New York.

Lewis, N. G. (1999). A 20th century roller coaster ride: a short account of lignification. *Current Opinion in Plant Biology*, 2(2):153–162.

Lewis, N. G. and G. P. Bolwell (2001). Special issues devoted to the biosynthesis of woody plant biopolymers and related substances. *Phytochemistry*, 57(6):803–804.

Lewis, N. G., L. B. Davin, and S. Sarkanen (1999). The nature and function of lignins. In: Pinto (1999), chapter 3.18, pages 617–745.

Lewis, N. G. and M. G. Paice (eds.) (1989). *Plant cell wall polymers : biogenesis and biodegradation*. Number 399 in ACS symposium series. American Chemical Society.

Lewis, N. G. and S. Sarkanen (eds.) (1998). *Lignin and lignan biosynthesis*. Number 697 in ACS symposium series. American Chemical Society, Washington, DC.

Li, J. Y. (1999). On micromechanics approximation for the effective thermoelastic moduli of multi-phase composite materials. *Mechanics of Materials*, 31:149–159.

Liang, C. Y., K. H. Bassett, E. A. McGinnes, and R. H. Marchessault (1960). Infrared Spectra of Crystalline Polysaccharides. VII: Thin Wood Sections. *Tappi*, 43(12):1017–1024.

Liang, C. Y. and R. H. Marchessault (1959). Infrared spectra of crystalline polysaccharides. I. Hydrogen bonds in native cellulose. *Journal of Polymer Science*, 37:385–395.

Libby, T. B. and J. G. Haygreen (1967). Moisture content change induced by tensile stress in whole wood. *J. Inst. Wood Sci.*, 18:54–60.

Lichtenegger, H., M. Müller, O. Paris, C. Riekel, and P. Fratzl (1999). Imaging of the helical arrangement of cellulose fibrils in wood by synchrotron X-ray microdiffraction. *Journal of Applied Crystallography*, 32(6):1127–1133.

Lichtenegger, H., A. Reiterer, S. Tschegg, and P. Fratzl (1998). Determination of spiral angles of elementary fibrils in the wood cell wall: comparison of small angle x-ray scattering and wide angle x-ray diffraction. In: Butterfield, B. G. (ed.), *Microfibril Angle in Wood*. IAWA/IUFRO.

Liese, W. (1963). Tertiary wall and warty layer in wood cells. *J. Polymer Sci. Part C.*, 2:213–229.

— (1965). The warty layer. In: Côté, W. A. (ed.), *Cellular Ultrastructure of Woody Plants*, pages 251–269. Syracuse University Press, Syracuse, N. Y.

Loewus, F. and V. C. Runeckles (eds.) (1977). *The Structure, Biosynthesis, and Degradation of Wood*. Recent advances in phytochemistry ; v. 11. Plenum Press, New York.

Long, J. M., A. B. Conn, W. J. Batchelor, and R. Evans (2000). Comparison of methods to measure fibril angle in wood fibres. *Appita Journal*, 53:206–209.

Lyons, W. J. (1958). Theoretical values of the dynamic stretch modulus of fiber-forming polymers. *J. Appl. Phys.*, 29:1429–1433.

— (1959). Theoretical value of the dynamic stretch moduli of cellulose. *J. Appl. Phys.*, 30:796–797.

Maeda, Y., T. Awano, K. Takabe, and M. Fujita (2000). Immunolocalization of glucomannans in the cell wall of differentiating tracheids in Chamaecyparis obtusa. *Protoplasma*, 213(3-4):148–156.

Maekawa, T., M. Fuijita, and H. Saiki (1993). Characterisation of cell arrangement by polar coordinate analysis of power spectral patterns. *J. Soc. Mat. Sci. Japan*, 42(473):126–131.

Malvern, L. E. (1969). *Introduction to the Mechanics of a Continuous Medium*. Prentice-Hall, Inc.

Manwiller, F. G. (1966). Sénarmont compensation for determining fibril angles of cell wall layers. *Forest Products Journal*, 16(10):26–30.

Marhöfer, R. J., S. Reiling, and J. Brickmann (1996). Computer simulations of crystal structures and elastic properties of cellulose. *Berichte der Bunsen Gesellschaft fur Physikalische Chemie-An International Journal of Physical Chemistry*, 100(8):1350–4.

Mark, R. E. (1965). Tensile Stress Analysis of the Cell Walls of Coniferous Tracheids. In: Côté (1965), pages 493–533.

— (1967). *Cell wall mechanics of tracheids*. Yale University Press., New Haven, CT.

— (1972). Mechanical behavior of the molecular components of fibers. In: Jayne, B. A. (ed.), *Theory and Design of Wood and Fiber Composite Materials*, Syracuse Wood Science Series, chapter 3, pages 49–82. Syracuse University Press, Syracuse, New York.

— (1980). Molecular and cell wall structure of wood. *J. Educ. Modules Mater. Sci. Engrg.*, 2(2):251–308.

Mark, R. E. and K. Murakami (eds.) (1983). *Handbook of Physical and Mechanical Testing of Paper and Paperboard: Vol. 1*. Marcel Dekker, Inc., New York.

Marts, R. O. (1955). Fluorescence microscopy for measuring fibril angles in pine tracheids. *Stain Technol.*, 30(5):243–248.

Matsumura, J. and B. G. Butterfield (2001). Microfibril angles in the root wood of *Pinus radiata* and *Pinus nigra*. *IAWA Journal*, 22(1):57–62.

Maurer, A. and D. Fengel (1991). Electron microscope representation of structural details in softwood cell walls by very thin ultramicrotome sections. *Holz als Roh-*

und Werkstoff, 49(2):53–56.

— (1992). On the origin of milled wood lignin. Part 1. The influence of ball-milling on the ultrastructure of wood cell walls and the solubility of lignin. *Holzforschung*, 46(5):417–423.

McCann, M., B. Wells, and K. Roberts (1990). Direct visualization of crosslinks in the primary plant cell wall. *J. Cell Sci.*, 96:323–334.

McCann, M. C., M. Bush, D. Milioni, P. Sado, N. J. Stacey, G. Catchpole, M. Defernez, N. C. Carpita, H. Hofte, P. Ulvskov, R. H. Wilson, and K. Roberts (2001). Approaches to understanding the functional architecture of the plant cell wall. *Phytochemistry*, 57(6):811–821.

McCann, M. C. and K. Roberts (1991). Architecture of the primary cell wall. In: Lloyd, C. W. (ed.), *The cytoskeletal basis of plant growth and form*, pages 109–129. Academic Press.

McEwan, M. I., J. J. Harrington, and M. D. Pugh (1998). Comparison of the directional elastic modulus of Pinus radiata with orthotropic theory. *Journal of the Institute of Wood Science*, 14(6):272–276.

McGinnis, G. D. and F. Shafizadeh (1991). Cellulose. In: Lewin and Goldstein (1991), chapter 4, pages 139–181.

McIntosh, D. C. (1965). Wall structure of loblolly pine summerwood holocellulose fibers in relation to individual fiber strength. In: Côté (1965), pages 561–573.

Mehrabadi, M. M. and S. C. Cowin (1990). Eigentensors of Linear Anisotropic Elastic Materials. *Quarterly Journal of Mechanics and Applied Mathematics*, 43(1):15–41.

Meier, H. (1961). The distribution of polysaccharides in wood fibres. *J. Polym. Science*, 51:11–18.

— (1964). General chemistry of cell-walls and distribution of chemical constituents across the walls. In: Zimmermann (1964).

— (1985). Localization of polysaccharides in wood cell walls. In: Higuchi, T. (ed.), *Biosynthesis and Biodegradation of Wood Components*, pages 43–62. Academic Press, Orlando.

Meier, H. and K. C. B. Wilkie (1959). The distribution of polysaccharides in the cell-wall of tracheids of pine (Pinus silvestris L.). *Holzforschung*, 13:177–182.

Meredith, R. (1951). On the technique of measuring orientation in cotton by X-rays. *J. Textile Inst.*, 42:T275–290.

— (1956). Dynamic mechanical properties. In: Meredith, R. (ed.), *The Mechanical Properties of Textile Fibres*, pages 106–128. Interscience, New York.

— (1959). Mechanical properties of cellulose and cellulose derivatives. In: Honeyman, J. (ed.), *Recent Advances in the Chemistry of Cellulose and Starch*, pages 213–239. Interscience, New York.

Meyer, K. H. (1942). *Natural and Synthetic High Polymers*. Interscience, New York.

Meyer, K. H. and W. Lotmar (1936). Sur l'élasticité de la cellulose. *Helv. Chim. Acta*, 19:68–86.

Meylan, B. A. (1967). Measurement of Microfibril Angle By X-ray Diffraction. *Forest Products Journal*, 17(5):51–58.

— (1968). On the cause of high longitudinal shrinkage in wood. *Forest Products Journal*, 18:75–78.

— (1972). The influence of microfibril angle on the longitudinal shrinkage-moisture content relationship. *Wood Science and Technology*, 6(4):293–301.

Meylan, B. A. and B. G. Butterfield (1972). Scanning Electron Micrographs of New Zealand woods 1. *Entelea arborescens*R. Br. *New Zealand Journal of Botany*, 10:437–446.

— (1978). Helical orientation of the microfibrils in tracheids, fibres and vessels. *Wood Science and Technology*, 12(3):219–222.

Michel, J. C., H. Moulinec, and P. Suquet (1999). Effective properties of composite materials with periodic microstructure: a computational approach. *Comp. Meth. Applied Mech. Engng.*, 172:109–143.

— (2000). A computational method based on augmented Lagrangians and fast Fourier transforms for composites with high contrast. *Comp. Modeling in Engng. and Sci.*, 1:79–88.

Michel, J. C. and P. Suquet (1998). A numerical method for computing the overall response of nonlinear composites with complex microstructure. *Comp. Meth. Applied Mech. Engng.*, 157:69–94.

Millane, R. P. (1998). The ups and downs of native cellulose structure. *Fibre Diffraction Review. The CCP13 Newsletter*, Issue 7.

Millane, R. P. and T. L. Hendrixson (1994). Crystal structures of mannan and glucomannans. *Carbohydrate Polymers*, 25:245–251.

Milne-Thomson, L. M. (1968). *Theoretical Hydrodynamics*. Dover, 5th edition. Unabridged republication of the 1974 printing of the 5th edition (1968).

Miniutti, V. P. (1964). Microscale changes in cell structure at softwood surfaces during weathering. *Forest Products Journal*, 14(12):571–6.

Miyakawa, M., M. Fujita, H. Saiki, and H. Harada (1973). The cell-wall structure of the secondary phloem elements in *Cryptomeria japonica*D. Don. *Bulletin of the Kyoto University Forests*, (45):181–191.

Moon, P. and D. E. Spencer (1971). *Field theory handbook: including coordinate systems, differential equations and their solutions*. Springer-Verlag, Berlin, 2nd edition.

Mori, T. and K. Tanaka (1973). Average stress in matrix and average elastic energy of materials with misfitting inclusions. *Acta Metall.*, 21:571–574.

Muller-Stoll, W. R. and G. Casperson (1987). Electron microscope studies of intracellular bars (trabeculae) in the wood of Larix and Juniperus. *Kulturpflanze*, 35:441–452.

Mura, T. (1987). *Micromechanics of Defects in Solids*. Martinus Nijhoff.

Naciri, T., P. Navi, and A. Ehrlacher (1994a). Harmonic wave propagation in viscoelastic heterogenous materials. Part I: dispersion and damping relations. *Mechanics of Materials*, 18(4):313–333.

— (1994b). Harmonic wave propagation in viscoelastic heterogenous materials. Part II : Effective complex moduli. *Mechanics of Materials*, 18(4):335–350.

Nakashima, J., T. Mizuno, K. Takabe, M. Fujita, and H. Saiki (1997). Direct Visualization of Lignifying Secondary Wall Thickenings in Zinnia-Elegans Cells in Culture. *Plant and Cell Physiology*, 38(7):818–827.

Navi, P. (1988). Three dimensional analysis of the wood microstructural influences on wood elastic properties. In: Itani, R. Y. (ed.), *Proceedings of the 1988 International Conference on Timber Engineering. Westin Hotel, Seattle, Washington, September 19-22 1988*, volume 2, page 915. Forest Products Research Society. Madison, Wis.

Navi, P. and C. Huet (1989). A three dimensional multilevel technique to study the influence of the fiber microstructure on wood macroscopic elastic properties. In: *The Third Joint ASCE/ASME Mechanics Conference. University of California, San Dieago, La Jolla, July 9-12, 1989*, volume 99 of *AMD (Symposia Series) (American Society of Mechanical Engineers, Applied Mechanics Division)*, pages 61–67.

Negi, A. (1999). Turbulence in the wood system with small and short stresses. *Wood Science and Technology*, 33(3):209–214.

Nemat-Nasser, S. and M. Hori (1993). *Micromechanics: Overall Properties of Heterogenous Materials*, volume 37 of *Applied Mathematics and Mechanics*. North-Holland, Amsterdam.

Nemat-Nasser, S., T. Iwakuma, and M. Hejazi (1982). On composites with periodic microstructure. *Mechanics of Materials*, 1:239–267.

Neville, A. C. (1993). *Biology of Fibrous Composites - Development Beyond the Cell Membrane*. Cambridge University Press, Cambridge.

Neville, A. C. and S. Levy (1985). The helicoidal concept in plant cell wall ultrastructure and morphogenesis. In: Brett, C. T. and J. R. Hillman (eds.), *Biochemistry of Plant Cell Walls*, pages 99–124. Cambridge University Press, Cambridge.

Newman, R. (1998). How stiff is an individual cellulose microfibril? In: Butterfield, B. G. (ed.), *Microfibril Angle in Wood*. IAWA/IUFRO.

Newman, R. H. (1992). Nuclear Magnetic Resonance Study of the Spatial Relationships Between Chemical Components in Wood Cell Walls. *Holzforschung*, 46(3):205–210.

— (1994). Crystalline forms of cellulose in softwoods and hardwoods. *Journal of Wood Chemistry and Technology*, 14(3):451–466.

— (1999a). Estimation of the lateral dimensions of cellulose crystallites using C-13 NMR signal strengths. *Solid State Nuclear Magnetic Resonance*, 15:21–29.

— (1999b). Estimation of the relative proportions of cellulose I_α and I_β in wood by

carbon-13 spectroscopy. *Holzforschung*, 53(4):335–340.

Newman, R. H., L. M. Davies, and P. J. Harris (1996). Solid-state C-13 nuclear magnetic resonance characterization of cellulose in the cell walls of Arabidopsis thaliana leaves. *Plant Physiology*, 111:475–485.

Newman, R. H., J. A. Hemmingson, and I. D. Suckling (1993). Carbon-13 nuclear magnetic resonance studies of kraft pulping. *Holzforschung*, 47:234–238.

Nicholls, J. W. P. (1982). Wind Action, Leaning Trees and Compression Wood in *Pinus radiata*D. Don. *Australian Forest Research*, 12(2):75–91.

Nielsen, L. E. and R. F. Landel (1994). *Mechanical properties of polymers and composites*. M. Dekker, 2nd edition.

Nishino, T., K. Takano, and K. Nakamae (1995). Elastic modulus of the crystalline regions of cellulose polymorphs. *Journal of Polymer Science: Part B: Polymer Physics*, 33(11):1647–1651.

Nissan, A. H. (1987). Unified theory of the mechanical properties of paper and other H-bond-dominated solids - Part II. *Tappi*, 70(10):128–131.

Nissan, A. H. and G. L. Batten, Jr. (1997). The link between the molecular and structural theories of paper elasticity. *Tappi*, 80(4):153–158.

Nomura, T. and T. Yamada (1972). Structural observation on wood and bamboo by X-ray. *Wood Research*, (52):1–12.

Norimoto, M., S. Hayashi, and T. Yamada (1978). Anisotropy of dielectric constant in coniferous wood. *Holzforschung*, 32(5):167–172.

Norris, A. N. (1985). A differential scheme for the effective medium approximation for multiphase composites. *Mech. Mater.*, 4:1–16.

Northcote, D. H., R. Davey, and J. Lay (1989). Use of antisera to localize callose, xylan and arabinogalactan in the cell-plate, primary and secondary walls of plant cells. *Planta*, 178:353–366.

Northolt, M. G. and H. de Vries (1985). Tensile deformation of regenerated and native cellulose fibres. *Angewandte Makromol. Chem.*, 113:183–203.

Nowick, A. S. (1995). *Crystal Properties Via Group Theory*. Cambridge University Press.

Nye, J. F. (1957). *Physical Properties of Crystals*. Clarendon Press, Oxford.

Ogniewicz, R. L. (1992). *Discrete Voronoi Skeletons*. Ph.D. thesis, Swiss Federal Institute of Technology.

Ohta, S., S. Hata, M. Fujita, and H. Saiki (1992). Measurement of fibril angles in mature wood of sugi (Cryptomeria japonica D. Don) - a polarizing microscopic method on splitted sections and an x-ray diffraction method on pressed sections. *Bulletin of the Kyoto University Forests*, 64:181–191.

Ohtani, J., K. Fukazawa, and T. Fukumorita (1987). SEM observations on indented rings. *IAWA Bulletin*, 8(2):113–124.

Ohtani, J., B. A. Meylan, and B. G. Butterfield (1984). Vestures or warts - proposed terminology. *IAWA Bulletin*, 5(1):3–8.

Okabe, A., B. Boots, and K. Sugihara (1992). *Spatial Tessellations: Concepts and Applications of Voronoi Diagrams*. John Wiley & Sons, Ltd., Chichester.

Okamura, K. (1990). Structure of Cellulose. In: Hon and Shiraishi (1990), chapter 3, pages 89–112.

Okano, T. (1972). On the possibility of plane orientation of micells in the cell wall of wood. *Mokuzai Gakkaishi*, 18(12):583–585.

Okumura, S., H. Harada, and H. Saiki (1974). The variation in the cell wall thickness along the length of a conifer tracheid. *Bulletin of the Kyoto University Forests*, 46:162–169.

— (1976). Thickness variation of the secondary wall layers along a differentiating latewood tracheid in Pinus densiflora. *Mokuzai Gakkaishi*, 22(10):543–549.

Oleinik, O. A., A. S. Shamaev, and G. A. Yosifan (1992). *Mathematical problems in elasticity and homogenization*. North Holland, Amsterdam.

Olsson, A.-M. and L. Salmén (1997). Humidity and temperature affecting hemicellulose softening in wood. In: *International Conference of COST Action E8, Mechanical Performance of Wood and Wood Products, Theme: Wood-water relations, Copenhagen, Denmark, June 16-17, 1997*.

Ormarsson, S., O. Dahlblom, and H. Petersson (1998). A numerical study of the shape stability of sawn timber subjected to moisture variation. *Wood Science and Technology*, 32(5):325–334.

O'Sullivan, A. (1997). Cellulose: the structure slowly unravels. *Cellulose*, 4(3):173–207.

Oudjehane, A. and J. Raclin (1995). Behavior of oakwood in a general state of stress. *Wood Science and Technology*, 29:1–11.

Paakkari, T. and R. Serimaa (1984). A study of the structure of wood cells by X-ray diffraction. *Wood Science and Technology*, 18(2):79–85.

Page, D. H. (1969). A method for determining the fibrillar angle in wood tracheids. *Journal of Microscopy*, 90(2):137–43.

— (1976). A Note on the Cell Wall Structure of Softwood Tracheids. *Wood and Fiber*, 7(4):246–248.

Page, D. H. and J. H. DeGrace (1967). The delamination of fibre walls by beating and refining. *Tappi*, 50:489–495.

Page, D. H. and F. El-Hosseiny (1974). The birefringence of wood pulp fibres and the thickness of the S1 and S3 layers. *Wood and Fiber*, 6(3):186–192.

Painter, P. C. and M. M. Coleman (1997). *Fundamentals of Polymer Science*. Technomic, second edition.

Paley, M. and J. Aboudi (1992). Micromechanical analysis of composites by the generalized cells method. *Mechanics of Materials*, 14:127–139.

Pang, S. (2001). Modelling of stresses and deformation of radiata pine lumber during drying. In: *7th International IUFRO Wood Drying Conference – 2001*, pages 238–245.

Panshin, A. J. and C. de Zeeuw (1980). *Textbook of Wood Technology*. McGraw-Hill Book Company, New York, 4th edition.

Parameswaran, N. and W. Liese (1982). Ultrastructural Localisation of Wall Components in Wood Cells. *Holz als Roh- und Werkstoff*, 40:145–155.

Parkus, H. (1968). *Thermoelasticity*. Blaisdell Publishing.

Patel, R. N. (1971). Anatomy of stem and root wood of *Pinus radiata* D. Don. *New Zealand Journal of Forestry Science*, 1(1):37–49.

Patscheke, G. and S. Poller (1980). ? *Cell. Chem. Technol.*, 14:3.

Perré, P. (2001). Wood as a multi-scale porous medium: observation, experiment and modelling. In: *Proccedings of the First International Conference of the European Society for Wood Mechanics. April 19-21, 2001 Ecole Polytechnique Fédérale de Lausanne (Swiss Federal Institute of Technology)*, pages 403–422.

Persson, K. (1997). Modelling of wood properties by a micromechanical approach. Report TVSM-3020, Lund University, Lund Institute of Technology, Division of Structural Mechanics.

— (2000). *Micromechanical modelling of wood and fibre properties*. Ph.D. thesis, Department of Mechanics and Materials, Division of Structural Mechanics, Lund University, Sweden.

Persson, L. E., L. Persson, N. Svanstedt, and J. Wyller (1993). *The Homogenization Method : An Introduction*. Studentlitteratur, Lund, Sweden.

Pillow, M. Y., B. Z. Terrell, and C. H. Hiller (1953). Patterns of variation in fibril angles in Loblolly Pine. Technical Report D1935, U.S. For. Prod. Lab., Madison.

Pinto, B. M. (ed.) (1999). *Comprehensive natural products chemistry*, volume 3. Elsevier, Amsterdam.

Pizzi, A. (1989). The Structure of Cellulose I Parallel Model by Conformational Analysis. *Holzforschung und Holzverwertung*, 41(2):31–33.

Pizzi, A., M. Bariska, and N. J. Eaton (1987a). Theoretical water sorption energies by conformational analysis. Part 2: amorphous cellulose and the sorption isotherm. *Wood Science and Technology*, 21(4):317–327.

Pizzi, A., N. J. Eaton, and M. Bariska (1987b). Theoretical water sorption energies by conformational analysis. Part 1: crystalline cellulose I. *Wood Science and Technology*, 21(3):235–248.

Pleasants, S., W. J. Batchelor, and I. H. Parker (1998). Measuring the fibril angle of bleached fibres using micro-Raman spectroscopy. *Appita*, 51(5):373–376.

Pochiraju, K. and T. W. Chou (1999). Three-dimensionally woven and braided composites. I: A model for anisotropic stiffness prediction. *Polymer Composites*, 20(4):565–

580.

Ponte Castaneda, P. and J. R. Willis (1995). The effect of spatial distribution on the effective behavior of composite materials and cracked media. *J. Mech. Phys. Solids*, 43:1919–1951.

Press, W. H., B. P. Flannery, S. A. Teukolsky, and W. T. Vetterling (1989). *Numerical Recipes*. Cambridge University Press.

Preston, R. D. (1934). The organization of the cell wall of the conifer tracheid. *Philosophical Transactions of the Royal Society, London. Series B*, 224:131–172.

— (1946). The fine structure of the walls of the conifer tracheid. I. The X-ray diagram of conifer wood. *Proc. Roy. Soc. B*, 133(872):327.

— (1964). Structural and Mechanical Aspects of Plant Cell Walls with Particular Reference to Synthesis and Growth. In: Zimmermann (1964).

— (1974). *The Physical Biology of Plant Cell Walls*. Chapman & Hall, London.

— (1986). Natural celluloses. In: Young, R. A. and R. M. Rowell (eds.), *Cellulose: structure, modification and hydrolysis*, chapter 1, pages 3–27. Wiley, New York.

Price, A. T. (1928). A mathematical discussion on the structure of wood in relation to its elastic properties. *Phil. Trans. Roy. Soc., London*, 228 A:1–62.

Prud'homme, R. E. and J. Noah (1975). Determination of fibril angle distribution in wood fibers: A comparison between the X-ray diffraction and the polarized microscope methods. *Wood and Fiber*, 6(4):282–289.

Rammerstorfer, F. G. and H. J. Böhm (1994). Micromechanics for macroscopic material description of FRPs. In: Hult and Rammerstorfer (1994), chapter 2.

Rammerstorfer, F. G., A. F. Plankensteiner, F. D. Fischer, and T. Antretter (1999). Hierarchical models for simulating the mechanical behavior of heterogeneous materials: an approach to high speed tool steel. *Materials Science and Engineering A-Structural Materials Properties Microstructure and Processing*, 259(1):73–84.

Rawat, S. P. S. and D. P. Khali (1999). Studies on adsorption behaviour of water vapour in lignin using the Brunauer-Emmett-Teller theory. *Holz als Roh- und Werkstoff*, 57(3):203–204.

Rawat, S. P. S., D. P. Khali, M. D. Hale, and M. C. Breese (1998). Studies on the moisture adsorption behaviour of brown rot decayed and undecayed wood blocks of pinus sylvestris using the brunauer-emmett-teller theory. *Holzforschung*, 52(5):463–466.

Reese, E. T. (1977). Degradation of polymeric carbohydrates by microbial enzymes. In: Loewus and Runeckles (1977), chapter 8, pages 311–368.

Reiling, S. and J. Brickmann (1995). Theoretical Investigations on the Structure and Physical Properties of Cellulose. *Macromolecular Theory and Simulation*, 4:725–743.

Reiterer, A., H. F. Jakob, S. E. Stanzltschegg, and P. Fratzl (1998). Spiral angle of elementary cellulose fibrils in cell walls of *Picea abies* determined by small-angle

x-ray scattering. *Wood Science and Technology*, 32(5):335–345.

Reiterer, A., H. Lictenegger, S. Tschegg, and P. Fratzl (1999). Experimental evidence for a mechanical function of the cellulose microfibril angle in wood cell-walls. *Philosophical Magazine A - Physics of Condensed Matter Defects & Mechanical Properties*, 79(9):2173–2184.

Reuss, A. (1929). Berechnung der Fliessgrenze von Mischkristallen auf Grund der Plastizitätsbedingung für Einkristalle. *Z. Angew. Math. Mech.*, 9:49–58.

Revol, J. F., C. Gancet, and D. A. I. Goring (1982). Orientation of cellulose crystallites in the S2 layer of spruce and birch wood cell walls. *Wood Science*, 14(3):120–126.

Rho, J. Y., L. Kuhnspearing, and P. Zioupos (1998). Mechanical properties and the hierarchical structure of bone. *Medical Engineering and Physics*, 20(2):92–102.

Richmond, P. A. (1991). Occurence and functions of native cellulose. In: Haigler, C. H. and P. J. Weimer (eds.), *Biosynthesis and Biodegradation of Cellulose*, pages 5–23. Marcel Dekker, New York.

Roe, R.-J. and W. R. Krigbaum (1964). Description of crystallite orientation in polycrystalline material having fiber texture. *The Journal of Chemical Physics*, 40(9):2608–2615.

Rogers, H. J. and H. R. Perkins (1968). *Cell Walls and Membranes*. E. & F.N. Spon Ltd., London.

Roland, J.-C. and M. Mosiniak (1983). On the twisting pattern, texture and layering of the secondary walls of limewood. Proposal of an unifying model. *IAWA Bulletin*, 4:15–26.

Roland, J. C., D. Reis, B. Vian, B. Satiat-Jeunemaitre, and M. Mosiniak (1987). Morphogenesis of Plant Cell Walls at the Supramolecular Level: Internal Geometry and Versatility of Helicoidal Expression. *Protoplasma*, 140:75–91.

Rosen, B. W. and Z. Hashin (1970). Effective thermal expansion coefficients and specific heats of composite materials. *Int. J. Eng. Sci.*, 8:157–173.

Ruben, G. C., G. H. Bokelman, and W. Krakow (1989). Triple-stranded left-hand helical cellulose microfibril in *Acetobacter xylinum* and in tobacco primary cell wall. In: Lewis and Paice (1989), chapter 20, pages 278–298.

Ruel, K., F. Barnoud, and D. A. I. Goring (1978). Lamellation in the S2 layer of softwood tracheids as demonstrated by scanning transmission electron microscopy. *Wood Science and Technology*, 12(4):287–291.

Ruel, K., V. Burlat, and J.-P. Joseleau (1999). Relationship between ultrastructural topochemistry of lignin and wood properties. *IAWA Journal*, 20(2):203–211.

Runkel, R. O. H. (1954). Sorption of wood fibres from the morphological and chemical points of view. *Holz als Roh- und Werkstoff*, 12(6):226–32.

Runkel, R. O. H. and M. Luthgens (1956). Studies on sorption by wood fibres. 2nd communication : Investigations on the differences in water sorption of the chem-

ical and morphological components of lignified cell-walls. *Holz Roh u Werkstoff*, 14(11):424–41.

Russell, W. R., A. R. Forrester, and A. Chesson (2000). Predicting the macromolecular structure and properties of lignin and comparison with synthetically produced polymers. *Holzforschung*, 54:505–510.

Sachs, I. B., I. T. Clark, and J. C. Pew (1963). Investigation of lignin distribution in the cell wall of certain woods. *J. Polymer Sci. C.*, 2:203–212.

Sadoh, T. (1959). The effect of pre-treatment on wood hemicellulose in moisture adsorption. *Mokuzai Gakkaishi*, 5(6):218–222.

— (1960). Studies on the sorption of water vapour by wood hemicellulose. II. Amount of vapour adsorbed. *Sci. Rep. Kyoto Prefect. Univ. (Agric.) No. 12,*, pages 119–23.

— (1961a). Studies on the sorption of water vapour by wood hemicellulose. III. Heat of adsorption. IV. Swelling and dissolving. *Mokuzai Gakkaishi*, 7(1):1–7.

— (1961b). Studies on the sorption of water vapour by wood hemicellulose. V. Hysteresis. *Mokuzai Gakkaishi*, 7(2):51–3.

— (1962). Study on the sorption of water vapour by softwood hemicelluloses. *Sci. Rep. Kyoto Prefect. Univ. (Agric.) No. 14,*, pages 99–105.

Sadoh, T. and S. Kadita (1957). Studies on the relations between physical properties and chemical constituents of wood. III. On the moisture adsorption of hardwood (*Fagus crenata*) hemicellulose. *Mokuzai Gakkaishi*, 3(3):100–102.

Sahlberg, U., L. Salmén, and A. Oscarsson (1997). The fibrillar orientation in the S2-layer of wood fibres as determined by X-ray diffraction analysis. *Wood Science and Technology*, 31(2):77–86.

Saiki, H. (1970). Proportion of Component Layers in Tracheid Wall of Early Wood and Late Wood of some Conifers. *Mokuzai Gakkaishi*, 16(5):244–249. Written in Japanese. Summary and tables in English.

Saiki, H., Y. J. Xu, and M. Fujita (1989). The fibrillar orientation and microscopic measurement of the fibril angles in young tracheid walls of sugi (Cryptomeria japonica). *Mokuzai Gakkaishi*, 35(9):786–792.

Saka, S. (1990). Chemical composition and distribution. In: Hon and Shiraishi (1990), pages 89–112.

Saka, S. and R. J. Thomas (1982). A study of lignification in loblolly pine tracheids by the SEM-EDXA technique. *Wood Science and Technology*, 16(3):167–179.

Sakakibara, A. (1990). Chemistry of lignin. In: Hon and Shiraishi (1990), chapter 4, pages 113–175.

Sakata, I. and R. Senju (1975). Thermoplastic behaviour of lignin with various synthetic plasticizers. *J. Appl. Polym. Sci*, 19:2799–2810.

Sakurada, I., T. Ito, and K. Nakamae (1964). ? *Makromol. Chem.*, 75:1.

— (1966). ? *J. Polym. Sci. C, Polym. Symp.*, 15:75.

Sakurada, I. and K. Kaji (1970). ? *J. Polym. Sci. C, Polym. Symp.*, 31:57.

Sakurada, I., Y. Nukushina, and T. Ito (1962). Experimental determination of the elastic modulus of crystalline regions in oriented polymers. *J. Polymer Sci*, 57:651–60.

Salmén, L. (1982). *Temperature and water induced softening behaviour of wood fiber based materials*. Ph.D. thesis, Royal Institute of Technology, Stockholm, Sweden, The Royal Institute of Technology, S-100 44 Stockholm 70, Sweden.

— (1984). Viscoelastic properties of *in situ* lignin under water-saturated conditions. *Journal of Materials Science*, 19(9):3090–3096.

— (1990). Thermal expansion of water-saturated wood. *Holzforschung*, 44(1):17–19.

— (1991). Viscoelastic properties of wood polymers. In: Salmén, L. and M. Htun (eds.), *Properties of ionic polymers natural and synthetic*, pages 285–294. STFI-Meddelande.

— (1997). The sorption behaviour of wood. In: *International Conference of COST Action E8, Mechanical Performance of Wood and Wood Products, Theme: Wood-water relations, Copenhagen, Denmark, June 16-17, 1997*.

Salmén, L. and A. de Ruvo (1985). A model for the prediction of fiber elasticity. *Wood and Fiber Science*, 17(3):336–350.

Salmén, L. and A. M. Olsson (1998). Interaction between hemicelluloses, lignin and cellulose: structure-property relationships. *Journal of Pulp and Paper Science*, 24(3):99–103.

Salmén, L. and B. Petterson (1995). The primary wall - important for fibre separation in mechanical pulping. *Cellulose Chemistry and Technology*, 29(3):331–337.

Salmén, N. L. and E. L. Back (1977). The influence of water on the glass transition temperature of cellulose. *Tappi*, 60(12):137–140.

Sanchez-Palencia, E. (1980). *Non homogenous Media and Vibration Theory*. Number 127 in Lecture Notes in Physics. Springer Verlag.

Sarkanen, K. V. and C. H. Ludwig (eds.) (1971). *Lignins: Occurrence, Formation, Structure and Reactions*. Wiley-Interscience.

Sarko, A. (1976). ? *J. Appl. Polym. Sci., Appl. Polym. Symp.*, 28:729.

Scallan, A. M. and H. V. Green (1974). A technique for determining the transverse dimensions of the fibres in wood. *Wood and Fiber*, 5(4):323–333.

Schniewind, A. P. and J. D. Barrett (1969). Cell Wall Model with Complete Shear Restraint. *Wood and Fiber*, 1(3):205–214.

Schwarze, F. W. M. R. and J. Engels (1998). Cavity formation and the exposure of peculiar structures in the secondary wall (S2) of tracheids and fibres by wood degrading basidiomycetes. *Holzforschung*, 52(2):117–123.

Schweingruber, F. H. (1978). *Microscopic Wood Anatomy*. Zürcher A. G., CH-6301 ZUG.

Seifert, J. (1972). On the sorption and swelling of wood and wood base materials – Part

3: The volume contraction between wood and water. *Holz als Roh- und Werkstoff*, 30:332–342.

Sell, J. (1994). Confirmation of a Sandwich-like Model of the Cell Wall of Softwoods by the Light Microscope. *Holz als Roh- und Werkstoff*, 52:234.

Sell, J. and T. Zimmermann (1993). Radial Fibril Agglomerations of the S2 on Transverse-fracture Surfaces of Tracheids of Tension-loaded Spruce and White Fir. *Holz als Roh- und Werkstoff*, 51:384.

Selvendran, R. R. (1985). Developments in the chemistry and biochemistry of pectic and hemicellulosic polymers. In: Roberts, K., A. W. B. Johnston, C. W. Lloyd, P. Shaw, and H. W. Woolhouse (eds.), *The Cell Surface in Plant Growth and Development*, pages 51–88. The Company of Biologists Ltd. Proceedings of the Sixth John Innes Symposium, Norwich 1984. Also published as the Journal of Cell Science Supplement 2.

Senft, J. F. and B. A. Bendtsen (1985). Measuring microfibrillar angles using light microscopy. *Wood and Fiber Science*, 17(4):564–567.

Sethian, J. A. (1999). *Level set methods and fast marching methods: evolving interfaces in computational geometry, fluid mechanics, computer vision and materials science*. Cambridge University Press, 2nd edition.

Shimizu, K. (1990). Chemistry of Hemicelluloses. In: Hon and Shiraishi (1990), chapter 5, pages 177–214.

Shumway, R. S., N. P. Kutscha, and J. E. Shottafer (1971). The relationship of fibril angle to certain factors in plantation-grown Red Pine.

Siau, J. F. (1971). *Flow in wood*. Syracuse University Press, Syracuse, N.Y.

Siddiqui, K. M. (1976). Relationship between cell wall morphology and chemical composition of earlywood and latewood in two coniferous species. *Pakistan Journal of Forestry*, 26(1):21–34.

Simson, B. W. and T. E. Timell (1978). Polysaccharides in cambial tissues of Populus tremuloides and Tilia americana. *Cellulose Chemistry and Technology*, 12(1):39–84.

Singh, A. and R. E. Booker (2000). Effect of wood structure variability on properties. Technical report.

Singh, A. P. and G. Daniel (2001). The S2 layer in the tracheid walls of Picea abies wood: Inhomogeneity in lignin distribution and cell wall microstructure. *Holzforschung*, 55(4):373–378.

Singh, A. P. and L. A. Donaldson (1999). Ultrastructure of tracheid cell walls in radiate pine (Pinus radiata) mild compression wood. *Can. J. Bot.-Rev. Can. Bot.*, 77:32–40.

Singh, A. P., J. Sell, U. Schmitt, T. Zimmermann, and B. Dawson (1998). Radial striation of the S2 layer in mild compression wood tracheids of pinus radiata. *Holzforschung*, 52(6):563–566.

Sisson, W. A. (1935). X-ray studies of crystallite orientation in cellulose fibers. *Ind.*

Eng. Chem., 27(1):51–56.

Sjöström, E. (1981). *Wood Chemistry: Fundamentals and Application*. Academic Press, New York.

Sjöstrøm, E. and R. Alén (eds.) (1999). *Analytical Methods in Wood Chemistry, Pulping, and Papermaking*. Springer Series in Wood Science. Springer, Berlin.

Sjöström, E. and U. Westermark (1999). Chemical composition of wood and pulps: Basic constituents and their distribution. In: Sjöstrøm and Alén (1999), chapter 1, pages 1–19.

Sobue, N., N. Hirai, and I. Asano (1971). Studies on structure of wood by X-ray. II. Estimation of the orientation of micelles in cell wall. *Mokuzai Gakkaishi*, 17(2):44–50.

Sovari, J., V. Pietarila, A. Nygren-Konttinen, A. Klemola, E. J. Laine, and E. Sjostrom (1983). Attempts at isolating and characterizing secondary wall and middle lamella from spruce woods (Picea abies). *Paperi ja Puu*, 65(3):117–121.

Spencer, A. J. M. (1980). *Continuum Mechanics*. Longman Group Limited, London.

Sporne, K. R. (1965). *The Morphology of Gymnosperms*. Hutchison & Co., London.

Srinavasan, P. S. (1942). The elastic and thermal properties of timber. *Journal of the Indian Institute of Science*, 23B, Part II:222–314.

Stamm, A. J. (1964). *Wood and Cellulose Science*. Ronald Press Co., New York.

— (1969). Correlation of structural variations of lignins with their specific gravities. *Tappi*, 52(8):1498–1502.

Stamm, A. J. and H. T. Sanders (1966). Specific Gravity of the Wood Substance of Loblolly Pine as Affected by Chemical Composition. *Tappi*, 49:397–400.

Stamm, A. J. and M. Seborg (1935). Adsorption compression in cellulose and wood. I. Density measurements in benzene. *J. Phys. Chem.*, 39:133–142.

Stol, K. (1996a). Adjacent cells with different S2 microfibril angles. Technical report, Department of Mechanical Engineering, University of Canterbury.

— (1996b). Assessing the effect of partial cyclic constraints. Technical report, Department of Mechanical Engineering, University of Canterbury.

— (1996c). Voronoi model. Technical report, Department of Mechanical Engineering, University of Canterbury.

Stol, K. A. (1995). Finite Element Shell Analysis of Cyclical Cellular Structures with ANSYS 5.0. A report submitted to Prof J. Astley on work done while employed over the summer.

Stone, J. E., A. M. Scallan, and P. A. V. Ahlgren (1971). The ultrastructural distribution of lignin in tracheid cell walls. *Tappi*, 54(9):1527–30.

Stuart, S.-A. and R. Evans (1995). X-ray diffraction estimation of the microfibril angle variation in eucalypt wood. *Appita*, 48(3):197–200.

Su, X. W. and F. Z. Cui (1999). Hierarchical structure of ivory: from nanometer to centimeter. *Materials Science & Engineering C: Biomimetic Materials, Sensors &*

Systems, 7(1):19–29.

Sugiyama, J., H. Harada, H. Saiki, and S. Sudo (1984). Crystalline ultrastructure of cellulose microfibrils in Valonia macrophysa.

Sugiyama, J., T. Okano, H. Yamamoto, F. Horii, and H. Odani (1990). Crystal Structure of Native Celluloses Observed by Electron and X-ray Diffraction. *IAWA Bulletin*, 11(2):137.

Sugiyama, J., Y. Otsuka, H. Murase, and H. Harada (1986). Toward direct imaging of cellulose microfibrils in wood. *Holzforschung*, 40 (Supplement):31–36.

Sugiyama, J., R. Vuong, and H. Chanzy (1991). Electron diffraction study on the two crystalline phases occurring in native cellulose from an algal cell wall. *Macromolecules*, 24:4168–4175.

Tadmor, E. B., R. Phillips, and M. Ortiz (2000). Hierarchical modeling in the mechanics of materials. *International Journal of Solids and Structures*, 37(1–2):379–389.

Takabe, K., M. Fujita, H. Harada, and H. Saiki (1983). Changes in the composition and the absolute amount of sugars with the development of Cryptomeria tracheids. *Mokuzai Gakkaishi*, 29(3):183–189.

Takabe, K., K. Fukazawa, H. Harada, and M. G. Paice (1989). Deposition of cell wall components in conifer tracheids. In: Lewis and Paice (1989), pages 47–66.

Takabe, K., T. Miyauchi, and K. Fukazawa (1992). Cell wall formation of compression wood in todo fir (Abies sachalinensis) - I. Deposition of polysaccharides. *IAWA Bulletin*, 13(3):283–296.

Takahara, S., T. Nobuchi, H. Harada, and H. Saiki (1983). Wall structure of parenchyma cells surrounding axial resin canals in the wood of European spruce. *Journal of the Japan Wood Research Society*, 29(5):355–360.

Takano, N., Y. Uetsuji, Y. Kashiwagi, and M. Zako (1999). Hierarchical modelling of textile composite materials and structures by the homogenization method. *Modelling & Simulation in Materials Science & Engineering*, 7(2):207–231.

Takiya, K., H. Harada, and H. Saiki (1976). The formation of the wart structure in conifer tracheids. *Bulletin of the Kyoto University Forests*, (48):187–191.

Tanaka, F. and T. Koshijima (1984). Orientation distributions of cellulose crystallites in *Pinus densiflora*. *Wood Science and Technology*, 18:177–186.

Tanaka, F., T. Koshijima, and K. Okamura (1981). Characterization of cellulose in compression and opposite woods of a *Pinu densiflora* tree grown under the influence of strong wind. *Wood Science and Technology*, 15:265–273.

Tang, R. C. (1973). The microfibrillar orientation in cell-wall layers of Virginia pine tracheids. *Wood Science*, 5(3):181–186.

Tang, S. (1997). Random generation of wood cell mesh using statistical data. Internal Report, Dept. Mech. Eng., UoC.

Tashiro, K. and M. Kobayashi (1985). ? *Polym. Bull.*, 14:213–218.

— (1991). Theoretical evaluation of three-dimensional elastic constants of native and regenerated celluloses: role of hydrogen bonds. *Polymer*, 32(8):1516–1526.

— (1996). Molecular theoretical study of the intimate relationships between structure and mechanical properties of polymer crystals. *Polymer*, 37(10):1775–1786.

Tashiro, K., M. Kobayashi, and H. Tadokoro (1978). ?? *Macromolecules*, 11:904.

Taya, M. and R. J. Arsenault (1989). *Metal matrix composites : thermomechanical behavior*. Pergamon Press, Oxford.

Terashima, N., K. Fukushima, L.-F. He, and K. Takabe (1993). Comprehensive Model of the Lignified Plant Cell Wall. In: *Forage Cell Wall Structure and Digestibility*, chapter 10. ASA-CSSA-SSSA, 677 S. Segoe Rd., Madison, WI 53711, USA.

Timell, T. E. (1961). Isolation of galactoglucomannans from the wood of gymnosperms. *Tappi*, 44(2):88–96.

— (1967). Recent progress in the chemistry of wood hemicelluloses. *Wood Science and Technology*, 1(1):45–70.

— (1978). Helical thickenings and helical cavities in normal and compression woods of Taxus baccata. *Wood Science and Technology*, 12(1):1–15.

— (1982). Recent progress in the chemistry and topochemistry of compression wood. *Wood Science and Technology*, 16(2):83–122.

— (1986a). *Compression wood in Gymnosperms.*. Springer-Verlag, Berlin. Three volumes.

— (1986b). Wood: chemical composition. In: Bever, M. B. (ed.), *Encylopedia of Materials Science and Engineering*. Pergamon Press, Oxford.

Torquato, S. (1991). Random heterogenous media: Microstructures and improved bounds on effective properties. *Appl. Mech. Rev.*, 44(2):37–76.

— (2000). Modeling of physical properties of composite materials. *International Journal of Solids and Structures*, 37(1–2):29–44.

Treiber, E. (1957). *Die Chemie der Pflanzenzellwand*. Springer, Berlin.

Treloar, L. R. G. (1953). The adsorption of water by cellulose and its dependence on applied stress. *Trans. Faraday Soc.*, 49:816.

— (1960). Calculation of elastic moduli of polymer crystals III: Cellulose. *Polymer*, 1(3):290–303.

Truesdell, C. and W. Noll (1965). The Non-linear Field Theories of Mechanics. In: *Encyclopedia of Physics*, volume Vol. III/3. Springer-Verlag.

Truesdell, C. and R. Toupin (1960). The Classical Field Theories. In: *Encyclopedia of Physics*, volume Vol. III/1. Springer-Verlag.

Tsai, S. W. (1980). *Introduction to composite materials*. Technomic Publishing Company, Westport, Conneticut 06880.

Tsehaye, A., A. H. Buchanan, R. Meder, R. H. Newman, and J. C. F. Walker (1998). Microfibril angle: determining wood stiffness in radiata pine. In: Butterfield, B. G.

(ed.), *Microfibril Angle in Wood*. IAWA/IUFRO.

Tsoumis, G. (1991). *Science and Technology of Wood: Structures, Properties, Utilization*. Van Nostrand Reinhold, New York.

Tucker III, C. L. and E. Liang (1999). Stiffness predictions for unidirectional short-fiber comosites: review and evaluation. *Composites Science and Technology*, 59:655–671.

Uhlin, K. I., R. H. Atalla, and N. S. Thompson (1995). Influence of hemicelluloses on the aggregation patterns of bacterial cellulose. *Cellulose*, 2:129–144.

Uprichard, J. M. (1991). Chemistry of wood and bark. In: Kininmonth and Whitehouse (1991), chapter 4.

van der Hart, D. L. and R. H. Atalla (1984). Studies of microstructure in native celluloses using solid-state 13C NMR. *Macromolecules*, 17:1465–1472.

Verbelen, J. P. and D. Stickens (1995). *In vivo* determination of fibril orientation in plant cell walls with polarization CSLM. *J. Microscopy*, 177(1):1–6.

Verhoff, S. and W. Knigge (1976). The size, number and distribution of warts on the radial wall of the tracheids of Fir (Abies alba M.). *Holz als Roh- und Werkstoff*, 34(5):175–180.

Vieville, P. and D. Guitard (1996). Numerical simulation of the relation between microstructure and anisotropy of wood at various levels of heterogeneity. *Annales des Sciences Forestieres*, 53(6):1137–1151.

Vincent, J. F. V. (1998). Structure of Wood. *Current Opinion in Solid State & Materials Science*, 3:228–231.

— (1999). From cellulose to cell. *Journal of Experimental Biology*, 202:3263–3268.

Voigt, W. (1889). Über die Beziehung zwischen den beiden Elastizitätskonstanten isotroper Körper. *Wied. Ann.*, 38:573–587.

Wada, M. and T. Okano (1999). Crystalline phase transition from cellulose I_α to I_β by heat treatment. In: *10th International Symposium on Wood and Pulping Chemistry. Yokohama, Japan June 7–10, 1999*, volume III, pages 142–145.

Wada, M., J. Sugiyama, and T. Okano (1994). The Monoclinic Phase is Dominant in Wood Cellulose. *Mokuzai Gakkaishi*, 40(1):50–56.

Walpole, L. J. (1969). On the overall elastic moduli of composite materials. *J. Mech. Phys. Solids*, 17:235–251.

Wangaard, F. F. (ed.) (1981). *Wood: Its Structure and Properties*. Pennsylvania State University, University Park, PA.

Ward, I. M. (ed.) (1997). *Structure and properties of oriented polymers*. Chapman & Hall, London, 2nd edition.

Wardrop, A. B. (1952). The low-angle scattering of X-rays by conifer tracheids. *Textile Research Journal*, 22(4):288–91.

— (1957a). The organization and properties of the outer layer of the secondary wall in conifer tracheids. *Holzforschung, Berlin*, 11(4):102–10.

— (1957b). The phase of lignification in the differentiation of wood fibers. *Tappi*, 40(4):225–43.

— (1963). Morphological factors involved in the pulping and beating of wood fibres. *Svensk Papperstid.*, 66(7):231–47.

— (1964). The structure and formation of the cell wall in xylem. In: Zimmermann (1964), pages 87–136.

Wardrop, A. B. and H. E. Dadswell (1951). Helical thickenings and micellar orientation in the secondary wall of conifer tracheids. *Nature, Lond.*, 168(4275):610–612.

— (1953). The development of the conifer tracheid.

Wardrop, A. B. and G. W. Davies (1962). Wart structure of gymnosperm tracheids. *Nature (Lond.)*, 194(4827):497–498.

— (1964). The nature of reaction wood. VIII. The structure and differentiation of compression wood. *Aust. J. Bot.*, 12(1):24–38.

Wardrop, A. B. and H. Harada (1965). The formation and structure of the cell wall in fibres and tracheids. *Journal of Experimental Botany*, 16(47):356–71.

Wardrop, A. B. and R. D. Preston (1947). Organisation of the cell walls of tracheids and wood fibres. *Nature, Lond.*, 160(4078):911–913.

Warren, W. E. and A. M. Kreynik (1987). Foam Mechanics: The Elastic Response of 2-D Spatially Periodic Cellular Materials. *Mechanics of Materials*, 6:27–37.

Watanabe, U. (1998). Shrinking and Elastic Properties of Coniferous Wood in Relation to Cellular Structure. *Wood Research*, 85:1–47.

Watanabe, U., M. Fujita, and M. Norimoto (1998a). Transverse shrinkage of coniferous wood cells examined using replica method and power spectrum analysis. *Holzforschung*, 52(2):200–206.

Watanabe, U., M. Norimoto, M. Fujita, and J. Gril (1998b). Transverse shrinkage anisotropy of coniferous wood investigated by the power spectrum analysis. *Journal of Wood Science*, 44:9–14.

Watanabe, U., M. Norimoto, and T. Morooka (2000). Cell wall thickness and tangential Young's modulus in coniferous early wood. *J. Wood Sci.*, 46:109–114.

Watanabe, U., M. Norimoto, T. Ohgama, and M. Fujita (1999). Tangential Young's modulus of coniferous early wood investigated using cell models. *Holzforschung*, 53(2):209–214.

Watson, A. J. and H. E. Dadswell (1957). Papermaking properties of compression wood from *Pinus radiata*. *Appita*, 11:56–70.

Wegst, U. G. K. (1996). *The mechanical properties of natural materials*. Ph.D. thesis, Cambridge University, Cambridge.

Wellwood, R. W., G. Ifju, and J. W. Wilson (1965). Intra-increment physical properties of certain Western Canadian coniferous species. In: Jr, W. A. C. (ed.), *Cellular Ultrastructure of Woody Plants*, pages 539–549. Syracuse University Press.

Westermark, U., H. L. Hardell, and T. Iversen (1986). The content of protein and pectin in the lignified middle lamella/primary wall from spruce fibers. *Holzforschung*, 40(2):65–68.

Westermark, U., O. Lindbrandt, and I. Eriksson (1988). Lignin distribution in spruce (Picea abies) determined by mercurization with SEM-EDXA technique. *Wood Science and Technology*, 22(3):243–250.

Whistler, R. L. and C.-C. Chen (1991). *Hemicelluloses*, chapter 7, pages 287–319. In: Lewin and Goldstein (1991).

Whitney, J. M. and R. L. McCullough (1990). *Delaware Composites Design Encyclopedia - Volume 2: Micromechanical Materials Modelling*. Technomic Publishing Company, Inc., Lancaster, Pennsylvania, U.S.A.

Whitney, S. E. C., J. E. Brigham, A. H. Drake, M. J. Gidley, and J. S. G. Reid (1997). The interaction of mannan-based polysaccharides with bacterial cellulose. In: Jeronimidis, G. and J. F. V. Vincent (eds.), *Plant Biomechanics 1997. Conference Proceedings II: Posters*. Centre for Biomimetics, University of Reading, 1 Early Gate, Reading RG6 6AT, UK.

Willison, J. H. M. and R. M. Abeysekera (1985). On the form and arrangement of cell wall microfibrils. In: Robards, A. W. (ed.), *Botanical Microscopy 1985*, chapter 8, pages 181–203. Oxford University Press, Oxford.

Wilson, J. W. and R. W. Wellwood (1965). Intra-increment chemical properties of certain Western Canadian coniferous species. In: Jr, W. A. C. (ed.), *Cellular Ultrastructure of Woody Plants*, pages 551–559. Syracuse University Press.

Wilson, K. and D. J. B. White (1986). *The Anatomy of Wood: Its Diversity and Variability*. Stobart and Son Ltd.

Wloch, W. and Z. Hejnowicz (1983). Location of laricinan in compression wood tracheids. *Acta Societatis Botanicorum Poloniae*, 52:3–4.

Wu, C.-T. D. and R. L. McCullough (1977). Constitutive relationships for heterogenous materials. In: Holister, G. S. (ed.), *Developments in composite materials*, volume 1, pages 119–187. Applied Science Publishers, London.

Yamamoto, H., F. Horii, and H. Odani (1989). Structural changes of native cellulose crystals induced by annealing in aqueous alkaline and acidic solutions at high temperatures. *Macromolecules*, 22:4130–4132.

Yamamoto, H., T. Okuyama, and M. Yoshida (1993). Method of Determining the Mean Microfibril Angle of Wood over a Wide-Range by the Improved Caves Method. *Mokuzai Gakkaishi*, 39(4):375–381.

Yamanaka, K. (1969). *The Structure of Vessel Walls of Several Tropical Woods*. Master's thesis, Kyoto University.

Yang, G. Y., J. Kabel, B. van Rietbergen, A. Odgaard, R. Huiskes, and S. C. Cowin (1998). The anisotropic Hooke's law for cancellous bone and wood. *Journal of*

Elasticity, 53(2):125–146.

Ye, C. (1999). Photopolarimetric measurement of single, intact pulp fibers by Mueller matrix imaging polarimetry. *Applied Optics*, 38(10):1975–1985.

Ye, C., M. O. Sundstrom, and K. Remes (1994). Microscopic transmission ellipsometry: measurement of the fibril angle and the relative phase retardation of single, intact wood pulp fibers. *Applied Optics*, 33(10):6626.

Ye, C. and O. Sundström (1997). Determination of S2-fibril-angle and fiber-wall thickness by microscopic transmission ellipsometry. *Tappi*, 80(6):181–190.

Ying, L., D. E. Kretschmann, and B. A. Bendtsen (1994). Longitudinal shrinkage in fast-grown loblolly pine plantation wood. *Forest Products Journal*, 44(1):58–62.

Yumoto, M. (1984). The trabecula and its related structures. *Research Bulletins of the College Experiment Forests, Hokkaido University*, 41(1):205–259.

Zhang, J. and N. Katsube (1995). A hybrid finite element method for heterogenous materials with randomly dispersed rigid inclusions. *Int. J. Num. Meth. engr*, 38:1635–1653.

Zhang, Y. Z., X. L. Chen, J. Liu, P. J. Gao, D. X. Shi, and S. J. Pang (1997). Size and Arrangement of Elementary Fibrils in Crystalline Cellulose Studied with Scanning-Tunneling-Microscopy. *Journal of Vacuum Science and Technology, B*, 15(4):1502–1505.

Ziegler, G. A. and F. C. Beall (1974). Water vapor sorption by softwood cell wall constituents. *Research Briefs, School of Forest Resources, Pennsylvania State University*, 8(2):10–12.

Zienkiewicz, O. C. and R. L. Taylor (2000). *The Finite Element Method. Fifth Edition. Volume 1: The Basis*. Butterworth Heinemann, Oxford.

Zimmermann, M. G. (1997). Global Bifurcations and Chaotic Dynamics in Physical Applications. Comprehensive Summaries of Uppsala Dissertations from the Faculty of Science and Technology 279.

Zimmermann, M. H. (ed.) (1964). *The Formation of Wood in Forest Trees*. Academic Press, New York.

Zobel, B. J. and J. R. Sprague (1998). *Juvenile wood in forest trees*. Springer series in wood science. Springer, Berlin.